Journal of Agricultural Engineering

VOL. 59, No. 1, January-March 2022

INDIAN SOCIETY OF AGRICULTURAL ENGINEERS

Publication Enquiries

The Journal of Agricultural Engineering, a publication of the Indian Society of Agricultural Engineers, is published in four issues per year. This journal is not responsible for statements and opinions expressed by the authors of papers published in it. Reprints may be made from this publication on the condition that full credit is given to the author(s) and the Journal of Agricultural Engineering.

All communications regarding the publication or submission of manuscripts should be addressed to The Chief Editor, Journal of Agricultural Engineering at the address given below or at the email address mentioned above.

Subscription Rate

Annual subscription: Rs. 3000/- or US $400 ($ 50 extra for air mail dispatch)

Per copy   : Rs. 800/- or US $ 150 ($ 25 extra for air mail dispatch)

Payment are to be made by crossed cheque/ draft including bank charges in favour of "Indian Society of Agricultural Engineers", payable at New Delhi, India, and directly sent to the Society Headquarters at the address given below. Online payment gateway details are available on the website of the Society.
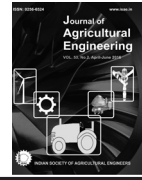
Indian Society of Agricultural Engineers

G-4, National Societies Block, National Agricultural Science Centre Complex, Dev Prakash Shastri Marg, Pusa Campus, New Delhi – 110012, India

Tel / Fax: 091-11-21520143
E-mail: isae1960@gmail.com
Web: www.isae.in

Performance Assessment of Tractor-operated Bund Former for Mulched Field

Ashish Sood[1*], Anoop Kumar Dixit[2], Manpreet Singh[3], Rajesh U. Modi[4], Arshdeep Singh[5] and Apoorv Prakash[5]

[1]Senior Research Fellow, Division of Agricultural Engineering, ICAR- Indian Agricultural Research Institute, New Delhi; [2]Principal Scientist, [3]Extension Scientist, [5]Scientist, Department of Farm Machinery and Power Engineering, Punjab Agricultural University, Ludhiana, Punjab, India; [4]Scientist, Division of Agricultural Engineering, ICAR-Indian Institute of Sugarcane Research, Lucknow, Uttar Pradesh, India. *Corresponding author email address: ashishsood27@gmail.com

Article Info	ABSTRACT
	Managing paddy field loaded with straw before wheat sowing in paddy-wheat crop production system is cumbersome due to various operations involved in the process. Bund forming for irrigation remains difficult among these operations due to mulched conditions. Simultaneous removal of straw (up to 1.25 m width), soil pulverization, and trapezoidal-shaped soil bund forming in one pass is required. Field evaluation of a tractor-operated bund former for mulched fields was conducted to observe the effects of rotor speed ratios (3:1, 4:1, 5:1), opening width of bund forming plates (270, 340, 410 mm), and straw loads (4.0-4.5, 6.0-6.5 t.ha^{-1}) on the pulverization index (mm), height of bund (mm), width of bund (mm), fuel consumption (l.h^{-1}) and field capacity (ha.h^{-1}) of the machine. The effects of rotor speed ratio, opening width of bund forming plates, and straw load were significant ($p<0.05$) on pulverization index, bund height, bund width, and fuel consumption. Best performances were obtained at rotor speed ratio of 4:1 and bund forming plates opening width of 340 mm under both straw loads. This combination gave the optimum height of bund (277.6 mm), bund width (720 mm), pulverization index (12.76 mm), and fuel consumption (7.05 l.h^{-1}) under both straw loads. The effective field capacity of the tractor-operated bund former was 1.17 ha.h^{-1} at forward travel speed of 1.5 km.h^{-1}. The operational cost of the bund former was 792.36 ₹.ha^{-1}.

Globally, paddy cultivation is under 164.19 Mha area with paddy production is 756.74 Mt with expected straw production of 938 Mt for the year 2020 (Anon., 2022). In South and South-East Asia, countries as China, India, Indonesia, Bangladesh, and Vietnam are the major paddy producing countries. In India, the area under paddy is about 45.00 Mha generating 178.30 Mt of paddy straw (Anon., 2022). Rice-wheat cropping system is being followed in the Indo-Gangetic plains of India covering about 10.5 Mha area, out of which 39.05% (4.1 Mha) area is in North-western (NW) states including Punjab, Haryana, Uttarakhand, and Western Uttar Pradesh. Presently, in the Northern states of India as in Punjab, Haryana, and Uttar Pradesh there is a huge

surplus of paddy straw (about 140 Mt), out of which 65.7% (92 Mt) straw is annually burnt (Bhuvaneshwari *et al*., 2019). The area under paddy cultivation in Punjab was about 3.06 Mha with paddy production of about 20.07 Mt, generating 20.17 Mt of paddy straw (Anon., 2020a). About 50% of paddy straw in Punjab and 16.9% in Haryana (7.93 Mt) was burnt in the fields during the year 2018-19 (Anon., 2019a). Farmers chose to burn paddy straw in the field due to a lesser window period (15 days) between harvesting of paddy crop and sowing of wheat (Modi *et al*., 2020). Paddy straw is not being used as animal fodder in Northern India due to high silica content (Kumar *et al.,* 2014). Hence, timely management of paddy residues (6.0-6.5

t.ha^{-1}) before sowing of wheat becomes a cumbersome job for the farmers. However, in the past 2-3 years the burning of paddy straw residue has been reduced due to the availability of farm machinery to manage it in the fields within the short window period.

Ex-situ and *in-situ* methods are normally used as straw management techniques. In the former method, paddy straw is either removed or collected from the harvested field. This is done by machines like farm mulch collector, balers, and head feed combines. A farm mulch collector removes loose straw followed by straw loading into a trolley attached at the rear. The latter method (*In-situ*) includes incorporating technique in which the operation of straw chopping machinery is followed by tillage machinery for straw mixing in the soil. The chopped straw can be mixed into the soil with a reversible mould board plough or equipment like disc harrow, cultivator, and planker (Mahal *et al*., 2019; Modi *et al*., 2020). Mulching is another useful method of *in-situ* straw management technique. Mulching is the retention of straw over the soil surface which facilitates various benefits like conservation of soil moisture, regulates thermal regimes, diminishing weed growth, improvement in soil health and rise in crop yield as well as decreased consumption of irrigation water (Anon., 2010; Modi *et al.,* 2020), and is also beneficial under rainfed or irrigated conditions (Anon., 2010). Happy seeder is popular for mulching paddy straw and simultaneous wheat sowing. The area under Happy Seeder in Punjab was 25,600 ha and 4,74,000 ha in the year 2017 and 2018, respectively (Mahal *et al*., 2019).

The time period between harvesting of paddy and sowing of successive crop (known as window period) is limited to 2-3 weeks only, and requires completion of residue management, land preparation, and bund formation in a field. Among these, bund forming requires significant energy and time as number of individual operations (straw removal, mulching, bund formation) are performed separately. Therefore, it becomes difficult to carry out all these operations in a limited interval of time (Anon., 2019b). It is recommended to prepare 20 and 40 plots (*kiara*) per hectare in heavy textured and light textured soils, respectively, for efficient use of irrigation water in wheat fields (Anon., 2019c). This can be achieved by constructing proper bunds around the plots in the fields. Currently, the bunds are made using forming board-type, mouldboard-type, or using disc ridger. Creating bunds involves numerous operations such as manual removal of straw from field, followed by rotavator operation and then use of disc type or forming board type bund former. The residue on ground hinders the formation of bunds in the field as they cause breakage of bunds after application of irrigation water. The residue also prevents compaction of the soil during bund making process. Due to this the farmers do not put bunds in the fields and go with existing bunds in paddy fields that are larger in size. The bunds in field covering large area have negative impact on wheat crop as the quantity of water applied to soil is more which results in yellowing of wheat because of anaerobic conditions (Anon., 2003).

To form bund in a field, the required area for bund formation should be straw free as well as pulverized. The issue is of major concern because they disturb the sowing operation of the successive crop which can further lead to yield and productivity losses. Farmers normally use disc-type or rectangular board-type bund formers in the region. Among these, the disc-type is being directly used in the mulched fields to form bund, but it fails to deliver straw-free and lesser porous bund. On the other hand, rectangular-type bund former is incapable to work in mulch fields due to prior rotary tilling requirement. This happens because of straw mixing into a bund due to rolling disc action (Nkakini, 2014). Additional straw removal operation using human labour and rotary tilling is required for such bund formers to work, which make the bund forming operation costly and inefficient.

In view of the above-mentioned factors, a tractor-operated bund former operable after paddy harvesting (either combined with Super SMS or without Super SMS) and before wheat sowing in the same field was developed at Prototype Production Centre, Department of Farm Machinery and Power Engineering, Punjab Agricultural University, Ludhiana (Sood, 2020). The developed tractor-operated bund former is able to simultaneously perform straw removal, soil pulverization, and trapezoidal-shaped soil bund forming in one pass. This study was undertaken to carry out performance assessment of the tractor-operated bund former under actual straw mulched field conditions.

MATERIALS AND METHODS

Description of Tractor-operated Bund Former

A tractor-operated bund former is a mounted-type machine that makes bunds in mulched fields. It performs three operations such as straw removing (up to 1.25 m width), followed by soil pulverization, and

trapezoidal shaped soil bund formation simultaneously in one pass.

The machine consisted of a mulcher, rotavator, and bund former unit operating simultaneously. The mulcher had horizontally rotating shaft (168 mm in diameter) perpendicular to the direction of travel on which 10 flat flail-type blades without serrations (156 mm 100 mm 4 mm) rotated in vertical plane at 1100 rpm in a direction parallel to the direction of travel. The blades were bent at an angle of 22° from its straight surface to the curved tip. This angle assisted in an updraft of the chopped straw, and thus lifting it to throw out of the chute/opening. The blades acted on standing stubble through impact action which picked the stubble and loose straw to throw it out with centrifugal force from the chute opening on the bund formed. The mulcher rotor rotated at 1100 rpm in the direction opposite to forward travel of the tractor, and removed the straw from front of rotavator operational width of 1250 mm.

The rotavator (88 mm in diameter), second working unit, had C-type blades (total 30 blades) arranged in pairs on each side of the flange alternately in staggered position. The overlapping range of the blades mounted on adjacent flanges was 35 - 40 mm and operated at rotational speed of 210 rpm. A rubber flapper (6 mm thickness) was used for separation in between the

rotavator and mulcher unit.

The bund forming unit ($830 \times 320 \times 7$ mm) was placed at the rear, and consisted of a main frame, holding mild steel angles, and a pair of rectangular plates on both sides. The plates had outward bends near the longer edges at equal distance (550 mm) from centre of plates for shaping and compaction the bund. The plates were inclined towards each other with specified distance ranging between 270-410 mm at the rear end of the frame. The side of the plates with wider opening had same width as that of rotavator (1250 mm).

According to Sood (2020), the machine developed at Prototype Production Centre, Punjab Agricultural University, Ludhiana was intended to work under straw mulch field conditions while facilitating bund forming. The machine left the soil straw free to allow easy binding of pulverized soil using bund forming plates. Table 1 gives brief machine specifications. A view of tractor-operated bund former is presented in Fig.1.

The machine was fabricated at Prototype Production Centre, Department of Farm Machinery and Power Engineering, Punjab Agricultural University, Ludhiana. Initially, CAD model of the frame was prepared and mild steel plates (8 mm thick) were cut using laser cutters. After assembling the frame, a locally procured

Table 1. Technical specifications of developed bund former

| Sl. No.	Description	Specifications			
		Gear box	Rotavator	Mulcher	Bund former
1.	Type	T-type	Mounted using 3-point linkage		
2.	Power source, kW	PTO/ 31.66			
3.	Blade/ Plate type	-	C	Flat	Rectangular
4.	Number of blades or plates/ flanges	-	30/5	10	2
5.	Diameter of rotor pipe, mm	-	88	168	-
	Diameter of pulleys, mm	-	-	203.2; 254; 330.2	-
6.	Number of teeth on sprockets	-	18;12	-	-
7.	Overall dimensions, mm	$200 \times 200 \times 230$	$1150 \times 210 \times 66$	$1240 \times 208 \times 46$	$830 \times 320 \times 7$
8.	Power Transmission ratio/ operational speed, rpm	1:1	210	1100	-
9.	Medium for power transmission	Helical bevel gears	Double strand sprockets with duplex chains (20 B)	Dual V -pulleys and belts (C63 section)	-
10.	Gross weight, kg	2785			
11.	Net weight, kg	675			
12.	Material used				
	Housing/ plates	Cast iron	Mild steel	Mild steel	Mild steel
	Gears/ blades	Cast carbon steel	High carbon steel	Mild steel	-
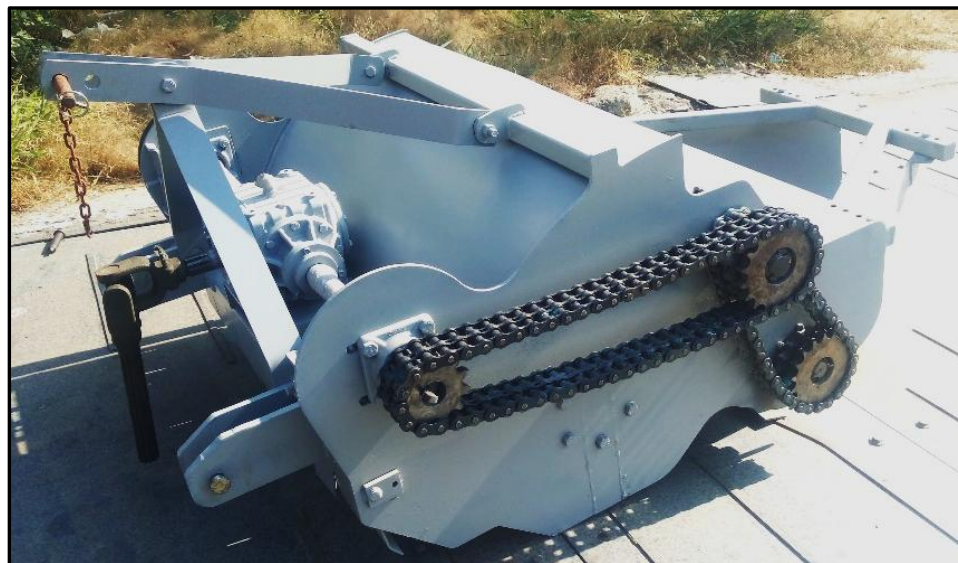
Fig. 1: A stationary view of tractor-operated bund former

gearbox was fitted onto the structure. One side of the shaft was coupled with sprockets, while the other was coupled with pulleys. Further, the mulcher rotor was integrated with the frame using ball bearings supporting each end of the rotor. Flat blades (mild steel) were screwed over the periphery of the rotor. The rotavator was fabricated by fitting flanges at equal distance (250 mm) over the rotor hollow shaft. C-type blades made of high carbon steel were alternately screwed onto the flanges. The rotor was supported with the frame using tapered roller bearings. The bund forming unit was fabricated by fitting rectangular-shaped mild steel plates on angle iron that narrowed down towards the rearmost side. To transmit power to the mulcher and rotavator, double v-grooved cast iron pulleys (203.2, 254.0, and 330.2 mm in diameter) and belts (C 63 section) were used for the former and a pair of double-strand sprockets (18 and 12 teeth) with duplex chain (20 B) for the latter were employed.

Field Evaluation Procedure

Experimental site and field layout

Field experiments were performed to evaluate the developed tractor-operated bund former under mulch conditions in paddy fields at University Seed Farm, Ladhowal, Punjab Agricultural University, Ludhiana (75°45'25.0"E and 30°58'24.5' N). The soil type was silt loam having sand, silt, and clay content as 14.44%, 74.94%, and 10.62%, respectively. The soil moisture content of the field ranged 13-14% (d.b.). The machine was operated in field with standing stubble of average height of 540 mm after 15 days of combine harvesting of paddy crop.

The bund former was attached with three-point hitch and PTO shaft of a 37.3 kW tractor (John Deere- 5310). The depth of operation was maintained at about 100 mm, and the speed of operation was maintained at 1.2 -1.5 km.h^{-1}.

Experimental Design

The first field considered had dimensions as 44 m × 15 m while the other field had dimensions of 25 m × 55 m, both located at the University Seed Farm, Ladhowal. The layout of the experiments was done randomly. The purpose of determining the dependent parameters was fulfilled by replicating each treatment thrice. The bunds were formed in a random order of treatments, each having length of 7.0 m. A total of 54 bunds was formed in each field using 18 different treatments with three replications.

Parameters as rotor speed ratio, opening width of bund forming plates, and straw load in the field affects the performance of a bund former (Sood, 2020). Therefore, field evaluation of the developed bund former was done under different straw loads at variable speed ratio of mulcher rotor and rotary tiller rotor. Rotor speed ratios of 3:1, 4:1, and 5:1 was maintained by using pulleys of diameter 203.2, 254.0, and 330.2 mm, respectively, and the plates adjusted with an angle iron by changing its position (35 mm from each end) using holes at ends of the machine frame. The intermediate distance between two holes (diameter of 17 mm) was kept as 35 mm. Details of independent parameters are given in Table 2.

Table 2. Details of independent parameters selected for the study

Sl. No.	Parameter	Description	Level	Remarks
1.	Rotor speed ratio (R)	Ratio of rotational speed of mulcher to rotavator (3:1, 4:1 and 5:1)	3	Based on existing mulcher-rotor rotational speed ratio
2.	Opening width of bund forming plates (W)	Adjustment of distance between the plates (270, 340 and 410 mm)	3	Based on desired bund dimensions
3.	Straw load (L)	Straw load (4.0-4.5 t.ha^{-1} and 6.0-6.5 t.ha^{-1})	2	Based on preliminary evaluation

The bund size (bund height, bund width) was determined to assess bund quality. Pulverization index, fuel consumption, soil bulk density, and field capacity of the machine were determined.

Measurement of Parameters

Straw load

The straw load in the field was determined using a rectangular square iron frame (3.0 mm thick) having dimensions of 1.0 m × 1.0 m. The iron frame was placed randomly in the field at three locations (three samples) and the straw enclosed within the 1.0 m^2 area was collected. The straw load was calculated as weight of straw per square meter for each sample, followed by average of all samples.

The collected straw was dried in a laboratory oven (Accumax, thermostatic type, capacity: 45 l, heat load: 1.50 kW, temperature range: 50 -200˚ C) for 24 h, and the samples were weighed using a digital weighing balance (Fulcrum make, range 0-10 kg, accuracy 1.0 g) before and after drying.

Moisture content of straw samples was determined using the Eq. 1.

$$M.C.\,(\%) = \frac{\text{Weight of straw before drying (g)} - \text{Weight of straw after drying (g)}}{\text{Weight of straw before drying (g)}}$$

$$…(1)$$

The lengths of stubble and removed loose straw was measured using Omega make steel ruler (0-1.0 m) having least count of 1.0 mm before and after the operation of machine.

Pulverization index

The amount of soil pulverization (pulverization index, PI) was measured by determining the mean mass diameter of clod (MMD) using sieve analysis method. Soil samples were collected from top of each formed bund using a 500 g mild steel soil sampler

(150×150×100 mm) by removing straw thrown by chopping unit lying above the bund. A set of brass sieves (Efficacy make) consisting of 18 sieves of sizes ranging from 0.425 mm to 75.0 mm was used. The weight of sample (Fulcrum make digital weighing scale, range: 0-10 kg, accuracy: 1.0 g) was recorded after drying in oven for 24 h. After weighing, the dried samples were allowed to pass through sieves and eccentrically shaken. The weight of soil retained on each sieve including pan was recorded.

Pulverisation index (Mehta *et al.,* 2005) was calculated as:

$$PI = \frac{1}{W_T} \sum_{i=0}^{n} \overline{d_i}\, W_i \qquad …(2)$$

Where,

$\overline{d_i}$ = Average diameter of i and (i + 1)th sieve and $d_i < d_{i+1}$, mm,

W_i = Mass of soil retained on the ith sieve, g, and

$W_T = \sum_{i=0}^{n} W_i$ W_T = Total mass of soil sample, g.

$$…(3)$$

Bund height and width

The bund height was determined by placing a steel ruler (Omega make: 0-1.0 m, least count: 1.0 mm) vertically at endpoint of base span of bund on both sides. Another ruler was placed horizontally with one of its ends on the apex of the bund and the other end was intersected with the ruler placed vertically. Reading from the ruler at an intersecting point was noted.

Width of bund was recorded by keeping two rulers vertically at each endpoint on both side of the bund, and measuring the horizontal distance between the rulers.

Fuel consumption

Fuel consumed by the tractor during a field operation was noted by using a fuel meter (Aqua Metro Make, least count: 1.0 ml, working ambient temperature: (-)

25°C to (+) 70°C, flow pressure in pipe: <2500 kPa) fitted on the tractor fuel supply line. The readings (ml.s⁻¹) of fuel consumption of the tractor were taken during the field experiment for 20 m length of travel.

Soil bulk density

The bulk density (g.mm⁻³) was measured using a core soil sampler. The sampling was done by insertion of the sampler (diameter: 100 mm, height: 100 mm) into a bund. Samples were weighed and kept in laboratory oven (Accumax, thermostatic type, capacity: 45 l, heat load: 1.50 kW, temperature range: 50 -200˚ C) for 24 h at 105° C for drying. Dried sample were weighed again in order to determine the value of dry density. However, dry density determination requires moisture content to be known. The moisture content of soil was determined using the difference between wet weight and dry weight of soil sample. The given analytical formulas were followed for bulk density determination:

$$Volume\ of\ core\ =\ \frac{\pi}{4} \times Dc^2 \qquad …(4)$$

$$Wet\ Density\ (g.mm^{-3}) = \frac{Weight\ of\ wet\ excavated\ soil, g}{Volume\ of\ core,\ mm^3} \qquad …(5)$$

$$Dry\ Density\ (g.mm^{-3}) = \frac{Wet\ Density\ \times 100}{(Moisture\ content\ of\ soil + 100)} \qquad …(6)$$

Where,
Dc = diameter of core, mm.

Effective field capacity

The effective field capacity (E_f, ha.h⁻¹) of the machine was calculated by determining the total time taken per ha that was obtained by adding the theoretical time as well as the time consumed during turning, etc.

Field capacity of the bund former was determined by obtaining the number of bunds formed per ha by the machine as (Kepner *et al*., 2005):

$$Ef\ =\ 100(T_0/T_e + T_h + T_a) \qquad …(7)$$

Where,
T_0 = Theoretical time ha⁻¹, h,
T_e = $T_0 \times \frac{100}{K}$,
K = Percentage of actual implement used,
T_h = Time lost ha⁻¹ not proportional to area, h, and
T_a = Time lost ha⁻¹ proportional to area, h.

Cost of operation

The cost of operation was divided into fixed and variable costs. Fixed cost was determined by summing up, depreciation interest cost, taxes, insurance, and shelter costs based on particulars as fixed price of tractor and machine, life of machine (as per BIS code), and annual usage (h). The variable cost of the formation of bund in each treatment was computed by considering the input costs as fuel cost, labour cost, repair and maintenance cost, oil and lubrication cost. The depreciation of the machine along with tractor was calculated using the straight-line method.

The set of parameters assumed for cost evaluation were interest rate (12%), salvage value (10%), taxes, insurance and shelter (2% of price), labour wage rate (₹ 402.44 per day) and fuel (diesel) cost (₹ 66 per litre). The cost of operation was determined as per BIS code IS 9164 (BIS, 1979).

Statistical Analysis

The analysis of the data obtained through experiments was evaluated statistically using Statistical Analysis Software (SAS 9.3). The software's were used to determine the effect of independent parameters on the proposed dependent parameters. ANOVA with split-plot design was used for analysing the data. The probability (p value) was checked for its significance at 5% level of significance (α). If $p \leq \alpha$, then results were significant, whereas if $p > \alpha$ the results were non-significant.

RESULTS AND DISCUSSION

Description of Machine Operation under Mulch

The bund former was operated in combine harvested paddy field following Happy Seeder operation. After combine harvester operation, the field was demarcated by dividing it into compartments or *Kiaras* using bunds. The super SMS left loose straw into the field along with stubble. This straw was picked in vicinity of ground and tossed out of the chute opening of the mulcher. Further, as the mulcher cleared the residue it made way for rotary tiller for tillage that in turn guided the soil to the bund forming unit. After completion of the process, uniformly shaped raised soil granule structures in form of bunds with straw as a cover were left behind the machine.

A working view of the tractor-operated bund former and prepared bund in field are shown in Figs. 2-4.

Fig. 2: Working view of tractor-operated bund former

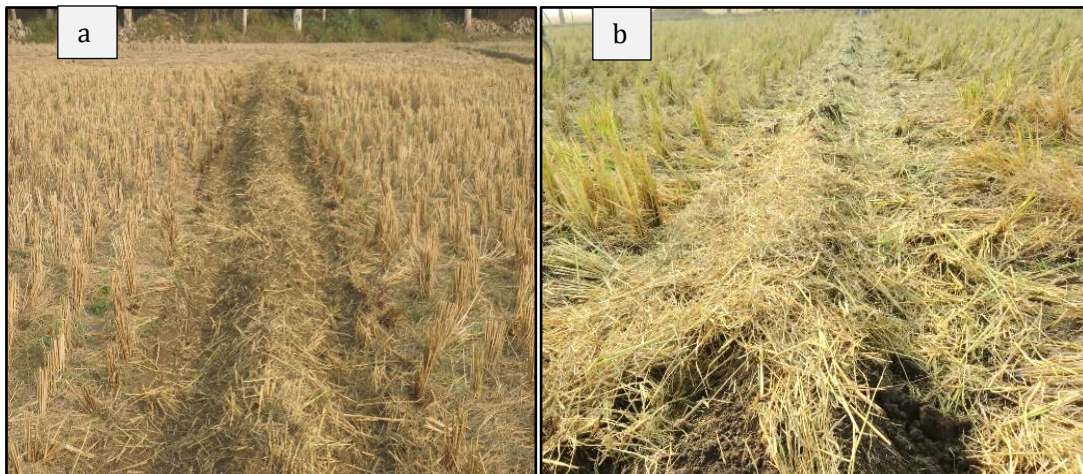**Fig. 3: Working view of tractor-operated bund former in field under straw load (a) 4.0-4.5 t.ha^{-1}, and (b) 6.0-6.5 t.ha^{-1}**

Fig. 4: Views of bunds formed by tractor-operated bund former under straw load of (a) 4.0-4.5 t.ha^{-1}, and (b) 6.0-6.5 t.ha^{-1}

Power Requirement of Tractor-operated Bund Former

The torque needed by rotavator and mulcher rotor for soil tillage and straw removal were the defining factors for determination of power requirement of the bund former. According to Sood (2020), 10 kW power is sufficient to operate rotavator and mulcher together having 1.25 m length each. Singh (2011) suggested that a tractor can produce a 16.70 kW power at 2000 engine rpm. However, the entire straw is being cleared by the mulcher, and the rotavator works deeper to extract soil volume that enhances load for operating the bund former in field. Hence, for safety reasons, factor of safety of 2 was appropriate (Sood, 2020). Additionally, for smoother operation and easy movement of machine in field, a 31.7 kW tractor was found to be suitable for proper operation of the bund former.
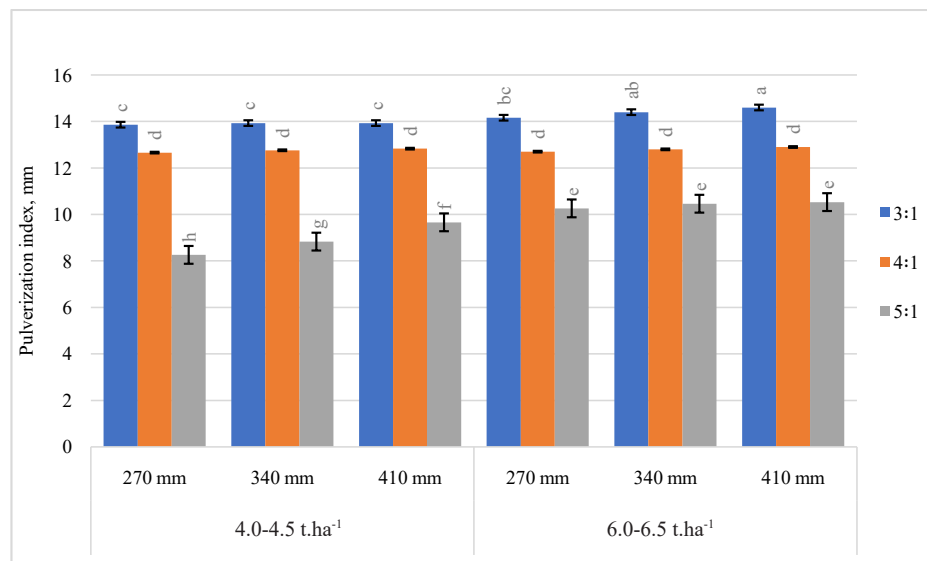
Soil Pulverization Index

Mean pulverization index (MMD) obtained during field evaluation of the tractor-operated bund former at three rotor speed ratio, three opening width of bund forming plates and two different loads are shown in Fig. 4.

The effect of rotor speed ratio, opening width of bund forming plates, and straw loads was significant ($p < 0.05$) on pulverization index, Table 3. It is clear from Fig. 5 that pulverization index decreased with increasing rotor speed ratio and increased opening width of bund

Table 3. ANOVA for effect of rotor speed ratio (R), straw load (L), and opening width of bund forming plates (W) on pulverization index

Source	DF	Type III SS	Mean Square	F-Value	Pr > F	S/NS
Replications	2	0.310	0.155	9.21	0.0007	S
Straw load (L)	1	6.134	6.134	364.50	<.0001	S
Rotor speed ratio (R)	2	0.618	0.309	18.37	<.0001	S
Opening width of bund forming plates (W)	2	189.467	94.733	5629.30	<.0001	S
L × R	2	1.604	0.802	47.67	<.0001	S
L × W	2	5.027	2.513	149.36	<.0001	S
R × W	4	0.143	0.0718	4.27	0.0227	S
L × R × W	4	0.774	0.193	11.50	<.0001	S

Note: DF: Degree of freedom, SS: Sum of square, S: Significant, NS: Non significant

(Same alphabets indicate the non-significance for a particular performance, $p > 0.05$)

Fig. 5: Effects of rotor speed ratio [(3:1), (4:1), (5:1)] and opening width of bund forming plates (270, 340, 410 mm) on pulverization index under straw load of 4.0-4.5 t.ha^{-1} and 6.0-6.5 t.ha^{-1}

forming plates under both levels of straw load. This was due to lower rotational speed ratio of mulcher and rotavator (3:1) which delivered coarse soil clods as compared to higher speeds of mulcher (1100 rpm) and rotavator (210 rpm) and vice versa**.** The minimum pulverization index (8.26 mm) was obtained for 270 mm opening width of the bund forming plates at 5:1 rotor speed ratio with 4.0 - 4.5 t.ha^{-1} straw load. The reason for lower pulverization index was higher rotational speed of rotavator (210 rpm) which provided proper tilth of soil resulting in finer soil clods. Higher rotational speed of rotavator (210 rpm) facilitated rotavator to perform effectively, and lesser opening width (270 mm) further broke the soil clods. A similar trend was observed for pulverization index under straw load of 6.0 - 6.5 t.ha^{-1}. The results were in affirmation with Libin *et al*. (2010), who stated that the rotational speed of rotavator at 250 rpm gave proper soil tilth.

Bund soil bulk density

Mean bund soil bulk density during field evaluation of the tractor-operated bund former at three rotor speed ratios, three opening widths of bund forming plates, and two straw loads are shown in Fig. 6. The effects of rotor speed ratio, opening width of bund forming plates, and straw load were significant ($p<0.05$) on bulk density of bund as shown in Table 4.

Bulk density of bund soil increased with increase in levels of rotor speed ratio from 3:1 to 4:1, but decreased at rotor speed ratio of 5:1. The maximum bulk density (0.00125 g.mm^{-3}) was obtained with 340 mm opening
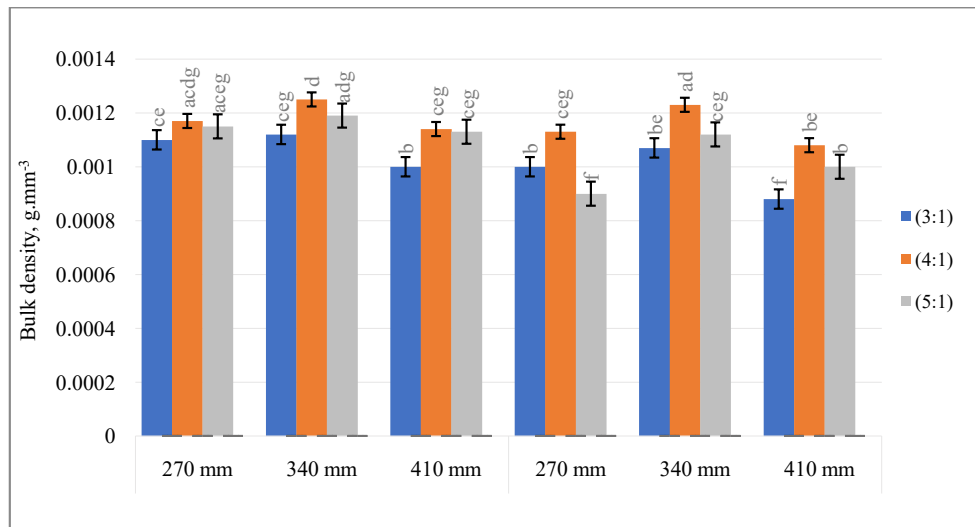
(Same alphabets indicate non-significance for a particular performance, p>0.05)

Fig. 6: Effects of rotor speed ratio [(3:1), (4:1), (5:1)] and opening width of bund forming plates (270, 340, 410 mm) on bulk density under straw load of 4.0-4.5 t.ha^{-1} and 6.0-6.5 t.ha^{-1}

Table 4. ANOVA for effect of rotor speed ratio (R), straw load (L), and opening width of bund forming plates (W) on bulk density

Source	DF	Type III SS	Mean Square	F Value	Pr > F	S/NS
Straw load (L)	1	0.0066	0.0066	5.73	0.0214	S
Rotor speed ratio (R)	2	0.0149	0.0074	6.42	0.0038	S
Opening width of bund forming plates (W)	2	0.1486	0.0743	63.92	<.0001	S
L × R	4	0.02726	0.00681	5.86	0.0008	S
L × W	2	0.02043	0.01021	8.79	0.0007	S
R × W	2	0.29853	0.14926	128.39	<.0001	S

Note: df: degree of freedom, ss: sum of square, s: significant, NS: Non significant
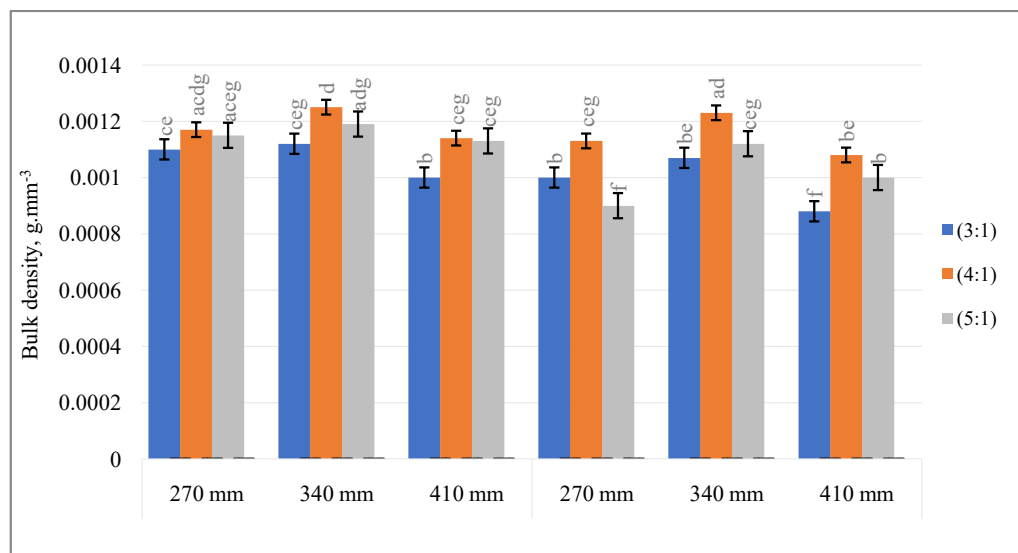
width of bund forming plates at rotor speed ratio of 4:1 under straw load of 4.0-4.5 t.ha^{-1}. Higher bulk density was due to the rotational speed of mulcher (710 rpm) and rotavator (180 rpm) allowed the mulcher to pick dense straw load without causing its interference with the tilled soil, and facilitated the rotavator to perform desired soil tilth that helped the bund forming plates to effectively held and bind the soil. The results were in affirmation with that of Xian-Jun and De-Ti (2009), who stated that bulk density under no residue conditions vary between 0.00125 -0.00128 g.mm^{-3}.

For rotor speed ratio of 5:1, lower bund soil bulk density (0.0009-0.00119 g.mm^{-3}) was obtained because of higher mulcher (1000 rpm) and rotavator rotational speed (210 rpm), as well as higher volume of soil pulverized by the rotavator causing restriction in soil flow from the width of bund former plates. This resulted in soil accumulation at the narrow end of the bund former allowing uprooted straw falling behind and being covered by tilled soil. The rotor speed ratio (3:1) and (4:1) showed close range of bulk density (0.0011;1, 0.00112;0.00107 and 0.001;0.00088 g.mm^{-3}) for opening width of bund forming plates (270, 340, 410 mm) under 4.0-4.5 t. ha^{-1} and 6.0-6.5 t.ha^{-1} straw load because of the soil volume being adequately handled and straw chopping at the forward speed of travel.

Bund Height

Mean height of bund obtained during field evaluation of tractor-operated bund former at three rotor speed ratios, three opening widths of bund forming plates, and two different straw loads are shown in Fig. 7. The effects of rotor speed ratio and opening width of bund forming plates were significant (p<0.05), whereas the effect of straw load was non-significant on the bund height, Table 5.

Under straw load of 4.0-4.5 t.ha^{-1}, the bund height increased from 340 mm to 410 mm with increase in levels of opening width of bund forming plates from 270 mm to 340 mm at all rotor speed ratios. A similar trend was observed for straw load of 6.0-6.5 t.ha^{-1}. Also, with increase in rotor speed ratios from 3:1 to 4:1, the height of bund initially increased; and decreased with rotor speed ratio further increasing from 4:1 to 5:1 at all opening widths of bund forming plates under both straw loads. However, at 410 mm opening width of bund forming plate with straw load of 4.0-4.5 t.ha^{-1}, maximum bund height attained was at 3:1 rotor speed (228 mm); followed by 4:1 (221 mm) and 5:1 (215 mm). The maximum mean bund height (277.6 mm) was observed for 340 mm opening width of bund forming plates at rotor speed ratio of 4:1; while the minimum bund height of 213.0 mm occurred at 410 mm opening width of bund forming plates and rotor speed ratio of

(Same alphabets indicate non-significance for a particular performance, p>0.05)

Fig. 7: Effects of rotor speed ratio [(3:1); (4:1); (5:1)] and opening width of bund forming plates (270, 340, 410 mm) on bund height under straw load of 4.0-4.5 t.h^{-1} and 6.0-6.5 t.ha^{-1}

Table 5.　ANOVA for effect of rotor speed ratio (R), opening width of bund forming plates (W), and straw load (L) on bund height

Source	DF	Type III SS	Mean Square	F-Value	Pr > F	S/NS
Replications	2	22.8811	11.4405	31.40	<.0001	S
Straw load (L)	1	0.0896	0.08962	0.25	0.6233	NS
Rotor speed ratio (R)	2	51.6677	25.8338	70.89	<.0001	S
Opening width of bund forming plates (W)	2	136.1033	68.0516	186.75	<.0001	S
L × R	2	0.6270	0.3135	0.86	0.4326	NS
L × W	2	0.1270	0.0635	0.17	0.8408	NS
R × W	4	6.9955	1.7488	4.80	0.0038	S
L × R × W	4	5.0829	1.2707	3.49	0.0179	S

Note: DF: Degree of freedom, SS: Sum of square, S: Significant, NS: Non significant

5:1 under straw load of 6.0 – 6.5 t.ha^{-1}. The reason for the higher bund height was that the rotational speed of the mulcher (710 rpm) and rotavator (180 rpm) was appropriate at which the mulcher could pick the straw (standing as well as loose) from the soil surface and facilitated the rotavator to obtain proper soil tilth and soil flow so that the opening width of bund forming plates could form increase height of bund. A similar trend of bund height was observed under 4.0 - 4.5 t.ha^{-1} straw load.

The results were in affirmation with that reported by Libin *et al*. (2010), Thakur *et al*. (2018), who stated that the rotational speed of rotavator of 250 rpm gives proper soil tilth, and a mulcher at 750 rpm rotational speed picks and effectively throws the straw.

Bund Width

Mean width of bund obtained during field evaluation of the tractor-operated bund former at three rotor speed ratios, three opening widths of bund forming plates, and two straw loads are shown in Fig. 6. The effects of rotor speed ratio and opening width of bund forming plates were significant (p<0.05), whereas the effect of straw load was non-significant on bund width, Table 6.

It is clear from Fig. 6 that the bund width increased with increase in levels of opening width of bund forming plates; 609.3 – 735 mm, 638- 743.6 mm, and 625.3 – 690 mm for rotor speed ratio 3:1, 4:1, and 5:1 under 4.0-4.5 and 6.0-6.5 t.ha^{-1} straw load respectively. This was due to wider opening of bund plates allowed increased the width of bund and vice versa. At a particular opening width of the plates, bund width increased from rotor speed ratio of 3:1(13.86 mm MMD) to 4:1(12.66 mm MMD) as rotavator and mulcher speed helped in proper soil pulverization compared to higher rotavator and mulcher speed at rotor speed ratio of 5:1 that caused

Table 6.　ANOVA for effect of rotor speed ratio (R), straw load (L), and opening width of bund forming plates (W) on bund width

Source	DF	Type III SS	Mean Square	F-Value	Pr > F	S/NS
Replications	2	22.7070	11.3535	5.49	0.0089	S
Straw load (L)	1	0.3112	0.3112	0.15	0.7006	NS
Rotor speed ratio (R)	2	175.2803	87.6401	42.39	<.0001	S
Opening width of bund forming plates (W)	2	769.9825	384.9912	186.19	<.0001	S
L × R	2	0.3670	0.1835	0.09	0.9153	NS
L × W	2	4.3625	2.1812	1.05	0.3600	NS
R × W	4	69.0074	17.2518	8.34	<.0001	S
L × R × W	4	2.0274	0.5068	0.25	0.9105	NS

Note: DF: Degree of freedom, SS: Sum of square, S: Significant, NS: Non significant

repeated pulverization (8.26 mm MMD) of the soil generating excess soil volume. The maximum mean value (743.6 mm) of bund width was observed for 410 mm opening width of bund forming plates at rotor speed ratio of 4:1 under straw load of 4.0 - 4.5 t.ha^{-1}; while the minimum (609.3 mm) bund width occurred for 270 mm opening width of bund forming plates at rotor speed ratio of 3:1 under straw load of 6.0 - 6.5 t.ha^{-1}. The maximum width of bund was derived by the rotational speed of mulcher (710 rpm) and rotavator (180 rpm) that allowed easy forward machine movement for the mulcher to pick straw and enable sufficient cutting/pulverization of soil so that wide opening width of bund forming plates could allow increasing of base width of the bund.

The results were in line with that of Bhambota *et al.* (2017); Thakur *et al.* (2018), who stated that rotavator rotational speed of 180 rpm gives proper soil tilth, and a mulcher at 750 rpm rotational speed properly picks and throw the straw. The increase in horizontal distance between the plates also allows bund base width to be increased and vice versa.

Proper sized bund was built by the machine which can prevent seepage of water. Irrigation water use efficiency will increase as less water is used by forming compartment in field and avoiding flood irrigation.

Fuel Consumption

Mean tractor fuel consumption obtained during field evaluation of the tractor-operated bund former at three rotor speed ratios, three opening widths of bund forming plates, and two straw loads are shown in Fig. 7. The effects of rotor speed ratio and opening width of bund forming plates were significant ($p<0.05$), whereas straw load was non-significant on fuel consumption of the tractor, Table 7.

Fuel consumption rate decreased with increase in levels of rotor speed ratio from 3:1 to 4:1, but increased at rotor speed ratio 5:1 (Fig. 7). The minimum fuel consumption rate (5.93 l.h^{-1}) was obtained for 340 mm opening width of bund forming plates at rotor speed ratio of 4:1 under straw load of 4.0-4.5 t.ha^{-1}. The reason for the lower fuel consumption was that the rotational speed of the mulcher (710 rpm) and rotavator (180 rpm) was the best combination for the mulcher to pick dense straw load and facilitate the rotavator having C-type blades to perform desired soil tilth at lower energy requirements of the machine. The results were in affirmation with that of Bhambota *et al.* (2017), who stated that the fuel consumption is lower for C-type of blades due to their lower energy requirements.

At rotor speed ratio 5:1, more fuel was consumed because of higher rotational speed of the mulcher (1000 rpm) and the rotavator (210 rpm), as also higher volume of soil pulverized by the rotavator causing more volume of soil movement from the front width of the bund former plates. The rotor speed ratio (3:1) and (4:1) showed closer range (6.8-7.3;6.1-8.43 l.h^{-1}) of fuel consumption because of sufficient soil volume and straw chopping handled by the machine at 1.5 km h^{-1} forward speed of travel.
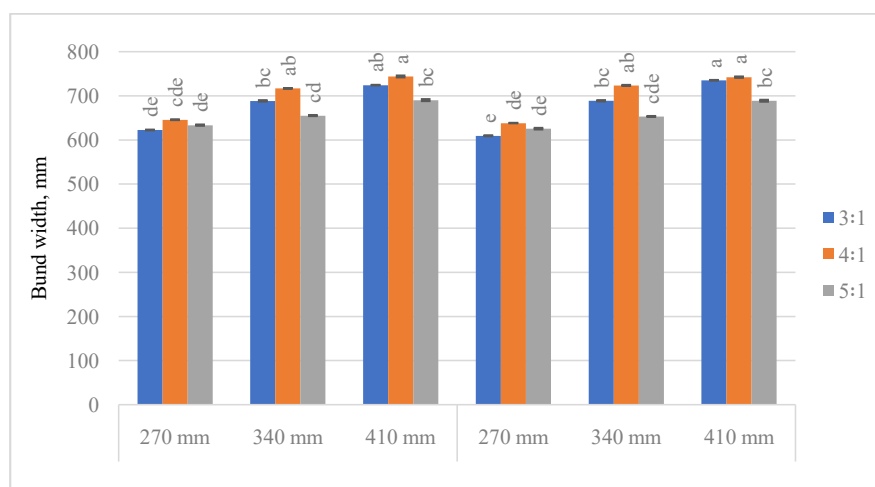
(Same alphabets indicate non-significance for a particular performance, p>0.05)

Fig. 8: Effects of rotor speed ratio [(3:1), (4:1), (5:1)] and opening width of bund forming plates (270, 340, 410 mm) on bund width under straw load of 4.0-4.5 t.ha^{-1} and 6.0-6.5 t.ha^{-1}

Table 7. ANOVA for effect of rotor speed ratio (R), straw load (L), and opening width of bund forming plates (W) on fuel consumption

| Source	DF	Type III SS	Mean Square	F-Value	Pr > F	S/NS
Replications	2	3.4903	1.7451	57.82	<.0001	S
Straw load (L)	1	1.2451	1.2451	41.25	<.0001	S
Rotor speed ratio (R)	2	38.2103	19.1051	632.93	<.0001	S
Opening width of bund forming plates (W)	2	0.2825	0.1412	4.68	0.0165	S
L × R	2	0.0414	0.0207	0.69	0.5103	NS
L × W	2	0.0448	0.0224	0.74	0.4840	NS
R × W	4	0.0140	0.0035	0.12	0.9757	NS
L × R × W	4	0.0251	0.0062	0.21	0.9318	NS

Note: DF: Degree of freedom, SS: Sum of square, S: Significant, NS: Non significant

Field Capacity

Mean field capacity of the tractor-operated bund former at three rotor speed ratios, three opening widths of bund forming plates, and two straw loads are shown in Fig. 9. The effects of rotor speed ratio, opening width of bund forming plates, and straw load were significant (p<0.05) on field capacity of bund, Table 9.

Field capacity decreased with increase in opening widths of bund forming plates at rotor speed ratio of 3:1 and 5:1 with both straw loads. The straws on the field were properly removed at higher mulcher rpm (1100 rpm), but the rotavator at higher rotavator rpm (210 rpm) repeatedly pulverized the same soil (8.26 mm MMD) at a location causing obstruction forward

motion of the machine and consequently affecting the field capacity. At straw load of 4.0-4.5 t.ha^{-1} and rotor speed ratio of 4:1, the field capacity initially increased with increase in level of opening width of bund forming plates from 270 mm (0.99 ha h^{-1}) to 340 mm (1.24 ha h^{-1}); followed by gradual decrease with blade opening width of 340 mm to 410 mm (1.07 ha.h^{-1}). This might be due to over accumulation of soil and removed straw in wide area between bund forming plates at the specific unit area. The highest field capacity (1.44 ha.h^{-1}) was found at rotor speed ratio of 5:1 under straw load of 4.0 – 4.5 t.ha^{-1}; and the lowest field capacity (0.87 ha.h^{-1}) at rotor speed ratio of 4:1 under straw load of 6.0 – 6.5 t.ha^{-1}.
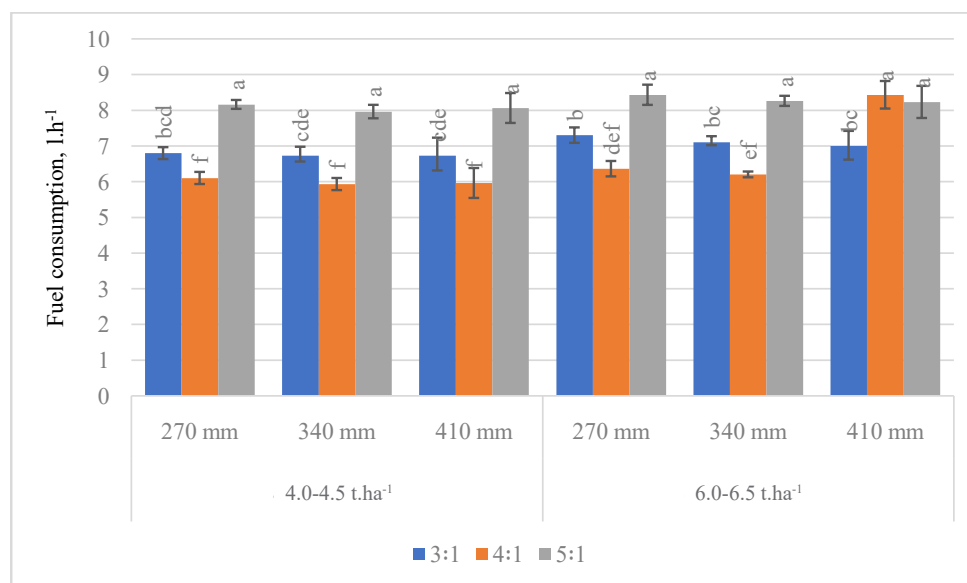
(Same alphabets indicate non-significance for a particular performance, p>0.05)

Fig. 9: Effects of rotor speed ratio [(3:1), (4:1), (5:1)] and opening width of bund forming plates (270, 340, 410 mm) on fuel consumption under straw load of 4.0-4.5 t.ha^{-1} and 6.0-6.5 t.ha^{-1}

Table 8. **ANOVA for effect of rotor speed ratio (R), straw load (L), and opening width of bund forming plates (W) on field capacity**

Source	DF	Type III SS	Mean Square	F-Value	Pr > F	S/NS
Replications	2	0.01584	0.00792	0.50	0.6123	NS
Straw load (L)	1	0.04605	0.04605	2.89	0.0986	NS
Rotor speed ratio (R)	2	0.65753	0.32876	20.67	<.0001	S
Opening width of bund forming plates (W)	2	0.31958	0.15979	10.04	0.0004	S
L × R	2	0.03688	0.01844	1.16	0.3266	NS
L × W	2	0.04508	0.02254	1.42	0.2572	NS
R × W	4	0.38179	0.09544	6.00	0.0010	S
L × R × W	4	0.08266	0.02066	1.30	0.2913	NS

Note: DF: Degree of freedom, SS: Sum of square, S: Significant, NS: Non significant

Field capacity at rotor speed ratio of 4:1 and 5:1 under straw load of 6.0-6.5 t.ha^{-1} were significantly different, but quality of bund in terms of bund height and width was best at rotor speed ratio of 4:1 and 340 mm opening width of bund forming plates.

Operating Parameter Combination

Best suited combination of parameters for optimal performance of the tractor-operated bund former was selected based on the quality of bund formed in terms of pulverization index, bund height, bund width, fuel consumption, bund soil bulk density, and field capacity (Table 9). The desired bund height of 270 mm (≥ 200 mm), bund width of 720 mm (≥ 600 mm), was obtained for all interactions of independent parameters. The rotor speed ratio (4:1 and 5:1) and opening width of bund forming plates (270, 340, 410 mm) showed statistically non-significant results under given straw loads (4.0-4.5 and 6.0-6.5 t.ha^{-1}) as shown in Table 9.

Selected operating parameter combinations should give maximum bund size (height and width) and field capacity with minimum pulverization index

Table 9. Operational parameters for better performance of tractor-operated bund former

Sl. No	Dependent parameter	Combination of operational parameters	Independent parameter		
			Rotor speed ratio	Opening width of bund forming plates, mm	Straw load, t.ha^{-1}
1.	Maximum height of bund, mm	266.3 (3:1; 340 mm)[a] and 271.6 (4:1; 340 mm)[a]	3:1; 4:1	340	4.0-4.5 and 6.0-6.5
2.	Maximum width of bund, mm	724.0 (3:1; 410 mm), 743.6 (4:1; 410 mm)[a] and 716.6 (4:1; 340 mm)[a]	3:1; 4:1	340; 410	4.0-4.5 and 6.0-6.5
3.	Minimum pulverization index, mm	8.26 (5:1; 270 mm)[a], 8.83 (5:1; 340 mm)[b], 9.66 (5:1; 410 mm)[c] and 12.76 (4:1; 340 mm)[d]	5:1	270; 340; 410	4.0-4.5 and 6.0-6.5
4.	Minimum fuel consumption, l.h[-1]	6.1 (4:1; 270 mm)[a], 5.93 (4:1; 340 mm)[a] and 5.96 (4:1; 410 mm)	4:1	270; 340; 410	4.0-4.5and 6.0-6.5
5.	Maximum bulk density, g.mm^{-3}	0.00125 (4:1;340 mm) and 0.00123 (4:1;340 mm)	4:1	340	4.0-4.5 and 6.0-6.5
6.	Maximum field capacity, ha.h^{-1}	1.44 (5:1; 270 mm)[a], 1.42 (5:1; 340 mm)[a] and 1.24 (4:1; 340 mm)	4:1; 5:1	270; 340	4.0-4.5 t.ha^{-1} and 6.0-6.5 t.ha^{-1}

Note: Same alphabets indicate non-significance for a particular performance, p>0.05
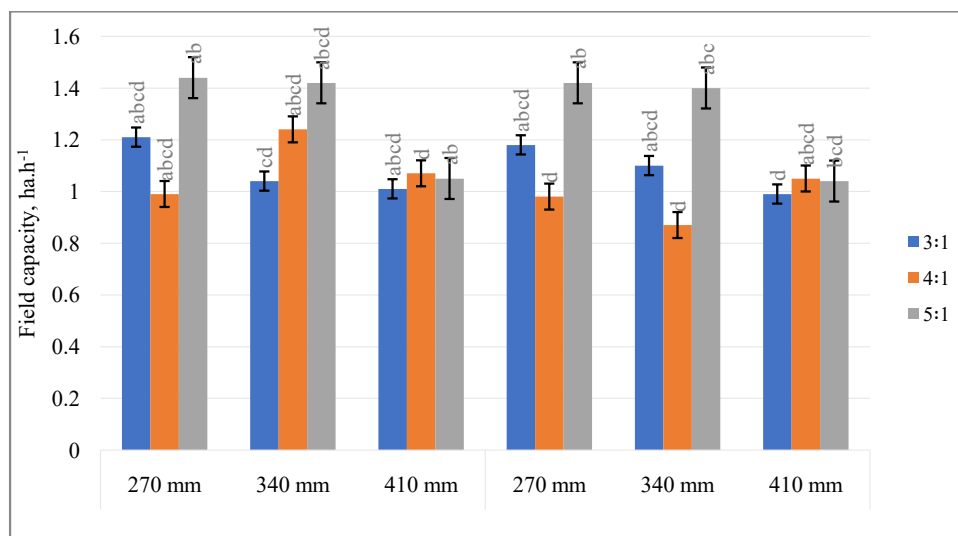
(Same alphabets indicate the non-significance for a particular performance, p>0.05)

Fig. 10: Effects of rotor speed ratio [(3:1), (4:1), (5:1)] and opening width of bund forming plates (270, 340, 410 mm) on field capacity under straw load of 4.0-4.5 t.ha^{-1} and 6.0-6.5 t.ha^{-1}

and fuel consumption. Maximum bund height (271.6 mm and 277.6 mm) was observed at rotor speed ratio of 4:1 for 340 mm opening width of bund forming plates under straw load of 4.0-4.5 and 6.0-6.5 t.ha^{-1}, respectively. The bund width (724, 743.6 and 410 mm) was statistically same (Table 9) at rotor speed ratio of 4:1 and 3:1 for 340 / 410 mm opening width of bund forming plates and 410 mm opening width of bund forming plates respectively. Minimum pulverization index value was obtained at rotor speed ratio of 5:1 and all levels of opening widths of bund forming plates which were significantly different (Table 9). Moreover, pulverization index was statistically different at rotor speed ratio of 4:1 and 340 mm opening width of bund forming plates. Fuel consumptions were low (6.1, 5.93 and 5.96 l.h^{-1}) and statistically same at rotor speed ratio of 4:1 and all levels of opening width of bund forming plates. The best combination of parameters for soil pulverization was thus 4:1 rotor speed ratio and 340 mm opening width of bund forming plates (Table 9).

Bund soil bulk density was highest at rotor speed ratio of 4:1 and at all levels of opening width of bund forming plates, and were statistically same. Thus, the best combination for bulk density was rotor speed ratio of 4:1 at opening width of 340 mm (Table 9).

Maximum field capacity was found at rotor speed ratio of 5:1 at 270 / 340 mm opening width of bund forming plates, which were non-significant to each other. The machine had field capacity of 1.24 ha.h^{-1} at rotor speed ratio of 4:1 and 340 mm opening width of bund forming plates was non-significant under 4.0-4.5 t.ha^{-1} straw load.

In light of the above, the desired bund height, bund width at lowest fuel consumption was achieved with rotor speed ratio of 4:1 and 340 mm opening width of bund forming plates under both straw loads. Although, field capacity of developed bund former was 14.5% higher at rotor speed ratio of 5:1 (compared to 1.24 ha.h^{-1} at rotor speed ratio of 4:1), but could be neglected to obtain better quality of bund formation by the machine.

Economics of Tractor-operated Bund Former

The cost analysis of tractor operated bund former was based on the cost of bund length per meter. Total cost of machine operation was 792.36 ₹.ha^{-1}. The cost of bund forming was 1.0 ₹.m^{-1}.

CONCLUSIONS

Evaluation of a developed tractor-operated bund former was conducted in harvested paddy field at University Seed Farm, Ladhowal, Ludhiana, Punjab. Paddy straw (350 mm length) removed by the machine was retained over the bund as mulch that formed a protective cover. It can be concluded from above discussion developed bund former forms bund that reduces seepage of water through the bunds by decreasing soil porosity due to

soil and straw separation. Irrigation water use efficiency upsurges with use of the developed bund former. The bund former is a single solution for *in-situ* straw management and irrigation management at the same time. The machine could develop bunds of 271.5 mm height and 720 mm width at rotor speed ratio of 4:1 with straw load of 4.0-4.5 t.ha^{-1} and 277.6 mm bund height and 720 mm bund width with straw load of 6.0-6.5 t.ha^{-1} with fuel consumption rate of 7.05 l.h^{-1}. Soil pulverization index ranged between 12.76 mm and 12.80 mm under both straw loads. Effective field capacity of the machine was 1.17 ha.h^{-1} at forward travel speed of 1.5 km.h^{-1}. The operational cost of the machine was 792.36 ₹.ha^{-1}.

ACKNOWLEDGMENT

REFERENCES

Anon. 2003. Addressing Resource Conservation Issues in Rice–Wheat Systems of South Asia: A Resource Book. Rice–Wheat Consortium of the Indo-Gangetic Plains – International Maize and Wheat Improvement Centre, New Delhi, ISBN 81-88572-00-4, pp: 304.

Anon. 2010. Options for Effective Utilization of Crop Residues. Punjab Agricultural University, Ludhiana, Research Bulletin No. 3, pp: 32.

Anon. 2017. Mechanical management of paddy straw. All India Coordinated Research Project on Farm Implements and Machinery, ICAR- Central Institute of Agricultural Engineering, Bhopal, pp: 30.

Anon. 2018. Agricultural Statistics at glance 2018. Directorate of Economics and Statistics, Department of Agriculture, Cooperation and Farmers Welfare, Ministry of Agriculture and Farmers Welfare, Government of India, New Delhi, 218-468.

Anon. 2019a. International Rice Research Institute. www.irri.org/rice-straw-management (Accessed on 26.07.2019).

Anon. 2019b. Review of the Scheme "Promotion of Agricultural Mechanisation for In-situ Management of Crop Residue in States of Punjab, Haryana, Uttar Pradesh and NCT of Delhi". Report of the Committee, Department. of Agriculture, Cooperation and Farmers Welfare, New Delhi, pp: 36.

Anon. 2019c. Package of Practices for Rabi Crops. Punjab Agricultural University, Ludhiana, pp:13.

Anon. 2020a. Handbook of Agriculture 2020. Punjab Agricultural University, Ludhiana, pp:125.

Anon. 2022. Food and Agriculture Organization of the United Nations. https://www.fao.org/faostat/en/#data/QCL (Accessed on 07.03.2022).

Bhambota S; Manes G S; Prakash A; Dixit A. 2017. IS: 9164, Studies on effect of blade shape and rotor speed of rotavator on pulverization and mixing quality. Agric. Res. J., 54, 394-397.

Bhuvaneshwari S; Hettiarachchi H; Meegoda J N. 2019. Crop residue burning in India: Policy challenges and potential solutions. Int. J. Environ. Res. Public Health, 16, 1-19.

BIS. 1979. Guide for Estimating Cost of Farm Machinery Operation. Bureau of Indian Standards, New Delhi, IS: 9164, pp: 18.

Kumar A; Singh V K; Narender; Kumar R. 2014. Utilization of paddy straw as animal feed. Forage Res., 40, 154-158.

Kepner R A; Bainer R; Barger E L. 2005. Principles of Farm Machinery. Third Edition, The AVI Publishing Company, Inc. USA, 368-382.

Libin Z; Jiandong J; Yanbiao L. 2010. Agricultural rotavator power requirement optimization using multi-objective probability parameter optimization. Int. Agric. Eng. J., 19 (19), 15-22.

Manpreet S. 2011. Design and development of tractor operated seeder for wheat as relay crop in cotton. Unpublished Ph.D. Dissertation, Punjab Agricultural University, Ludhiana, India. pp: 207.

Mahal J S; Manes G S; Singh A; Kaur S; Singh M. 2019. Complementing solutions and strategies for managing rice straw and their impact in the state of Punjab. Agric. Res. J., 56(3), 588-593.

Mehta M L; Verma S R; Mishra S R; Sharma V K. 2005. Testing and Evaluation of Agricultural Machinery. Daya Publishing House, Delhi-100 035, pp: 253.

Modi R U; Manjunatha K; Gauam P V; Nageshkumar T; Sanodiya R; Chaudhary V; Murthy G R K;

Srinivas I; Rao C S. 2020. Climate-smart technology-based farm mechanization for enhanced input use efficiency. In: Srinivasarao C; Srinivas T; Rao R V S; Rao N S; Vinayagam S S; Krishnan P (Eds.) Climate Change and Indian Agriculture: Challenges and Adaption Strategies, ICAR-National Academy of Agricultural Research and Management, Hyderabad, Telangana, India, 325-358.
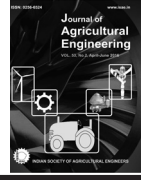
Nkakini. 2014. Performance evaluation of disc ridging tractive force model in loamy sand soil using sensitivity measured parameters. Agric. Eng. Int. CIGR J., 16, 15-21.

Sood A. 2020. Development and evaluation of tractor operated bund former for mulched fields. Unpublished M.Tech. Thesis, Punjab Agricultural University, Ludhiana, India, pp: 90.

Thakur S S; Chandel R; Narang M K. 2018. Studies on straw management techniques using paddy straw chopper-cum-spreader along with various tillage practices and subsequent effect of various sowing techniques on wheat yield and economics. Agric. Mech. Asia Afr. Latin Am., 49, 52-66.

Xian-Jun J; De-Ti X. 2009. Combining ridge with no-tillage in lowland rice- base cropping system: long-term effect on soil and rice yield. Pedosphere, 19, 515-522.

Development and Stability Analysis of a Self-propelled High Clearance Multi-utility Vehicle

Ajay Kumar Roul[1] and Dushyant Singh[2]

[1]Scientist, [2]Principal Scientist, ICAR-Central Institute of Agricultural Engineering, Bhopal-462038. Corresponding author e-mail address: Ajay.Roul@icar.gov.in

Article Info	ABSTRACT
	A self-propelled hydraulically actuated vehicle was developed for field crops of up to 2.0 m in height to carry out different operations like spraying, weeding, harvesting. The vehicle has provision for variable/adjustable ground clearance and track width to suit different spacing and heights of horticultural crops. Gradability, torque, and power required for the vehicle were calculated based on the dimensions of the selected bias ply traction tyre. The centre of gravity of the vehicle was calculated by the weight moment method. Microsoft Excel add-in was used to create a point manipulation programme, and the positions of the standard components were determined through an iterative process. The static load over the rear wheel and front wheel was kept at 60% and 40%, respectively, for design purposes. Analysis of chassis mechanics was done to find out weight transfer and impending stability on level ground as well as longitudinal and lateral slope. In longitudinal slope, the developed vehicle was found to be stable up to 45.19° and 20.68° under static and dynamic conditions, respectively; whereas in lateral slope, the vehicle was stable up to 39.08° and 22.10° under static and dynamic conditions, respectively. The developed vehicle was tested for weeding and spraying of okra and maize crops with an average height of 1.1 m to 1.5 m. The field capacity for the spraying and weeding operations was 1.9 ha.h^{-1} and 0.16 ha.h^{-1}, respectively. The cost of operation for spraying and weeding was 400 ₹.ha^{-1} and 1,500 ₹.ha^{-1}, respectively. Weeding efficiency and plant damage of the weeder were 92.58% and 1.55%, respectively.

India is endowed with a wide variety of agro-climatic conditions and records an important position in the production of various crops. With the increase in production and productivity in agriculture, the level of mechanization has also been increasing continuously and reached 2.761 kW.ha^{-1} in 2020–21 (Singh and Singh, 2021). The yearly domestic sale of tractors has reached 0.9 million in India (Balachandar, 2022). Though many of the farming operations like tillage and harvesting in India are on the verge of saturation and have achieved about 80% mechanization for major crops, the mechanization levels for many operations like planting and intercultural operations are still scanty (Anon., 2017). This might be due to the non-availability of suitable machinery for interculture or difficulty in operating in tall field crops. Different operations include intercultural (weeding), spraying, and fertilizer broadcasting. Intercultural operations in field crops like maize, pigeon pea, cotton, okra, etc. fall into that category where the level of mechanization is about 30% in India. Mechanization in intercultural operations is difficult due to diverse individual crop geometry and is a challenging task for tall crops like cotton, pigeon pea, okra, maize, sugarcane, etc. Because of the fast growth and tall nature of the crop, even first and second weeding operations are not possible with a normal tractor. Some Indian tractor manufacturers have already introduced high ground clearance tractors, but still their clearance is not sufficient. Many high ground clearance vehicles with a ground clearance

of between 1.0 m and 1.5 m have been developed in foreign countries to carry out spraying operations (LeeAgra, Inc., USA and Quinzhou Maite Cheqiao Zhizao Co. Ltd., China). Punjab Agricultural University has developed a tractor with a ground clearance of about 1 m and has successfully tested it in seeding and spraying operations (Mahal et al., 2007). A few Indian manufacturers (Standard Tractor, Punjab and Tirth Agro Technology Pvt. Ltd.) are also producing and marketing such tractors. All of the high ground clearance tractor manufacturers only provide spraying accessories with their tractors. These tractors with fixed ground clearance and track width do not come with weeding attachments. Therefore, there is a sufficient demand for such types of vehicles in India for doing spraying and weeding operations on tall crops.

Tractors are designed to adapt to a variety of terrain situations, and hence, stability determination is a key consideration. Studies on stability analysis of these high ground clearance tractors are not available. This paper presents a design procedure for the development of a self-propelled high clearance vehicle, its analysis of stability, the development of an innovative weeding attachment, and its performance evaluation under field conditions. The main research contribution of this work is the development of a Microsoft Excel point manipulator tool for weight distribution over the vehicle's chassis, as well as the establishment of mechanics of stability analysis for the design and development of any type of vehicle for field use.

MATERIALS AND METHODS

Hydraulic System Design

Slope and soil conditions are the critical factors for designing a high clearance vehicle. These factors directly decide the power requirement as well as the stability of the machine. Narrow lugged wheel (8.3-32, bias ply) can be accommodated within the rows and can provide enough traction.

With the above assumption, a self-propelled vehicle transmission system was designed. The transmission system was designed considering two conditions: (a) the vehicle will just climb a desired slope without slippage under design conditions, and (b) for a vehicle to start on a slope, it must have enough starting torque to drive the vehicle up the slope, and this starting torque must be more than the torque required to drive the vehicle up the slope. The total force required to drive the vehicle up the gradient is the summation of the

forces required to overcome the rolling resistance and the gradient. For designing the vehicle, the weight of the vehicle, the slope of the terrain and the cone index of the soil were considered as 15,000 N, 20° and 20,600 $N.m^{-2}$, respectively.

In order to calculate the rolling resistance, R, the expression proposed by Wismer and Luth (1974) was used and is given as:

$$R= \left(\frac{1.2 \times W}{CI \times b \times d} + 0.04 \right) \times W \qquad \qquad \dots(1)$$

Where,
W = Total weight on the wheels, N,
CI = Cone index of soil, $N.m^{-2}$,
b = Width of wheel, m, and
d = Wheel diameter, m.

Force required to overcome gradient, F_g, is given by the expression (Khurmi and Gupta, 2020),

$$F_g = W \times \sin\theta \qquad \qquad \dots(2)$$

Where,
θ = Slope of terrain with horizontal, degree.

Rolling resistance and the force required to drive the vehicle up the gradient were calculated as 3.7 kN and 5.0 kN, respectively, and the total force (F) required to drive the vehicle up the gradient was 8.7 kN.

The maximum force at the drive wheel before slip occurs is given as (Verma, 2020):

$$F_s = \mu \times N \qquad \qquad \dots(3)$$

Where,
μ = Coefficient of friction between wheel and ground surface, and
N = Normal reaction, N.

Considering the value of μ as 0.85 (Wong, 1993) and 60% of the total vehicle weight distributed over the rear traction wheel, F_s was calculated as 8.8 kN.

The wheel torque (T) was assumed to be equal to the total force required (F_t) acting on a moment arm equal to the rolling radius (r). The torque requirement was calculated for four conditions: (i) vehicle operating on level terrain, (ii) vehicle moving up a gradient, (iii) vehicle descending a gradient, and (iv) vehicle starting on a gradient. When the vehicle operates on level terrain, only rolling resistance was considered,

whereas when the vehicle moves up a gradient, both rolling resistance and gradient force are considered. For the condition of the vehicle descending on a gradient, the gradient would add to the drive. A vehicle starting on a gradient would require the maximum torque that can be applied at the wheel to cause the wheel to slip.

The torque requirements at the individual drive wheels of the vehicle for conditions such as vehicle operating on level terrain, vehicle moving up a gradient, vehicle descending a gradient, and vehicle starting on a gradient were calculated as 2614.4 N, 1104.5 N, (-) 405.28 N, and 2626.6 N, respectively.

Based on the maximum torque requirement, a hydraulic system was designed and the hydraulic circuit was developed (Fig. 1).

For movement of the vehicle, closed-loop hydrostatic transmission was adopted, whereas an open-loop hydraulic system was adopted for power steering, adjustment of ground clearance, hydraulic cooling, and spraying system. Since the machine was conceptualized with 2WD drive, the two rear wheels were powered. The main components of the hydraulic system consisted of a variable displacement servo pump, two fixed-displacement wheel motors, three fixed-displacement gear pumps, a mobile three-position, four-port directional control valve having a centre neutral line, double-acting cylinders, counter-balance valves, and a pressure relief valve.

Modelling of Vehicle

A CAD model of all the standard components and the chassis of the vehicle were developed. External dimensions as well as the weight of all components were measured. For asymmetric components, the centroid of the external dimension was assumed to be the position of the centre of gravity. One of the corners of the chassis was fixed as a reference point and assigned a zero coordinate. Components were placed randomly over the chassis and the coordinates of the centre of gravity were found.

Standard components were placed over the chassis to distribute 60% and 40% static load over the front and rear wheels, respectively. A point manipulation programme was developed by the Microsoft Excel add-in (Fig. 2) and, by numerous iterations, the positions of the standard components were determined.

The horizontal position and vertical position of the centre of gravity (CG) of the vehicle were calculated by the weight moment method (Verma, 2020) and using Eq. 4–6:

$$X_g = \frac{\sum x_{1...n} \times W_{1...n}}{\sum W_{1...n}} \qquad ...(4)$$
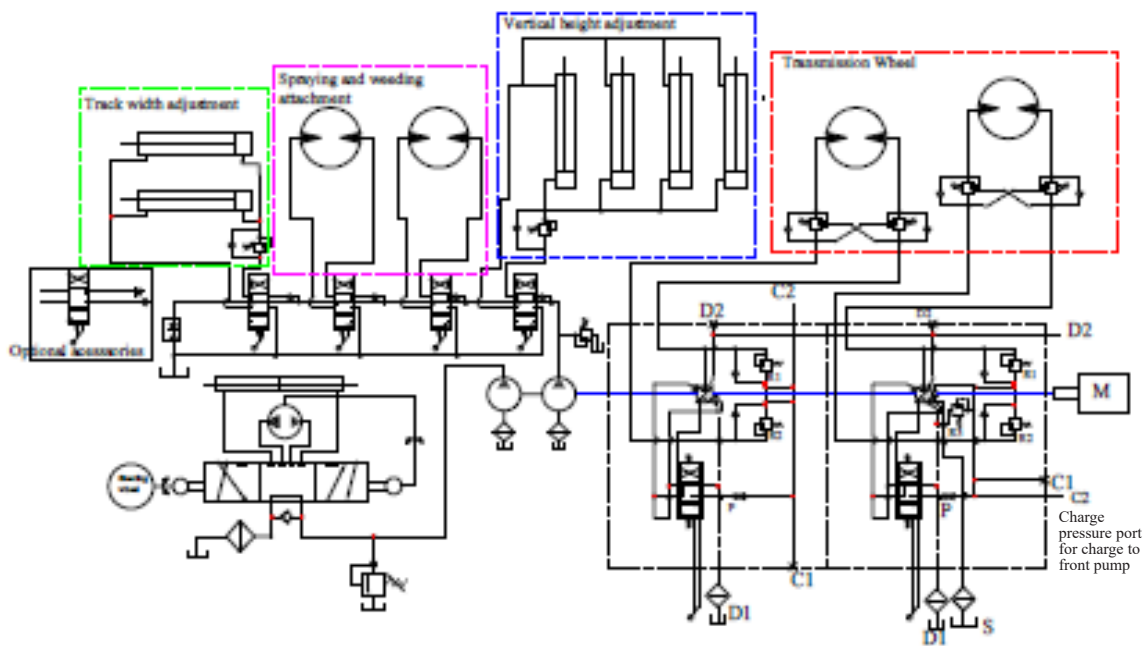

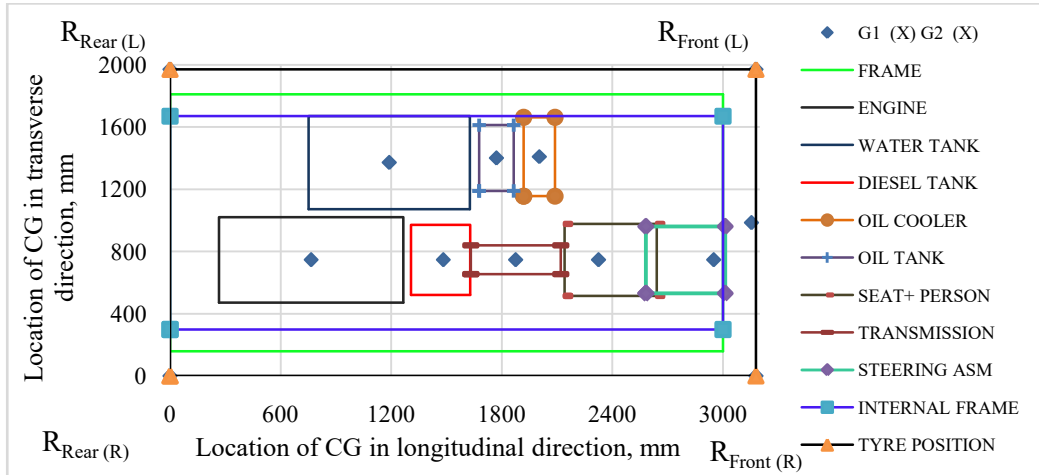**Fig. 1: Hydraulic circuit diagram of high clearance vehicle**

Fig. 2: Point manipulation method to optimize weight distribution

$$Y_g = \frac{\sum y_{1...n} \times W_{1...n}}{W_{1...n}} \qquad ...(5)$$

$$Z_g = \frac{\sum z_{1...n} \times W_{1...n}}{\sum W_{1...n}} \qquad ...(6)$$

Where,

X_g = Position of horizontal centre of gravity in X-coordinate, mm,

Y_g = Position of horizontal centre of gravity in Y-coordinate, mm,

Z_g = Position of vertical centre of gravity in Z-coordinate, mm,

$x_{1...n}, y_{1...n}, z_{1...n}$ = x, y, z coordinates of individual components, respectively, mm, and

$W_{1...n}$ = Weight of individual components, N.

The concept was translated into a solid model using CAD software PTC Creo Element 1 (Fig. 3). Analysis

of strength was performed based on the maximum weight of various components as well as forces and moments acting on those components (Segerlind, 2010). The allowable stress method based on IS/ISO 8686 (2006) was used to assess the strength of the components.

Fabrication and Assembly of Designed System

The vehicle consisted of a main chassis, a diesel engine with a fuel injection system (Make: Mahindra; Model: 275DI); hydraulic cooling and engine cooling systems; transmission system; steering system; braking system; hydraulic system for cooling, adjustment of ground clearance, steering, and spraying; spraying system; and electrical system. The chassis of the vehicle had two parts (Fig. 4). One central rigid part was made of mild steel rectangular hollow pipes and C-sections, and the two outer parts. The two outer parts were fitted to the central part as an inner beam of the telescopic beam

(a)   **(b)**
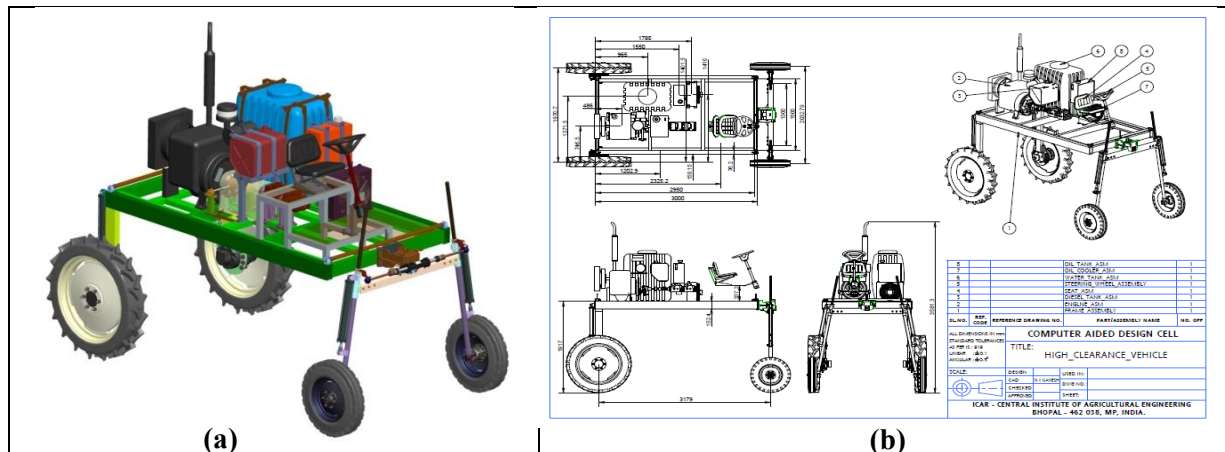
Fig. 3: Views of computer aided models of high clearance vehicle: (a) solid 3 D, and (b) wire frame
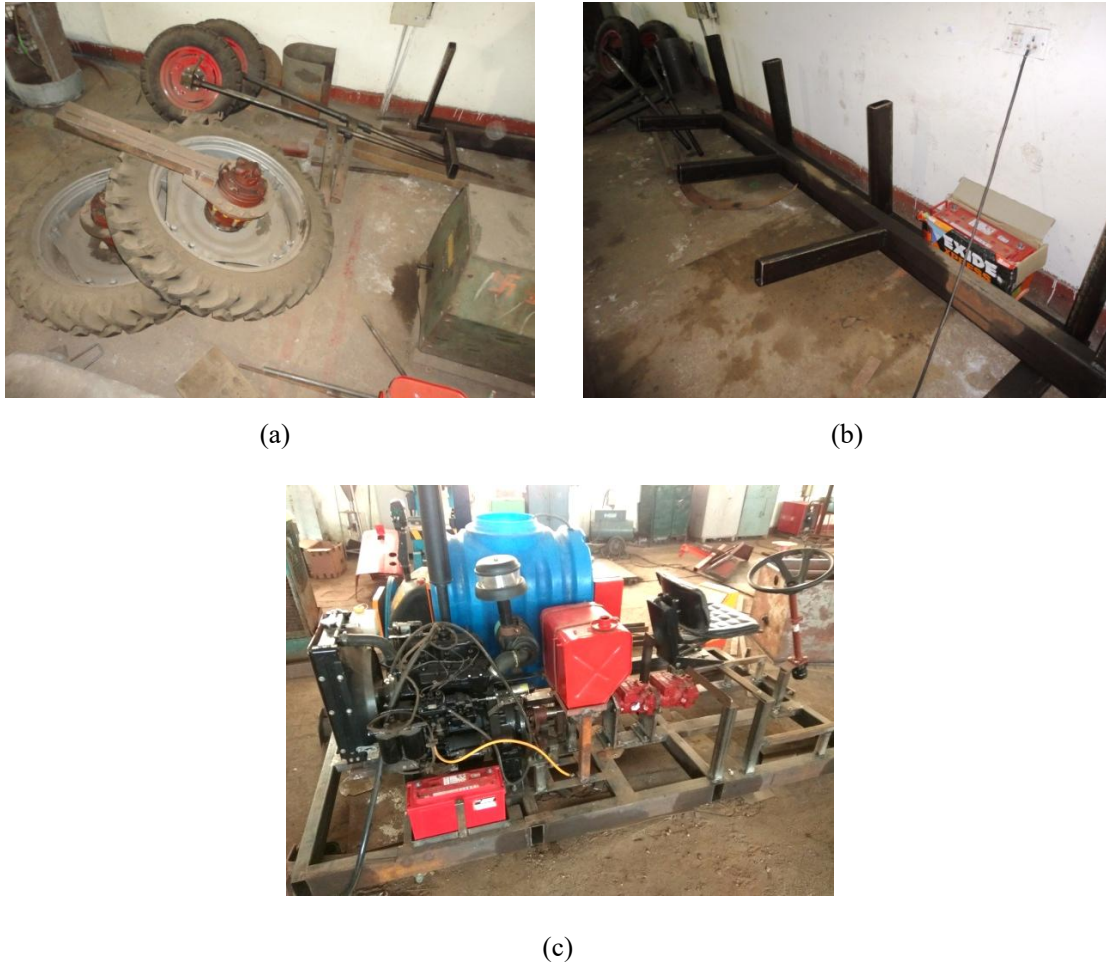
(a)

(b)

(c)

Fig. 4: View of various components of vehicle: (a) front and rear wheel assembly, (b) outer telescopic frame, (c) main chassis

system. The hollow rectangular sections of the central chassis were laid laterally parallel to each other at an equal distance. It worked as an outer for the telescopic beam system. The rear wheel system was attached to the outer part of the chassis. The telescopic beam arrangement was provided to easily adjust the track width. Adjustment of the track width was carried out by two lead screws, one attached at the front and another at the rear of the chassis. All systems of the vehicle were mounted on the central rigid section. The wheels were also mounted on a telescopic beam arrangement to adjust ground clearance.

The cooling system of the vehicle consisted of two parts. One part was responsible for cooling the engine and the other part was responsible for cooling the hydraulic system. Two radiators of different types were used. A high-pressure and high-capacity oil radiator (oil flow: 30–200 l.min^{-1}; oil cooling capacity: up to 11,400 Kcal.h^{-1}; pressure: 5 bar) was used for the hydraulic oil

cooling. For the engine cooling radiator, the fan was operated by the engine crankshaft through a belt pulley arrangement, whereas for the hydraulic oil cooling radiator, the fan was operated by the hydraulic motor (type: orbital; capacity: 12.5 cm^3.rev^{-1}).

A hydrostatic transmission (HST) system was used in the vehicle (Fig. 5 (a, b)). It comprised of a hydraulic step-less speed change mechanism composed of a hydraulic tandem variable displacement pump (Make: Eaton, Model: 72400, capacity: 40.6 cm^3.rev^{-1}) and two hydraulic fixed-displacement wheel motors (Make: Sai India, Model: GFK3A, capacity: 650 cm^3.rev^{-1}). Individual wheel motors were directly attached to the rear traction wheels, with each motor being adapted to be driven by oil forced out from the front and rear pumps of the tandem pump independently. The tandem pump was provided with a common pump drive shaft for receiving engine power at the front-end portion and a drive shaft having a rear-end portion extending
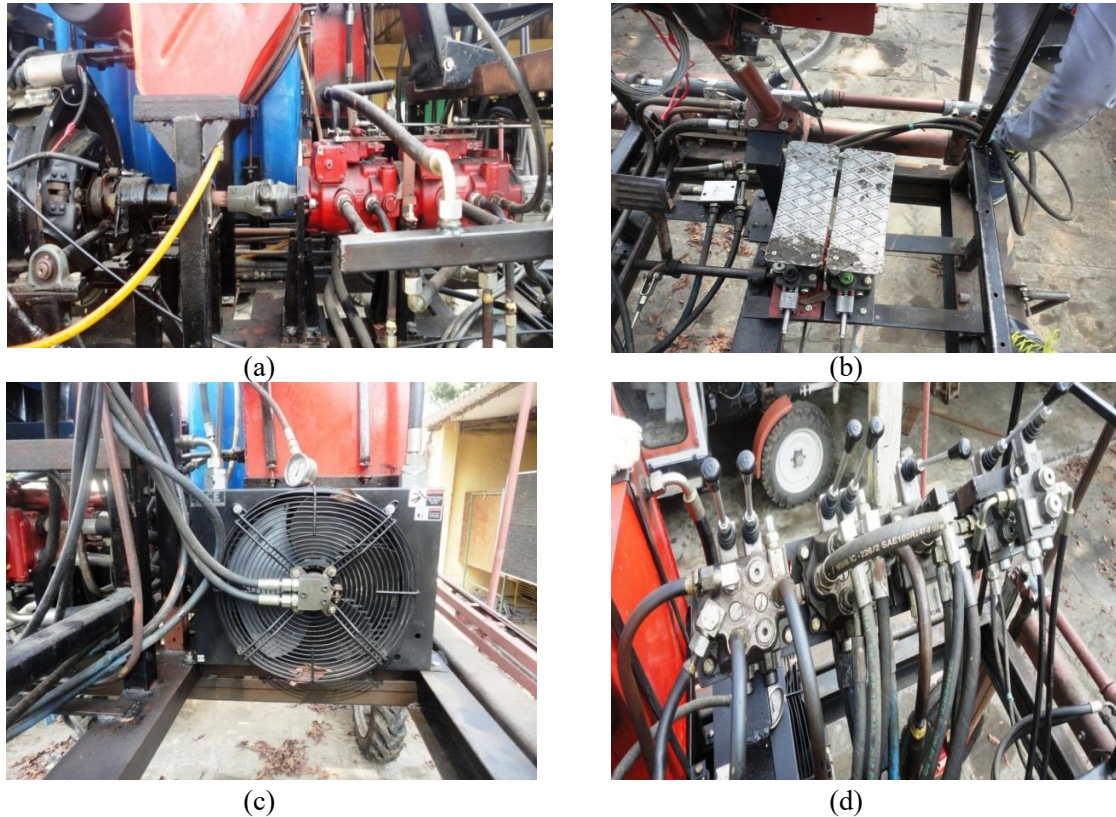
(a)

(b)

(c)

(d)

Fig. 5: Hydraulic system of high clearance vehicle: (a) hydraulic tandem servo pump, (b) foot pedal accelerator, (c) hydraulic cooling radiator, (d) open loop hydraulic system

rearward to fix the auxiliary pump for power take-off. A clutch arrangement was provided between the pump drive shaft and the engine for connecting or disconnecting the power to the pump from the engine. The individual pump had a mechanical servo control mechanism with a three-position servo valve actuating lever. At the centre position, no flow would be diverted to the motor even if the pump was in operation. Engaging the lever in one side position directed the flow to the motor, resulting in wheel rotation in one direction. Similarly, reversing the lever position to the other side rotated the wheel in the opposite direction. Thus, forward and reverse movement of the vehicle could be achieved. Four bar linkage arrangements were developed for independently controlling the two servo levers through a foot pedal. Differential action of the vehicle at turning could be achieved by controlling the rate of flow to the individual motor with the foot pedal.

The wheel motor had a spring-loaded hydraulically actuated disc brake system. A separate pressure line was provided to the individual motor, which received flow from the tandem pump. When the drive shaft received power from the engine, the pump auxiliary

port pressurized the brake line, resulting in the release of the brake. The brake would remain in the released position till the drive shaft of the tandem pump got power, regardless of whether the servo lever was engaged or not. A hydraulic power-assisted steering system was used in the vehicle.

A mobile open-loop hydraulic circuit (Fig. 5 (d)) was developed for operating the motor of the hydraulic cooling fan, the motor of the spraying system, the steering pump, and cylinders meant for adjustment of ground clearance. A combination of series, parallel, and tandem principles was adopted. The developed prototype of the high clearance vehicle is shown in Fig. 6, and its detailed specifications are given in Table 1.

Spraying System Attachment

The spraying system consisted of a chemical tank, a filter, a three-cylinder axial piston pump, a hydraulic motor, and a spray boom. The pump received the drive from a hydraulic motor directly coupled to it by a flexible drive coupling. The detailed specifications of the spraying system are given in Table 2. The boom

Fig. 6: Prototype of high clearance vehicle

Table 1. Specifications of self-propelled high clearance multi-utility vehicle

Sl No.	Parameter	Specification
1.	Power source	: 39 hp diesel
2.	Rated rpm	: 2600
3.	Tyre size	
	Rear	: 8.3-32
	Front	: 6.0-16
4.	Overall vehicle dimension	
	Length (without weeding attachment), mm	: 4440
		: 5000
	Length (with weeding attachment), mm	: 2220
		: 3400
	Width (With folded boom), mm	
	Height, mm	
5.	Total vehicle weight, kg	: 1580
6.	Maximum speed, km.h^{-1}	: 20
7.	Transmission type	: Hydrostatic
8.	Steering system	: Hydraulic
9.	Maximum Torque, N.m	: 2500 per wheel
10.	Adjustable track width, m	: 2.0-2.6
11.	Adjustable ground clearance, m	: 1.5-2

Table 2. Specifications of spraying system

Sl. No.	Parameter		Specification
1.	Power source	:	Hydraulic motor
2.	Capacity, cm^3.rev^{-1}	:	50
3.	Overall boom length, m	:	9.4
4.	Number of nozzles	:	21
5.	Type of nozzle	:	Hollow cone
6.	Discharge of nozzle, cm^3.min^{-1} at 2.8 kg.cm^{-2}	:	450
7.	Spraying tank capacity, l	:	400
8.	Pump	:	Three-cylinder axial position
9.	Pump discharge, l.min$_{-1}$ at 900 rpm	:	36

Straight vertical blades were arranged around the perimeter of a wheel, which was mounted on an individual vertical rotor shaft. A hydraulic motor (6 kW, 450 N.m torque at 150 rpm) was directly coupled to the centre rotor shaft, and the other rotor shaft got drive from the rotor shaft by a chain sprocket mechanism. The main components of the weeder were a main frame, vertical rotor shaft, cutting blades, and drive mechanism. The detailed specification of the weeder is given in Table 3. A four-bar lift mechanism was developed to mount the weeder, and it was fixed at the front of the vehicle. A hydraulic cylinder was used to raise and lower the lift mechanism.

Stability Analyses

As the vehicle was designed for field applications, it was required to ride over rough terrain. Safety of the operator should be a primary issue while designing the vehicle.

was fabricated into a three-fold system. The central part was fixed to the rear of the vehicle, and the two side folds were fitted with a hinge system to the central part. Arrangements were provided in the boom to adjust the height of spray (500–1500 mm) as required for the different heights of crops.

Weeding Attachment

A power weeder was developed for use with the developed high clearance vehicle (Fig. 7). A horizontal cutting concept was adopted in designing the weeder.

Fig. 7: Vertical axis rotary weeder

Table 3. Specification of weeding attachment

Sl. No.	Parameter		Specification
1.	Overall weeding width, mm	:	2250
2.	No. of rotor	:	5
3.	Diameter of rotor wheel, mm	:	210
4.	Length of cutting blade, mm	:	150
5.	Rotor speed, rpm	:	150
6.	Capacity of hydraulic motor, cm^3	:	200
7.	Maximum torque of motor, N.m	:	450

Stability calculations were done before being used for the field application. The complete process included the proper selection of shape and dimensions of the chassis, weight distribution, height of CG, wheel base, track width, turning radius, forward speed, and longitudinal and lateral slope.

Static and dynamic analysis of stability were analysed for the vehicle to find out wheel reaction forces, weight transfer, and impending stability on level ground as well as longitudinal and lateral slopes (Macmillan, 2002; Liljedahl *et al.*, 2004; Daryoush *et al.*, 2011). Free body diagrams for static and dynamic models with the application of forces were developed and presented in Fig. 8.

When the vehicle is on longitudinal slopes, static reaction forces on both the rear wheels and front wheels are formulated by the moment equilibrium method. The equations obtained are:

$$y' = y + R_f \qquad \ldots(7)$$

$$\alpha = \tan^{-1}\left(\left((R_r - R_f)/X\right) + \left((y' - R_r)/X''\right)\right) \qquad \ldots(8)$$

$$W'_f = \left(W * \cos\alpha * (X_r/X)\right) - \left(W * \sin\alpha * (Y_g/X)\right) \qquad \ldots(9)$$

$$W'_r = W * \cos\alpha - W'_f \qquad \ldots(10)$$

$$X'_r = \left(W'_f/W\right) * X'' \qquad \ldots(11)$$

Similarly, longitudinal stability of the vehicle was studied when the vehicle is on a slope. The dynamic reaction forces obtained are:

$$R_R = W'_r + \left(W * \sin\alpha * \left((R_r + y_g)/X\right)\right) + \left(P * \left((\acute{k}/X) * \cos\theta + ((\acute{x} + X)/X) * \sin\theta\right)\right) \qquad \ldots(12)$$

$$R_F = W'_f - \left(W * \sin\alpha * \left((R_r + y_g)/X\right)\right) - \left(P * \left((\acute{k}/X) * \cos\theta + (\acute{x}/X) * \sin\theta\right)\right) \qquad \ldots(13)$$

The vehicle would be stable as long as the reaction force on the wheels at the top of the slope is greater than zero. Equilibrium moment equations were developed and solved to find the reaction forces on the right and left wheels. The equations obtained are:

$$W = W_R + W_L \qquad \ldots(14)$$

$$X_r = (W_f/W) * X \qquad \ldots(15)$$

$$X_l = X - X_r \qquad \ldots(16)$$

$$\alpha = \tan^{-1}(Y/X) \qquad \ldots(17)$$

$$W'_l = \left(W * \cos\alpha * (X - X_l/X)\right) - \left(W * \sin\alpha * (Y_g/X)\right) \qquad \ldots(18)$$
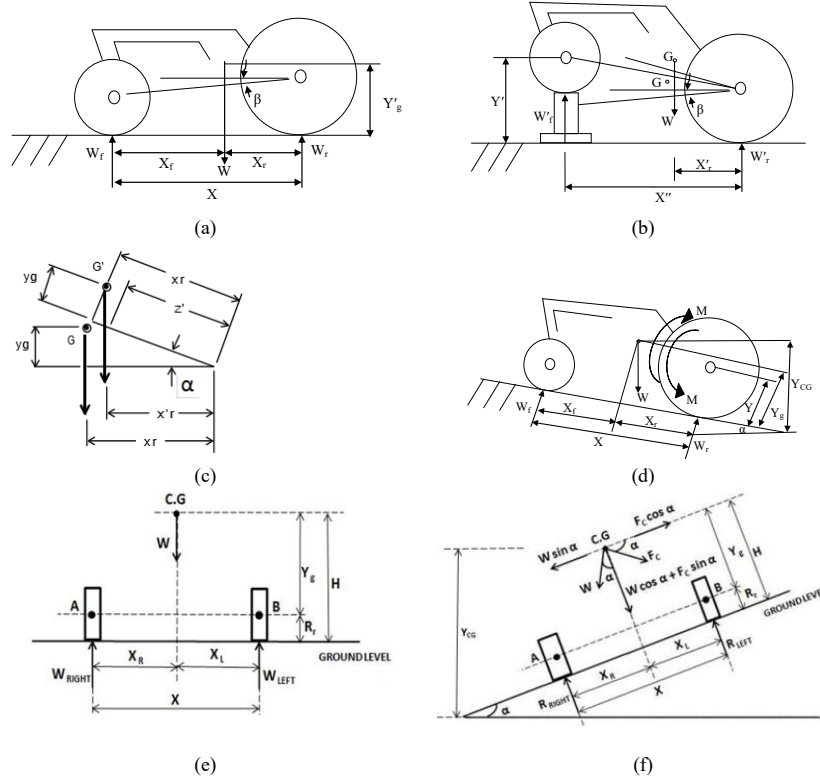
Fig. 8: Static and dynamic model of longitudinal and lateral stability: (a) on level ground, (b) on level ground with front wheel lifted, (c) vehicle longitudinal geometry, (d) on longitudinal slope, (e) vehicle lateral geometry, (f) on lateral slope

$$W'_r = W * \cos\alpha - W'_l \qquad ...(19)$$

Similarly, the dynamic reaction forces on the right and left wheels were studied when the vehicle is moving on the lateral slope. The expressions for the dynamic wheel reaction obtained are:

$$X'_r = (W'_l / W) * X'' \qquad ...(20)$$

$$Z' = (X'_r / \cos\alpha) \qquad ...(21)$$

$$Y_g = (X_r - Z) / \tan\alpha \qquad ...(22)$$

$$u = \sqrt{(R * g * \tan\alpha)} \qquad ...(23)$$

$$W'_R = W'_r + \left(\left(m*u^2/R\right) * \sin\alpha * ((X - X_r)/X)\right) + \left((Y_g/R) * \left(W * \sin\alpha - \left(m*u^2/R\right) * \cos\alpha\right)\right) \qquad ...(24)$$

$$W'_L = W'_l + \left(\left(m*u^2/R\right) * \sin\alpha * (X_r/X)\right) + \left((Y_g/R) * \left(\left(m*u^2/R\right) * \cos\alpha - W * \sin\alpha\right)\right) \qquad ...(25)$$

RESULTS AND DISCUSSIONS

Weight distributed on the rear wheels (R_r), front wheels (R_f), right wheels (R_R), and left wheels (R_L) of the vehicle and the position of the centre of gravity of the vehicle standing on level ground are summarized in Table 4. The resultant values of R_r, R_f, R_R, and R_L were found to be 6463.47, 9696.58, 8502.56, and 7657.49 N, respectively. The centre of gravity of the vehicle in x, y, and z directions (X_g, Y_g, and Z_g,) was found to be placed at 1271.49, 1036.51, and 1855.23 mm, respectively, from the right rear wheel.

Equations 7–25 were used to calculate the resulting

Table 4. Weight distribution and position of centre of gravity

R_r, N	R_f, N	R_r, %	R_f, %	R_R, N	R_L, N	R_R, %	R_L, %	X_g, mm	Y_g, mm	Z_g, mm
9696.6	6463.4	60.0	40.0	7657.5	8502.5	47.4	52.6	1271.5	1036.5	1855.2

wheel reaction forces at static and dynamic vehicle conditions. From these equations, it was well observed that the static stability of the vehicle was greatly affected by the weight of the vehicle, wheel base, height of the CG, distance of the CG from the rear axle, and ground slope. Under dynamic conditions, the forward speed of the vehicle, along with the factor responsible under static conditions greatly affected the impending stability. Figure 9 depicts the change in percentage of static and dynamic wheel reaction forces as the degree of slope increases in both the longitudinal and lateral directions. When the vehicle was on level ground, the reaction force on the rear and front wheels was 60% and 40%, respectively. With an increase in longitudinal slope, the percentage of reaction force on the front wheel was gradually transferred to the rear wheel. The

reaction force on the front wheel was reduced to zero at a slope of 45.19° under the static condition, and to 20.68° under the dynamic condition. When the vehicle was on level ground, the reaction force on the right and left wheels was 47.39 and 52.61%, respectively. With an increase in the lateral slope, the reaction force on the right wheel gradually increased and correspondingly decreased on the left wheel. At 39.08° under static conditions and at 22.10° under dynamic conditions, the wheel reaction on the left wheel was zero. Results of wheel reaction forces at impending stability are presented in Table 5.

The vehicle was tested extensively in on-road condition for at least 100 hours to find out if there was any failure of critical components. The vehicle was tested
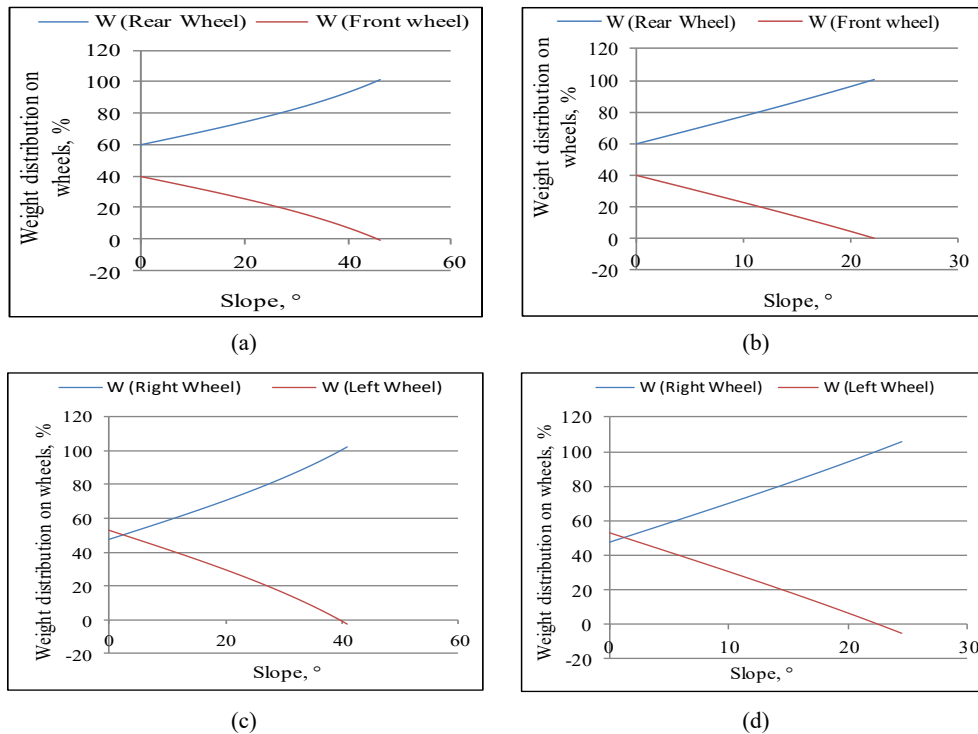

(a)

(b)

(c)

(d)

Fig. 9: Variation of percentage static and dynamic wheel reaction forces with increase of degree of slope: (a) longitudinal static reaction, (b) longitudinal dynamic reaction, (c) lateral static reaction, (d) lateral dynamic reaction

Table 5. Resulting wheel reaction forces at impending stability

Slope		Wheel reaction, N		Load distribution, %		Impending stability, Degree
		Rear	Front	Rear	Front	
Longitudinal	Static	11360.66	28.54	99.75	0.25	45.19
	Dynamic	14655.74	463.04	96.94	3.06	20.68
		Right	Left	Right	Left	
Lateral	Static	12435.55	108.44	99.14	0.86	39.08
	Dynamic	10968.97	4003.61	99.10	0.99	22.10

successfully on the road without any failures. The speed of the vehicle was measured by counting the revolution rate of the rear wheel at different throttle positions of the engine and at full throttle of the variable displacement pump. For the calculation of speed, the distance covered by the rear wheel for a definite number of rotations was observed and found to cover 3.75 m in one revolution. From the distance covered in one rotation and the RPM of the rear wheel at various throttles of the engine, the theoretical speed of the vehicle was calculated. The maximum speed of operation was found to be 20 km.h^{-1} as designed. The plot of engine RPM versus speed of the vehicle is presented in Fig. 10.

Performance of Spraying System

As the hydraulic motor used in the spraying system got driven by the pump coupled to the timing gear of the engine system, the revolution of the motor as well as pump discharge might vary with different throttle positions of the engine. Hence, the discharge from the whole boom system and the pressure generated at various throttle positions were observed. Discharge of the nozzles at various pressures and throttle positions was measured manually. Pressure developed by the sprayer pump at various RPM of the engine is presented in Fig. 11, and the discharge of the boom at various pressures is presented in Fig. 12. It was observed that the sprayer pump was not able to generate the required recommended discharge pressure (3 kg.cm^{-2}) for hollow cone nozzles up to 1200 engine RPM. Hence, for spraying operations, the throttle position was necessary to be adjusted to more than 1200 RPM.

Field Evaluation with Okra and Maize Crop

Performance of the spraying and weeding system was done on okra and maize crops (Fig. 13). Okra and maize were planted at a row spacing of 450 mm. Spraying
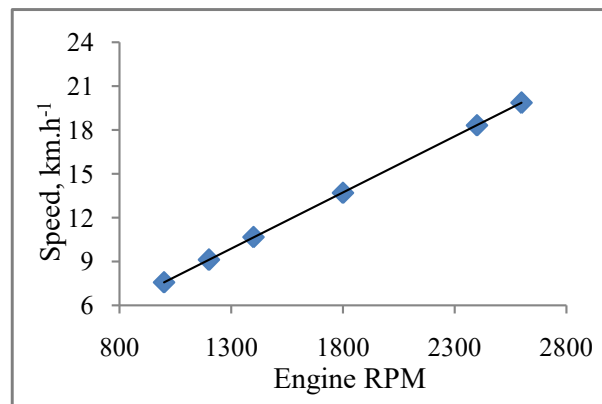

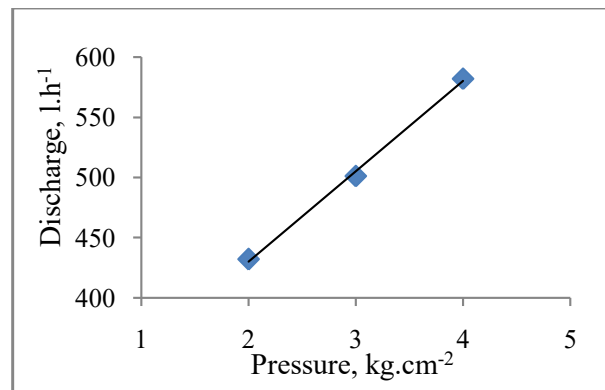**Fig. 10: Speed of vehicle at various throttle position of engine**

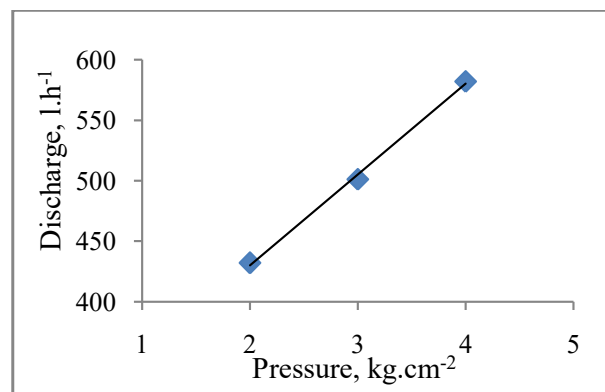**Fig. 11: Pressure developed by pump at various engine RPM**

Fig. 12: Discharge of boom at various pressure

and weeding were done in the fields having a plant height of 1.0-1.2 m and 250-300 mm, respectively. The moisture content of the field at weeding was 16.34±0.82% (d.b.). The vehicle was easily operated at 2-3 km.h^{-1} for spraying operations and 1.5–2.0 km.h^{-1} for weeding operations. Turning time loss at the head land was found to be 15 - 20 s. The field capacity for the spraying and weeding operations was found to be 1.9 ha.h^{-1} and 0.16 ha.h^{-1}, respectively. The cost of operation for spraying and weeding was 400 ₹.ha^{-1} and 1,500 ₹.ha^{-1}, respectively. Weeding efficiency and plant damage of the weeder were 92.58% and 1.55%, respectively.

CONCLUSIONS

An innovative method was employed to optimize the weight distribution over a chassis for designing a self-propelled vehicle using the Microsoft Excel point manipulator add-in tool. The position of the centre of gravity in any plane and the weight distribution over the ground-supported wheel can be easily determined by simply scrolling the horizontal and vertical scrollbar.

**Fig. 13: Performance evaluation of the vehicle in field**

The result showed that the vehicle was stable up to 45.19° and 20.68° at static and dynamic conditions, respectively, on the longitudinal slope. On the lateral slope, the vehicle was stable up to 39.08° and 22.10° at static and dynamic conditions, respectively. The stability analysis results showed possible approaches to increase the vehicle's stability. The design was found to be promising for future developments of similar type of high-clearance vehicle.

NOMENCLATURE

θ	:	Angle of implement
g	:	Acceleration due to gravity
K'	:	Height from base to implement
K	:	Height from implement to centre of rear wheel
m	:	Total mass of the vehicle
P	:	Implement force
R	:	Turning radius of vehicle CG
R_F	:	Dynamic weight on front wheel at slope
R_f	:	Radius of front wheel
R_R	:	Dynamic weight on rear wheel at slope
R_r	:	Radius of rear wheel
u	:	Forward velocity of vehicle
W	:	Vehicle weight
W'_f	:	Static weight on front wheel at slope
W'_l	:	Static weight on left wheel at slope
W'_l	:	Static weight on rear wheel at slope
W'_r	:	Static weight on right wheel at slope
W'_L	:	Dynamic weight on left wheel

W'_R	:	Dynamic weight on right wheel
W_f	:	Weight on front wheel
W_L	:	Weight on left wheel
W_r	:	Weight on rear wheel
W_R	:	Weight on right wheel
X	:	Wheel base
X'	:	Distance between implement to centre of rear
X'_f	:	Distance between front wheel to CG at slope
X''	:	Wheel base at raised condition
X_f	:	Distance between front wheel to CG
X_l	:	Distance between rear left wheel to CG
X_r	:	Distance between rear wheel to CG
X'_r	:	Distance between rear wheel to CG at slope
y'	:	Height from base to centre of front wheel
y	:	Height from base to front wheel
y_1	:	Height from CG to rear axle at slope condition
Y_{CG}	:	Total height of CG from ground (horizontal level at slope condition)
y_g	:	CG Height from centre of rear wheel at horizontal level
Y'_g	:	Height of CG from ground surface at horizontal level=(Y_1+R_r)
Z'	:	Slope distance at raised slope from rear right wheel
z'	:	Slope distance at raised slope from rear right wheel
α	:	Angle of slope
α_s	:	Tip angle of tractor rigid body (ground contact point under static condition)
ρ	:	Coefficient of rolling resistance

REFERENCES

Anon. 1989. Cranes - Design Principle for Loads and Load Combinations. Bureau of Indian Standards IS/ISO 8686-1: Part-1, 1-12

Anon. 2017. Report of National Round Table Conference on Farm Mechanization. Indian Council of Food and Agriculture, 31 January.

Balachandar G. 2022. Annual tractor production crosses 1million, exports surpass 1 lakh for the 1st time in 2021. The Hindu Business line, Chennai, https://www.thehindubusinessline.com/news. 9th January 2022.

Khurmi R S; Gupta J K. 2020. Theory of Machine. S. Chand Publishing, India, 14th edition, Chapter 19, 708-751.

Liljedahl J B; Turnquist P K; Smith D W. 2004. Tractors and Their Power Units. Wiley and Sons, New York, 247-248.

Macmillan R H. 2002. The Mechanics of Tractor - Implement Performance: Theory and Worked Examples. University of Melbourne, Australia. Printed from: http://www.eprints.unimelb.edu.au.

Mahal J S; Garg L K; Sharma V K; Dixit A K. 2007. Development of high clearance power sprayer for cotton. J. Agric. Eng., 44(3), 92-96.

Safarzadeh D; Sulaiman S; Abdul A F; Ahmad D B; Majzoobi G H. 2011. The design process of a self-propelled floor crane. J. Terramec., 48, 157-168.

Segerlind L J. 2010. Design of a Floor Crane. Designing Structural Components for Machine, ASABE, St. Joseph, Michigan, Chapter 13, 387-415.

Singh S P; Singh S. 2021. Farm power availability and its perspective in Indian agriculture. RASSA J. Sci. Soc., 3(2), 114-126.

Verma H C. 2020. Concepts of Physics. Bharati Bhawan, vol.1, Chapter 7, 127-151.

Wismer R D; Luth H J. 1974. Off-road traction prediction for wheeled vehicles. Trans. ASAE, 17(1), 8-10.

Wong J Y. 1993. Theory of Ground Vehicles. Wiley-Interscience, London, 2nd edition, 26.
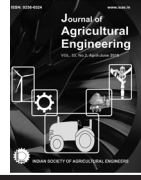
Development and Evaluation of Earthworm-cum-compost Separator

Shoaib Amin[1], Samir Kawoosa[2], Sadaf Mushtaq[3], Saima Hamid[4] and Jagvir Dixit*[1](LM 10045)

[1,2,3,4]Research Scholar, College of Agricultural Engineering & Technology, SKUAST-K, Srinagar; [5]Professor & Head, Division of Farm Machinery and Power Engineering, College of Agricultural Engineering & Technology, SKUAST-K, Srinagar. *Corresponding author e-mail address: jagvirdixit@yahoo.com

Article Info	ABSTRACT
  	A manually operated earthworm-cum-compost separator was designed, developed, and evaluated. The machine consisted of a separating unit, collecting tray, feed hopper, operating handle, sieving unit, and transporting wheels in order to separate the compost and earthworms from the compost material of vermin-culture. The rotating action of the cylinder caused the compost present in the vermi-culture to get separated at the sieving unit on the basis of size and the difference in specific gravity of clods and earthworms causing their separation at the discharge flume of the machine. The separator functioned properly as there was no damage caused to the earthworms. The throughput capacity, compost separation efficiency, earthworm separation efficiency, and overall efficiency were 600 kg.h^{-1}, 88.25%, 96.02% and 84.54%, respectively, at 20.47% (w.b.) moisture contents of vermicast, 23 rpm cylinder speed, and 9° cylinder inclination angle.

Around 58% of Indian population (directly or indirectly) depends upon the agriculture sector and currently it contributes to 17.8% of the Gross Domestic Product (Anon. 2022). Fertilizer plays an important role in improving the product quantity. Since the introduction of chemical fertilizers, efforts have been made to extract the maximum yield from the soil and left the health of soil on nature to restore. Globally, there is growing awareness of the adverse impact of chemical inputs on the soil, environment, and human health. The continuous use of chemical fertilizers degrades the soil health and quality causing soil pollution (Chandini *et al*., 2019). Resource poor farmers also cannot afford costly chemical fertilizers. The farmers, particularly in hilly areas, rely on natural fertilizers like vermicompost, industrial wastage, animal dung, spoiled food, biogas slurry, which are enriched with nitrogen oxides and are also eco-friendly (Urade *et al.,* 2016). Organic manures rejuvenate the soil health as well as the nutritional values of the produce. The crops grown under the umbrella of organic farming fetch higher price and more attention in national and international market. This has prompted both developed and developing countries to shift towards organic

farming. To reduce and eliminate the adverse effects of synthetic fertilizers on human health and environment, new agricultural practices as organic agriculture, sustainable agriculture or ecological agriculture have been developed. Organic farming is one amongst the broad spectrum of production methods that are supportive of the environment. Since 'Sevagram Declaration' made in January 1994 for promotion of organic agriculture in India, organic farming has grown many folds and number of initiatives at Government and Non-Government level has given it a firm direction (Maitra and Zaman, 2018). Organic farming not only produces healthy food products, but also improves the fertility and quality of soil (Isaacs, 2012). Organic agriculture is giving back to the environment what was taken from it (Singh *et al*., 2012).

Vermi-composting is the use of earthworms for the bio-conversion of organic waste into vermicasts and vermiwash. During vermin-composting, earthworms ingest the organic waste which is digested and expelled as granules called vermicasts (Anon., 2007). These vermicasts are odourless and dark brown in colour; and are in combination with unprocessed bedding

and earthworms before separation. Furthermore, a leachate called vermiwash is also produced during vermi-composting. Vermicasts and vermiwash are rich in nitrogen (1.6%), phosphorous (0.7%) and potassium (0.8%) as well as trace elements (Kaur *et al.*, 2015; Urade *et al*., 2016). The nutrient composition of the vermi-products creates a potential for them to be used as bio-fertilizers. Vermi-composting technology is widely being used worldwide as an organic solid waste management strategy. Vermi compost, vermicasts and vermiwash has been used for organic farming of rice, Indian borage, *kharif* crops, okra, and maize (Ansari and Sukhraj, 2010; Palanichamy *et al.,* 2011; Tharmaraj *et al*., 2011; Quaik *et al*., 2012**)**. Although, vermin-composting has been widely adopted as a solid waste management strategy, a challenge has been faced in terms of separation of the earthworms from the vermicasts. In vermiculture, manure is associated with inorganic materials (stones, pebbles etc.) and earthworms. The most important issue that a potential earthworm grower faces is sufficient market demand. The compost present in vermi-compost is needed to be separated from rest of the undesired material present so that it can be used in adopting and promoting organic farming in the current scenario. The earthworms separated are re-used in order to accelerate the process of decomposing in vermiculture and inorganic material is removed to reduce the load of decomposing on earthworms. Researchers have used different methods for separation of earthworms from vermi-compost. Fieldson (1988) used a trommel-type screen separator made of an inclined rotating cylinder with a woven wire mesh wall which was labour intensive and did not fit the high throughput in commercial vermin-composting. A modified separator without a screen wall gave improved results, but it required 80% or less moisture level for vermicompost. Mary (1997) used 'pyramidal heap method' which required simply dumping the worm bin onto a large sheet of plastic, sorting it into about several pyramidal piles, and shining a light on the piles. Left alone for a few minutes, the worms migrate to the bottom of the pyramids to avoid the light. Chaoui and Keener (2008) devised a mathematical model to express the effectiveness of an electric field at repelling earthworms based on the electrostatic potential created across earthworms; and found that the electrode depth, spacing, earthworm species (and the resulting diameter and resistance), and electric current level had a significant effect on electric field effectiveness at repelling earthworms. Moraes *et al.* (2012) utilized controlled electric-pulses to separate the earth worms from the vermi-culture

and worms were displaced towards the anode with the maximum displacement index of only 80%, occurring at the frequency of 1 Hz. Urade *et al.* (2016) designed a machine consisting of many hundreds of pins located inside a drum to pick up the worms as the drum rotated to separate the earthworms and manure. The worms normally progressed half a turn then fell into 1 of the 3 collection trays located on the rails inside the machine. Gopal and Gupta (2019) used a simple push–pull/pull–pull strategy for harvesting the earthworms, wherein freshly ground mustard solution was used as repellent (push agent) and cow dung (with or without bagasse/banana wastes) was used as an attractant (pull agent). The push–pull as well as pull–pull approach was able to attract adult earthworms with weights that ranged from 83 - 107 g per 100 worms.

Presently, harvesting of earthworms from the vermicasts is done using a manually operated sieve which is a time-consuming and labour-intensive process to handle large quantities of vermicasts. At some places, after vermin-compost production, the earthworm present in the tub / small bed are harvested by trapping method (Anon., 2019). Before harvesting the compost from a vermi-bed; small ball from fresh cow dung is made and inserted inside the bed at five or six places. After 24 hours, the cow dung ball is removed. All worms would adhere into the ball. Putting the cow dung ball in a bucket of water would separate the adhered worms. The collected worms can be used for next batch of composting. In Jammu and Kashmir, separation of vermicompost and earthworm are done using hand operated rectangular sieve. The main issue associated with the traditional methods is that individual separation of earthworms, vermicompost, and inorganic material is difficult, besides being time consuming at low work efficiency. Moreover, the earth worms separated by reciprocating movement of a mesh gets injured due to rubbing of their soft body opposing the rough mesh surface. Separating with traditional method is strenuous causing early fatigue, occupational health hazards, and labour intensive.

In view of the above, a study was undertaken to develop a machine for individual separation of earthworms, fine compost, and inorganic material efficiently and effectively.

MATERIALS AND METHODS

A conceptual view (Fig. 1) of the earthworm-cum-compost separator was prepared using AutoCAD-2016
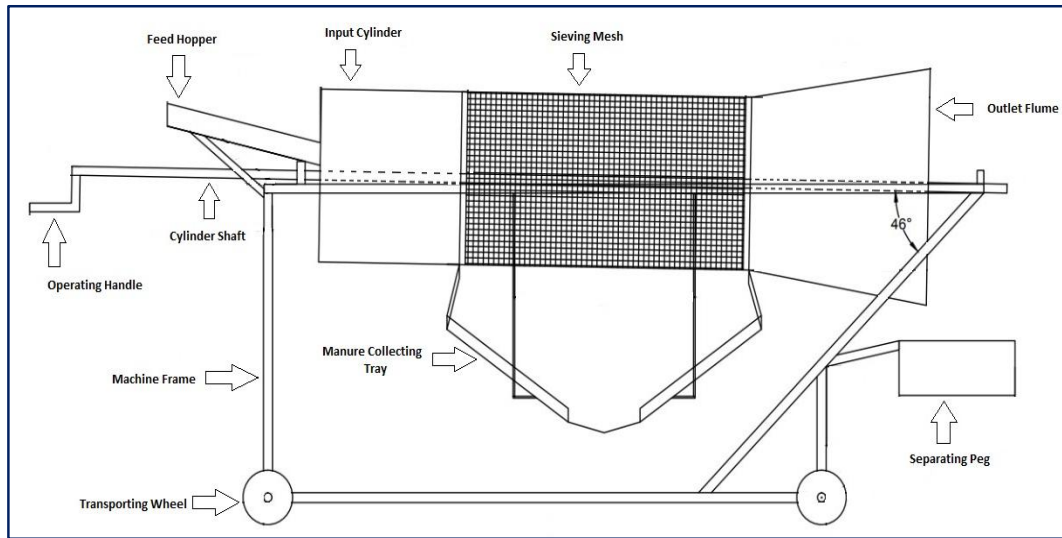
Fig.1: Conceptual view of earthworm-cum-compost separator

software, keeping in view of its functional requirement. The main design considerations were to obtain fine compost (< 2.5 mm) and maximum separation of earthworms (> 95 %) from the raw vermi-culture. Other considerations were taken as minimum injury to earthworms, use of locally available material, easy mobility, low initial cost, and ergonomical aspects.

Design of Machine Components

Cylinder size

The rotating cylinder diameter was selected so that it could accommodate enough vermicast material to have reasonable capacity (about 50 kg per batch) and the length of the cylinder on the basis that sufficient time should be available for proper separation of vermicast constituents. The cylinder size was considered so that one batch could be separated within 5-6 rpm of rotating cylinder. The cylinder diameter was accordingly considered as 482 mm, and the length of cylinder was considered as 1,993 mm. The plan and front view of the machine is given in **Fig**. 2.

Sieve size

The size of the separating sieve was selected keeping in view the size of worms so that they cannot pass through the sieve and only vermi-compost could pass through the sieve easily. The vermicompost had average particle diameters in the range of 300-500 µm, whilst the earthworms had an average weight range of 200- 250 mg (Manyuchi and Phiri, 2013). On the basis of trials with different wire mesh sizes with reciprocating motion, the appropriate size for

most effective separation was selected as 2.5 mm wire mesh of rectangular aperture made of mild steel. From the initial observations, it was found that more than 95% worms were retained on the sieve of size 2.5 mm. The length of the sieve was taken such that vermicompost material could get sufficient time (5-6 rpm) for sieving. Hence, it was taken as 914 mm as per different preliminary trials undertaken.

Cylinder inclination

Cylinder inclination should be such that it allows proper movement of vermicast material inside the cylinder. For proper separation of different moisture laden vermicast material, a suitable provision was provided in the frame to adjust it accordingly. Initial trials were conducted for separation of earthworms, fine compost, and inorganic materials with different cylinder inclination (0-15°) so that about 95% earthworms could be obtained at flume outlet. Based on these trials, the range of cylinder inclination was decided between 6° to 15° with the horizontal surface.

Cylinder outlet shape

Based on the principle of centrifugal force, the shape of the cylinder outlet was considered as flume type so that proper separation of inorganic/un-decomposed material and earthworm by the rotation of cylinder could be possible. The angle of the flume was taken as 15° based on the preliminary study conducted for separation of earthworms from inorganic/un-decomposed materials. The angle of the flume was considered as 15° so that earthworms could remain stuck with the flume at least
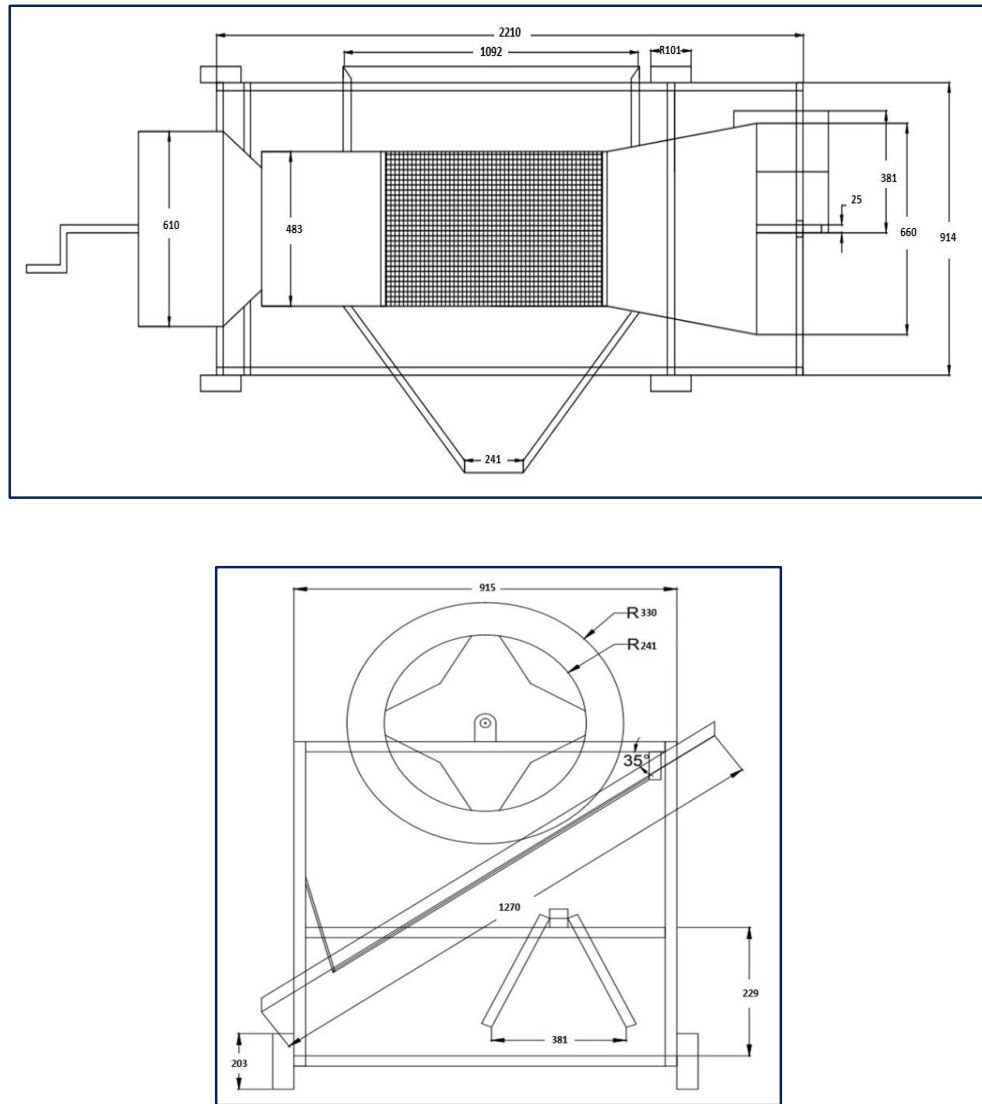
Note: Dimensions in mm

Fig. 2: Plan and front view of developed earthworm-cum-compost separator

for half rotation of the rotating cylinder. Angle of flume more than 15° led to fall of earthworms along with inorganic materials.

Feed hopper

A trapezoidal-shaped feed hopper with self-feed system having capacity of about 50 kg was used in the developed separator. The inclination of the hopper and the product outlet chute beneath the hopper was designed based on the angle of repose of vermin-compost material, which was about 34 degrees. The height of the feed hopper is an important parameter for proper and easy feeding of vermicast material into the hopper, and was designed based on the anthropometric data of the region. The height of feed hopper was selected so that feeding of vermicast material was

convenient to the users. Based on the 5th percentile value of shoulder height of female anthropometric data of the region, height of feed hopper was selected as 1220 mm (Dixit and Namgial, 2012)

Compost collecting tray size and inclination

Fine compost material after sieving was collected through a trapezoidal-shaped tray attached with frame beneath the rotating cylinder. The size of the collecting tray was taken so that all fine compost after sieving gets collected on the tray without falling outside. For proper flow of compost on the collecting tray towards its outlet, the inclination of the tray should be enough to overcome the repose angle of compost (34°). The inclination angle was selected as 35° with respect to the horizontal of cylinder frame. For accommodating

bags at the outlet of the tray, the height of the tray at its outlet was taken as 203 mm.

Offset of separating peg with respect to centre of cylinder shaft

After separation of fine compost at under sieve, the mixture of inorganic materials and earthworm reaches the outlet flume by action of rotating cylinder and slope of the rotating cylinder. A separating peg of invert V-notch type made of mild steel was provided below the outlet end of flume. During the cylinder rotation, the inorganic materials having higher specific gravity first fell on left side of the separating peg, while the earthworm stuck with the flume due to moist skinny layer and fell on the right side of separating peg. The final separation of inorganic material and earthworms occurred on the basis of the moisture of earthworms, gravitational effect, and centrifugal force of rotary action of the cylinder. The position of a separating peg is important parameters for efficient separation of earthworm from inorganic/un-decomposed materials at the final outlet. The position of separating peg was required to be standardized so that all inorganic materials fell on left side, while all earthworms fell on right (other) side of the peg. The offset of a peg with respect to the centre of the cylinder shaft was decided so that proper separation of inorganic material and earthworms could be attained with minimum losses. A provision was also provided to adjust the position of the peg with respect to the centre of the cylinder shaft as per change in moisture content of material and speed of cylinder rotation. The optimized position of peg based on preliminary trials was found to be 108 mm from the centre of the cylinder shaft towards the cylinder rotation at the outlet flume.

Fabrication of Earthworm-cum-compost Separator

Based on the conceptual view and design specifications, a prototype of the earthworm-cum-compost separator was fabricated in the workshop of the College of Agricultural Engineering and Technology, Sher-e-Kashmir University of Agricultural Sciences and Technology of Kashmir, Srinagar using locally available materials. Detailed technical specifications along with materials of construction are given in Table 1.

Machine Description

The developed machine consisted of a frame, feeding unit, sieving unit, compost collecting unit, separating/discharge unit, handle, and transport wheels. The frame was made of galvanized iron square pipes to support the

Table 1. Independent variables and their factor levels

SI. No.	Variable	Level		
		I	II	III
1.	Vermicast moisture content, % (w.b.)	-	20.47	26.32
2.	Cylinder speed, rpm	12.5	23	33
3.	Cylinder inclination, degree	6	9	12

rotating cylinder. The vertical square pipes were welded with 8 horizontal square pipes, four welded at upper side and 4 at lower side of the vertical square pipes to provide rigidity to the frame. Adjustable legs were used to set the desired inclination of the cylinder (with respect to the horizontal) with telescopic arrangement. The rotating cylinder was supported on the frame with the help of ball bearings at each end. This rotating cylinder had a hand operated crank mechanism to manually rotate the cylinder. The separator had four rubber wheels to support the weight of the machine.

The feeding unit consisted of a trapezoidal shaped hopper and input colander made of mild steel (18 gauge) through which vermicast (composed of decomposed inorganic material and earthworms) feeding was done. The sieving unit consisted of a cylindrical sieve with aperture size of 2.5 mm supported by 3 flat iron rings. The fine compost would get separated from rest of the material in this unit. The fine compost travelled through the sieve downwards (under sieve) while the earthworm and inorganic materials remained over the sieve and traverses towards the outlet flume. The fine compost after passing through the sieve would get collected on a collecting tray made of galvanized iron sheet. The other separating unit consisted of an outlet flume and separating peg to separate earthworms and inorganic materials. The final separation of inorganic material and earthworms took place on the basis of the moisture of earthworms, gravitational effect, and centrifugal force provided by rotary action of the cylinder.

Working principle

The earthworm-cum-compost separator was developed to works on the similar principle as followed in Air Screen Cleaner and Specific Gravity Separator used for seed processing. Three specific functional operations were accomplished: (a) movement of material by cylinder rotation and inclination, (b) separation of compost by rotating sieve, and (c) separation of earthworm at outlet flume due to difference of specific gravity and centrifugal force.

The machine is manually rotated by a crank handle at 20-25 rpm. The raw material (vermicast) is fed through the feeding unit. Due to the rotational motion, the raw feed moves forward into the sieving unit where fine manure (compost) gets separated and collected in the collecting tray (below sieving unit). The earthworms and the larger sized inorganic material (stone/clods) move forward towards outlet flume where centrifugal force and gravitational force act on the mix of earthworms and inorganic material. The centrifugal force caused by the rotation of the cylinder tends to move the earthworms and inorganic material tangentially outwards, but due to difference in specific gravity of earthworms and inorganic material they come out of the outlet flume at two different points resulting in the final separation which is further aided by the gable-shaped separating peg.

Performance Evaluation

The machine was evaluated to analyse the effect of independent parameters on individual dependent parameters at different levels of independent parameters. The operating factors affecting performance of the earthworm-cum-compost separator were the vermicast moisture content (M), cylinder speed (N), and cylinder inclination (A).

Cylinder speed was measured with the help of a digital tachometer (Make: Lutron, range: 1-10000 rpm, accuracy: ±0.05 % + 1 digit). Moisture content of raw vermin-compost material was determined by standard oven drying method. The samples were kept in an oven for 24 h at 105 °C and moisture content was calculated accordingly. The inclination angle of the cylinder was measured using a protractor.

The manually operated separator was operated by first feeding the vermicast material into the hopper with the feed gate closed, and then rotating the cylinder through the handle at a specified crank revolution of 12.5, 22, 33 rpm at full feed gate opening in a constant time of about 30 s; after which the fine compost, earthworms, and inorganic materials coming out of the various outlets were collected.

Experimental trials were conducted with three replications. For each experimental trial, 10 kg of vermicast sample was used. Initial average moisture content of vermicast sample was 26.32% (w.b.), and second level of average moisture content (20.47%) of vermicast sample was maintained after 10 days of the first evaluation. A factorial experimental design

(Table 1) was used for the study. Mean crank revolution was maintained at 12.5, 23.0, and 33.0 rpm. The cylinder inclination could be adjusted ranging from 0-15°, and three levels of cylinder inclination viz. 6°, 9°, and 12° were used during experimentations.

Determination of dependent parameters

The machine was evaluated with respect to four different parameters as manure (compost) separation efficiency, earthworm separation efficiency, throughput capacity, and overall efficiency. At the end of each experiment, the parameters throughput capacity, manure (compost) separation efficiency, earthworm separation efficiency, and overall efficiency were determined using the following formulae:

Throughput capacity

Throughput capacity (TC, kg.h^{-1}) was determined based on the quantity of vermicast separated per hour. The formula used by Ali *et al.* (2017) for determination of throughput capacity of a walnut dehuller was used and given in Eq. (1).

$$TC = \frac{\text{Quantity of vermicast material (kg)}}{\text{Time taken (h)}} \qquad ...(1)$$

Manure (compost) separation efficiency

Manure (compost) separation efficiency (MSE) was calculated by dividing the total quantity of manure (compost) present in a sample with the quantity of manure (compost) obtained at the under-sieve of machine (Burns and Moody, 2003) is given in Eq. (2).

$$MSE\ (\%) = \frac{\text{Total quantity of manure present in sample (kg)}}{\text{Quantity of manure obtained at undersieve (kg)}} \times 100$$

$$...(2)$$

Earthworm separation efficiency

Earthworm separation efficiency (ESE) was determined by dividing the total quantity of earthworm present in a sample with the quantity of earthworm obtained at the outlet flume of the machine (Burns and Moody, 2003) and given in Eq. (3).

$$ESE\ (\%) = \frac{\text{Total quantity of earthworms present in sample (g)}}{\text{Quantity of earthworms obtained at outlet of flume (g)}} \times 100$$

$$...(3)$$

Overall efficiency

Overall efficiency (OE) was determined by multiplying the earthworm separation efficiency (ESE) with the

manure separation efficiency (Burns and Moody, 2003) and given in Eq. (4).

$$OE~(\%) = MSE \times ESE \qquad ...(4)$$

Data Analysis

The results of the machine performance (cylinder speed, cylinder inclination, moisture content of vermi-cast) with different treatments on the earthworm, compost and inorganic material separation were analysed using Factorial Completely Randomized Block Design with three replications by using Opstat software package. Analysis of variance (ANOVA) at 0.05 level of significance was used to assess the effects of each machine parameter and treatments on the dependent variables. The optimum level of vermicast moisture content, cylinder speed, and cylinder inclination angle for the separation of earthworm, compost, and inorganic material were obtained by numerical optimization using Design-Expert software package (version 10; Stat-Ease Inc; Minneapolis, MN, USA.). All independent variables were kept in range for optimization purpose without imposing any constrains, while manure (compost) separation efficiency, earthworm separation efficiency, throughput capacity, and overall efficiency were maximized.

RESULTS AND DISCUSSION

Development of Earthworm-cum-compost Separator

Based on the design of various components and the functional requirements of the prototype, an earthworm-cum-compost separator was developed and fabricated (Fig. 3). The technical specifications of the earthworm-cum-compost separator are given in Table 2.

Performance of Earthworm-cum-compost Separator

The machine was evaluated (Fig. 4) to analyse the effects of independent parameters on individual dependent parameters at different levels of independent parameters.

Moisture content of vermicast, cylinder speed, and cylinder inclination were three independent factors which affected the machine performance. The performance of the developed machine was inter-dependent on these parameters. The different dependent parameters viz. throughput capacity, manure separation efficiency, earthworm separation efficiency, and overall efficiency of the developed machine were required to be as high as possible. Optimization of independent parameters was done to determine the values of the independent parameters for efficient separation of compost, earthworm, and inorganic material from the vermicast (feeding material).

Effect of moisture content

Moisture content of vermicast feed material played an important role in the performance of the machine. High moisture content of vermicast reduced the travel speed of material and decreases the throughput capacity and efficiency of the machine. The increase in moisture content of vermicast material from 20.47% to 26.32% (w.b.) retarded the travel motion of vermicast material

Fig. 3: Developed earthworm-cum-compost separator

Table 2. Technical specifications of earthworm-cum-compost separator

Sl. No.	Machine component	Size, mm	Material of construction	Dimension, mm
1.	Overall dimension (l x b x h)	-	-	2130 × 930 ×1010
2.	**Frame**			
	Upper long square pipe	31.75	Mild steel	2209.8×50.8
	Lower long square pipe	31.75	Mild steel	127.2×50.8
	Upper and lower short square pipe	31.75	Mild steel	914.4×76.2
	Slanting square pipes	31.75	Mild steel	1092.2×50.8
	Adjustable vertical pipes	25.4	Mild steel	457.2×50.8
3.	**Feeding unit**			
	Hopper		Mild steel 18-gauge sheet	914.4×609.6×25.4 (L×B×H)
	Input cylinder	482.6		457.2 (L)
4.	**Separating unit**			
	Separating Sieve	2.5	G. I.	914.4 (L)
	Outlet flume • Outer • Inner	660.4 482.6	Mild steel 18-Gauge	508 (L) 114.3 (L)
	Cylindrical solid shaft • Outlet side • Inlet Side	25.4 25.4		152.4 330.2
	Cylindrical hollow shaft	31.75	Mild steel	1981.2
	Separating peg		18-gauge MS sheet	355.6 ×381 (L ×B)
	Circular blades	19	12-gauge	
	Operating handle	31.75	Mild Steel	152.4
5.	**Collecting unit (Tray)**			
	• Inlet • Outlet		28-gauge GI sheet	1092.2 (W) 241.3(W)
6.	**Transport wheel**	203.2	Rubber	38.1 (Thickness)
7.	**Weight of machine, kg**	-	-	85.0

Fig. 4: Evaluation of earthworm-cum-compost separator

due to adhesive nature of material, which caused decrease in the throughput capacity of the machine about 4.72% (Table 3). Also, the increase in moisture content caused the manure (compost) and earthworms to stick with inorganic material forming aggregates at various sections of the machine, thereby decreasing the earthworm and manure separation efficiencies by 4.03% and 10.39%, respectively. Same trend was also reported by Musaida and Phiri (2013), who found that the earthworm trommel separation efficiency decreased with increased moisture content of the vermicasts at constant rotational speed of 50 rpm.

Effect of cylinder speed

It was observed that higher the cylinder speeds, higher was the separation efficiency of vermicast. Higher cylinder speed (33 rpm), however, decreased the earthworm separation efficiency. This indicated that the forward movement of the materials was fast, and aided the compost to pass through the rotary screen opening. At lower cylinder speed (12.5 rpm), the forward movement of the vermicast was slow. Because of this, the decrease in cylinder speed decreased the travel speed of the material through the cylinder and thus decreased the quantity of vermicast material to be

Table 3. Effect of vermicast moisture content, cylinder speed and cylinder inclination on dependent parameters

Moisture content (w.b.), %	Speed of cylinder, rpm	Angle of inclination, degree	Throughput capacity, kg.h⁻¹	Compost separation efficiency, %	Earthworm separation efficiency, %	Overall efficiency, %
Independent parameter			**Dependent parameter**			
M$_1$	N$_1$	A$_1$	551	96.67	82.65	79.89
		A$_2$	569	91.23	89.98	82.09
		A$_3$	590	91.40	77.91	71.21
	N$_2$	A$_1$	583	93.04	89.68	83.44
		A$_2$	600	88.25	96.02	84.74
		A$_3$	611	85.85	87.00	74.69
	N$_3$	A$_1$	605	88.01	94.04	82.76
		A$_2$	639	85.96	91.59	78.74
		A$_3$	650	77.25	89.76	69.34
M$_2$	N$_1$	A$_1$	501	87.66	80.28	70.37
		A$_2$	530	80.76	87.54	70.70
		A$_3$	563	84.33	76.07	64.15
	N$_2$	A$_1$	553	84.15	87.08	73.28
		A$_2$	580	77.31	93.50	72.29
		A$_3$	598	77.37	84.10	65.07
	N$_3$	A$_1$	596	77.19	92.13	71.11
		A$_2$	602	75.32	87.23	65.70
		A$_3$	620	70.64	78.44	55.41
CD $_{(0.05)}$						
Factor, A			2.038	0.298	0.395	0.118
Factor, B			2.496	0.365	0.484	0.177
Factor, C			2.496	0.365	0.484	0.177
A × B			3.530	N/A	0.685	N/A
A × C			3.530	0.517	0.685	0.354
B × C			4.323	0.633	0.839	0.531
A × B × C			6.114	0.895	1.186	1.061

M$_1$: 24.47%　　　M$_2$: 26.32%　　　N$_1$:12.5 rpm　　　N$_2$: 23 rpm　　　N$_3$: 33 rpm　A$_1$: 6　　　A$_2$: 9　　A$_3$: 12°

separated within a set time, and hence decreased the throughput capacity (Table 3). Lower cylinder speed (12.5 rpm) increased the accumulation of earthworms on the undesired side, thereby decreasing the earthworm separation efficiency and overall efficiency. Musaida and Phiri (2013) also reported that lower rotational speed promoted clumping together of the vermicasts causing ineffective separation.

Effect of cylinder inclination angle

The feedstock introduced at the centre of the rotary cylindrical drum with peripheral mesh opening along the length of the drum permitted fine compost to fall through the sieve onto the outlet chute. The remaining material (earthworm and inorganic compost) that did not fall through the mesh was discharged at the rear end of the drum. The increase in cylinder inclination with respect to the horizontal (6.0 to 12.0°) increased the travel speed of the material towards the outlet flume, and thus there was decrease in the amount of compost collected on the collecting tray since less sieving time was available for complete separation of manure (Table 3). This increased the throughput capacity from 564.83 to 605.33 kg.h⁻¹and decreased the compost separation efficiency by 7.56%. At lower cylinder inclination (6°), travel speed of material decreased, thereby decreasing the throughput capacity. The earthworm separation efficiency was found highest (90.98%) at cylinder inclination of 9°, while it was lowest (81.14%) at 12° cylinder inclination.

Operating Parameters Affecting Machine Performance Parameters

Throughput capacity

The results of ANOVA of the operating parameters affecting throughput capacity as shown in Table 3 indicated that moisture content (A), cylinder speed (B), and angle of inclination (C) had significant impact on the throughput capacity. The regression equation that determined the effect of operating parameters on throughput capacity is shown in Eq. (5).

$$TC = 585.33-14.1*A+34.02*B+20.28*C+3.38*AB+1.58*AC-4.02*BC \qquad ...(5)$$

Where,

TC = Throughput capacity, kg.h⁻¹,
A = Moisture content of feedstock, % (w.b.),
B = Cylinder speed, rpm, and
C = Angle of inclination, degree.

R^2 and adjusted R^2 values for the Eq. (5) were 0.97 and 0.96, respectively. Based on the Eq. (5), the response surface plot showing the effects of moisture content, angle of inclination, and cylinder speed on throughput capacity of the machine is given in Fig. 5.

From Fig. 5, it is clear that increasing cylinder speed and angle of inclination enhanced the throughput capacity of the machine, while moisture content had inverse effect. As the cylinder speed increased from 12.5 rpm to 33 rpm, the throughput capacity of the machine
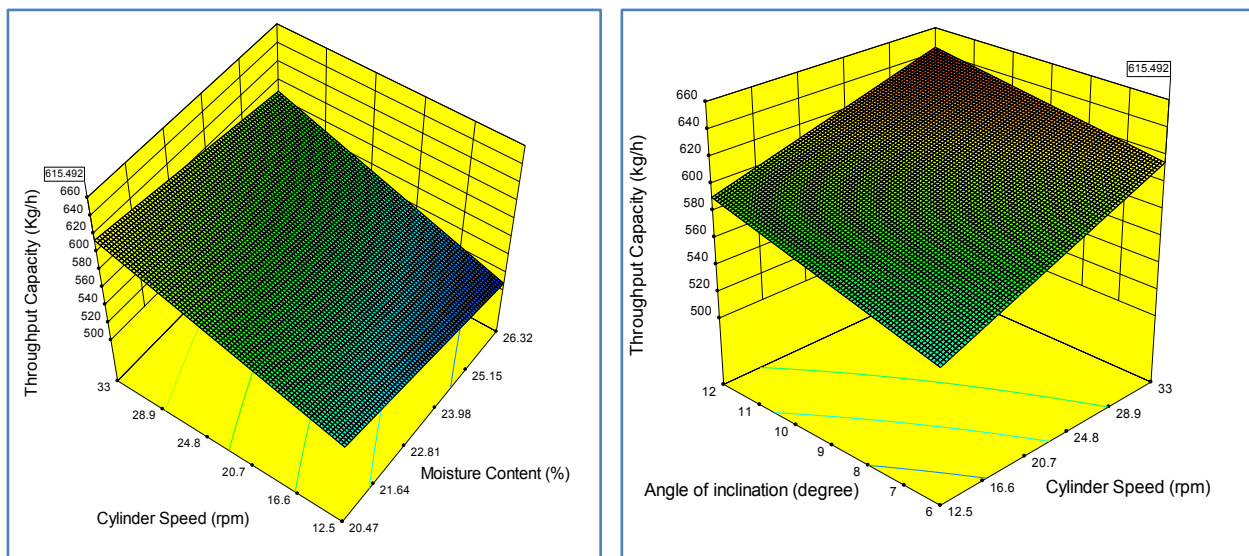

Fig. 5: Response surface plots showing effect of cylinder speed, cylinder inclination, and moisture content on throughput capacity

increased linearly from 550.66 kg.h⁻¹ to 618.67 kg.h⁻¹. Similarly, with increase in cylinder inclination angle from 6° to 12°, the throughput capacity of the separator increased from 564.83 kg.h⁻¹ to 605.33 kg.h⁻¹. As seen from Fig. 5, the interaction effect of cylinder speed, cylinder inclination, and vermicast moisture content on throughput capacity clearly showed that the cylinder speed had greater effect on the throughput capacity than the cylinder inclination and vermin-cast moisture content. The increase in crank rotation speed increased the travel speed of the material which increased the throughput capacity of the machine. However, with increase in moisture content of vermicast from 20.47% to 26.32% (w.b.), the throughput capacity decreased from 599.78 kg.h⁻¹to 571.44 kg.h⁻¹. This might be due to reduced travel speed caused by the adhesive nature of material.

Compost separation efficiency

The results of ANOVA of the operating parameters affecting compost separation efficiency as shown in Table 3 indicated that moisture content (A), cylinder speed (B), and angle of inclination (C) had significant impact on compost separation efficiency. Interaction of A*B did not have significant impact on the compost separation efficiency. The regression equation that determined the effect of operating parameters on compost separation efficiency is shown in Eq. (6).

CS = 84.06-4.61* A-4.80*B-3.31*C-0.13*AB+ 0.55*AC-1.09*BC   ...(6)

Where,

CS = Compost separation efficiency, %,
A = Moisture content of feedstock, % (w.b.),
B = Cylinder speed, rpm, and
C = Angle of inclination of drum, degree.

R^2 and adjusted R^2 values for the Eq. (6) were 0.95 and 0.92, respectively. Based on the Eq. (6), the response surface plot showing the effect of moisture content, angle of inclination, and cylinder speed on compost separation efficiency is given in Fig. 6. Operation of the machine demonstrated increase in compost separation efficiency with increase in cylinder speed and cylinder inclination; whereas, compost separation efficiency decreased with increase in vermicast moisture content. As the cylinder speed increased from 12.5 rpm to 33 rpm, the compost separation efficiency of the machine decreased linearly from 87.67% to 79.06 per cent. Similarly, with increase in cylinder inclination angle from 6° to 12°, the compost separation efficiency of the separator decreased from 87.79% to 81.14 per cent. This was mainly due to insufficient time available for sieving. However, with increase of vermicast moisture content from 20.47% to 26.32% (w.b.), the compost separation efficiency decreased from 88.63% to 79.41 per cent. The increase in crank rotation increased the compost separation efficiency, but it also increased the amount of un-decomposed material to fall towards the earthworm side at the outlet.

Earthworm separation efficiency

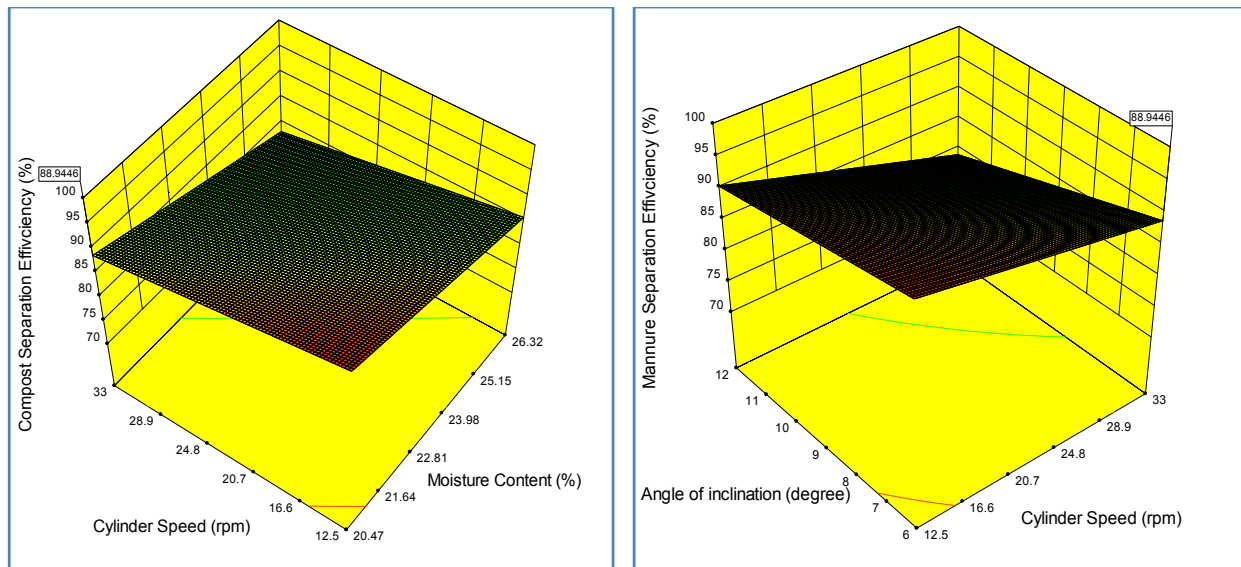The results of ANOVA of the operating parameters

Fig. 6: Response surface plots showing effect of cylinder speed, cylinder inclination, and moisture content on compost separation efficiency

affecting earthworm separation efficiency reported in Table 3 indicated that moisture content (A), cylinder speed (B), and angle of inclination (C) had significant impact on earthworm separation efficiency. The regression equation that determined the effect of operating parameters on earthworm separation efficiency is shown in Eq. (7).

$$ESE = 86.92 - 1.78*A + 3.26*B - 2.71*C - 0.91*AB - 0.76*AC - 1.11*BC \quad ...(7)$$

Where,
ESE = Earthworm separation efficiency, %,
A = Moisture content of feedstock, % (w.b.),
B = Cylinder speed, rpm, and
C = Angle of inclination of cylinder, degree.

R^2 and adjusted R^2 values for Eq. (7) were 0.95 and 0.92, respectively.

Based on the Eq. (7), the response surface plot showing the effect of moisture content, angle of inclination and cylinder speed on earthworm separation efficiency is given in Fig. 7. Operation of the developed machine demonstrated decrease in earthworm separation efficiency with increase in vermicast moisture content; whereas, earthworm separation efficiency increased with increase in cylinder speed (up to 23 rpm) and cylinder inclination angle (up to 9°), and then decreased with further increase in cylinder speed and cylinder inclination angle. With increase of cylinder speed from 12.5 rpm to 23 rpm, the earthworm separation

efficiency of the machine increased from 82.41% to 89.56%, and then decreased to 88.86% at cylinder speed of 33 rpm. The low crank rotation speed (12.5 rpm) aided the accumulation of earthworms on the undesired side, thereby decreasing the earthworm separation efficiency. Similarly, with increase in cylinder inclination angle from 6° to 9°, the earthworm separation efficiency of the separator increased from 87.64% to 90.98% and then decreased to 82.21% at cylinder inclination of 12°. However, with increase in moisture content of vermicast from 20.47% to 26.32% (w.b.), the earthworm separation efficiency decreased from 88.74% to 85.15 per cent. The increase in vermicompost moisture content caused the compost and earthworms to stick at various sections of the machine, and with un-decomposed material forming aggregates thereby decreased the earthworm and compost separation efficiencies.

Overall efficiency

The results of ANOVA of the operating parameters affecting overall efficiency reported in Table 3 indicated that moisture content (A), cylinder speed (B), and angle of inclination (C) had significant impact on overall efficiency, whereas the interaction of A*B did not have a significant impact on overall efficiency. The regression equation that determined the effect of operating parameters on overall efficiency is shown in Eq. (8).

$$OE = 73.06 - 5.48*A - 1.25*B - 5.07*C - 0.89*AB - 0.06*AC - 1.77*BC \quad ...(8)$$
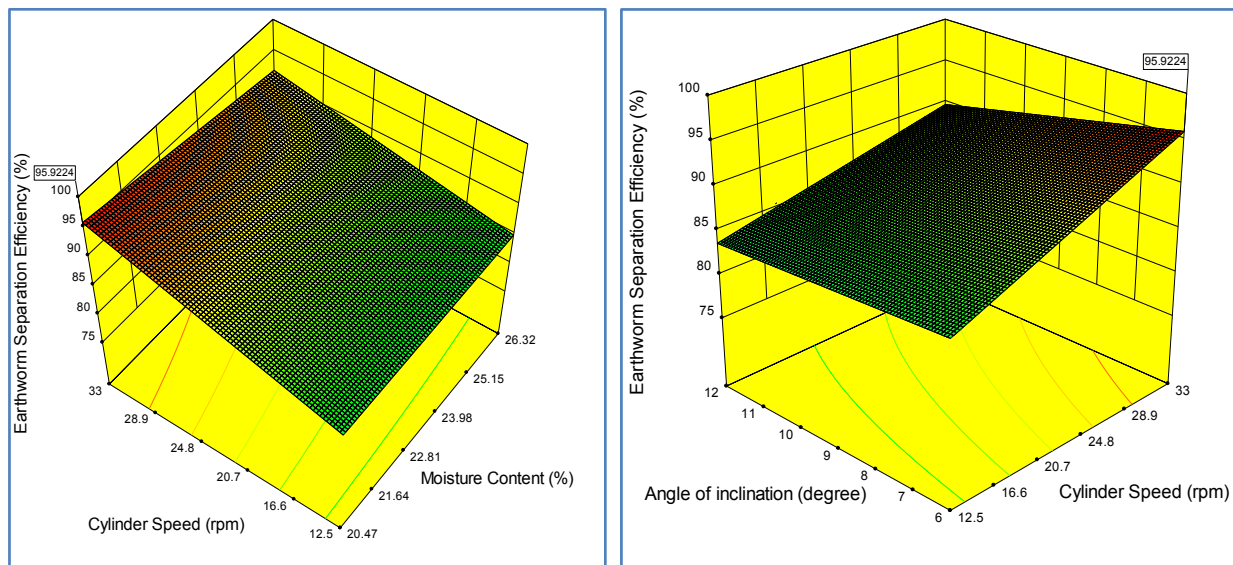

Fig. 7: Response surface plots showing effect of cylinder speed, cylinder inclination, and moisture content on earthworm separation efficiency

Where,
 OE = Overall efficiency, %,
A = Moisture content of feedstock, % (w.b.),
B = Cylinder speed, rpm, and
C = Angle of inclination of cylinder, degree.

R^2 and adjusted R^2 values for Eq. (8) were 0.87 and 0.79, respectively.

Based on Eq. (8), the response surface plot showing the effect of moisture content, angle of inclination, and cylinder speed on overall efficiency of the machine is given in Fig. 8. Operation of the machine demonstrated decrease in overall efficiency with increase in vermicast moisture content and cylinder inclination angle; whereas, overall efficiency increased with increase in cylinder speed (up to 23 rpm) and then decreased with further increase in cylinder speed. With increase of cylinder speed from 12.5 rpm to 23 rpm, the overall efficiency of the machine increased from 73.07% to 75.85%, and then decreased to 70.51% at cylinder speed of 33 rpm. However, as the cylinder inclination angle increased from 6° to 12°, the overall efficiency of the separator decreased from 76.80% to 66.64 per cent. Similarly, with increase in moisture content of vermicast from 20.47% to 26.32% (w.b.), the overall efficiency decreased from 78.54% to 67.56 per cent.

Effect of Peg Position with Respect to Cylinder Axis

The peg used as a separator for earthworm and inorganic material at outlet position, also affected the separation of earthworm and inorganic material at the

outlet of flume. The rotary motion of the outlet flume discharged the heavy inorganic material bottom hill at starting point of the discharge edge. The inorganic material fell first due to higher specific gravity, while the earthworm tended to remain stuck with the flume at the outlet and separated from the flume after travelling some distance. Thus, the peg position should be such that the earthworms and inorganic materials fall in their respective containers at the outlet of the flume.

As the distance of the separating peg from the axis of the shaft of the cylinder was increased towards direction of rotation, large numbers of earthworms were forced towards the inorganic material. When the distance of the separating peg was brought closer towards the axis of the shaft of the cylinder, large amount of inorganic material was forced towards the earthworms at the peg (Fig. 9). Thus, for reducing the interference of each material from entering the others side, the peg position (shown by position 1, 2, 3) with distance of 76 mm, 108 mm, 152 mm, respectively, from the centre of the shaft of cylinder towards the direction of rotation of cylinder was standardized at position 2.

Optimization of Operating Parameters

The optimum level of vermicast moisture content, cylinder speed, and cylinder inclination angle for the separation of earthworm, compost (manure), and inorganic material were obtained by numerical optimization. Product optimization was carried out by applying specific goals to each response variable (Table 4). The optimum values of vermicast moisture
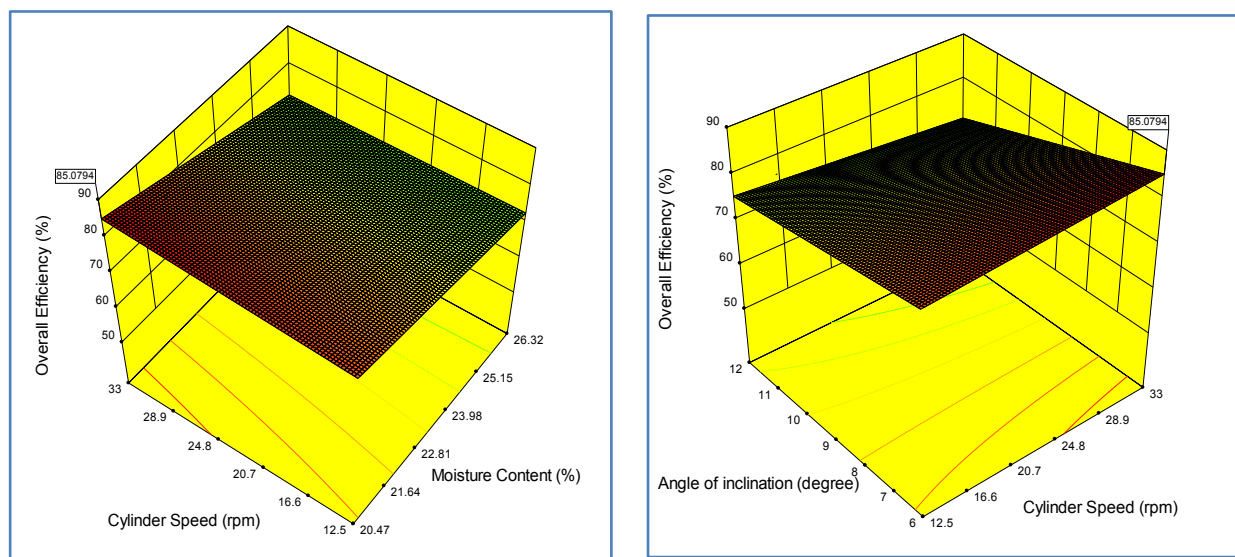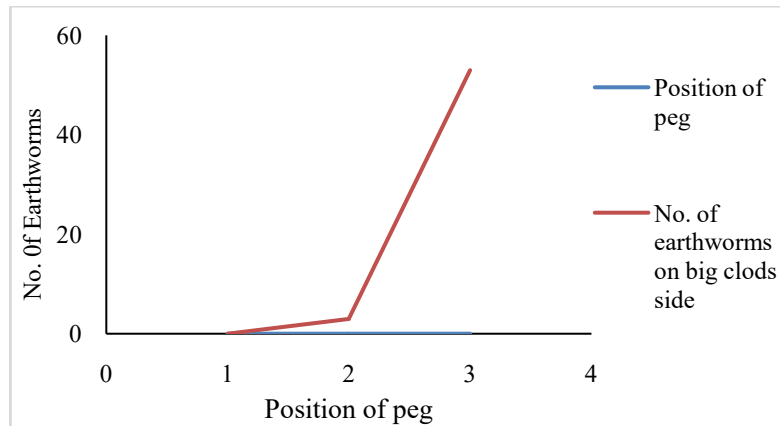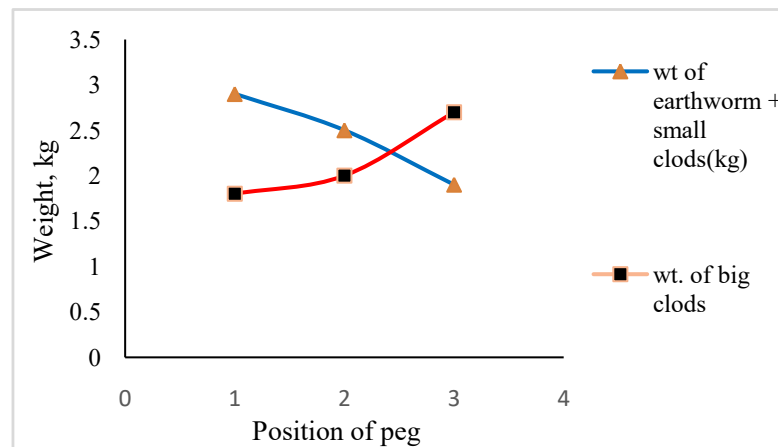

Fig. 8: Response surface plots showing effect of cylinder speed, cylinder inclination, and moisture content on overall efficiency

Position of peg: 0 represent peg at the centre of axis of rotation
                               1 represents peg at 76 mm offset to axis of rotation
                               2 represents 108 mm offset to axis of rotation
                               3 represents 152 mm offset to axis of rotation

Position of peg: 0 represent peg at the centre of axis of rotation
                               1 represents peg at 76 mm offset to axis of rotation
                               2 represents 108 mm offset to axis of rotation
                               3 represents 152 mm offset to axis of rotation

Fig. 9: Effect of peg position on weight of inorganic material and earthworms

content, cylinder speed, and cylinder inclination angle were 20.47%, 23 rpm, and 9°, respectively. The optimum response parameters obtained were 602.33 kg.h^{-1}, 88.23%, 95.85%, and 84.54% for throughput capacity, manure (compost) separation efficiency, earthworm separation efficiency, and overall efficiency, respectively.

CONCLUSIONS

A manually operated earthworm-cum-compost separator was developed at the College of Agricultural Engineering and Technology, SKUAST-K, Srinagar and evaluated for separation of earthworm, compost, and un-decomposed materials from a heap of vermin-cast. The machine efficiently separated earthworms, fine compost, and inorganic material from vermicasts (feed material). It was observed that higher the cylinder speeds, higher was the separation efficiency of vermicast, but with decreased earthworm separation efficiency. Similarly, increase in cylinder inclination increased the travel speed of the material towards the outlet flume resulting in decrease in amount of manure (compost) collected on the collecting tray. At lower cylinder inclination, travel speed of material decreased, thereby decreasing the throughput capacity. Hence, the vermicast moisture content of around 20%, cylinder speed of 23 rpm, and cylinder inclination angle

Table 4. Numerical optimization of vermicast moisture content, cylinder speed, and cylinder inclination angle and predicted responses

Variable	Goal	Optimum/ predicted value
Input variable		
Vermicast moisture content, %	In range	20.47
Cylinder speed, rpm	In range	23
Cylinder inclination angle, degree	In range	9
Output variable/response		
Throughput capacity, kg.h^{-1}	Maximize	602.33
Compost separation efficiency, %	Maximize	88.23
Earthworm separation efficiency, %	Maximize	95.85
Overall efficiency, %	Maximize	84.54
Desirability		0.843

of 9° are recommended for optimum earthworm and compost separation. The developed machine can help to increase the production capacity in vermi-composting processes due to 6-times more capacity (602 kg.h^{-1}) and 70% cheaper compared to traditional method (manually-operated sieve) of separating earthworms from vermicast.

REFERENCES

Ali M; Dixit J; Lohan S K. 2017. Development of motorized walnut dehuller. J. Agric. Eng., 54(4), 43-48.

Anon. 2007. Low-cost Home Built Worm Cast Harvester. Available online whatcom.wsu.edu/ag/compost/pdfs/LowCostWormCastingHarvester.pdf.

Anon. 2019. TNAU AgriTech Portal: Organic Farming. Available online at http://agritech.tnau.ac.in/org_farm/orgfarm_vermicompost.html

Anon. 2022. Indian agriculture Industry analysis. India Brand Equity Foundation, New Delhi. Available at: Agriculture in India: Industry Overview, Market Size, Role in Development [accessed Jan 25 2022]

Ansari A Aggrotech; Sukhraj K. 2010. Effect of vermiwash and vermicompost on soil parameters and productivity of okra (Abelmoschus esculentus) in Guyana. Pak. J. Agric. Resour., 23, 137-142.

Burns R T; Moody L B. 2003. Development of a standard method for testing mechanical manure solids separators. ASAE Annual International Meeting, Paper No. 034131, St. Joseph, MI.

Chandini Kumar; Kumar R; Prakash O. 2019. The Impact of Chemical Fertilizers on our Environment and Ecosystem. In: Research Trends in Environmental Sciences, 2nd Edition, Chapter5. Available at:https://www.researchgate.net/publication/331132826_The_Impact_of_Chemical_Fertilizers_on_our_Environment_and_Ecosystem [accessed Jan 21 2022].

Chaoui H; Keener H M. 2008. Modeling the effectiveness of an electric field at repelling earthworms. Biosyst. Eng., 100 (3), 409-421.

Dixit J; Namgial D. 2012. Anthropometry of farm workers of Kashmir region of India for equipment design. J. Agric. Eng., 49(2), 8-15.

Fieldson R S. 1988. Economic viability of earthworm culture on animal wastes. C. Edwards, F. Neuhauser (Eds.), Earthworms in Waste and Environmental Management, The Hague, 145-156.

Gopal M; Gupta A. 2019. A simple push-pull strategy to harvest earthworms from coconut leaf vermicompost produced in tanks. Current Sci., 117(1), 138-144.

Isaacs J R. 2012. Organic farming keeps carbon out of the atmosphere. http://news.mongabay.com/2012/1128-isaacs-organic-carbon. [Accessed on Jan 21, 2022].

Kaur P; Bhardwaj M; Babbar I. 2015. Effect of vermicompost and vermiwash on growth of vegetables. Res. J. Anim. Vet. Fish. Sci., 3(4), 9-12.

Maitra S; Zaman A. 2018. Organic farming in India: status, scope and potential. M S Swaminathan School of Agriculture, Centurion University of Technology &Management, Paralakhemundi 761211, Odisha, India, pp: 10. Available online https://www.aditicert.net/newsletter/Organic-farming- in-India-Status-Scope-and potential.pdf.

Mary A. 1997. Worms Eat My Garbage. Flower Press, Kalamazoo, Mich., USA, pp: 100.

Moraes M J; Filho D O; Martins J H; Santos L C. 2012. Electric signals for separation of earthworms. Energy Agric., 16(10), 1137-1142.

Musaida M M; Phiri A. 2013. Effective separation of vermicasts from earthworms using a cylindrical rotary

trommel separator. Int. J. Innovative Res. Sci. Eng. Technol., 2(8), 4069-4072.

Palanichamy V; Mitra B; Reddy N; Katiyar M; Rajkumari R B; Ramalingam C; Arangantham. 2011. Utilizing food waste by vermicomposting, extracting vermiwash, castings and increasing relative growth of plants. Int. J. Chem. Anal. Sci., 2(11), 1241-1246.

Quaik S; Embrandiri A P; Rupani F R; Singh P; Ibrahim M H. 2012 Effect of vermiwash and vermicompost leachate in hydroponics culture of Indian borage (Plectranthus amboinicus) plantlets. In: Proc. 1th International Annual Symposium on Sustainability Science and Management, 210-214.

Singh S; George R; Prafull B. 2012. Organic farming practices of plains and hills farmers and their extent of compliance with National Program for Organic Production (NPOP) guidelines. J. Agric. Sci., 3, 55-62.

Tharmaraj K; Ganesh P; Kolanjinathan K; Suresh R; Anandan A. 2011. Influence of vermicompost and vermiwash on physicochemical properties of rice cultivated soil. Current Bot., 2, 18-21.

Urade A; Satone N; Sutsonkar N; Zade H ; Rangari D R. 2016. Effective separation of vermicast from earthworms: A review study. Res. Recent Trends Eng. Technol., 3(3), 380-383.

Yadav S K; Babu S.; Yadav M K; Singh K; Yadav G S; Pal S. 2013. A review of organic farming for sustainable agriculture in northern India. Int. J. Agron., 2013,1-8.

Development of Sensor-based Automatic Colour Sorting System for Tomato

Yogesh Bhaskar Kalnar[1], Sandeep P. Dawange[1], Sandeep Mann[2], Bhupendra M. Ghodki[1] and Th. Bidyalakshmi Devi[1]

[1]Scientist, [2]Principal Scientist, ICAR–Central Institute of Post-Harvest Engineering and Technology, Ludhiana, India. Corresponding author email address: bhupendra.ghodki@icar.gov.in, yogeshkalnar2506@gmail.com

Article Info	ABSTRACT

The present study was aimed to develop an automatic colour sorting apparatus for tomatoes by utilizing a microcontroller, colour sensor array, servo motors, and mechanical components. When an object was passed through the sensing region of the colour sorting system, a colour sensor array sent input signals, attenuation level of colours to a processing unit/microcontroller Arduino board. Further, the output signal (colour frequency) of microcontroller was sent to an actuator (servo motor) for sorting coloured objects into separate collecting pans. The process algorithm was programmed in Arduino IDE software. The detected colour frequencies were expressed in red, green, and blue on an LCD and computer screen along with the colour of the respective samples. The developed system was initially tested with six distinct coloured balls of 70 mm diameter, and calibrated at three different lighting conditions of a lit room, dark room, and daylight. Subsequently, tomatoes of 41.97–56.57 mm geometric mean diameter of three different colours, i.e., red, pink, and green, were used for automatic sorting. The system automatically separated tomatoes of a particular colour into three subclasses of large, medium, and small as per their colour values. Under all lighting conditions, the automatic sorting system precisely separated 1,800 sample.h^{-1}.

Industrial automation and control are a modern way of managing different processes via a combination of sensors, computers, and robots associated with other electrical, electronics, and mechanical components. The food Industry is also utilizing this approach to increase production efficiency and productivity with minimal human interventions/efforts. Harvested food products are generally cleaned, graded, sorted, and dehulled before further processing to obtain quality and safe products. In developing nations such as India, these operations are usually performed manually, which are subjective, slow, and unreliable (human error). Automation of such operations may lead to overcoming shortfalls of the manual process.

Food products can be sorted/separated based on their measurable physical characteristics such as density,

firmness, weight, colour, shape, and size. However, sorting based on optical properties or colour of food products is primarily used since it aids in efficient/ easy assessment of food quality. Moreover, the electro-optical technique is one of the most practical and successful methods of separation and quality evaluation (Inamdar and Suresh, 2014). Hence, the quality of food material can be better analyzed by visualizing the colour variation of the sample that further assist in sorting.

Automated sensor-based sorting machines separate materials based on the variation in their colour or brightness. Colour sensor array is the heart of colour sorting machine, which consists of a light source and an appropriate photodiode array. These machines can operate in a wide range of electromagnetic spectrum

which is outside the human eye range. In the past, some attempts have been made on the development and application of colour sorter in the field of post-harvest engineering and technology such as for sorting citrus, apple, tomatoes, rice, wheat, beans, coffee, peanuts and other agricultural commodities (Rokunuzzaman and Jayasuriya, 2013; Inamdar and Suresh, 2014). Besides, it has been reported that shape, size, density, texture, defects, and colour affect the sorting of different horticultural produce via non-destructive technologies (Moreda *et al.*, 2009). In general, colour sorting apparatus has a singulator section, a colour sorter, and a conveyor which place sorted samples/fruits into suitable collection bins. The system was calibrated for one or more colour with reference to a predetermined colour standard. The colour classification of red and white wheat was reported using a commercial colour sorter utilizing visible-near infrared wavelength of the electromagnetic spectrum (Inamdar and Suresh, 2014). In India, the tomato growers are getting low profits due to non-availability of automated sorting and grading system. Further, at the time of peak production season, the return rate is very low that can be improved by selling graded tomatoes.

In the same line, a programmed Raspberry Pi board coupled with camera, microcontroller/Arduino, and servo motor control boards along with an image processing tool was reported for developing a low-cost robotic sorting unit with 100% accuracy under normal room light condition (Pereira *et al.*, 2014) which is an open source Linux based board. Shen and Hassan (2015) developed a colour sorting robot using microcontroller/Arduino Uno, colour sensor array, servo motors, and other electrical components for different colour balls. Moreover, Arduino programming was used for logically sorting colour balls as well as for calibration and testing the robotic sorter. Both these studies utilized open-source hardware and (or) software for the development of cost-efficient robotic colour sorter where lighting conditions significantly influenced the sorting efficiency. The technical aspects, including design, programming, illumination condition, and component details are generally not reported in

detail in the available literature. Although automated sensor-based sorter or optical sorter has been used for the separation of food products for over three decades; it is still the subject of research, particularly for enhancing separation efficiency, versatility, sorting speed, and accuracy as well as minimising power requirement and cost of the system. The available automated sorting and grading units are mostly imported for industrial applications, and expensive as per farmers' perspective. A cost-effective and indigenous machine for automated grading and sorting of tomatoes can be made using advanced computing and sensor technologies. Thus, this investigation was aimed to develop a sensor-based automatic colour sorting system for tomatoes using a microcontroller, colour sensor array, servo motors, and mechanical components.

MATERIALS AND METHODS

Sample

Fresh and defect-free tomatoes (Seminis hybrid) of three colours, i.e., red, pink, and green having 43.93–60.89 mm length, 42.94–59.00 mm width, 39.64–51.03 mm thickness and 0.93–0.96 sphericity were procured from a local market of Ludhiana, India in June 2019. The properties were determined using standard methods/formula (Ghodki *et al*., 2016; Ghodki and Goswami, 2016; Singh *et al*., 2018). The length, width, and thickness of 100 samples were measured at three different locations of the respective dimension (end-points and mid-point) using a digital Vernier Calliper (Mitutoyo, CD-12" PSX, Japan, range: 0-300 mm, resolution: 0.01 mm, accuracy: ± 0.02 mm).

Sphericity was determined as the ratio of geometric mean diameter by length (longest dimension). Moreover, based on these properties, the tomatoes were sub-divided into three classes as 31 large, 30 medium, and 39 small (Table 1), and were used for further colour sorting experimentations. Colour ball samples of six different colours (red, orange, green, yellow, pink, blue) of 70 mm diameter were sourced from the local market of Ludhiana, and utilized for testing colour sensitivity of the developed automated sorting system

Table 1. Dimensional detail of tomato samples

Sl. No.	Class/grade of tomato	Length, mm	Width, mm	Thickness, mm	Geometric mean diameter, mm	Sphericity
1.	Large	60.89 ± 1.12	59.00 ± 2.05	51.03 ± 1.99	56.57 ± 1.46	0.93 ± < 0.01
2.	Medium	54.08 ± 2.15	53.25 ± 1.78	47.62 ± 2.89	51.32 ± 1.18	0.95 ± 0.03
3.	Small	43.93 ± 1.36	42.94 ± 1.72	39.64 ± 0.29	41.97 ± 1.01	0.96 ± < 0.01

at ICAR-Central Institute of Post-Harvest Engineering and Technology, Ludhiana.

Sensor-based Automatic Sorting System

The sensor-based automated sorting system consisted of four primary components: (i) feeding system consisting of hopper and actuator/top servo motor connected with grooved (cylindrical) mobile plate; (ii) presentation system consisting of back-and-forth mechanism; (iii) identification system consisting of colour sensor array, microcontroller, and computer; (iv) separation system consisting of actuator/bottom servo motor connected to mobile discharge chute and collection pans (Fig. 1).

Design of automatic colour sorting system

The overall design of the sensor-based automatic colour sorting system includes two essential parts: (i) mechanical components, and (ii) sensor node. Both components were interlinked with each other with a pre-defined logic/programming. The mechanical and sensor node components were mounted on a wooden frame (Fig. 1).

Dimensions of tomatoes, angle of repose, motion, sphericity, and optical properties were considered as major design considerations for the development of mechanical components. Design details of the automated sorter mainly emphasising the mechanical components along with the dimensions are shown in

Fig. 2. The mechanical parts including feed hopper, grooved mobile plate driven by top servo motor, mobile chute driven by bottom servo motor, and collection pans were made of stainless steel 304. The samples were fed through a hopper and grooved mobile plate for colour identification of tomato in the sensing chamber. Once the colour was identified, the mobile chute placed the samples into different collection pans.

Sensor node architecture

The architecture of the sensor node used in the present study is presented in Fig. 3. The sensor node consisted of a colour sensor array (TCS 3200, Bytesware Electronics, Bangalore, India, 2.7-5.5 V, (-) 2 mA to (+) 2 mA), microcontroller board (Arduino Mega 2560), liquid crystal display (LCD, 16×2 alphanumeric LCD I2C), servo motors (MG995, Tower Pro. Pvt. Ltd., Taiwan, stall torque: 8.5-10 kgf.cm, 4.8-7.2 V) and power source (5 V, 1 A). The connections of each component of sensor node are shown in pin diagram (Fig. 3b). Colour sensor array and input device detected the colour of a given sample/object and sent the signal to the microcontroller. Consequently, microcontroller and processing unit sent the signal to the servo motors as per the programme. The detected colour was displayed on the LCD/computer screen, while the data was stored in the computer via a universal serial bus (USB). A power source (5 V DC, 1 A) supplied energy to the components of the automated sorter. The details

a: Hopper Tube
b: Colour Sensor
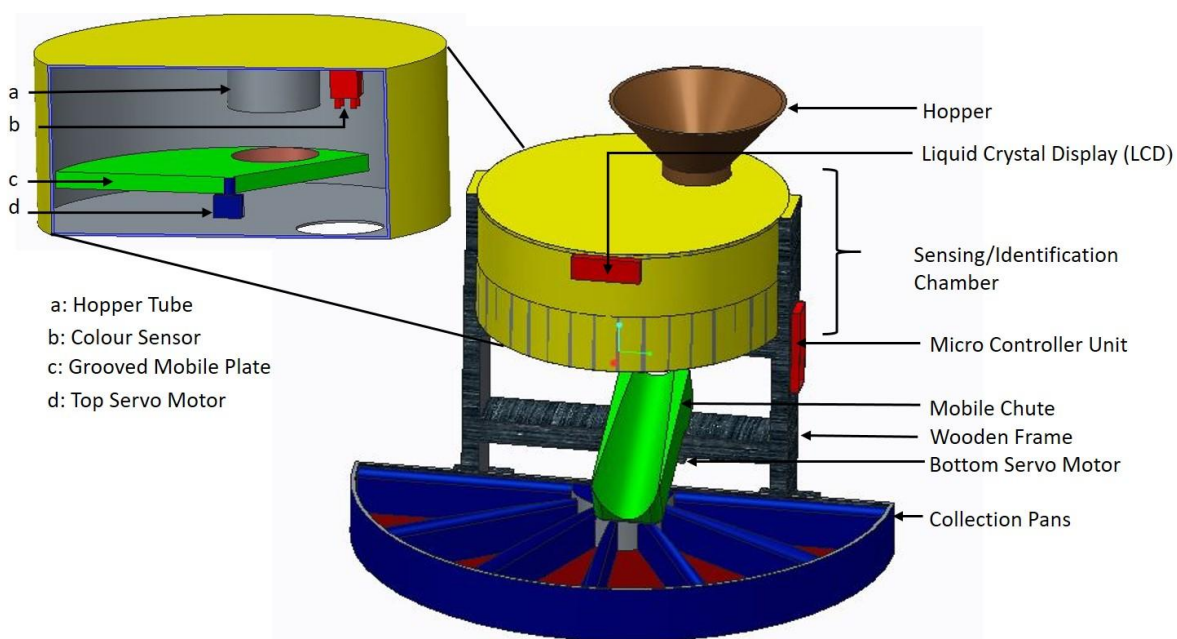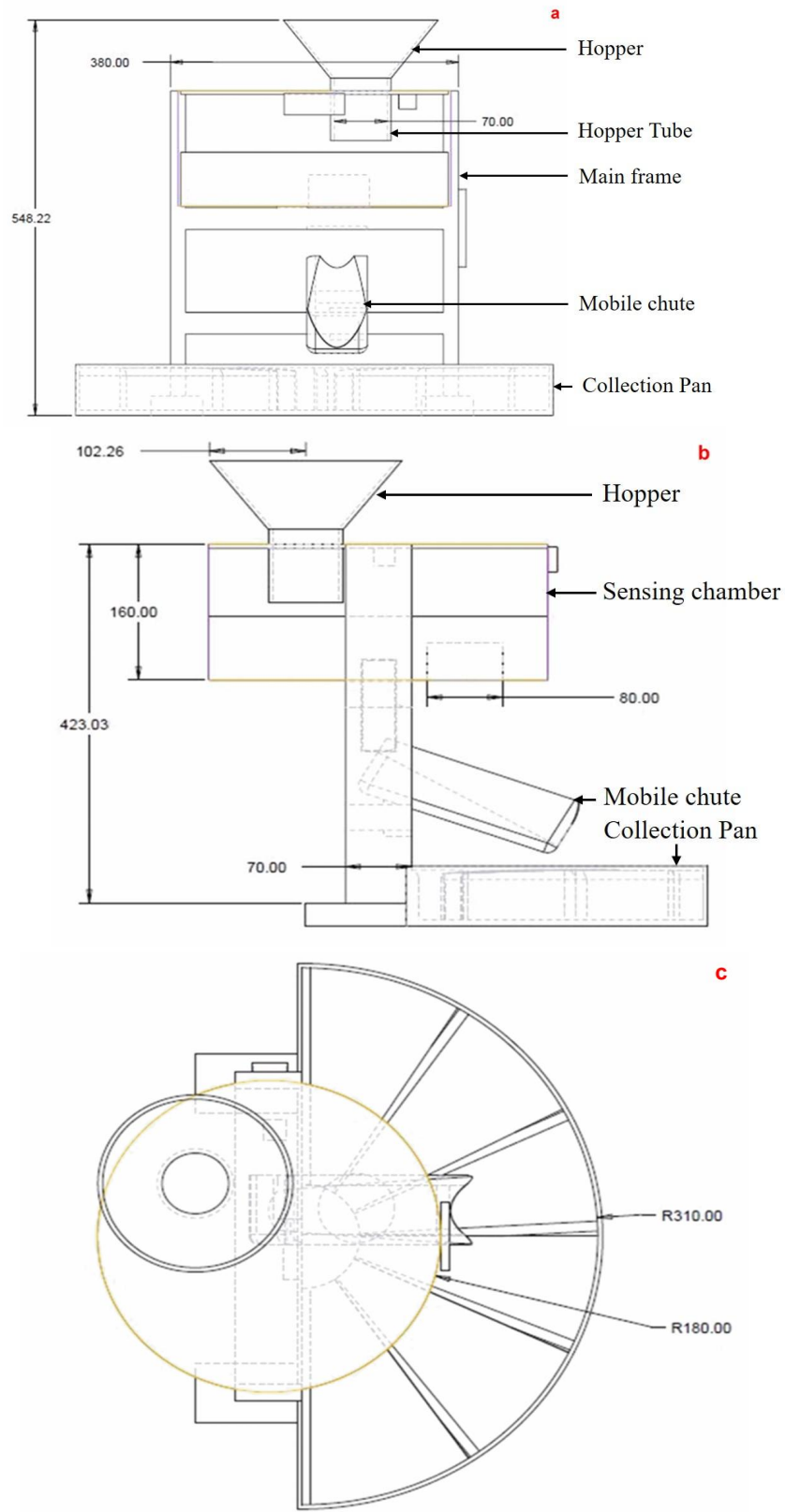c: Grooved Mobile Plate
d: Top Servo Motor

Fig. 1: Isometric view of colour sorting system highlighting its sensing/identification chamber

(All dimensions are in mm)

Fig. 2: Design details of colour sorting system: (a) front view, (b) side view, (c) top view
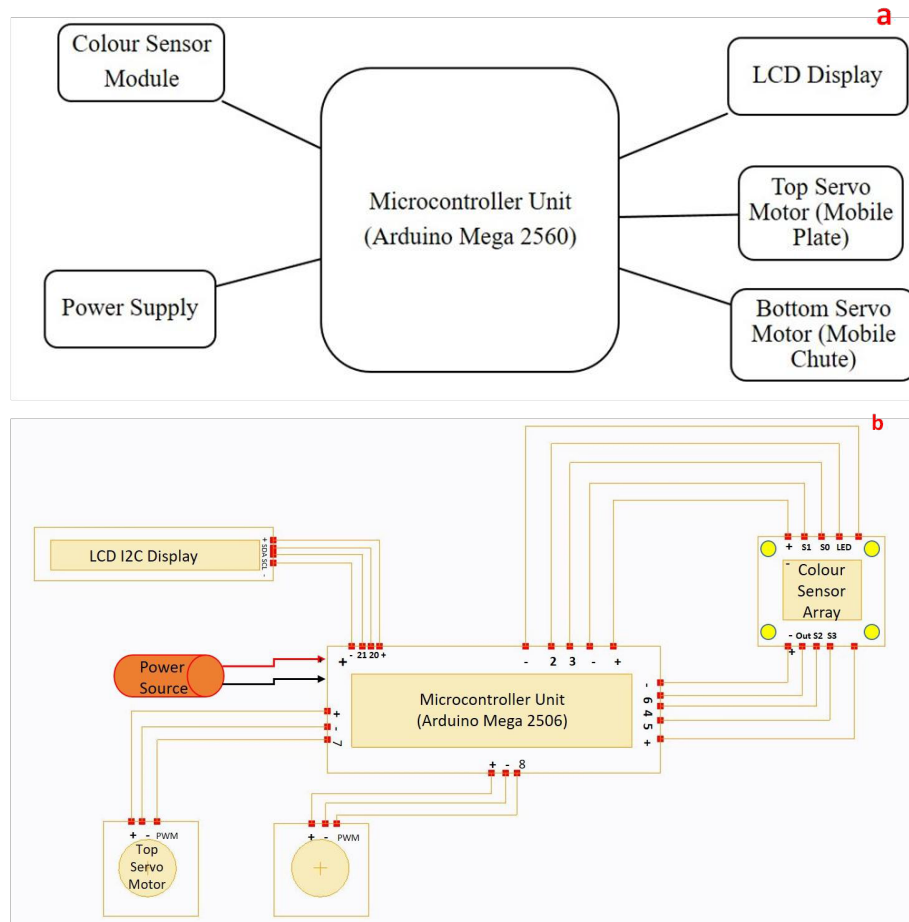
Fig. 3: Sensor node architecture: (a) block diagram, and (b) schematic of connection setup

of the connection setup (Fig. 3b) of the colour sorting system are presented in Table 2.

Microcontroller unit

Arduino board (Arduino Mega 2560) based on ATmega2560 processor was utilized as a microcontroller unit. Arduino is an open-source platform for hardware and software. Microcontroller unit made separation/ sorting related decisions after receiving output from the colour sensor array. The Arduino board has 54 digital input/output pins, 16 analog inputs, four universal asynchronous receiver/transmitter, a 16 MHz crystal oscillator, a USB connection, a power jack, an in-circuit serial programming header, and a reset button.

Colour sensor array

The colour sensor array TCS3200 was used in this study due to its compatibility with the selected microcontroller along with appropriate features such as size, high-resolution conversion of light into frequency, programmable colour, and power down aid. The

colour sensor array was composed of photodiode array along with four white light-emitting diodes (LED), as shown in Fig. 4a. It sensed the colour with photodiode array (Fig. 4a) using a current-to-frequency converter (Fig. 4b). The sensor had 8×8 arrays of photodiodes having 16 photodiodes of red filters, 16 photodiodes of blue filters, 16 photodiodes of green filters, and 16 photodiodes were clear with no filters. Each 16 arrays of photodiodes were connected in parallel. Thus, by sending different voltages (coded as 0 - low voltage and 1 - high voltage/5 V in photodiode) to two control ports S2 and S3, the user could select the readability of colour (Table 3). For example, with 1 for S2 and 1 for S3, the colour detected in photodiode would be green.

The output (readings of photodiode) of the colour sensor array was a square wave, 50% duty cycle, with the frequency being directly proportional to light intensity (irradiance). Digital inputs and digital output allowed a direct interface to a microcontroller or other logic circuitry. In this study, the microcontroller calculated

Table 2. Details of connection of peripherals with microcontroller

Peripheral	Pins of peripheral	Pins of microcontroller
Colour sensor array	S0	2
	S1	3
	S2	4
	S3	5
	OE	GND
	OUT	6
Top servo motor	PWM	7
	VCC	VCC
	GND	GND
Bottom servo motor	PWM	8
	VCC	VCC
	GND	GND
LCD I2C	SDA	20
	SCL	21
	VCC	VCC
	GND	GND

Note:
OUT – Output frequency, OE –Output enabled, GND - Ground, VCC – Voltage at the common collector (+5 V),
PWM - Pulse width modulation, SDA –Serial data line, and SCL-Serial clock line
The terms S0 and S1 indicate line for output frequency scaling; S2 and S3 represent line for photodiode type
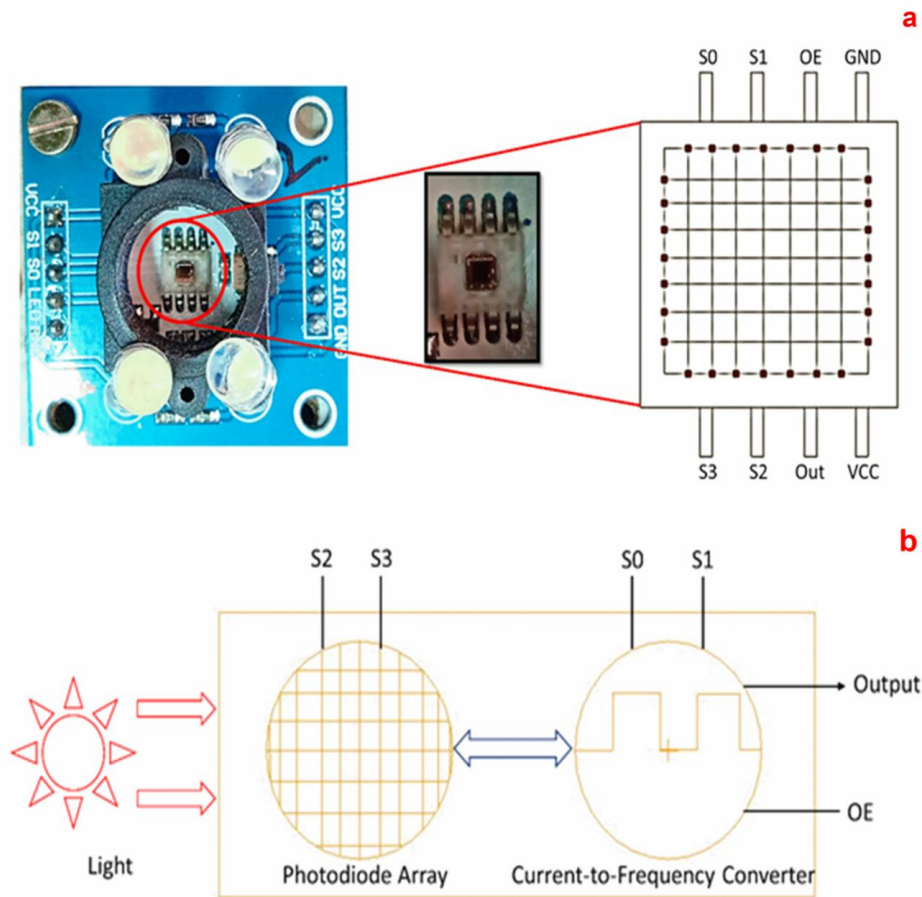Numeric values are number on microcontroller board

Fig. 4: Illustration of (a) TCS 3200 colour sensor array highlighting array of photodiode, and (b) current to frequency conversion in the colour sensor array

Table 3. **Details of port/peripherals in TCS3200 colour sensor array along with respective colour detected in photodiode**

Port		Colour detected in photodiode
S2	**S3**	
0	0	Red
0	1	Blue
1	0	No colour
1	1	Green

Note:
The terms S2 and S3 represent line for photodiode type
The values 0 and 1 indicate low voltage and high voltage (5 V), respectively.

red (R), green (G), and blue (B) colour channel value/ colour frequency/colour value/coefficients of the given colour sample by sending a high or low signal to S2 and S3 inputs of the colour sensor array. In general, the combination of these three primary colours made other secondary colours which are visible to the human eye.

Actuator

Two servo motors MG995 (or actuators) were connected to a mobile plate and chute, respectively, via a motor shaft that rotated at various programmed angles (Fig. 1). The top servo motor was utilized to present the object below colour sensor array for sensing and identification of its colour, while the bottom servo motor-assisted in placing objects of various colours in different collection pans (separation).

The servo motors were controlled by sending electrical pulse of variable width (Pulse width modulation, PWM) through the control wire, which determined the amount of movement of the motor shaft. Microcontroller generated PWM signal to run the servo motors. In general, the duty cycle of PWM decided the angle of movement of the servo motor. Servo motor had three wire terminals, namely red, brown, and orange. These wires were connected in the following manner: red wire to Vcc voltage, brown wire to ground (GND), and orange wire (PWM input) to the microcontroller.

Liquid crystal display

A liquid crystal display (LCD) using the light adjusting characteristics of liquid crystals was selected as the display unit. Solid monochromatic 16×2 alphanumeric LCD I2C was coupled with the Arduino board to display the values of colour frequency and colour of the sample. The 16×2 LCD means that it could display a total of 32 characters at a time consisting of 16 characters per row (total two rows).

Working of Automatic Colour Sorting System

Colour ball samples (70 mm diameter) of red, orange, green, yellow, pink, and blue were used for colour calibration and experimentation. Subsequently, tomatoes of three colours of red, pink, and green were tested for automatic sorting. The tomatoes of each colour category were further classified/sorted into three subclasses of large, medium, and small based on colour channel values.

Programming of microcontroller unit was done in Arduino Integrated Development Environment (IDE) software installed in the computer. Furthermore, different rotation angles were programmed in the software for sorting of coloured samples. The working of the algorithm of the programme of the colour sorter is illustrated in Fig. 5. The microcontroller was

```
Start
   ↓
Initialize all peripherals, i.e., microcontroller, servo motors,
colour sensor array, and LCD
   ↓
Placing samples in hopper that needs to be
sorted
   ↓
Presenting individual samples (one at a time) below colour
sensor using top servo motor
   ↓
Deciding the colour of samples by calculating its R, G, and B
coefficients/values using colour sensor array & microcontroller
   ↓
Rotating bottom servo motor shaft to programmed orientation
depending on detected colour of object
   ↓
Continue above steps till samples to be sorted are finished
   ↓
End
```
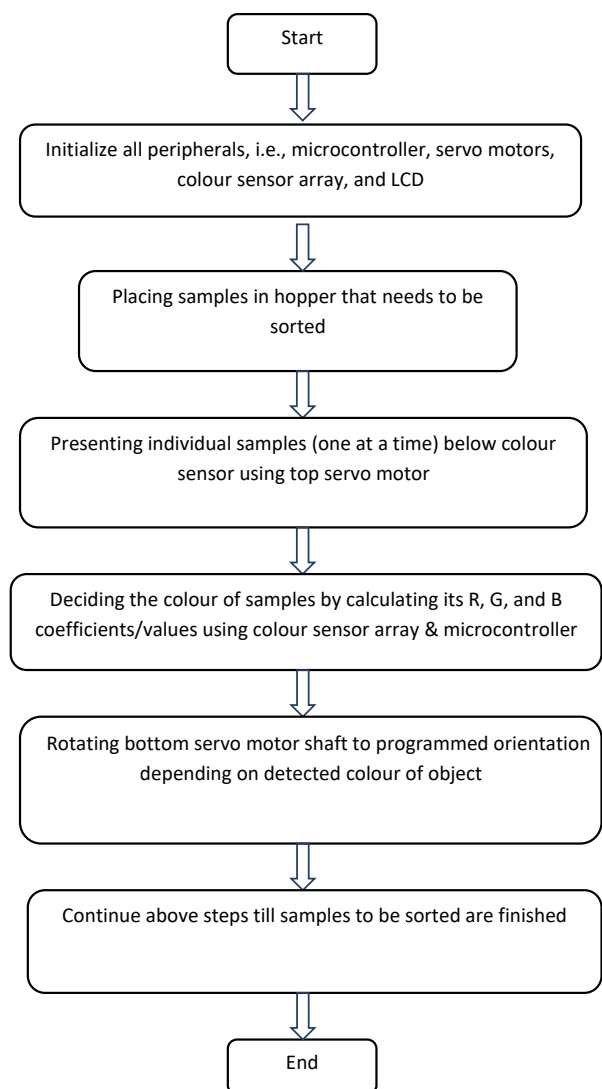
Fig.5: Algorithm of colour sorting programme

programmed in a manner that it first initializes all peripherals (microcontroller, servo motors, LCD, and colour sensor array). Initialization of colour sensor included choosing output pins of the microcontroller for lines of the colour sensor array (S0, S1, S2, S3) as well as selecting the input pin of the microcontroller for colour sensor's output enabled pin (OE). The microcontroller also selected the output frequency scaling using S0 and S1 control pins.

After the initialization step, the samples were conveyed/fed to a rotating grooved plate via a feed hopper having a cylindrical pipe arrangement at its bottom (Fig. 1). The cylindrical grove allowed an individual/singulated sample to be easily placed in it. The grooved plate was attached with a top servo motor (top of sorter) to present the samples in the sensing/identification region via the programmed mechanism. The program was written in a loop such that the top servo motor continuously rotates the grooved plate/groove from the bottom of the feed hopper to a position below the colour sensor (for sensing/identification), followed by the position just above the mobile chute (for separation). The mobile chute rotated at a programmed angle and places the sample in the collection bin as per the colour. Simultaneously, the microcontroller sent the signal to the LCD for display of the sample's colour and values of colour frequency. After the separation step, the grooved plate returned to the original position. For continuous sorting of samples, this separation process continued in a loop till objects to be sorted were not available.

Calibration

Colour calibration of the automatic colour sorting unit was done for setting up the range of different colour samples as well as training the programme. Six different colour ball samples (red, orange, green, yellow, pink, blue) as well as colourless/blank, were utilised to test the colour sensitivity of the unit. Consequently, tomatoes of three different colours (red, pink, green) were used for testing and training the setup/programme.

Calibration was performed at three different lighting conditions of lit room, dark room, and daylight for robust separation. The calibration process includes repeated measurements (average of five readings) of individual colour coefficients, namely, R, G, and B of different samples in different lighting intensities. The R, G, and B values noted for six colour samples and blank reading were statistically analysed using analysis of variance (ANOVA) and reported to be significant if $p \leq 0.05$. For obtaining higher accuracy, the colour

sensor array was encompassed in a closed chamber (Fig. 1). Moreover, the complete assembly was covered with black paint. The results of calibration were used for deciding the range of colour channel values of different colour samples. In the case of colour ball samples, the upper limit of colour channel values was kept 15% higher than the highest observed data, while the lower limit was considered as 15% lower than the lowest observed value. However, upper and lower limits for tomato samples were kept the same as of maximum and minimum observed values, respectively, due to marginal differences in the observed values. These values were embedded in the programme for appropriate functioning. Accordingly, the automatic sorting system was trained for sorting operation. After calibration, the system was tested for its speed/processing time and accuracy.

RESULTS AND DISCUSSION

The developed sensor-based automatic colour sorting system is shown in Fig. 6. The recorded values of colour frequency/colour channel value, namely R, G, and B for each colour sample (10 values per sample) used for calibration are reported in Table 4 for sample colour balls and Table 5 for tomato samples.

The R, G, and B colour frequency of no colour/blank under different lighting conditions were highest for dark room compared to lit room and daylight conditions. The ranges of each channel (R, G, B) were fed to the

Fig. 6: Sensor-based automatic colour sorting system

Table 4. Colour channel values of different colour ball samples used for training automatic sorting system via programming

Lighting condition	Colour channel	No colour/ Blank	Sensor response/Colour of sample					
			Red	Orange	Green	Yellow	Pink	Blue
Lit Room	R	1826 ± 10^{b1}	153 ± 2^{c1}	277 ± 3^{c1}	229 ± 9^{a1}	223 ± 3^{c1}	170 ± 5^{b1}	719 ± 36
		1829 ± 6^{b1}	153 ± 2^{c1}	286 ± 3^{c1}	239 ± 3^{a1}	222 ± 3^{c1}	169 ± 1^{b1}	763 ± 22
		1815 ± 12^{b1}	152 ± 1^{c1}	289 ± 5^{c1}	243 ± 8^{a1}	225 ± 4^{c1}	171 ± 6^{b1}	757 ± 30
		1825 ± 7^{b1}	153 ± 2^{c1}	288 ± 12^{c1}	243 ± 4^{a1}	225 ± 3^{c1}	171 ± 5^{b1}	765 ± 32
		1826 ± 12^{b1}	152 ± 1^{c1}	286 ± 12^{c1}	243 ± 4^{a1}	225 ± 6^{c1}	170 ± 4^{b1}	762 ± 35
		1823 ± 5^{b1}	154 ± 2^{c1}	289 ± 4^{c1}	240 ± 13^{a1}	219 ± 5^{c1}	172 ± 1^{b1}	743 ± 18
		1823 ± 12^{b1}	153 ± 1^{c1}	289 ± 5^{c1}	239 ± 4^{a1}	221 ± 4^{c1}	171 ± 3^{b1}	749 ± 25
		1822 ± 11^{b1}	152 ± 1^{c1}	292 ± 3^{c1}	242 ± 12^{a1}	220 ± 1^{c1}	167 ± 3^{b1}	752 ± 36
		1827 ± 10^{b1}	153 ± 2^{c1}	290 ± 9^{c1}	241 ± 8^{a1}	223 ± 4^{c1}	170 ± 3^{b1}	758 ± 30
		1818 ± 3^{b1}	155 ± 2^{c1}	290 ± 11^{c1}	240 ± 3^{a1}	225 ± 2^{c1}	173 ± 1^{b1}	746 ± 36
	G	1657 ± 9^{b2}	396 ± 3^{a2}	400 ± 19^{b2}	142 ± 12^{a2}	144 ± 3^{b2}	402 ± 5^{b2}	487 ± 9^{a2}
		1666 ± 10^{b2}	396 ± 3^{a2}	425 ± 13^{b2}	156 ± 11^{a2}	145 ± 1^{b2}	395 ± 6^{b2}	512 ± 9^{a2}
		1662 ± 8^{b2}	397 ± 1^{a2}	421 ± 19^{b2}	155 ± 5^{a2}	146 ± 1^{b2}	395 ± 3^{b2}	510 ± 2^{a2}
		1663 ± 5^{b2}	395 ± 2^{a2}	425 ± 13^{b2}	152 ± 12^{a2}	145 ± 3^{b2}	397 ± 6^{b2}	507 ± 13^{a2}
		1664 ± 6^{b2}	395 ± 1^{a2}	425 ± 14^{b2}	150 ± 9^{a2}	144 ± 2^{b2}	397 ± 7^{b2}	503 ± 3^{a2}
		1670 ± 12^{b2}	394 ± 2^{a2}	421 ± 15^{b2}	154 ± 5^{a2}	144 ± 2^{b2}	398 ± 5^{b2}	505 ± 3^{a2}
		1669 ± 9^{b2}	394 ± 3^{a2}	423 ± 18^{b2}	154 ± 8^{a2}	144 ± 2^{b2}	393 ± 6^{b2}	495 ± 9^{a2}
		1652 ± 13^{b2}	396 ± 1^{a2}	426 ± 17^{b2}	153 ± 8^{a2}	143 ± 3^{b2}	398 ± 7^{b2}	505 ± 12^{a2}
		1669 ± 6^{b2}	396 ± 1^{a2}	420 ± 15^{b2}	152 ± 11^{a2}	146 ± 2^{b2}	398 ± 2^{b2}	502 ± 5^{a2}
		1657 ± 11^{b2}	395 ± 3^{a2}	425 ± 14^{b2}	152 ± 5^{a2}	143 ± 3^{b2}	398 ± 3^{b2}	496 ± 11^{a2}
	B	1027 ± 5^{b3}	171 ± 1^{a3}	534 ± 18	216 ± 8^{a3}	213 ± 1^{b3}	169 ± 2^{c3}	197 ± 4^{b3}
		1029 ± 2^{b3}	171 ± 1^{a3}	562 ± 33	227 ± 12^{a3}	210 ± 8^{b3}	169 ± 2^{c3}	205 ± 7^{b3}
		1027 ± 10^{b3}	173 ± 2^{a3}	563 ± 10	228 ± 11^{a3}	217 ± 2^{b3}	170 ± 2^{c3}	205 ± 5^{b3}
		1030 ± 7^{b3}	173 ± 7^{a3}	569 ± 26	227 ± 8^{a3}	207 ± 7^{b3}	168 ± 3^{c3}	205 ± 4^{b3}
		1034 ± 2^{b3}	174 ± 3^{a3}	567 ± 30	227 ± 10^{a3}	213 ± 8^{b3}	170 ± 2^{c3}	201 ± 6^{b3}
		1027 ± 10^{b3}	168 ± 3^{a3}	567 ± 30	227 ± 8^{a3}	214 ± 8^{b3}	168 ± 3^{c3}	204 ± 6^{b3}
		1031 ± 11^{b3}	171 ± 2^{a3}	570 ± 29	227 ± 12^{a3}	211 ± 4^{b3}	168 ± 2^{c3}	202 ± 5^{b3}
		1034 ± 7^{b3}	171 ± 7^{a3}	562 ± 24	225 ± 12^{a3}	213 ± 6^{b3}	169 ± 3^{c3}	198 ± 4^{b3}
		1033 ± 11^{b3}	166 ± 4^{a3}	567 ± 15	227 ± 7^{a3}	214 ± 6^{b3}	170 ± 2^{c3}	204 ± 1^{b3}
		1023 ± 6^{b3}	166 ± 1^{a3}	554 ± 30	228 ± 11^{a3}	217 ± 5^{b3}	166 ± 2^{c3}	202 ± 3^{b3}
Dark	R	2166 ± 5^{c1}	141 ± 6^{b1}	240 ± 2^{a1}	557 ± 5^{b1}	230 ± 4^{b1}	132 ± 3^{a1}	766 ± 6
		2172 ± 7^{c1}	$149\pm7^{b1\,c1}$	240 ± 2^{a1}	558 ± 9^{b1}	243 ± 6^{b1}	142 ± 7^{a1}	784 ± 6
		2157 ± 17^{c1}	$149\pm5^{b1\,c1}$	240 ± 1^{a1}	554 ± 7^{b1}	247 ± 5^{b1}	139 ± 2^{a1}	783 ± 7
		2152 ± 12^{c1}	147 ± 3^{b1}	238 ± 2^{a1}	560 ± 9^{b1}	248 ± 3^{b1}	142 ± 2^{b1}	783 ± 11
		2151 ± 2^{c1}	150 ± 1^{b1}	241 ± 2^{a1}	561 ± 8^{b1}	249 ± 7^{b1}	142 ± 9^{a1}	779 ± 16
		2148 ± 12^{c1}	$151\pm1^{b1\,c1}$	239 ± 1^{a1}	561 ± 9^{b1}	248 ± 9^{b1}	140 ± 5^{a1}	783 ± 2
		2142 ± 9^{c1}	$146\pm3^{b1\,c1}$	241 ± 3^{a1}	555 ± 1^{b1}	247 ± 5^{b1}	140 ± 8^{a1}	778 ± 13
		2150 ± 19^{c1}	$149\pm2^{b1\,c1}$	239 ± 1^{a1}	554 ± 8^{b1}	244 ± 2^{b1}	142 ± 7^{a1}	778 ± 15
		2149 ± 4^{c1}	$149\pm3^{b1\,c1}$	239 ± 1^{a1}	557 ± 1^{b1}	248 ± 3^{b1}	141 ± 10^{a1}	784 ± 13
		2157 ± 4^{c1}	$149\pm1^{b1\,c1}$	241 ± 2^{a1}	545 ± 8^{b1}	248 ± 3^{b1}	141 ± 9^{a1}	785 ± 9
	G	1845 ± 3^{c2}	392 ± 2^{a2}	365 ± 3^{a2}	188 ± 2^{b2}	148 ± 1^{b2}	364 ± 10^{a2}	508 ± 4^{a2}
		1861 ± 16^{c2}	392 ± 1^{a2}	364 ± 2^{a2}	187 ± 3^{b2}	157 ± 4^{c2}	382 ± 4^{a2}	509 ± 2^{a2}
		1862 ± 13^{c2}	391 ± 2^{a2}	366 ± 3^{a2}	189 ± 4^{b2}	155 ± 3^{c2}	381 ± 3^{a2}	505 ± 7^{a2}
		1854 ± 3^{c2}	388 ± 4^{a2}	365 ± 1^{a2}	189 ± 1^{b2}	155 ± 2^{c2}	382 ± 9^{a2}	507 ± 5^{a2}
		1853 ± 10^{c2}	392 ± 2^{a2}	365 ± 1^{a2}	189 ± 5^{b2}	156 ± 3^{c2}	380 ± 4^{a2}	514 ± 3^{a2}
		1856 ± 6^{c2}	388 ± 2^{a2}	366 ± 2^{a2}	192 ± 4^{b2}	158 ± 5^{c2}	381 ± 5^{a2}	513 ± 4^{a2}
		1848 ± 7^{c2}	389 ± 1^{a2}	365 ± 3^{a2}	187 ± 2^{b2}	161 ± 9^{c2}	381 ± 5^{a2}	507 ± 2^{a2}
		1844 ± 15^{c2}	390 ± 1^{a2}	366 ± 2^{a2}	187 ± 1^{b2}	160 ± 2^{c2}	384 ± 4^{a2}	511 ± 8^{a2}
		1857 ± 6^{c2}	389 ± 1^{a2}	363 ± 1^{a2}	188 ± 4^{b2}	161 ± 2^{c2}	382 ± 3^{a2}	512 ± 5^{a2}
		1859 ± 13^{c2}	391 ± 3^{a2}	366 ± 1^{a2}	185 ± 2^{b2}	153 ± 3^{c2}	384 ± 8^{a2}	513 ± 7^{a2}
	B	1112 ± 6^{c3}	282 ± 4^{b3}	477 ± 3^{a3}	234 ± 3^{a3}	220 ± 7^{c3}	151 ± 7^{b3}	187 ± 7^{a3}
		1114 ± 8^{c3}	279 ± 6^{b3}	478 ± 2^{a3}	233 ± 6^{a3}	229 ± 10^{c3}	155 ± 9^{b3}	187 ± 2^{a3}
		1119 ± 4^{c3}	275 ± 2^{b3}	470 ± 6^{a3}	233 ± 2^{a3}	230 ± 10^{c3}	157 ± 4^{b3}	183 ± 6^{a3}
		1116 ± 3^{c3}	280 ± 4^{b3}	470 ± 5^{a3}	234 ± 3^{a3}	232 ± 4^{c3}	157 ± 2^{b3}	181 ± 4^{a3}
		1116 ± 4^{c3}	280 ± 4^{b3}	472 ± 3^{a3}	235 ± 2^{a3}	230 ± 7^{c3}	159 ± 3^{b3}	184 ± 2^{a3}
		1119 ± 3^{c3}	282 ± 3^{b3}	471 ± 6^{a3}	232 ± 3^{a3}	232 ± 5^{c3}	161 ± 2^{b3}	184 ± 3^{a3}
		1117 ± 3^{c3}	280 ± 4^{b3}	472 ± 7^{a3}	236 ± 2^{a3}	231 ± 6^{c3}	159 ± 4^{b3}	183 ± 4^{a3}
		1108 ± 7^{c3}	281 ± 4^{b3}	473 ± 6^{a3}	234 ± 3^{a3}	229 ± 5^{c3}	159 ± 7^{b3}	186 ± 7^{a3}
		1114 ± 3^{c3}	282 ± 2^{b3}	472 ± 6^{a3}	230 ± 5^{a3}	231 ± 5^{c3}	161 ± 6^{b3}	189 ± 4^{a3}
		1118 ± 3^{c3}	281 ± 3^{b3}	472 ± 6^{a3}	233 ± 4^{a3}	231 ± 2^{c3}	159 ± 5^{b3}	186 ± 6^{a3}

Lighting	Channel							
	R	1577±52 a1	107±4 a1	279±7 b1	533±6 d1	182±3 a1	143±30 a1	753±16
		1567±43 a1	112±5 a1	303±2 b1	554±2 b1 c1	187±4 a1	178±2 c1	762±21
		1528±41 a1	111±3 a1	303±2 b1	567±2 c1	188±4 a1	182±8 c1	768±18
		1533±48 a1	113±6 a1	303±8 b1	566±3 c1	185±4 a1	180±2 c1	780±12
		1549±54 a1	111±5 a1	300±4 b1	567±6 c1	186±4 a1	180±5 c1	773±21
		1546±37 a1	113±5 a1	302±9 b1	566±5 c1	192±7 a1	182±7 c1	780±25
		1507±55 a1	112±6 a1	304±2 b1	570±6 c1	189±5 a1	179±6 c1	781±13
		1519±38 a1	112±4 a1	301±2 b1	562±3 c1	190±8 a1	179±6 c1	778±19
		1550±50 a1	112±4 a1	302±3 b1	565±2 c1	190±2 a1	179±2 c1	779±21
		1531±53 a1	112±4 a1	302±7 b1	565±3 c1	190±5 a1	181±4 c1	782±12
Daylight	G	1477±31 a2	386±5 a2	407±10 b2	183±13 b2	124±3 a2	373±26 a2	524±3 b2
		1467±41 a2	404±6 b2	417±14 b2	197±7 c2	120±1 a2	430±10 c2	525±8 b2
		1453±44 a2	405±7 b2	426±7 b2	197±3 c2	123±4 a2	436±14 c2	534±7 b2
		1441±39 a2	403±2 b2	424±4 b2	199±7 c2	124±3 a2	430±9 c2	534±8 b2
		1452±40 a2	405±5 b2	422±6 b2	196±3 c2	122±1 a2	429±11 c2	532±8 b2
		1458±23 a2	405±4 b2	427±10 b2	198±7 c2	121±4 a2	434±16 c2	533±4 b2
		1428±25 a2	405±5 b2	423±12 b2	198±2 c2	123±2 a2	439±14 c2	532±12 b2
		1449±22 a2	404±4 b2	424±7 b2	198±9 c2	124±3 a2	434±8 c2	537±8 b2
		1456±21 a2	403±3 b2	417±4 b2	197±6 c2	124±2 a2	436±21 c2	539±6 b2
		1449±27 a2	405±2 b2	424±11 b2	195±2 c2	123±3 a2	437±17 c2	536±2 b2
	B	927±12 a3	282±9 b3	508±24 b3	220±6 a3	194±5 a3	159±13 b3	215±5 c3
		920±17 a3	295±16 b3	545±29 b3	243±8 a3	196±3 a3	189±22 c3	218±8 c3
		923±10 a3	297±15 b3	541±33 b3	239±16 a3	197±5 a3	191±14 c3	225±8 c3
		910±14 a3	298±15 b3	544±35 b3	242±19 a3	196±5 a3	186±15 c3	224±9 c3
		915±9 a3	298±19 b3	541±35 b3	239±16 a3	196±3 a3	190±15 c3	222±5 c3
		925±15 a3	299±19 b3	537±19 b3	237±10 a3	196±6 a3	189±17 c3	226±4 c3
		903±10 a3	299±8 b3	535±31 b3	241±20 a3	194±2 a3	189±13 c3	223±8 c3
		919±11 a3	300±9 b3	539±15 b3	243±10 a3	189±5 a3	187±21 c3	222±3 c3
		919±18 a3	298±19 b3	537±33 b3	240±19 a3	193±6 a3	189±22 c3	221±5 c3
		915±16 a3	299±11 b3	539±29 b3	240±10 a3	197±6 a3	190±22 c3	223±5 c3

Note: (1) Each numerical data is the average of five values± SD and; (2) The colour channel values R represents red, G represents green, and B represents blue.

[a1, b1, c1] : values of sensor response are significantly different ($p \leq 0.05$) between R, G, B channels for different lighting condition.

Table 5. Colour channel values of tomato samples used for training automatic sorting system via programming

Lighting condition	Colour channel	No colour/ Blank	Sensor response/Colour of sample								
			Red			Pink			Green		
			Small	Medium	Large	Small	Medium	Large	Small	Medium	Large
Lit Room	R	2464±315 a1	1333±17 a1	888±18 b1	786±14 b1	1014±12 a1	711±44 a1	575±21 a1	1461±49 a1	851±20 a1	686±10 a1
		2784±310 a1	1345±15 a1	872±21 b1	797±23 b1	1077±18 a1	750±52 a1	570±20 a1	1495±42 a1	856±19 a1	684±18 a1
		2794±291 a1	1363±18 a1	898±26 b1	790±13 b1	1076±21 a1	754±42 a1	569±14 a1	1465±45 a1	852±16 a1	668±22 a1
		2816±329 a1	1325±12 a1	886±18 b1	787±18 b1	1076±22 a1	761±50 a1	584±19 a1	1466±51 a1	859±23 a1	667±15 a1
		2828±296 a1	1315±10 a1	875±24 b1	790±19 b1	1079±12 a1	742±49 a1	576±17 a1	1462±44 a1	854±18 a1	676±13 a1
		2809±348 a1	1317±18 a1	877±27 b1	773±15 b1	1073±11 a1	750±53 a1	594±21 a1	1451±54 a1	846±21 a1	678±18 a1
		2792±321 a1	1322±17 a1	874±22 b1	794±17 b1	1092±20 a1	748±41 a1	589±15 a1	1455±49 a1	835±18 a1	677±20 a1
		2816±297 a1	1360±18 a1	877±21 b1	781±13 b1	1072±23 a1	743±50 a1	592±12 a1	1455±53 a1	846±13 a1	653±19 a1
		2828±322 a1	1359±14 a1	868±21 b1	795±17 b1	1077±14 a1	769±51 a1	581±21 a1	1454±56 a1	844±13 a1	661±19 a1
		2809±307 a1	1334±13 a1	873±22 b1	792±12 b1	1089±12 a1	764±50 a1	594±22 a1	1433±43 a1	858±16 a1	645±18 a1
	G	2275±161 a2	2082±55 a2	1774±18 c2	1706±17 c2	1501±79 a2	1310±72 a2	1118±17 a2	1440±46 a2	995±15 a2	700±12 a2
		2430±160 a2	2113±43 a2	1773±15 c2	1733±17 c2	1554±66 a2	1355±71 a2	1109±17 a2	1461±56 a2	988±16 a2	706±17 a2
		2440±163 a2	2114±62 a2	1790±18 c2	1729±18 c2	1594±69 a2	1351±58 a2	1116±15 a2	1430±53 a2	995±16 a2	690±9 a2
		2459±163 a2	2099±47 a2	1785±1 c2	1725±24 c2	1568±81 a2	1363±66 a2	1115±12 a2	1434±45 a2	993±18 a2	701±11 a2
		2474±155 a2	2044±36 a2	1766±11 c2	1732±25 c2	1568±92 a2	1331±67 a2	1109±19 a2	1425±44 a2	992±14 a2	688±8 a2
		2459±154 a2	2055±54 a2	1763±13 c2	1709±25 c2	1567±93 a2	1346±55 a2	1131±20 a2	1413±54 a2	990±13 a2	694±18 a2
		2439±164 a2	2060±51 a2	1755±20 c2	1729±21 c2	1575±59 a2	1330±74 a2	1128±16 a2	1421±59 a2	973±12 a2	702±22 a2
		2459±161 a2	2104±57 a2	1757±18 c2	1732±15 c2	1575±66 a2	1337±73 a2	1128±16 a2	1421±48 a2	978±20 a2	684±22 a2
		2474±191 a2	2100±53 a2	1764±12 c2	1715±22 c2	1561±60 a2	1386±52 a2	1106±17 a2	1423±60 a2	988±14 a2	683±21 a2
		2459±174 a2	2073±36 a2	1768±5 c2	1732±15 c2	1584±58	1366±41 a2	1123±22 a2	1396±49 a2	995±12 a2	698±14 a2
	B	1402±76 a3	1359±45 a3	1173±26 c3	1154±20 b3	1131±27 a3	1080±45 a3	839±15 a3	1214±39 a3	1046±15 a3	605±18 a3
		1459±67 a3	1388±50 a3	1174±21 c3	1164±19 b3	1145±26 a3	1109±42 a3	836±18 a3	1216±30 a3	1042±15 a3	604±11 a3
		1466±61 a3	1384±43 a3	1192±20 c3	1148±15 b3	1172±28 a3	1110±46 a3	832±16 a3	1192±36 a3	1043±10 a3	585±12 a3
		1486±69 a3	1361±47 a3	1178±34 c3	1168±14 b3	1155±40 a3	1118±51 a3	834±24 a3	1205±29 a3	1046±9 a3	600±21 a3
		1486±79 a3	1337±43 a3	1171±29 c3	1156±20 b3	1150±30 a3	1094±49 a3	841±28 a3	1191±35 a3	1042±8 a3	586±16 a3
		1470±82 a3	1339±36 a3	1172±22 c3	1158±14 b3	1158±20 a3	1102±47 a3	854±28 a3	1183±35 a3	1042±8 a3	584±19 a3
		1461±52 a3	1339±38 a3	1161±23 c3	1159±20 b3	1166±32 a3	1088±51 a3	852±27 a3	1182±34 a3	1027±12 a3	599±20 a3
		1464±65 a3	1369±36 a3	1157±24 c3	1161±21 b3	1151±23 a3	1095±42 a3	852±13 a3	1193±35 a3	1031±14 a3	586±22 a3
		1458±79 a3	1355±32 a3	1172±32 c3	1145±20 b3	1145±31 a3	1133±46 a3	825±16 a3	1192±37 a3	1046±18 a3	582±14 a3
		1456±63 a3	1348±41 a3	1158±22 c3	1169±21 b3	1169±35 a3	1123±50 a3	850±25 a3	1175±31 a3	1043±12	582±13 a3

Lighting	Channel										
Dark	R	3802±124 [c1]	1423±14 [c1]	864±20 [b1]	726±19 [a1]	1105±14 [b1]	827±12 [b1]	648±13 [b1]	1445±15 [a1]	896±27 [b1]	782±55 [c1]
		3839±123 [c1]	1412±26 [c1]	882±19 [b1]	720±14 [a1]	1103±13 [b1]	822±15 [b1]	645±16 [b1]	1447±19 [a1]	882±19 [b1]	731±60 [b1]
		3912±126 [c1]	1405±18 [c1]	861±11 [b1]	720±11 [a1]	1090±17 [b1]	823±12 [b1]	648±13 [b1]	1447±18 [a1]	886±27 [b1]	797±54 [c1]
		3834±124 [c1]	1443±30 [c1]	885±15 [b1]	738±18 [a1]	1111±10 [b1]	825±11 [b1]	649±16 [b1]	1442±17 [a1]	875±30 [b1]	799±46 [c1]
		3788±128 [c1]	1438±39 [c1]	873±22 [b1]	713±12 [a1]	1108±19 [b1]	821±12 [b1]	640±16 [b1]	1441±19 [a1]	877±27 [b1]	785±46 [c1]
		3937±143 [c1]	1446±37 [c1]	884±17 [b1]	723±20 [a1]	1104±11 [b1]	822±13 [b1]	643±17 [b1]	1436±20 [a1]	898±26 [b1]	794±59 [c1]
		3834±135 [c1]	1440±16 [c1]	876±19 [b1]	722±20 [a1]	1117±10 [b1]	824±15 [b1]	639±16 [b1]	1425±16 [a1]	862±26 [b1]	804±57 [c1]
		3788±124 [c1]	1445±38 [c1]	878±19 [b1]	710±18 [a1]	1111±14 [b1]	821±14 [b1]	641±12 [b1]	1447±14 [a1]	887±29 [b1]	794±69 [c1]
		3937±127 [c1]	1434±36 [c1]	887±18 [b1]	711±14 [a1]	1127±14 [b1]	821±15 [b1]	628±16 [b1]	1441±12 [a1]	878±30 [b1]	772±53 [c1]
		3898±123 [c1]	1437±40 [c1]	868±19 [b1]	714±11 [a1]	1134±11 [b1]	821±11 [b1]	634±14 [b1]	1439±17 [a1]	892±30 [b1]	764±62 [c1]
	G	3586±130 [c2]	2251±29 [c2]	1741±16 [b2]	1487±14 [a2]	1696±38 [b2]	1436±4 [b2]	1272±14 [b2]	1413±16 [b2]	1063±29 [b2]	777±56 [b2]
		3588±125 [c2]	2245±36 [c2]	1745±18 [b2]	1502±20 [a2]	1690±32 [b2]	1428±2 [b2]	1267±19 [b2]	1412±11 [b2]	1050±30 [b2]	753±67 [b2]
		3614±145 [c2]	2242±28 [c2]	1710±21 [b2]	1492±13 [a2]	1676±33 [b2]	1441±3 [b2]	1263±17 [b2]	1401±15 [b2]	1042±32 [b2]	824±63 [b2]
		3719±143 [c2]	2297±27 [c2]	1746±23 [b2]	1527±20 [a2]	1705±36 [b2]	1431±4 [b2]	1260±17 [b2]	1409±20 [b2]	1035±29 [b2]	826±55 [b2]
		3693±120 [c2]	2293±36 [c2]	1742±15 [b2]	1494±13 [a2]	1710±40 [b2]	1419±3 [b2]	1260±19 [b2]	1406±13 [b2]	1038±24 [b2]	796±64 [b2]
		3623±133 [c2]	2310±29 [c2]	1738±14 [b2]	1496±12 [a2]	1697±31 [b2]	1438±3 [b2]	1265±11 [b2]	1411±14 [b2]	1061±30 [b2]	816±63 [b2]
		3588±128 [c2]	2297±36 [c2]	1743±15 [b2]	1491±17 [a2]	1712±34 [b2]	1435±1 [b2]	1252±14 [b2]	1402±11 [b2]	1030±33 [b2]	844±70 [b2]
		3644±124 [c2]	2295±32 [c2]	1746±16 [b2]	1473±14 [a2]	1708±34 [b2]	1427±2 [b2]	1253±12 [b2]	1400±14 [b2]	1049±31 [b2]	815±61 [b2]
		3759±138 [c2]	2292±28 [c2]	1761±13 [b2]	1483±22 [a2]	1734±39 [b2]	1432±5 [b2]	1260±14 [b2]	1405±20 [b2]	1040±29 [b2]	790±70 [b2]
		3739±121 [c2]	2284±38 [c2]	1756±18 [b2]	1472±25 [a2]	1729±34 [b2]	1435±4 [b2]	1257±11 [b2]	1401±14 [b2]	1055±27 [b2]	787±70 [b2]
	B	2231±198 [c3]	1474±34 [c3]	1149±11 [b3]	1060±41 [a3]	1294±31 [b3]	1168±10 [a3]	939±9 [b3]	1183±8 [a3]	1146±37 [b3]	699±40 [c3]
		2233±185 [c3]	1475±28 [c3]	1140±13 [b3]	1069±29 [a3]	1281±49 [b3]	1148±14 [a3]	937±20 [b3]	1181±7 [a3]	1135±23 [b3]	664±61 [b3]
		2238±176 [c3]	1479±27 [c3]	1144±17 [b3]	1060±37 [a3]	1269±29 [b3]	1177±14 [a3]	932±18 [b3]	1174±7 [a3]	1133±39 [b3]	727±69 [c3]
		2314±194 [c3]	1509±30 [c3]	1138±21 [b3]	1088±20 [a3]	1287±50 [b3]	1161±25 [a3]	938±17 [b3]	1170±8 [a3]	1122±38 [b3]	735±65 [c3]
		2308±208 [c3]	1510±29 [c3]	1151±16 [b3]	1050±22 [a3]	1294±48 [b3]	1159±11 [a3]	938±14 [b3]	1178±9 [a3]	1134±21 [b3]	713±38 [c3]
		2100±169 [c3]	1516±31 [c3]	1145±17 [b3]	1067±24 [a3]	1297±20 [b3]	1170±10 [a3]	938±8 [b3]	1177±8 [a3]	1145±23 [b3]	726±58 [c3]
		2253±166 [c3]	1513±35 [c3]	1152±15 [b3]	1054±22 [a3]	1299±42 [b3]	1167±2 [a3]	927±18 [b3]	1171±9 [a3]	1100±40 [b3]	718±40 [c3]
		2238±190 [c3]	1508±38 [c3]	1148±17 [b3]	1043±41 [a3]	1313±41 [b3]	1171±5 [a3]	926±14 [b3]	1173±10 [a3]	1130±35 [b3]	722±58 [c3]
		2334±207 [c3]	1501±26 [c3]	1155±17 [b3]	1043±27 [a3]	1323±32 [b3]	1167±14 [a3]	919±7 [b3]	1174±4 [a3]	1123±28 [b3]	693±53 [c3]
		2318±201 [c3]	1506±34 [c3]	1161±12 [b3]	1044±17 [a3]	1320±47 [b3]	1168±23 [a3]	930±13 [b3]	1171±10 [a3]	1135±23 [b3]	704±46 [c3]
Daylight	R	3151±67 [b1]	1382±21 [b1]	779±6 [b1]	713±14 [b1]	1179±22 [c1]	819±27 [b1]	654±15 [b1]	1550±54 [b1]	893±15 [b1]	701±20 [b1]
		3104±57 [b1]	1395±16 [b1]	786±5 [a1]	797±17 [b1]	1175±14 [c1]	820±12 [b1]	662±19 [b1]	1594±48 [b1]	906±10 [b1]	729±19 [b1]
		3102±64 [b1]	1388±21 [b1]	778±10 [a1]	800±14 [b1]	1164±20 [c1]	807±14 [b1]	653±11 [b1]	1579±55 [b1]	893±6 [b1]	726±25 [b1]
		3087±65 [b1]	1390±25 [b1]	785±5 [a1]	752±10 [b1]	1165±16 [c1]	814±26 [b1]	641±26 [b1]	1538±60 [b1]	885±9 [b1]	729±19 [b1]
		3074±81 [b1]	1386±18 [b1]	777±9 [a1]	757±12 [b1]	1153±21 [c1]	811±29 [b1]	651±24 [b1]	1532±64 [b1]	897±10 [b1]	732±27 [b1]
		3055±72 [b1]	1385±15 [b1]	787±3 [a1]	775±10 [b1]	1159±20 [c1]	786±25 [a1]	659±26 [b1]	1520±59 [b1]	905±15 [b1]	728±16 [b1]
		3122±88 [b1]	1390±20 [b1]	784±9 [a1]	783±18 [b1]	1161±20 [c1]	794±19 [b1]	676±12 [b1]	1533±63 [b1]	900±15 [b1]	719±22 [b1]
		3097±84 [b1]	1372±15 [b1]	782±8 [a1]	787±15 [b1]	1164±21 [c1]	820±15 [b1]	661±17 [b1]	1539±46 [b1]	904±12 [b1]	729±17 [b1]
		3054±71 [b1]	1371±16 [b1]	778±7 [a1]	839±17 [b1]	1161±11 [c1]	794±19 [b1]	666±25 [b1]	1525±55 [b1]	895±15 [b1]	729±18 [b1]
		3115±76 [b1]	1365±15 [b1]	785±5 [a1]	798±12 [b1]	1161±12 [c1]	796±11 [b1]	665±15 [b1]	1535±49 [b1]	887±9 [b1]	718±23 [b1]
	G	2857±58 [b2]	2146±18 [b2]	1610±26 [a2]	1503±21 [b2]	1729±13 [b2]	1453±30 [b2]	1327±21 [c2]	1533±44 [c2]	1014±16 [c2]	735±16 [b2]
		2849±67 [b2]	2164±18 [b2]	1600±21 [a2]	1649±20 [b2]	1718±20 [b2]	1457±40 [b2]	1332±25 [c2]	1556±52 [c2]	1021±5 [c2]	767±26 [b2]
		2830±55 [b2]	2163±18 [b2]	1592±21 [a2]	1652±22 [b2]	1702±20 [b2]	1446±11 [b2]	1310±34 [c2]	1558±53 [c2]	1014±6 [c2]	759±20 [b2]
		2826±74 [b2]	2165±22 [b2]	1597±20 [a2]	1574±27 [b2]	1703±13 [b2]	1451±23 [b2]	1311±34 [c2]	1516±52 [c2]	1007±11 [b2]	760±20 [b2]
		2819±72 [b2]	2169±17 [b2]	1596±21 [a2]	1579±29 [b2]	1709±14 [b2]	1443±24 [b2]	1311±22 [c2]	1497±62 [c2]	1016±20 [b2]	765±29 [b2]
		2808±58 [b2]	2162±25 [b2]	1605±21 [a2]	1567±33 [b2]	1706±22 [b2]	1404±17 [b2]	1332±35 [c2]	1495±51 [c2]	1025±7 [c2]	758±24 [b2]
		2887±71 [b2]	2159±24 [b2]	1610±16 [a2]	1624±23 [b2]	1703±14 [b2]	1410±37 [b2]	1360±30 [c2]	1501±58 [c2]	1017±11 [c2]	768±30 [b2]
		2869±60 [b2]	2148±17 [b2]	1597±28 [a2]	1650±20 [b2]	1701±20 [b2]	1456±21 [b2]	1345±31 [c2]	1489±49 [c2]	1011±19 [c2]	767±25 [b2]
		2838±55 [b2]	2143±16 [b2]	1576±23 [a2]	1736±17 [b2]	1711±15 [b2]	1405±30 [b2]	1332±16 [c2]	1511±44 [c2]	1002±16 [c2]	762±21 [b2]
		2849±53 [b2]	2147±17 [b2]	1597±30 [a2]	1647±45 [b2]	1702±11 [b2]	1412±13 [b2]	1338±13 [c2]	1496±52 [c2]	1008±6 [c2]	759±27 [b2]
	B	1762±36 [b3]	1407±15 [b3]	1045±15 [a3]	1084±11 [a3]	1277±12 [b3]	1185±24 [a3]	1028±19 [c3]	1293±33 [b3]	1039±6 [a3]	636±13 [b3]
		1743±44 [b3]	1415±18 [b3]	1035±11 [a3]	1158±16 [b3]	1272±10 [b3]	1183±30 [a3]	1033±16 [c3]	1324±46 [b3]	1049±18 [a3]	653±9 [b3]
		1714±38 [b3]	1415±16 [b3]	1047±14 [a3]	1154±77 [b3]	1264±12 [b3]	1171±21 [a3]	1014±19 [c3]	1297±28 [b3]	1039±14 [a3]	651±6 [b3]
		1736±35 [b3]	1421±15 [b3]	1043±17 [a3]	1109±89 [b3]	1270±15 [b3]	1179±24 [a3]	1009±39 [c3]	1268±56 [b3]	1027±10 [a3]	659±14 [b3]
		1724±41 [b3]	1424±15 [b3]	1045±17 [a3]	1104±85 [b3]	1272±11 [b3]	1171±43 [a3]	1017±13 [c3]	1262±35 [b3]	1039±10 [a3]	659±11 [b3]
		1720±35 [b3]	1416±20 [b3]	1046±20 [a3]	1101±90 [b3]	1272±12 [b3]	1138±42 [a3]	1057±23 [c3]	1265±47 [b3]	1049±19 [a3]	649±7 [b3]
		1764±41 [b3]	1419±24 [b3]	1048±14 [a3]	1141±77 [b3]	1261±6 [b3]	1143±37 [a3]	1043±32 [c3]	1270±44 [b3]	1045±18 [a3]	658±20 [b3]
		1736±40 [b3]	1415±23 [b3]	1039±20 [a3]	1169±75 [b3]	1274±13 [b3]	1185±15 [a3]	1031±39 [c3]	1271±31 [b3]	1042±20 [a3]	659±14 [b3]
		1754±34 [b3]	1406±22 [b3]	1027±14 [a3]	1229±107 [c3]	1267±12 [b3]	1141±32 [a3]	1044±27 [c3]	1279±31 [b3]	1033±9 [a3]	658±18 [b3]
		1740±44 [b3]	1398±24 [b3]	1043±18 [a3]	1163±101 [b3]	1273±9 [b3]	1127±20 [a3]	1034±28 [c3]	1275±32 [b3]	1040±9 [a3]	657±19 [b3]

Note: (1) Each numerical data is the average of five values; (2) The colour channel values R represents red, G represents green, and B represents blue.
[a1, b1, c1] : *values of sensor response are significantly different (p ≤ 0.05) between R, G, B channels for different lighting condition.*

programme for colour sorting. The maximum and minimum colour values for each colour are presented in Table 6 for colour balls and Table 7 for tomato samples. The values for specific sensor response were non-significantly different ($p \leq 0.05$) under each lightening condition and colour channels. However, a significantly difference ($p \leq 0.05$) is noted among R, G, B channels and lighting condition (Table 4-5). As per the programme, the microcontroller sent signals to the bottom servo motor for sorting the samples (via mobile chute) and LCD for display of colour and channel values.

In general, the coloured ball samples were sorted at a different rotation angle of the bottom servo motor, for example, 30° for red, 60° for orange, 90° for green, 120° for yellow, 150° for pink, and 180° for blue. The selected angle/range was programmed equally for sorting of six different colour ball samples in collection pans. However, tomatoes were sorted in the ranges of 0-60° for red samples, 61-120° for pink samples, and 121-180° for green samples due to the availability of

tomatoes in three colours (equal angle). In each class/range, an increment of 20° was provided such that large, medium, and small samples (as presented in Table 1) get separated into different collection bins based on their colour values.

The values of R, G, and B colour frequency of colour ball samples sorted in different pans as per their characteristics colour of red, orange, green, yellow, pink, and blue are shown in Fig. 7. Furthermore, the observed values of colour frequency for 60 samples (10 balls in each pan) were well within the range of programmed values (Table 4). It is interesting to note that in the case of primary colour samples as the red sample, the frequency of R was lowest compared to G and B frequency readings (Fig. 7a). Similar results were noted for green (Fig. 7c) and blue samples (Fig. 7f). In the cases of secondary colour samples, such as orange sample colour frequency of B> G >R (Fig. 7b), while for yellow sample, the trend is R> B >G with closer values of R and B (Fig. 7d). For pink colour samples, the frequency of G is higher than B and R,

Table 6. Ranges of calibrated values of different colour ball samples

Colour	Colour channel value					
	R		G		B	
	Min	Max	Min	Max	Min	Max
Red	75	202	270	527	116	390
Orange	166	396	254	556	329	741
Green	160	741	99	259	151	316
Yellow	127	324	84	210	132	302
Pink	92	237	254	571	105	249
Blue	503	1020	340	701	128	294

Note:
(1) The terms Min and Max indicate minimum and maximum, respectively.
(2) The colour channel values R represents red, G represents green, and B represents blue.

Table 7. Ranges of calibrated values of tomato samples

Colour channel value	Lower and upper limit	Sensor response/Colour of tomato sample								
		Red			Pink			Green		
		Small	Medium	Large	Small	Medium	Large	Small	Medium	Large
R	Min	1315	777	710	1014	711	569	1425	835	645
	Max	1446	898	839	1179	827	676	1594	906	804
G	Min	2044	1576	1472	1501	1310	1106	1396	973	683
	Max	2310	1790	1736	1734	1457	1360	1558	1063	844
B	Min	1337	1027	1043	1131	1080	825	1170	1027	582
	Max	1516	1192	1229	1323	1185	1057	1324	1146	735

Note:
(1) The terms Min and Max indicate minimum and maximum, respectively.
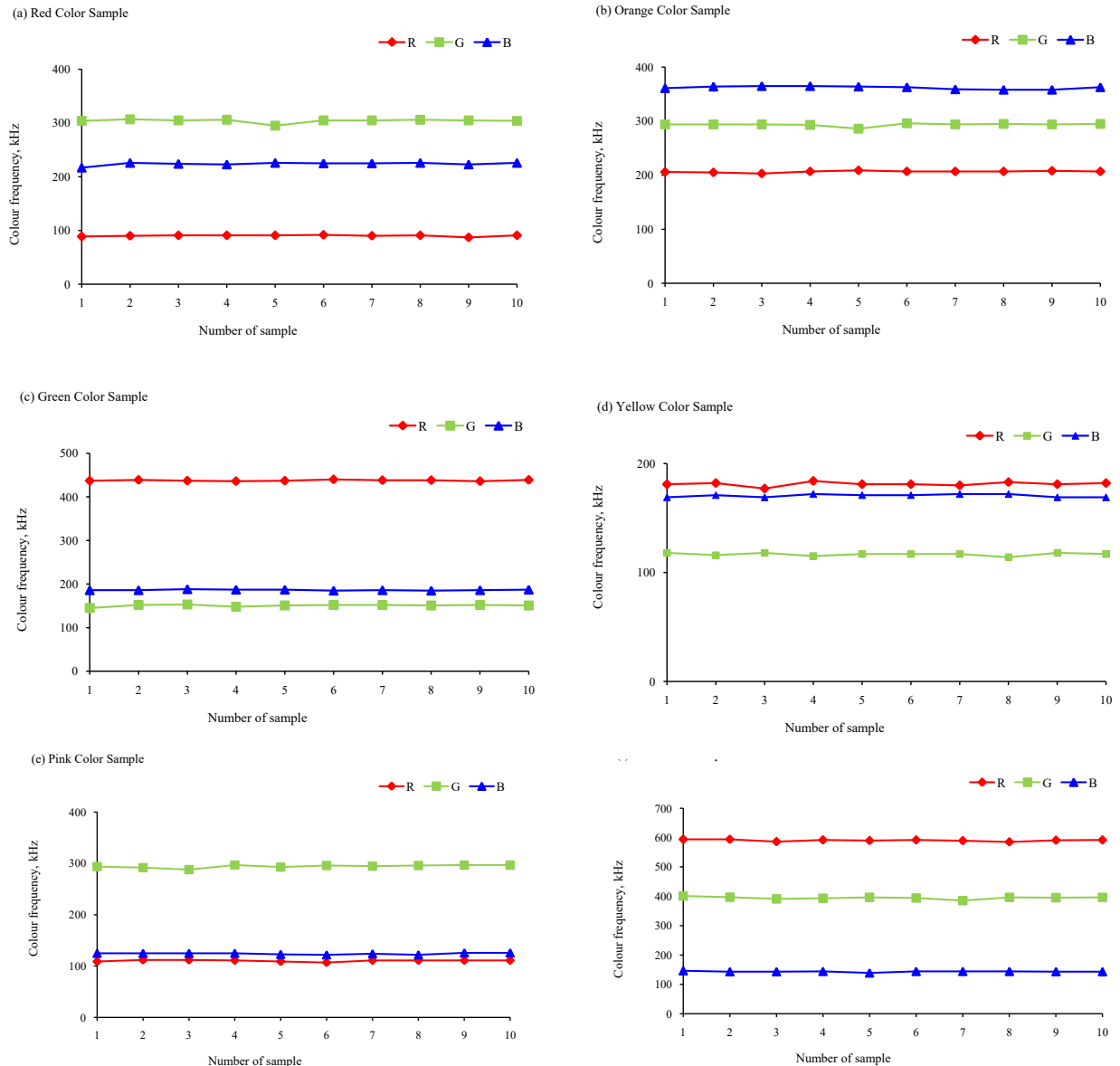*(2) The colour channel values R represents red, G represents green, and B represents blue.*

Fig. 7: Graphical representation of observed colour values of corresponding colour: (a) red, (b) orange, (c) green, (d) yellow, (e) pink, and (f) blue of sorted ball samples

but non-remarkable differences existed among B and R (Fig. 7e).

Similarly, the developed system automatically separated red, pink, and green tomatoes based on their colour channel values. Moreover, the system was capable of sorting each colour into three sub-classes of large, medium, and small, as per their colour channel values (Table 7). The physical properties such as length, width, thickness, geometric mean diameter, and sphericity of sorted samples under each sub-class were in line with the values reported in Table 1. The

developed system had 1,800 sample.h^{-1} processing speed (or speed of sorting) with an accuracy of nearly 95 per cent. However, the system developed using machine vision or computer vision techniques have been reported to have 84-87.5% accuracy in detecting effects and colour sorting of tomatoes (Rokunuzzaman and Jayasuriya, 2013). Thus, the developed automated colour sorting system proved to be accurate, and precise in sorting the uniformly coloured spherical object. In the future, the mapping feature of programming might be used to represent the values of colour frequency in 0-255 colour values. In addition, colour values of

tomatoes might be used to develop a model for maturity investigation. The reports on the prediction of maturity of mango (Jha *et al*., 2007) and apple quality (Jha *et al.*, 2010) using colour values can be considered as reference. Codes might be developed as a function of shape, size, texture, defects, maturity, and colour of the samples, which would aid in increasing versatility of the automatic sorter for separation of food and non-food products.

CONCLUSIONS

Microcontroller, colour sensor array, servo motors coupled with mechanical components were utilised for the development of a sensor-based automatic colour sorting system. The programming of the process algorithm was done using Arduino IDE software. The machine was calibrated for red, pink, and green tomato samples along with 70 mm sample balls of six different colours. Calibration was done under lit room, dark room, and daylight. Appropriate calibration of the automated colour sorting system resulted in obtaining a processing speed of 1,800 sample.h^{-1} with an accuracy of nearly 95 per cent. The values for specific sensor response were non-significantly different (p ≤ 0.05) under each lightening condition and colour channels. However, a significantly difference was noted among R, G, B channels and lighting condition. Based on the colour values, the system sorted tomatoes in red, pink, and green collection bins with each colour having three sub-classes of large, medium, and small. Versatility of the developed unit may be increased for sorting various food and non-food components by incorporating necessary changes in codes and components.

ACKNOWLEDGEMENT

REFERENCES

Ghodki B M; Goswami T K. 2016. Effect of moisture on physical and mechanical properties of cassia. Cogent Food Agric., 2, 1192975. https://doi.org/10.1080/23311932.2016.1192975

Ghodki B M; Tangirala A D S; Goswami T K. 2016. Moisture dependent thermal properties of cassia. Cogent Food Agric., 2, 1227110. https://doi.org/10.1080/23311932.2016.1227110

Inamdar A A; Suresh D S. 2014. Application of color sorter in wheat milling. Int. Food Res. J., 21, 2083–2089.

Jha S N; Chopra S; Kingsly A R P. 2007. Modeling of color values for nondestructive evaluation of maturity of mango. J. Food Eng., 78 (1), 22-26. https://doi.org/10.1016/j.jfoodeng.2005.08.048

Jha S N; Rai R D; Gunasekaran S. 2010. Visual spectroscopy and colour modelling for nondestructive quality evaluation of apple. J. Agric. Eng., 47 (2), 9-13.

Moreda G P; Ortiz-Cañavate J; García-Ramos F J; Ruiz-Altisent M. 2009. Non-destructive technologies for fruit and vegetable size determination - A review. J. Food Eng., 92, 119-136. https://doi.org/10.1016/j.jfoodeng.2008.11.004

Pereira V; Fernandes V A; Sequeira J. 2014. Low cost object sorting robotic arm using Raspberry Pi. In: Proc. IEEE Global Humanitarian Technology Conference - South Asia Satellite (GHTC-SAS). IEEE, Trivandrum, 1-6. https://doi.org/10.1109/GHTC-SAS.2014.6967550

Rokunuzzaman M; Jayasuriya H P. 2013. Defects and calyx detection using rule-based and neural network approaches for sorting of tomatoes. Agric. Eng. Int. CIGR J., 15, 173-180.

Shen L J; Hassan I. 2015. Design and development of color sorting robot. J. Eng. Sci. Technol., 10, 71–81.

Singh S S; Ghodki B M; Goswami T K. 2018. Effect of grinding methods on powder quality of king chilli. J. Food Meas. Charact., 12, 1686-1694. https://doi.org/10.1007/s11694-018-9784-6**.**

Characterisation of Curcumin-loaded Egg Albumin Powder

D. S. Aniesrani Delfiya*[1], K. Thangavel[2] and D. Amirtham[2]

[1]Scientist, Engineering Division, ICAR-Central Institute of Fisheries Technology, Cochin - 682029, Kerala, India; [2]Department of Food and Agricultural Process Engineering, Tamil Nadu Agricultural University, Coimbatore – 641 003, India. Corresponding author email address: delfy.lenin@gmail.com

Article Info	ABSTRACT
	Curcumin was encapsulated using egg albumin as a carrier material by desolvation and spray drying methods. Curcumin-loaded egg albumin powder was analysed for its *in vitro* release pattern, structural changes, morphology, stability, and antioxidant capacity. *In vitro* release studies showed that the cumulative release of 5.32, 47.76, 50.58, and 60.63% from pure curcumin from the powders prepared using ethanol, acetone, and spray drying, respectively, in 72 h. The FT-NIR spectrum of curcumin-loaded egg albumin powder confirmed that the curcumin and egg albumin maintained their chemical structure during drying process. FESEM images revealed that particles were in spherical shape and in the size ranges of 50 nm to 400 nm and 50 nm to 350 nm for nanoparticles prepared using ethanol and acetone, respectively. SEM images of spray dried particles showed that the particle size ranged from 1 μm to 15 μm without any agglomeration. Curcumin retentions of 74.66, 75.93, and 70.64% were observed in powder prepared using ethanol, acetone, and spray drying, respectively, after 50 min of heating at 100 ºC. Thus, the encapsulated samples were thermally stable, and could be used in food preparations as natural yellow colourant as functional food ingredient. Total antioxidant capacity of curcumin-loaded egg albumin powder prepared using ethanol, acetone, and spray drying was 5.96 ± 0.89, 4.58 ± 0.23, and 6.97 ± 0.44 μg of ascorbic acid equivalents, respectively, at 100 μg.ml^{-1} sample concentration. Curcumin retained within the formulations was found to be stable without any change in the physical appearance throughout the storage period.

Curcumin is a natural yellow coloured pigment found in turmeric (*Curcuma longa* Linn), and is used as a food colouring agent. It has promising medical uses due to its low toxicity (Shang *et al*., 2010). Application of curcumin as a functional ingredient in food products and as a therapeutic agent has been limited due to its low water solubility (aqueous solubility of about 11 ng.ml^{-1}), sensitivity to alkaline conditions, rapid metabolism and poor bioavailability (Liu *et al*., 2016). Encapsulation of curcumin using suitable carrier material can be used to improve the solubility and bioavailability of curcumin.

Food proteins are commonly used as drug carriers because of their high nutritional value, low toxicity, and excellent functional properties as well as their application as ingredients in the food industry. Binding of curcumin to proteins might help in improving the solubility and arresting the degradation. Albumin is an abundant human plasma protein and is a commonly used drug delivery vehicle because it is stable at physiological conditions, readily soluble, and nontoxic. Egg albumin has been used for the encapsulation of functional food ingredients and drugs, because it is a natural and biodegradable polymer with good water solubility. It also has a property of protein binding and physical entrapment, and it facilitates the release of core material from polymer matrix (Shailesh *et al*., 2010). Hence, egg albumin was chosen as a carrier for curcumin due to its availability and low cost as compared with other proteins. Limited studies are available on usage of egg protein for curcumin encapsulation. Chang *et al*. (2019) investigated the encapsulation of curcumin

into egg white protein nanoparticles and reported the nanoparticles as promising candidates for high-efficiency delivery system for curcumin. Wang *et al*. (2020) suggested the encapsulation of curcumin in egg white protein isolate to improve dispersity, antioxidant capacity, and thermal stability of curcumin.

Albumin nanoparticles are commonly prepared by desolvation of protein using organic solvents, followed by chemical cross-linking. Organic solvent modifies the structure of protein to give a hydrophobic material, which forms small aggregates of desolvated albumin (coacervates) (Irache and Espuelas, 2006). Formed coacervates have to be hardened by cross-linking using glutaraldehyde (Elzoghby *et al*., 2012). Spray drying is one of the suitable methods to prepare encapsulated powders with required size and release characteristics. Basic steps involved in spray drying are preparation and atomization of emulsion, followed by dehydration of the atomized particles. Spray drying has gained more attention in the recent years due to the flexibility of a spray drying system.

Zheng and McClements (2020) highlighted some colloidal delivery systems such as micelles, liposomes, microemulsions, emulsions, solid lipid system which have been used to improve the solubility and bioavailability of curcumin. They also suggested that the selection of most suitable delivery system for curcumin in future should be based on the cost, ease of manufacturing, robustness, bioavailability, sustainability, and environment impact. Hence, in this study an attempt was made to encapsulate curcumin using egg albumin as carrier material by desolvation and spray drying methods; and to analyse the *in vitro* release characteristics, structural characteristics, morphology, and stability of prepared curcumin-loaded egg albumin powder.

MATERIALS AND METHODS

Egg albumin powder (with 85% protein) was supplied by M/s SKM Egg Products, Erode, Tamil Nadu; while curcumin (minimum 95% purity) was procured from M/s Synthite Industries Ltd, Kolenchery, Kerala. Glutaraldehyde (25% w/v solution) was purchased from M/s Astron Chemicals (India), Ahmedabad. All other reagents used in the experiments were of AR grade. The study was conducted at Tamil Nadu Agricultural University, Coimbatore.

Design of Experiment

Factors such as pH, albumin concentration, and curcumin concentration could influence the albumin nanoparticles production in desolvation process. Based on the literature review, egg albumin solution concentration in the range of 5 - 15% w/v, pH of 5 – 7, and curcumin concentration of 0.25% w/v of egg albumin solution were selected as process parameters for encapsulation by desolvation. In authors' previous study (Delfiya *et al*., 2016a), desolvation process using ethanol as desolvation agent was optimised using response surface methodology. Similarly, desolvation process parameters using acetone as desolvation agent was optimised in another study of Delfiya *et al*. (2016b). Egg albumin concentration of 2.5 - 7.5 (%w/v), curcumin concentration of 0.25 - 0.75% (w/v), and air inlet temperature of 110 - 130 ºC were selected as low and high levels of independent variables and the process parameters were optimised as in the study of Delfiya (2016c). In this study curcumin-loaded egg albumin powder was prepared under the optimum process parameters which were obtained from the earlier studies (Delfiya *et al*., 2016a; Delfiya *et al*., 2016b, Delfiya, 2016c). Optimised process parameters of desolvation using ethanol, acetone as desolvation agents, and spray drying and the formulation codes of optimum processes are presented in Table 1, and

Table 1. Formulation codes of optimally prepared samples

Process	Optimised factors	Formulation code
Desolvation	Desolvation agent: Ethanol Egg albumin solution concentration: 8.06 (%w/v) Solution pH: 5.34	EA-CUR NPs-Ethanol
Desolvation	Desolvation agent: Acetone Egg albumin solution concentration: 8.85 (%w/v) Solution pH: 5	EA-CUR NPs-Acetone
Spray drying	Egg albumin solution concentration: 5.51 (%w/v) Curcumin concentration: 0.63 (%w/v) Inlet air temperature: 130 ºC	EA-CUR MPs-Spray drying

would be used in subsequent sections to represent the curcumin-loaded egg albumin powder prepared under optimum condition.

Preparation of Curcumin-loaded Egg Albumin Powder

Curcumin nanoparticles were prepared using egg albumin as the polymer by desolvation technique. For the preparation of curcumin nanoparticles, the method described by Weber *et al*. (2000) was followed with some modifications. Egg albumin solution of 8.06(%w/v) and 8.85 (%w/v) concentrations and pH of 5.34 and 5 was prepared in distilled water at room temperature (28±2 °C) for ethanol and acetone desolvation, respectively. Subsequently, 0.25 (%w/v based on egg albumin solution) curcumin was dissolved in 20 ml ethanol or acetone, which was added intermittently into the aqueous egg albumin solutions under magnetic stirring at 500 rpm at room temperature. Each five minutes interval, 2 ml of curcumin dissolved ethanol or acetone was added in egg albumin solution and this addition was continued until the solution became just turbid. This resulted in the formation of an opalescent suspension spontaneously at room temperature. After this desolvation process, 0.11 ml of 8% (v/v) glutaraldehyde in water was added to the turbid solution to induce particle crosslinking. Then this

solution was stirred continuously at 500 rpm at room temperature for 1 h. The complete cross-linking process of the colloidal suspension was performed over a time period of 24 h. Formed nanoparticles were subsequently purified by three cycles of centrifugation (3000 rpm, 30 min) and re-dispersion with distilled water to remove unreacted chemicals and desolvation agents. Purified pellets were transferred to a Teflon plate and dried in an oven at 50 °C for 6 h. The resulting curcumin-loaded egg albumin particles were gently pulverized using mortar and pestle to obtain the dried fine curcumin nanoparticles.

Microencapsulation of curcumin was carried out in a two-step process. The first step was the emulsification of curcumin and wall material, followed by spray drying of the resultant emulsion. Curcumin-egg albumin emulsion was prepared by dissolving egg albumin (5.51%w/v) in distilled water and subsequent addition of curcumin (0.63%w/v) into it. This mixture was stirred at 700 rpm for 10 min using magnetic stirrer (SPINIT, (Tarsons, Kolkata, 100-1000 rpm, 5 l) and kept at room temperature (28±2 ºC) prior to spray drying process. Spray drying was carried out in a laboratory model spray drier (Spray Mate, JISL, Mumbai, l.h^{-1} evaporation capacity) (Fig. 1) with a

1.	Air heater
2.	Atomizer
3.	Drying chamber
4.	Collection bottle
5.	Cyclone separator
6.	Collection pot
7.	Scrubber
8.	Control panel
9.	Aspirator blower
10.	Sample
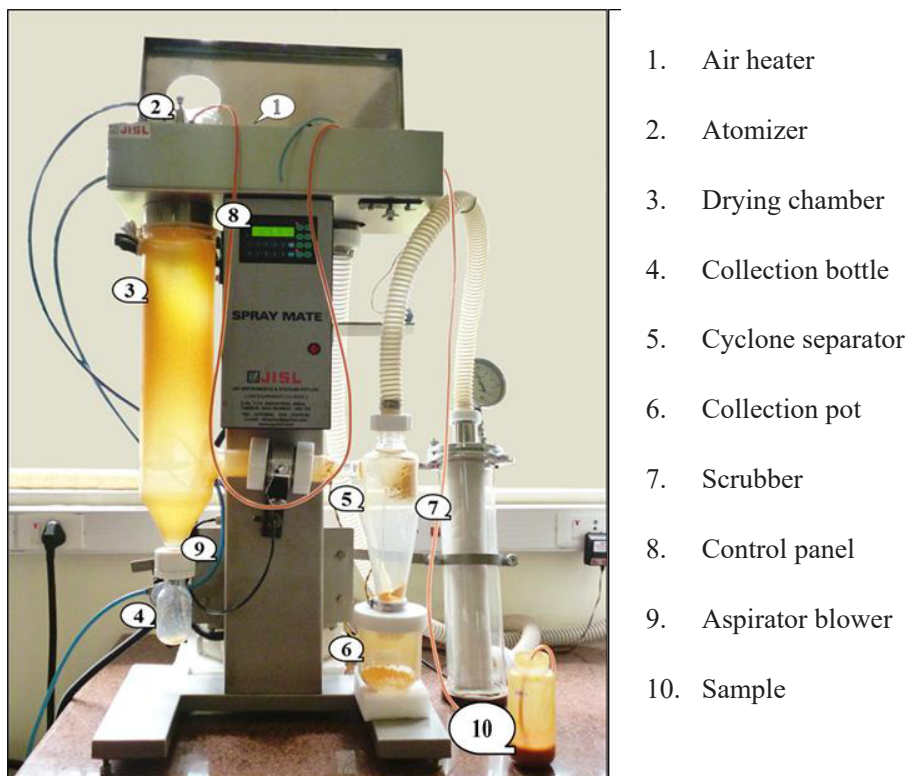
Fig. 1: Lab model spray drier

spray nozzle of 0.7 mm. Emulsion was fed into the spray drier equipped with two fluid nozzle atomizer using a peristaltic pump. Emulsion was fed into the main chamber through a peristaltic pump at the rate of 2 ml.min⁻¹. The pressure of compressed air for the flow of the spray was adjusted to 2 bar. The vacuum pressure was maintained at -80 mm of water column. Air outlet temperature was maintained in the range of 50 - 60 ºC. Inlet temperature of air was maintained at 130 °C. Microencapsulated powders were collected from spray drier and filled in airtight, self-sealable polyethylene pouches and stored at refrigeration temperature (4±2 ºC) until further studies.

Characterisation of Curcumin-loaded Egg Albumin Powder

Curcumin-loaded egg albumin powder prepared under optimum process parameters were analysed for its *in vitro* release pattern, structural changes, morphology and stability.

Water activity

Water activity of curcumin-loaded egg albumin powder was determined using a pre-calibrated water activity meter (M/s Decagon Devices, Inc., Pullman, USA, Aqua Lab series 3) at 30±1 ºC during tests.

In vitro release study

Curcumin-loaded egg albumin powder was analysed for the *in vitro* release characteristics (Jithan *et al*., 2011). *In vitro* release studies were conducted in a closed chamber (under dark conditions) to avoid curcumin degradation in presence of light. Phosphate-buffered saline (PBS 0.1M, pH 7.4) was used as a release medium, which contained 1% ascorbic acid and 0.1% butylated hydroxytoluene to prevent further degradation of curcumin.

Optimally prepared powders (100 mg) were re-dispersed in 200 ml of the release medium (PBS) and kept in a digital incubator-cum-orbital shaker (Neolab instruments, Mumbai, India, capacity: 8 flasks; temperature: ambient plus 5 ºC to 60 ºC) at 37±1 ºC under stirring at 100 rpm. Release medium (20 ml) was removed at 0, 2, 4, 6, 8, 24, 48, and 72 h intervals and replaced with the same volume of fresh medium. The samples withdrawn were filtered using 0.2µm sterile filter, and the amount of curcumin in release medium was determined by UV-VIS spectrophotometer 108 (Systronics, Ahmedabad, India, single beam, 200 – 900 nm, manual) at 425 nm.

A standard calibration curve of curcumin concentration vs. absorbance was plotted for this purpose. Regression equation of the standard curve is as follows:

$$y = 0.2461x - 0.0052 \qquad \text{...(1)}$$

Where,
y = Absorbance value, and
x = Concentration of curcumin, µg.ml⁻¹.

Furthermore, its R^2 was 0.998. Concentration of curcumin in release medium was calculated by substituting the absorbance value in the regression equation. All measurements were performed in triplicate.

The release was quantified as follows:

$$\text{Release (\%)} = \frac{\text{Released curcumin µg.ml}^{-1}}{\text{Total curcumin µg.ml}^{-1}} \times 100 \qquad \text{...(2)}$$

Curcumin-egg albumin interaction

Curcumin-egg albumin interaction was analysed using Fourier Transform Near Infra-Red (FT-NIR) Spectroscopy MATRIX-I (Make: Bruker optics, Germany). The system was operated by Spectral Acquisition and Processing Software (OPUS software, version 7.2, Bruker optics, Germany). The spectra were obtained using the light source of tungsten halogen lamp at a resolution of 8 cm⁻¹ over a wavelength range of 12,500-3,600 cm⁻¹ with 64 scans per sample. Michelson interferometer equipped with beam splitter with lead sulphide (PbS) detector was capable of detecting the interference of the light beam passing through the sample. The interferogram collected by the detector was converted into a spectrum by Fourier transforming the interferogram. NIR spectra for each powder sample were collected in triplicate by scanning directly through the base of the glass sample vials. Each replication is recorded by shuffling the orientation in the sample cup, so as to standardize the orientation of particles. Individual sample vials were rotated 120° between triplicate scans, and respective spectra were recorded separately. To remove the baseline shifts in the spectra caused by particle size and packing differences, standard normal variate transform was applied (Tanaka *et al*., 2008).

Morphology

Curcumin-loaded egg albumin powder was spread over the stubs and examined in a Field Emission Scanning Electron Microscope ZEISS Sigma 500 (a resolution of 1.3 nm at 1

kV) (FESEM, Carl Zeiss Microscopy Ltd, SIGMA, UK) and scanning electron microscope (SEM) (FEI Quanta 250, FEI, Hillsboro, Oregon, USA) (Resolution: in 30 kV and High vacuum conditions: 1.2 nm, in 30 kV and Low vacuum conditions: 3.0 nm) to investigate the morphology of powder. Encapsulated powder (10 mg) was dusted on carbon tape, which was mounted over the stub. Samples were viewed in scanning electron microscope and the images were taken to measure the size and shape of the encapsulated powder.

Stability of Curcumin-loaded Egg Albumin Powder

Storage stability

Prepared curcumin-loaded egg albumin particles (20 mg) were kept in sealed glass vials and maintained at 4 ºC for a period of 6 months. Particles were analysed for changes in curcumin per cent at each month interval during the storage period (Ranjan *et al*., 2012).

Heat stability

Heat stability of curcumin-loaded egg albumin particles were evaluated by preparing the mixture of encapsulated powder in water solution (0.5 %w/v). Ten ml of prepared solutions were kept at 100 ºC for 0, 10, 20, 30, 40, and 50 min of heating time and absorbance values of the solutions after heating were determined by the spectrophotometer at 425 nm. Using these absorbance values, concentrations of curcumin (μg/ml) were determined from the standard curcumin curve and its regression equation (1). Curcumin retention per cent (the ratio of curcumin retained in water solution after heating to initial curcumin solution) of samples was determined after heating it at 100 ºC for certain time using the following equation (Wang *et al*., 2009):

RESULTS AND DISCUSSION

Quality characteristics of optimally prepared powder

Numerical optimization technique was adopted to optimise the process parameters for preparation of curcumin-loaded egg albumin powder (Delfiya, 2016; Delfiya *et al*., 2016a; Delfiya *et al*., 2016b). Egg albumin solution concentration of 8.06 (%w/v) and pH of 5.34 were found to be the optimum conditions of encapsulation using ethanol as desolvation agent with the maximum desirability of 0.499. The optimum conditions for encapsulation using acetone were found to be the egg albumin solution concentration of 8.85%w/v and pH of egg albumin solution of 5 with the desirability of 0.533. Optimum condition for spray

drying were egg albumin solution concentration of 5.51%w/v, curcumin concentration of 0.63%w/v, and inlet air temperature of 130 ºC. Encapsulation was done under the derived optimum process parameters, and the quality characteristics of the resulting particles were determined and reported in Table 2.

Characterisation of Curcumin-loaded Egg Albumin Powder

Curcumin-loaded egg albumin powders prepared under optimum process parameters were analysed for its *in vitro* release pattern, structural changes, morphology, and stability.

Water activity

Water activity is an index of shelf life of powders, and food with water activity less than 0.6 is considered as microbiologically stable (Goula *et al*., 2005). Water activity values of optimally prepared samples were observed as 0.406, 0.403, and 0.404 for EA-CUR NPs-Ethanol, EA-CUR NPs-Acetone nanoparticles, and EA-CUR MPs-Spray drying microparticles, respectively. Results showed that prepared powders were microbiologically stable. This low water activity completely inhibits the growth of all types of microorganism (Abbas *et al*., 2009). Neves *et al*. (2019) evaluated the efficiency of milk for curcumin encapsulation and reported the water activity of 0.14.

In vitro release profile

Curcumin release profile analysis is important to explain the controlled delivery of curucmin to targeted site. Optimally prepared curcumin-loaded egg albumin powder and pure curcumin were analysed for its *in vitro* release profile in PBS (pH 7.4) for 72 h. The cumulative curcumin release per cent at specified time intervals are presented in Table 3.

Table 2. Characteristics of optimally prepared curcumin loaded egg albumin powder

Response	EA-CUR NPs-Ethanol	EA-CUR NPs-Acetone	EA-CUR MPs-Spray drying
Solubility, %	30.54	33.57	78.56
Curcumin , %	5.78	4.125	22.87
Curcumin entrapment efficiency, %	56.78	55.23	64.87
Powder yield, %	71.65	72.85	50.89
Particle size, nm	263.5	232.6	-

**Table 3. Curcumin release per cent of optimally prepared samples during *in vitro* release study**

Sample	Cumulative curcumin release, %							
	0 h	2 h	4 h	6 h	8 h	24 h	48 h	72 h
EA-CUR NPs-Ethanol	3.87±0.18	10.6±0.28	18.75±0.56	28.32±0.57	36.47±1.67	41.45±0.83	45.2±1.63	47.76±1.43
EA-CUR NPs-Acetone	6.43±0.29	13.31±0.35	20.48±0.74	28.83±0.61	35.65±0.71	42.63±1.54	48.31±0.97	50.58±1.82
EA-CUR MPs-Spray drying	5.43±0.25	12.34±0.37	21.46±0.98	31.83±1.15	40.9±1.23	49.43±2.26	55.66±1.47	60.63±1.82
Curcumin	0.058	1.69±0.06	2.35±0.08	2.98±0.09	3.56±0.13	4.21±0.15	4.76±0.12	5.32±0.24

Slow release of curcumin from all formulations was observed either due to the diffusion of curcumin from formulations or the slow degradation of egg albumin in aqueous solution. Pure curcumin showed cumulative release of 5.32% in 72 h. In case of encapsulated curcumin, sustained release of curcumin from all formulations was observed in 72 h. Release of 47.76% was observed from EA-CUR NPs-Ethanol, and EA-CUR NPs-Acetone showed release of 50.58% in 72 h. Powder prepared by spray drying had released curcumin of 60.63% within 72 h. Thus, formulations prepared by encapsulation could release higher amount of curcumin in a sustained manner than the pure curcumin at physiological pH conditions. Encapsulation of curcumin using egg albumin resulted in sustained release of curcumin and enhanced the bioavailability of it. Li *et al*. (2015) studied the *in vitro* release profile of curcumin (Ccn)-loaded albumin nanoparticles (BNPs) which are surface-functionalized with glycyrrhetinic acid (Ccn-BNP-GA) and reported that Ccn-BNP-GA showed an initial burst release for up to 12 h, followed by a slow-release pattern of curcumin over 72 h in PBS solution (pH 7.4). Results indicated that the curcumin-loaded egg albumin powders prepared under optimal conditions were capable of releasing curcumin in a controlled manner through diffusion-controlled release. The initial burst effect due to the weakly bound curcumin on the surface of formulations and later sustained release over 72 h was observed in all formulations. Diffusion of curcumin from formulations was the mechanism responsible for the slower curcumin release kinetics from the formulations. Curcumin-loaded egg albumin powder was found to be a suitable controlled release system of curcumin.

Curcumin-egg albumin interaction

Curcumin-egg albumin interactions during the encapsulation process were assessed using FT-NIR spectroscopy. The spectra of curcumin, egg albumin, EA-CUR NPs-Ethanol, EA-CUR NPs-Acetone, and EA-CUR MPs-Spray drying were obtained using FT-NIR. Figure 2 shows the FT-NIR spectrum of
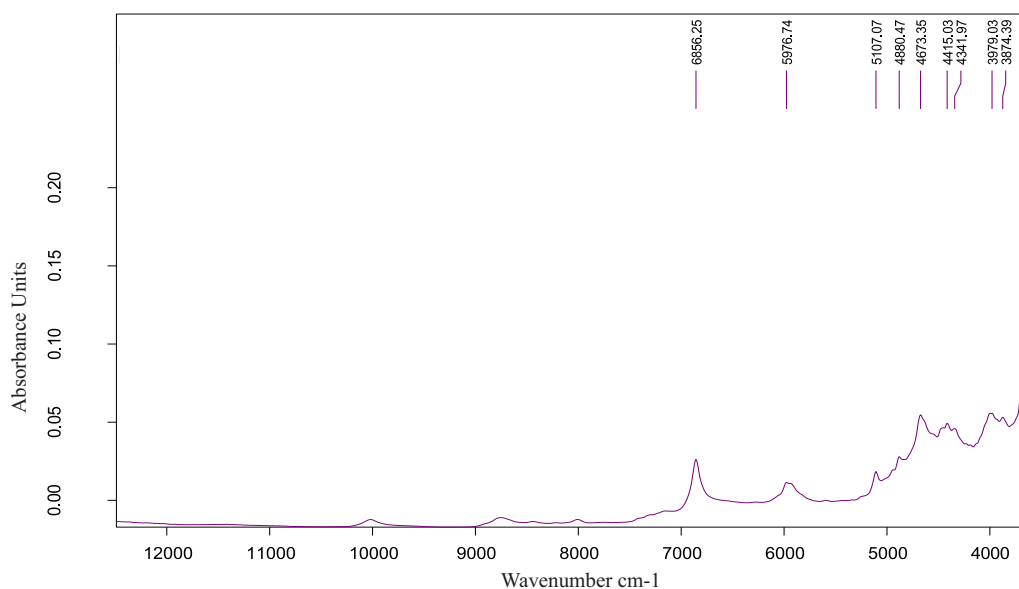
Fig. 2: FT-NIR Spectra of pure curcumin and its characteristic peaks

pure curcumin and its characteristic peaks of C-N-C stretching (Protein) at 3,874 cm^{-1}, C-H stretching (Starch) at 3,979 cm^{-1}, C-H bending (Protein) at 4,341 cm^{-1}, O-H/C-O stretching (Cellulose) at 4,415 cm^{-1}, C-H stretching/C-H deformation (HC==CH) at 4,673 cm^{-1}, N−−H stretching/amide Ib combination (Protein) at 4,880 cm^{-1}, O−H stretch/O−H bend (Starch) at 5,107 cm^{-1}, C-H stretching (Aromatic) at 5,976 cm^{-1}, and C=O stretching (C=O) at 6,856 cm^{-1} were observed in the wavenumber range of 3,800 – 6,900 cm^{-1}. The characteristic peaks contributed by the functional groups of egg albumin could be observed as C−N−C stretching (Protein) at 3,967 cm^{-1}, C-H bending (Protein) at 4,354 cm^{-1}, C=O stretching/amide IIIb (Protein) at 4,592 cm^{-1}, N−H stretching/amide Ib at 4,865 cm^{-1}, O−H bending (H$_2$O) at 5,152 cm^{-1}, S−H stretching (-SH) at 5,755 cm^{-1}, and N−H stretching (Protein) at 6,635 cm^{-1} (Fig. 3).

FT-NIR spectra (Fig. 4) of EA-CUR NPs-Ethanol shows the characteristic peaks of C−N−C stretching (Protein) at 3,946 cm^{-1}, C-H bending (Protein) at 4,352 cm^{-1}, C=O stretching/amide IIIb (Protein) at 4,593 cm^{-1}, N−H stretching/amide Ib at 4,863 cm^{-1}, O−H
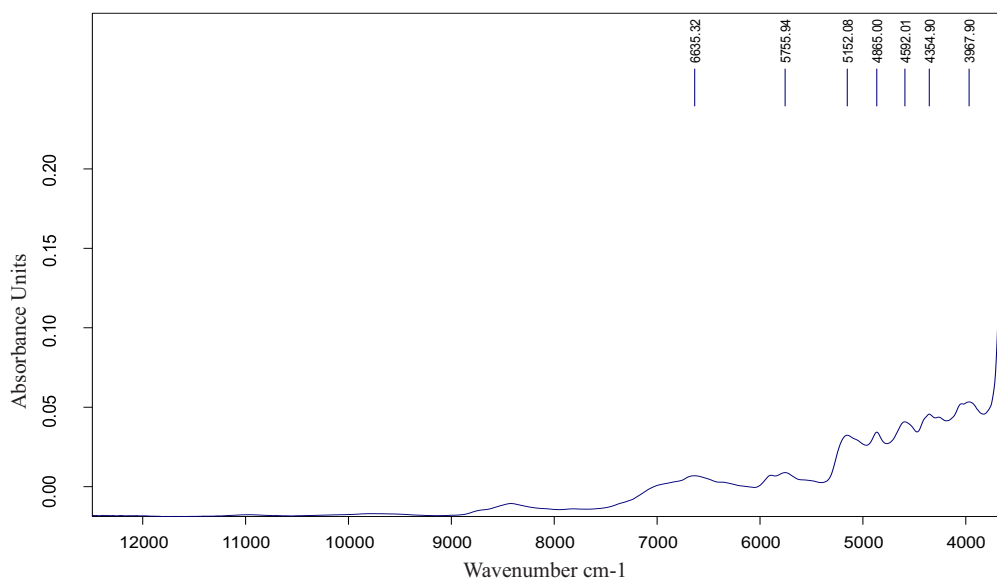
Fig. 3: FT-NIR Spectra of egg albumin and its characteristic peaks
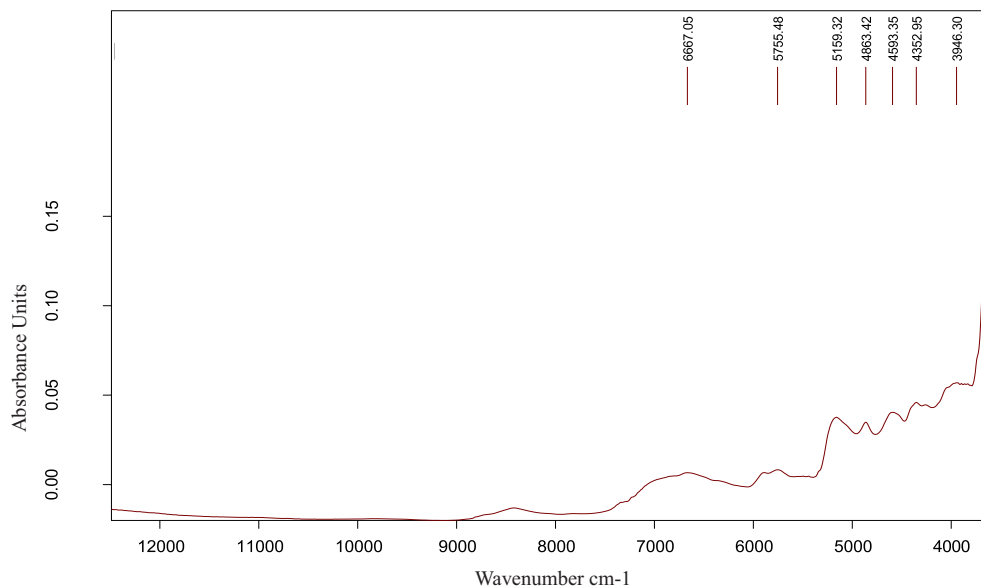
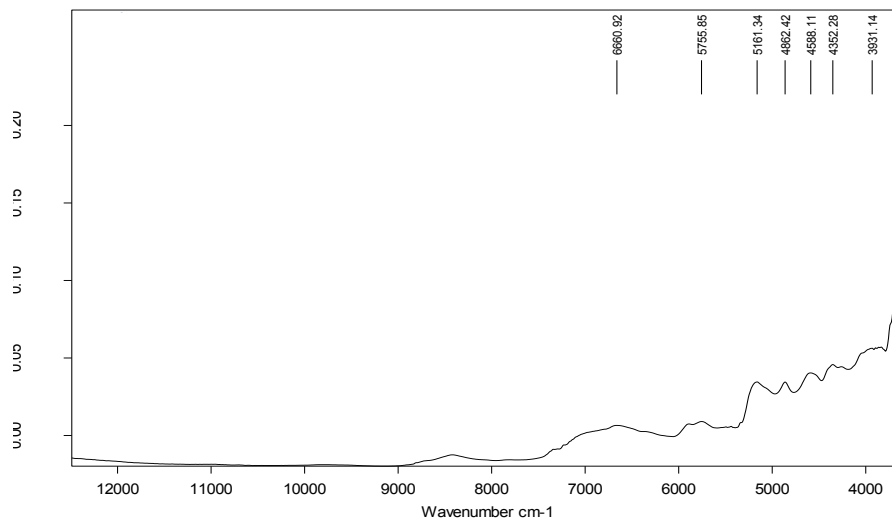**Fig. 4: FT-NIR Spectra of curcumin-loaded egg albumin nanoparticles prepared using ethanol as desolvation agent and its characteristic peaks**

bending (H_2O) at 5,159 cm^{-1}, S−H stretching (-SH) at 5,755 cm^{-1}, and N−H stretching (Protein) at 6,667 cm^{-1}. While comparing the characteristic peaks of egg albumin and curcumin-loaded powder, peak shifts were observed from 3,967 cm^{-1} to 3,946 cm^{-1}, 5,159 cm^{-1} to 5,152 cm^{-1}, and 6,667 cm^{-1} to 6,635 cm^{-1}. These peak shifts indicated the presence of curcumin in powder. Absence of additional peak in spectra indicated the lack of curcumin and egg albumin interactions during desolvation process.

FT-NIR spectrum of EA-CUR NPs-Acetone is shown in Fig. 5. From the characteristic peaks, it could be observed that as C−N−C stretching (Protein) at 3,931

cm^{-1}, C-H bending (Protein) at 4,352 cm^{-1}, C=O stretching/amide IIIb (Protein) at 4,588 cm^{-1}, N−H stretching/amide Ib at 4,862 cm^{-1}, O−H bending (H_2O) at 5,161 cm^{-1}, S−H stretching (-SH) at 5,755 cm^{-1}, and N−H stretching (Protein) at 6,660 cm^{-1}. Peak shifts were observed from 3,967 cm^{-1} to 3 cm^{-1} ,931 cm^{-1}, 5,161 cm^{-1} to 5,152 cm^{-1}, and 6,660 cm^{-1} to 6,635 cm^{-1} in the spectra and no additional peak was observed in the range of 3,900 – 6,700 cm^{-1}. This indicated the presence of curcumin as well as lack of curcumin and egg albumin interactions during desolvation process.

Figure 6 shows the FT-NIR spectrum of EA-CUR MPs-Spray drying, and the characteristic peaks showed

Fig. 5: FT-NIR Spectra of curcumin-loaded egg albumin nanoparticles prepared using acetone as desolvation agent and its characteristic peaks
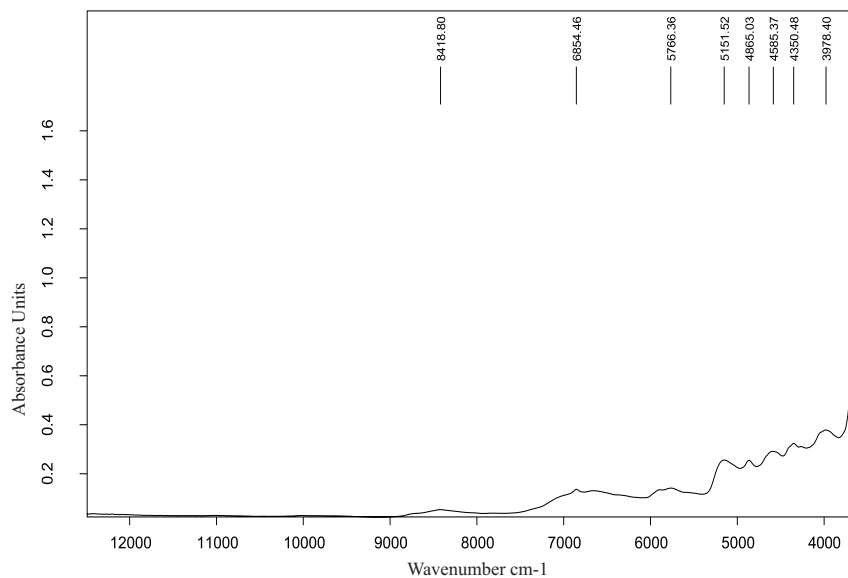
Fig. 6: FT-NIR Spectra of curcumin-loaded egg albumin microparticles and its characteristic peaks

C−N−C stretching (Protein) at 3,978 cm^{-1}, C-H bending (Protein) at 4,350 cm^{-1}, C=O stretching/amide IIIb (Protein) at 4,585 cm^{-1}, N−H stretching/amide Ib at 4,865 cm^{-1}, O−H bending (H$_2$O) at 5,151 cm^{-1}, S−H stretching (-SH) at 5,766 cm^{-1}, and N−H stretching (Protein) at 6,854 cm^{-1}. Peak shifts were observed from 3,978 cm^{-1} to 3,967 cm^{-1}, 4,354 cm^{-1} to 4,350 cm^{-1}, 4,592 cm^{-1} to 4,585 cm^{-1}, 5,766 cm^{-1} to 5,755 cm^{-1}, 6,854 cm^{-1} to 6,635 cm^{-1}, which indicated the presence of curcumin in powder after spray drying. Similar peak shifts were observed in spectra of curcumin loaded O-carboxymethyl chitosan nanoparticles while comparing the FT-IR spectrum of O-carboxymethyl chitosan and curcumin-O-carboxymethyl chitosan nanoparticles (Anitha *et al*., 2011). Jithan *et al*. (2011) reported that lack of additional peak in the FT-IR spectra of BSA-curcumin nanoparticles indicated the lack of drug polymer interactions in the formulation. The FT-NIR spectrum of curcumin-loaded egg albumin powder was similar to that of curcumin spectra and egg albumin spectra, which indicated that the curcumin and egg albumin maintained their chemical structure during and after desolvation and spray drying processes.

Morphology

Morphology of the optimally prepared EA-CUR NPs-Ethanol was examined using FESEM and the images are shown in Fig. 7. It was observed that particles in powder were in spherical shape and in the size range of 50 - 400 nm. Powder was aggregated together and formed clusters. FESEM images of EA-CUR NPs-Acetone are presented in Fig. 8, and particles were found to be spherical in shape and combined densely together. EA-CUR NPs-Acetone were observed in the size range of 50 - 350 nm. Jana *et al*. (2014) observed similar denser particles of aceclofenac-loaded chitosan-egg albumin nanoparticles during SEM analysis.

SEM micrographs showing the external morphology of spray dried curcumin-loaded egg albumin powder is presented in Fig. 9. It was seen that the powder microcapsules were spherical in shape, and had smooth outer surface with no cracks or pores, ensuring the protection and retention of curcumin inside the microcapsules. SEM images showed that particles were single and separate without any agglomeration. This indicated good flowability and easy handling of the powder, and the size of the powder ranged from 1 μm to 15 μm. Shrinkage during drying and cooling processes created dents on the surface of particles. These imperfections are characteristic of the spray drying process and it is associated with the characteristics of encapsulating agent or process conditions (Fernandes *et al*., 2013).

Stability

Storage stability

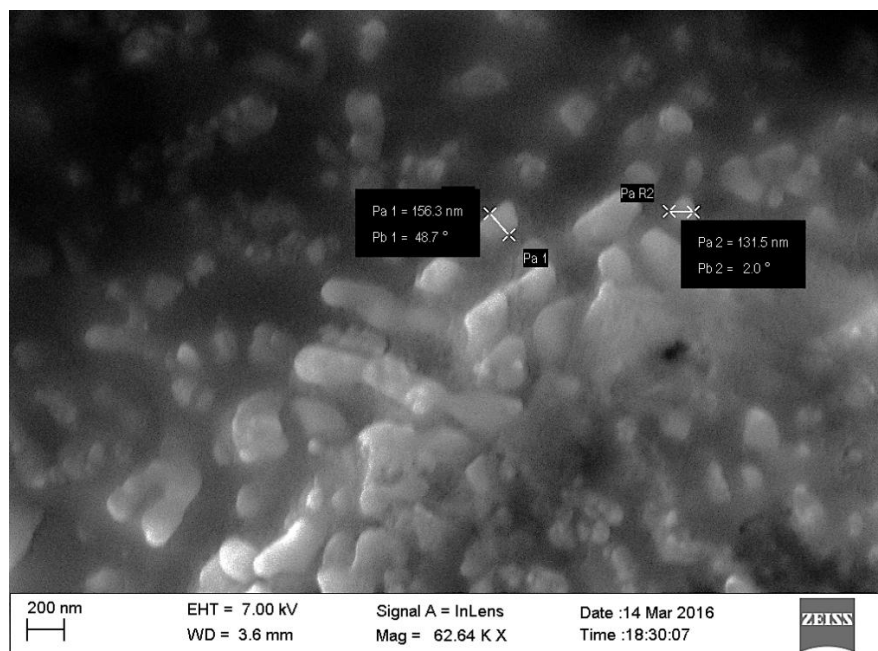Storage stability of the samples prepared under

Fig. 7: FESEM image of curcumin-loaded egg albumin nanoparticles prepared by ethanol at 60 K magnification
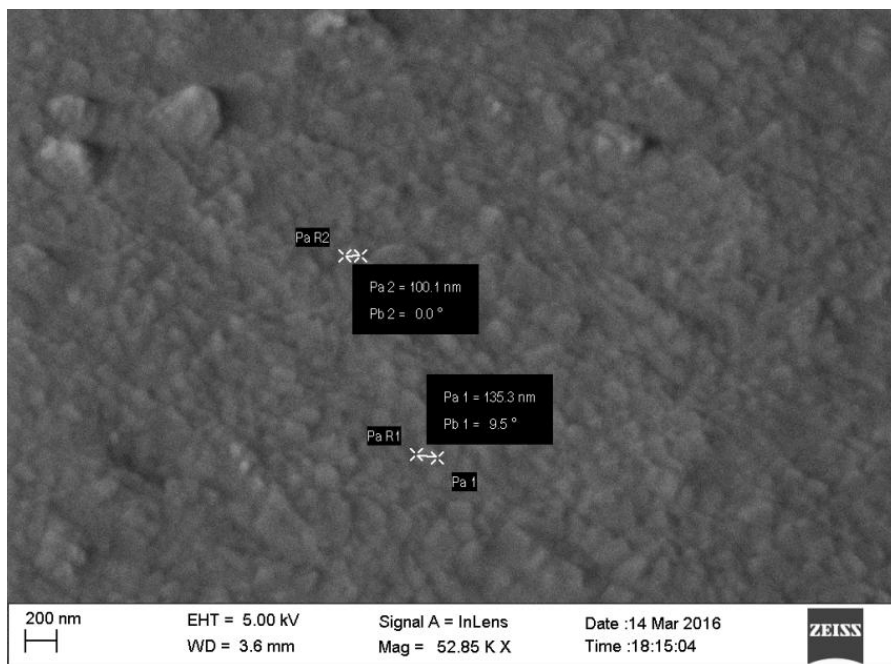
Fig. 8: FESEM image of curcumin-loaded egg albumin nanoparticles prepared by acetone at 50 kX magnification
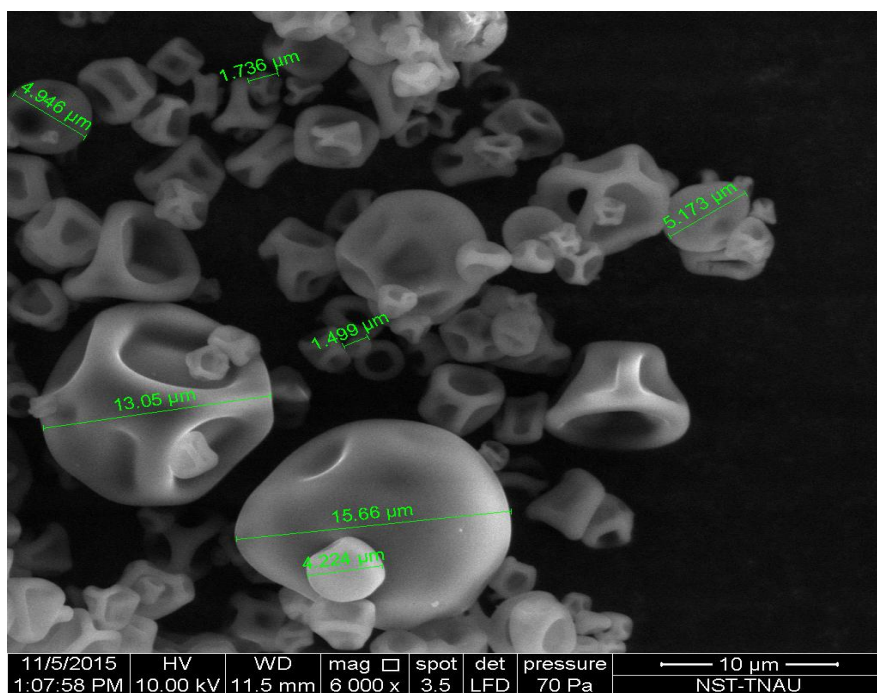

Fig. 9: SEM micrograph of spray dried curcumin-loaded egg albumin microparticles at 6000 X magnification

optimum process parameters was evaluated by storing it in glass vials at 4 °C for six months. Curcumin content of samples was analysed at each month interval up to six months of storage. The changes in curcumin content of EA-CUR NPs-Ethanol, EA-CUR NPs-Acetone, and EA-CUR MPs-Spray drying are reported in Table 4.

A slight reduction in curcumin content was observed for all samples due to the loss of surface curcumin during storage. Curcumin content of EA-CUR NPs-Ethanol was reduced from 4.01% to 3.20 per cent. In case of EA-CUR NPs-Acetone, curcumin content decreased from 4.12% to 3.41 per cent. EA-CUR MPs-Spray drying

Table 4. Curcumin content of optimally prepared samples during storage of six months

Storage period, month	Curcumin content, % (Mean±SD)		
	EA-CUR NPs-Ethanol	**EA-CUR NPs-Acetone**	**EA-CUR MPs-Spray drying**
0	4.02±0.17	4.12±0.11	12.16±0.36
1	3.94±0.11	3.92±0.14	12.09±0.36
2	3.83±0.14	3.81±0.04	12.01±0.24
3	3.62±0.11	3.63±0.05	11.98±0.36
4	3.48±0.09	3.53±0.07	11.86±0.31
5	3.28±0.09	3.46±0.03	11.57±0.42
6	3.17±0.11	3.37±0.03	10.90±0.33

showed the curcumin content reduction from 12.16% to 10.90% during the six-month period of storage. During the storage period no visible aggregations were found in all samples. Hence, it could be concluded that the curcumin that was retained within the formulations was stable, and the physical appearance was not changed throughout the storage period. Ranjan *et al*. (2012) had also observed a slight decrease in encapsulation efficiency, and drug loading during the assessment of long-term storage stability of encapsulated curcumin nanoparticles.

Heat stability

Thermal stability of samples prepared at optimum process conditions was analysed by heating the sample solution (0.5% w/v in water) at 100 °C for 0, 10, 20-, 30-, 40-, and 50-min. Effect of heating time at 100 °C on thermal stability of samples in terms of curcumin retention per cent is shown in Fig. 10. Results showed that curcumin retention per cent decreased during heating time increase from 0 - 50 min in all samples. Curcumin retention of EA-CUR NPs-Ethanol, EA-

CUR NPs-Acetone, and EA-CUR MPs-Spray drying were observed as 74.66±2.24, 75.93±2.28, and 70.64±2.12% after 50 min of heating at 100 °C. Even though curcumin content of the samples reduced during heating, up to 70% of curcumin was retained after heating it for 50 min. Thus, the encapsulated samples were found to be thermally stable, and could be used in food preparations as natural yellow colourant as well as functional food ingredient. Wang *et al*. (2009) had reported that microencapsulated curcumin showed better heat resistance stability while heating it from 10 min to 50 min at 100 °C.

CONCLUSIONS

Curcumin-loaded egg albumin powders prepared under optimum process parameters were found to release higher amount of curcumin in a sustained manner than the pure curcumin at physiological pH conditions. Optimally prepared curcumin-loaded egg albumin powders were capable of releasing curcumin in a sustained manner through diffusion-controlled
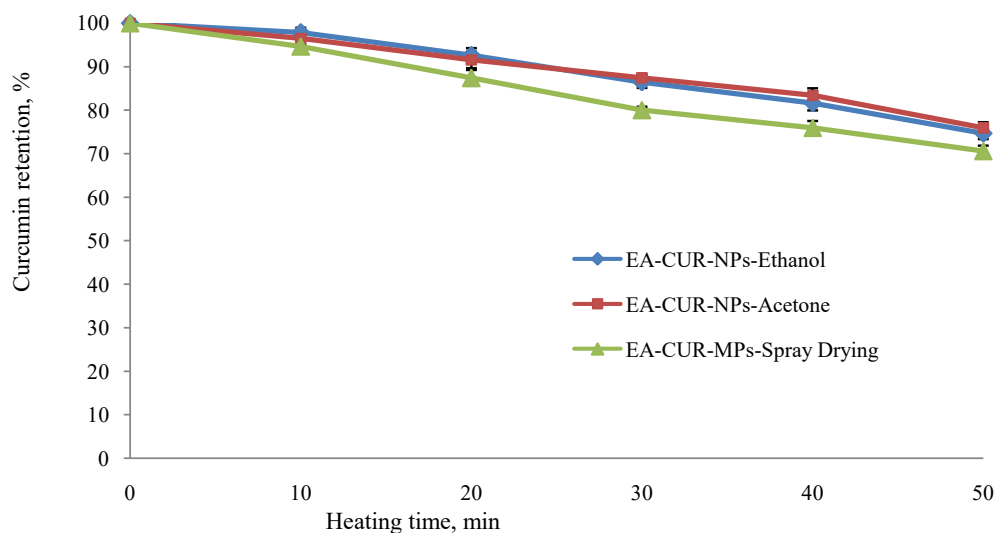

Fig. 10: Effect of heating time on retention period of curcumin-loaded egg albumin powder

release. EA-CUR NPs-Ethanol and EA-CUR NPs-Acetone were found to be spherical in shape and combined densely together. EA-CUR MPs-Spray dried particles were spherical in shape and had smooth outer surface with no cracks or pores. Curcumin-loaded egg albumin powder was found to be stable and the physical appearance was also not changed throughout the storage period. Curcumin retention of 74.66 ± 2.24, 75.93 ± 2.28, and $70.64 \pm 2.12\%$ was observed in nanoparticles prepared using ethanol, acetone, and microparticles prepared by spray drying, respectively, after 50 min of heating at 100 °C. Thus, the encapsulated samples were found to be thermally stable and could be used in food preparations as natural yellow colourant as well as functional food ingredient.

ACKNOWLEDGEMENT

REFERENCES

Abbas K A; Saleh A M; Mohamed A; Lasekan O. 2009. The relationship between water activity and fish spoilage during cold storage: A review. J. Food Agric. Environ., 7, 86-90.

Anitha A; Mayaa S; Deepaa N; Chennazhia K P; Naira S V; Tamurab H; Jayakumara R. 2011. Efficient water soluble O-carboxymethyl chitosan nanocarrier for the delivery of curcumin to cancer cells. Carbohyd. Polym., 83(2), 452-461.

Chang C; Meikle T G; Su Y; Wang X; Dekiwadia C; Drummond C J; Conn C E; Yang Y. 2019. Encapsulation in egg white protein nanoparticles protects anti-oxidant activity of curcumin. Food Chem., 280, 65-72.

Delfiya A D S; Thangavel K; Natarajan N; Amirtham D. 2016a. Preparation of curcumin-loaded egg albumin noparticles using ethanol as desolvation agent. Asian J. Chem., 28(7), 1536-1544.

Delfiya A D S; Thangavel K; Amirtham D. 2016b. Preparation of curcumin loaded egg albumin nanoparticles using acetone and optimization of desolvation process. Protein J., 35(2), 124-135.

Delfiya Aniesrani D S. 2016c. Encapsulation of curcumin by desolvation and spray drying methods and evaluation of *in vitro* release characteristics and stability of curcumin-loaded egg albumin powder. Unpublished Doctoral Dissertation, Tamil Nadu Agricultural University, Coimbatore, Tamil Nadu.

Elzoghby A O; Samy W M; Elgindy N A. 2012. Albumin-based nanoparticles as potential controlled release drug delivery systems. J. Controlled Release, 157, 168-182.

Fernandes R V D B; Borges S V; Botrel D A; Silva E K; Costa J M G D; Queiroz F. 2013. Microencapsulation of rosemary essential oil: Characterisation of particles. Drying Technol., 31(11), 1245-1254.

Goula A M; Adamopoulos K G. 2005. Stability of lycopene during spray drying of tomato pulp. LWT-Food Sci. Technol., 38, 479-487.

Irache J M; Espuelas S. 2006. Biological and Pharmaceuticals Nanomaterials, Nanotechnologies for the Life Sciences. Wiley-VCH, Weinheim, Germany, 185–218.

Jana S; Manna S; Nayak A K; Sen K K; Basua S K. 2014. Carbopol gel containing chitosan-egg albumin nanoparticles for transdermal aceclofenac delivery. Colloids Surf B Biointerfaces, 114(1), 36-44.

Jithan A V; Madhavi K; Madhavi M; Prabhakar K. 2011. Preparation and characterization of albumin nanoparticles encapsulating curcumin intended for the treatment of breast cancer. Int. J. Pharm. Invest., 1(2), 119-125.

Li J; Chen T; Deng F; Wan J; Tang Y; Yuan P; Zhang L. 2015. Synthesis, characterization, and *in vitro* evaluation of curcumin-loaded albumin nanoparticles surface-functionalized with glycyrrhetinic acid. Int. J. Nanomed., 10, 5475–5487.

Liu W; Zhai Y; Heng X; Che F Y; Chen W; Sun D; Zhai G. 2016. Oral bioavailability of curcumin: problems and advancements. J. Drug Target., 24, 694-702.

Neves M I L; Desobry-Banon S; Perrone I T; Desobry S; Petit J. 2019. Encapsulation of curcumin in milk powders by spray-drying: Physicochemistry, rehydration properties, and stability during storage. Powder Technol., 345, 601-607. DOI: 10.1016/j.powtec.2019.01.049

Ranjan A P; Mukerjee A; Helson A; Vishwanatha J K. 2012. Scale up, optimization and stability analysis of curcumin C3 complex-loaded nanoparticles for cancer

therapy. J. Nanobiotechnol., 10, 38 (2012). https://doi.org/10.1186/1477-3155-10-38

Shailesh T P; Vipul P D; Girishbhai J K; Manish C J. 2010. Preparation and *in-vitro* evaluation of ethyl cellulose coated egg albumin microspheres of diltiazem hydrochloride. J. Young Pharm., 2(1), 27-34.

Shang Y J; Jin X L; Shang X L; Tang J J; Liu G Y; Dai F; Qian Y P; Fan G J; Liu Q; Zhou B. 2010. Antioxidant capacity of curcumin-directed analogues: Structure-activity relationship and influence of microenvironment. Food Chem., 119(4), 1435-1442.

Tanaka K; Kuba Y; Sasaki T; Hiwatashi F; Komatsu A. 2008. Quantitation of curcuminoids in *curcuma* rhizome by near-infrared spectroscopic analysis. J. Agric. Food Chem., 56, 8787-8792.

Wang Y; Lu Z; Lv F; Bie X. 2009. Study of microencapsulation of curcumin pigments by spray drying. Eur. Food Res. Technol., 229(3), 391-396.

Wang Y; Zhang L; Wang P; Xu X; Zhou G. 2020. pH-shifting encapsulation of curcumin in egg white protein isolate for improved dispersity, antioxidant capacity and thermal stability. Food Res. Int., 137, 109366. DOI: 10.1016/j.foodres.2020.109366.

Weber C; Coester C; Kreuter J; Langer K. 2000. Desolvation process and surface characterization of protein nanoparticles. Int. J. Pharm., 194(1), 91–102.

Zheng B; McClements D J. 2020. Formulation of more efficacious curcumin delivery systems using colloid science: enhanced solubility, stability, and bioavailability. Mol., 25, 2791. DOI:10.3390/molecules25122791.
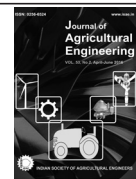
Design and Development of Bamboo Polyhouse as Entrepreneurship Model of Nutri-Garden

Dnyaneshwar Sanap[1], N. G. Shah[2] and S. B. Agnihotri[3]

[1]M. Tech. Student (Technology & Development), Centre for Technology Alternatives for Rural Areas; [2]Professor; [3]Emeritus Fellow Professor, Centre for Technology Alternatives for Rural Areas, IIT Bombay, Powai- 400076. Corresponding authors e-mail address: dnyaneshwar@iitb.ac.in, nshah@iitb.ac.in, sbagnihotri@iitb.ac.in

Article Info	ABSTRACT
        	Agriculture directly connects with nutrition. Despite substantial increase in agriculture productivities, malnutrition prevails. The reason lies in the 'hidden hunger' or micro-nutrient deficiencies, which can be fulfilled by increasing dietary diversity. Various organizations promote kitchen garden / Nutri-Garden to achieve the minimum dietary diversity. The design, structural analysis, construction details, and performance analysis of a bamboo-polyhouse to support a Nutri-garden are reported. ETABS software was used to evaluate stability to withstand wind up to 36 m.s^{-1}. The maximum temperature difference (inside and ambient) of 1.6 ^{o}C was observed in the naturally ventilated polyhouse structure when the top vent was open. Production data of vegetables produced and sold in nearby markets indicated a payback period of 2.41 years. The technical solution developed and demonstrated on farmers' field to obtain year-round production of fresh vegetables for the nutrition of family and revenue after selling marketable surpluses is a solution that awaits further dissemination. The potential of large-scale adoption of bamboo polyhouse for Nutri-gardens as an entrepreneurship route by small farmers can be explored through support from existing government programmes.

Good nutrition is a human right, a basic need, and is fundamental to health and well-being. The well-being of citizens plays an important role in the development of a nation. Dietary diversity is an essential factor that is also an indirect cause of malnutrition through factors like wealth index, socio-economic status, caste, and gender. Data (Anon., 2019) indicated that in India, only 21% of children receive minimum dietary diversity.

Nutrition-Garden is a concept evolved from "kitchen-garden", growing vegetables in the backyard, which will help in increasing the dietary diversity of a household. Analysis for the intervention of the Nutri-Garden project by Suri (2020) shows the increase in average vegetable consumption by 22%, and impacted 62% of households to meet the daily vegetable requirement of 400 g per person. It has also shown a 32% decrease in anaemia after the intervention of Nutri-Garden.

Recent directives of the state and Central Government, along with the activities of NGOs in the Nutri-Garden / Kitchen Garden, the development in Nutri-Gardens can be gainfully tapped to achieve dietary diversity.

There are seven possible pathways showing the link between agriculture and nutrition (Gillespie *et al*., 2012) – such as agriculture as a source of food and income, the link between agricultural policy and food prices, income derived from agriculture, and how it is actually spent, women's socio-economic status and their ability to influence household decision-making, women's ability to manage the care, feeding, and health of young children, and women's own nutritional status. The multivariable regression analysis conclusively pointed towards the small, but positive, association between crop diversity and dietary diversity at the household level for a study area in Maharashtra and

Telangana states in India (Kavitha *et al*., 2016). COVID 19 pandemic affected almost all sectors; Carriappa *et al*. (2021) have shown the impact of COVID 19 on the production, marketing, and consumption pattern of agri-commodities. In addition, the reverse migration and the income shock in rural areas have created a demand for innovative ways of employment avenues at the village level.

Kumar *et al*. (2021) performed a study to analyse the impact of protected cultivation in Uttarakhand. Based on the focused group discussion with 96 protected cultivators and economic analysis, the authors concluded that protected cultivation is profitable. They also mentioned about the possibility of wooden small scale (100 m^2) polyhouse developed by the Vivekananda Parvatiya Krishi Anusandhan Sansthan, Almora, costing ₹71,000. This article also creates an evidence-based on the performance of the bamboo polyhouse as an add-on to Nutri-Garden in the Palghar district of Maharashtra. This protected cultivation technology will help the farmers to grow nutritious vegetables and sell the surplus in a nearby market, which will work as a livelihood option for a household. The installed structures of bamboo polyhouse had shown stability against the wind speed of 36 m.s^{-1} during the evaluation and sustained a Tauktae Cyclone with 114 km.h^{-1} wind speed after construction in May 2021. Existing polyhouses are mostly constructed using steel / GI structures, which has initial cost impediment. The market survey and quotations received indicated an average cost of making a polyhouse in a 100 m^2 area was ₹2,77,000. Therefore, locally available bamboo has been considered as alternative material for construction which helps to reduce initial cost.

Making bamboo-buildings is common in disaster-prone or earthquake-prone areas due to the resilience and lightweight of bamboo material (Baghel and Thakkar, 2017). Handicrafts from bamboo also provide livelihood to some families in rural areas. Based on the bamboo varieties in India, the compressive strength of bamboos varies from 20 Mpa to 30 MPa (National Bamboo Code, 2005a). Bhalla *et al*. (2008) developed a parabolic arch from bamboo, which can be used to develop a roof of an industrial shed or a warehouse for a farmer. This structure was for an area of 250 m^2 with span of 25 m (25 m x 10 m), and height of 5 m. After the analysis, Bhalla *et al*. (2008) found that the structure was stable against the loading combinations of dead load, live load, and wind loads. The wind speed for Delhi (47 m.s^{-1}) developed a design wind pressure of

1.325 kN.m^{-2}, against which the structure was analysed. Korde *et al*. (2014) developed a bamcrete arch by joining two bamboos with an innovative method called HIB (Haritha – IIT Delhi - Bamcrete). This arch was tested under various cyclic loading conditions. Under the increasing cycles of loading, the arch showed linear structural behaviour up to 15 MPa of compressive stress.

Yadav *et al*. (2014) reported an experimental study to check the feasibility of a low-cost bamboo polyhouse (50 m^2) for the nursery and vegetables for India's north cold climatic region. The authors provided the local joinery methods used for the polyhouse. Jadhav and Rosentrater (2017) developed a Bamboo-Polyhouse of 192 m^2 (8 m x 24 m) area for vegetable (tomato) cultivation. Global Warming Potential (GWP) of the Bamboo-Polyhouse was 5 kg of CO_2.m^{-2} of polyhouse, nearly one-fifth of the GWP of GI polyhouse (26.9 kg of CO_2.m^{-2}). This overall literature analysis encourages replacing the steel structure of polyhouse with bamboo members. The life of bamboo can be increased by the process of bamboo treatment, but bamboo joineries integrating with steel nails/screws often leads to bamboo cracks, which needs to be handled with innovative joinery solutions.

The objectives of this work were to design and construct bamboo polyhouse structure on farmers field, and to analyse its performance as an addition to the Nutri-Garden for providing reliable and climate resilient food and income source.

MATERIALS AND METHODS

This study was undertaken at Centre for Technology Alternatives for Rural Areas, IIT, Bombay. BAIF Development NGO provided the field connect to conduct interviews, field visits, and identification of farmers for construction of the polyhouses. The on-field construction was completed with the help of Eastern Star Company's workshop for pre-fab items such as joineries located in Nashik.

Selection of Study Area

Palghar district, being one of the hotspots of malnutrition in Maharashtra state, was selected for this study. Majority of the area in Palghar consists of hilly terrain, forest cover. The area is characterised by water scarcity in non-monsoon months. Majority of the population are tribals, who have poor wealth index.

Problem Identification and Needs Assessment Through Farmers' Survey

To understand the current status in terms of use and performance of Nutri-Gardens, 20 telephonic interviews and field visits to 5 Nutri-Garden sites from 5 villages (Shiroshi, Wanganpada, Chauk, Ramkhind, Pathardi) were conducted. A structured questionnaire enabled to seek inputs from targeted farmers that helped design the structure in terms of area, water requirement for the identified crops, choice of cladding material, and possible markets. Current farming practices, consumption pattern, source of food items, water requirement for household and farming, advantages and constraints of Nutri-Garden, key fruits and vegetables grown in the Nutri-Garden, and allied information were the main components of the structured questionnaire. The minimum meal frequency of 3 times/day was observed in all surveyed villages. The WHO recommends 400 $g.day^{-1}$. $person^{-1}$ consumption of vegetables, but survey indicated 210 $g.day^{-1}$. $person^{-1}$ consumption of vegetables in the diet of an adult of Jawhar block. The maximum consumption of 300 $g.day^{-1}.person^{-1}$ was found for the months of winter, which was still below the recommended level. This was the major motivation to introduce low-cost bamboo polyhouses as a tool for ensuring sustained supply of vegetables to the target population.

The survey clearly indicated that water scarcity in summer and heavy rainfall during monsoon are two major constraints faced in growing vegetables in open-cultivation in Jawhar block of Palghar District, Maharashtra. The third constraint of open-farm cultivation of vegetables was the need of protection from free animals, often on account of the uncontrolled grazing of the cattle in this area.

Design of Bamboo Polyhouse

The bamboo polyhouse was designed using the National Horticulture Board (NHB) guidelines and Indian Standard Codes (BIS 14462, 1997; BIS 14485, 1996; BIS 15912, 2012). The height of the polyhouse at the central ridge was taken as 4.5 m. For orientation of the polyhouse, a length of the polyhouse was placed along the North-South direction to overcome the impact of wind from the west (BIS 14462: 1997, section 5.3). The designed polyhouse had the top vent area of 6.4 m^2, making an angle of $67.97°$ with one of the roof surfaces. The inclination of the roof was designed as per the conditions by BIS 14485:1996, section 8. The stability of the structure was vetted for a wind speed of 36 $m.s^{-1}$ (NHB, 2011). Since the area of the polyhouse was less than 250 m^2, it was designed using a single span (NHB, 2011). Foundations of the polyhouse were 600 mm deep as per the BIS 14462, 1997, section 6. The bottom apron of 1 m in height helped in retaining CO_2 inside the polyhouse, which complied with the NHB norm. An insect-proof net of 40 mesh size was used as side shading material (NHB, 2011). The polyfilm used for top shading material was of 200-micron thickness, UV stabilized, and 200 GSM, which was selected based on the guidelines of NHB (2011). The same design considerations were followed for both polyhouses (Polyhouse 1 in Jawhar block, Polyhouse 2 in Vikramgad block).

Sizing of polyhouse

Considering the land availability of the tribal farmers from Palghar district, along with constraint of getting more flat land in the hilly region, the polyhouse of 128 m^2 (16 m x 8 m) area in a single span was designed with optimal resource utilization. The bay size of 4 m x4m was considered to reduce the effect of bending of the bamboo members (beams). Depending on the bay size, the length (16 m) and breadth (8 m) were selected for low-cost model of bamboo polyhouse. The available polyfilm, insect-proof net and G-Fab sheet dimensions were considered to define the exact dimensions of length, breadth, and height to reduce the wastage of materials. Figure 1 shows the sectional views of the bamboo polyhouse. The door of the polyhouse was sized (2.13 m x 1 m) based on the requirements of the farmer.

Selection of bamboo

Treated bamboos of _Pseudoxytenanthera Madhavi (local name – Mes)_ variety were used to construct the polyhouse. Treatment of the bamboos was done using CCB solution (copper sulphate, sodium dichromate, boric acid in ratio of 1.5:3:4) (BIS 15912:2018). The treatment was done using Vacuum Pressure Impregnation technique. Treated bamboo provides safety from termite and stem borer attack, thus ensuring longer life than normal (untreated) bamboo. Figure 2 shows the difference between the treated bamboo and the normal bamboo after three years of use.

Mechanical properties of bamboo and measuring instruments

Table 1 indicates the properties used for _Pseudoxytenanthera Madhavi,_ which were used for analysing the structure in ETABS software against dead
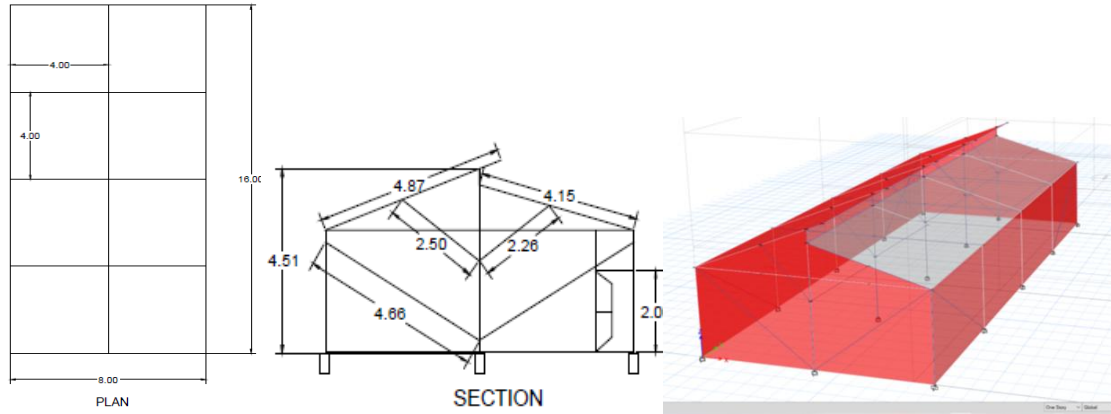
Fig. 1: Bamboo polyhouse CAD model with sectional plan and isometric view

Fig. 2: Difference between 1) non-treated bamboo, 2) treated bamboo, and 3) treated bamboo with polish

and wind loading conditions. Analysis of environmental conditions was carried out for the inside as well as at immediate outside the polyhouse by collecting the temperature and wind speed data using Vane type digital anemometer (Range: 0.4 – 30 m.s^{-1}, resolution: 0.1, accuracy: ($\pm$) 2%) for wind speed after the construction of the polyhouse sites. Temperatures and humidity were monitored using HTC-1 thermometer (Range: (-) 50 - 70 ^{o}C, accuracy: $\pm$1 ^{o}C) and hygrometer (Range: 10- 99% RH, accuracy: $\pm$5%).

Structural analysis

A 3D model of bamboo polyhouse was created in the ETABS software (version 17) for validating the design. To analyse the structure against the wind load and dead load in ETABS, the method of shell-wise (surface where the load is applied) loading case was used. Weight of the roofing material and self-weight of the bamboos were considered for the dead load calculations.

Total dead load by self weight of bamboos= 0.024 kN.m^{-2}

Table 1. Properties of bamboo assigned in ETABS

Sl. No.	Property	Reference	Assigned value
1.	Density	(IS 15912: 2018)	728 kg.m^{-3}
2.	Modulus of elasticity	(IS 15912: 2018)	15 GPa
3.	Minimum yield stress	(IS 15912: 2018)	60 MPa
4.	Minimum tensile strength	(Kurhekar *et al.*, (2015))	48.5 MPa
5.	Maximum compressive strength	(IS 15912, 2018)	69.1 MPa
	Sectional Properties		
6.	Cross-sectional details		Outer dia – 55 mm Inner dia – 25 mm

Polyfilm (roof) contributed 0.002 kN.m^{-2} of dead load

Total dead load = 0.024 kN.m^{-2}

Wind load calculations were performed using the BIS 875, Part 3, 2015. The structure was simulated against wind speeds up to V = 36 m.s^{-1}.

Design wind speed is expressed as:

$$Vz = k_1 * k_2 * k_3 * k_4 * V \qquad \dots (1)$$

Where,

K_1 = Risk coefficient, 0.91 for farm buildings other than residential (Fig. 1, BIS 875, Part 3, 2015),

K_2 = Multiplication factor based on the terrain category [height of surrounding elements like trees and other structures], (Table 2, BIS 875, Part 3, 2015) = 1,

K_3 = Topography factor [slope of land less than 3^0 (section 6.3.3, BIS 875, Part 3, 2015)] = 1, and

K_4 = Importance factor [both sites more than 65 km away from the coastal area (section 6.3.4, BIS 875, Part 3, 2015)] = 1.

Design wind pressure with multiplication factors is expressed as -

$$P_d = K_d * K_a * K_c * P_z \qquad \dots (2)$$

Where,

P_d = Design wind pressure, 701.24 N. m^{-2} ,
K_d = Directionality factor,
K_c = Pressure combination factor, and
K_a = Area average factor.

P_d = 701.24 N. m^{-2} when P_z (wind pressure at height z) = 0.6 * V_z^2

To calculate the effective wind load on a surface,

$$F = C_p * P_d * Area \qquad \dots (3)$$

$$C_p = (C_{pe} - C_{pi}) \qquad \dots (4)$$

Where,

Cp = Difference between external and internal pressure coefficients,

C_{pe} = External pressure coefficient (calculated using Table 5 of IS 875, part 3),

C_{pi} = Internal Pressure Coefficient, and

Area = Surface area of the respective walls / inclined roofs

The internal pressure coefficient (C_{pi}) depends on the percentage of open area of the wall surface. The percentage openings for the insect-proof net were 13.17 % (between 5% and 20%). Therefore, C_{pi} for the insect-proof net was considered as 0.5. After deciding the values of C_{pi} and C_{pe}, the value of C_p for different cases were calculated based on wind direction (along the ridge, across the ridge), and nature of internal pressure coefficient (positive or negative value of C_{pi}).

After calculations of the C_p values, the shell-wise loading was assigned in the ETABS software for the following 4 cases: (a) Positive C_{pi} and wind along the ridge, (b) Positive C_{pi} and wind across the ridge, (c) Negative Cpi and wind along the ridge, and (d) Negative C_{pi} and wind across the ridge.

Construction details of pilot bamboo polyhouse

The impact of the surroundings (presence of trees & buildings) and elevation of the site for drainage of irrigation water was considered for the site selection. Foundations for the polyhouse (design shown in Fig. 3)

Table 2. Performance of structural members of bamboo polyhouse using ETABS simulation

Sl. No.	Wind speed, m.s^{-1}	Simulation results
1	20	Stress in all members less than 50% of allowable stress
2	25	4 members shown stress > 50% and less than 70% of allowable stress
3	30	4 members reached stress above 70% of allowable limit and 2 members stressed above 50 % of allowable limit
4	36	1 member critically loaded up to 100% of allowable stress, 2 members loaded above 90% of allowable stress, 1 member loaded above 70% of allowable stress, 3 members loaded with more than 50% of allowable stress

were pre-casted in the workshop, and they were fixed inside the pits of 0.46 m x 0.46 m made by the farmer. Preconstruction machining of bamboos was done in the workshop. On-site construction activities as erection of bamboo frames, purlins, and other members were done in-situ. Bamboo members were joined by using metal clamps, metal strips, and metal fixtures. The bamboos (Purlins) were joined along the length using inserts, side plates, and sleeve type joints (IS 15912:2018). The polyfilm and insect-proof nets were fixed using the zig-zag springs and metal profile strips. The constructed bamboo polyhouse is shown in Fig. 4.

Gravity-based drip irrigation system was integrated by considering the daily water requirement. This drip system consisted of a main, lateral, inline drippers (discharge 4 $l.h^{-1}$), a water filter, micro sprinklers, and a water tank at elevation of 1 m from the ground level and located near the polyhouse. Crop water requirements were calculated using the water requirements for tomato and capsicum. The maximum daily water requirement for tomatoes considered was 4.58 $mm.day^{-1}$ (Sharma *et al*., 2015), and for 6.25 $mm.day^{-1}$ for capsicum (Dimple *et al*., 2017). Considering the maximum daily water requirement for capsicum as 6.25 $mm.day^{-1}$, or 800 $l/128$ m^2/day, a tank of 1000 litre capacity was used.
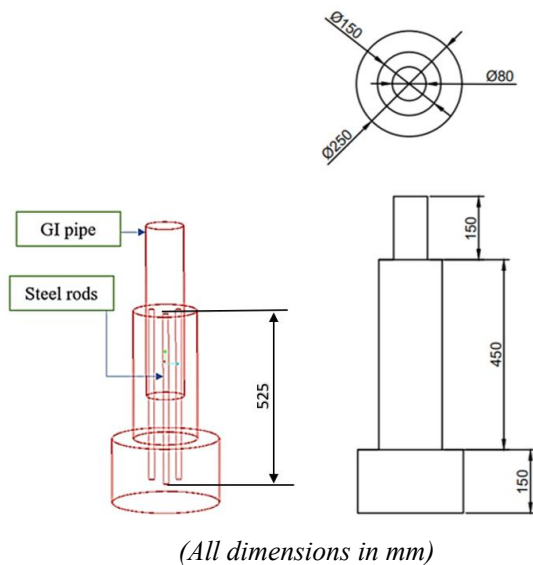
Cultivation in Polyhouse

After installation of two bamboo polyhouses in the Palghar district, a variety of vegetables were cultivated in them. To have the connect with Nutri-Garden, the cropping plan was selected in a way to maximize the variety of the vegetables for improving the dietary diversity. Out of 128 m^2 polyhouse area, the cultivable area was 63 m^2. Sterameal (100 kg), neem powder (50 kg), cocopeat (50 kg), and compost (50 kg) was mixed and used with soil for making the beds. Sowing / transplanting in the bamboo polyhouse was done in the first week of March, 2021 in a zig zag manner on each bed. Capsicum, chili, radish, spinach, fenugreek, French-beans, tomato, and brinjal were cultivated on 20 beds in each polyhouse. These beds were made with 200-250 mm in height, 450 mm in width, and 7 m in length with gap of 300 mm between two beds. Tomato and brinjal were transplanted a month after other vegetables due to lag in getting the saplings. The seeds of French beans, radish, carrot, spinach, and fenugreek were received from TIDE-India NGO.

(All dimensions in mm)

Fig. 3: CAD drawing of pre-casted foundation

Fig. 4 (a): Bamboo polyhouse installed at Ramkhind village (Polyhouse 1)

Fig. 4 (b): Bamboo polyhouse installed at Balapur village (Polyhouse 2)

Design and Development of Bamboo Polyhouse as Entrepreneurship Model of Nutri-Garden

Farmers were trained to make fertilizers like Jivamrut (liquid & solid) and bio-organic fertilizers by BAIF agriculture experts. The fertigation of organic manure through drip was practiced by the 2nd polyhouse owner. The 1st polyhouse owner with the red loose-sandy soil irrigated the land twice a day in the morning and evening, while the 2nd polyhouse had a black-peat soil which was irrigated once in a day, or only if required. The farmers were also informed to control the excess irrigation by monitoring the soil.

RESULTS AND DISCUSSION

Structural Analysis of Bamboo Polyhouse

The simulation for 128 m² bamboo-polyhouse against the wind load and dead load conditions in ETABS software showed the stability of structure against a wind velocity of 36 m.s⁻¹. Bamboo was not a pre-defined material in ETABS; therefore, the properties of bamboo were applied to newly defined material, as given in Table 1. The shell/surfaces of the polyhouse were assigned with the properties of HDPE, which is a material used to make polyfilm. The stress developed in the bamboos on account of wind and dead load was in the range of 0.69 MPa to 68.47 MPa. The results of the analysis provide stresses developed in the bamboo members as shown in Fig. 5, where the members of the bamboo polyhouse are shown in different colours enabling interpretation of the permissible stress levels using the colour codes. For example, the red-coloured members of the polyhouse structure in Fig. 5 had reached maximum allowable stress when wind speed

is 36 m.s⁻¹. At this wind speed, two members showed induced stress above 90% of the allowable stress (shown in purple colour). All the other members showed the induced stress below 90% of the allowable stress. In this way, the structure was simulated for different wind speeds, and the results are mentioned in Table 2. This analysis enabled the choice of bamboo diameter based on the prevalence of wind speeds in the region where the bamboo polyhouse is to be constructed.

Based on the values given in Table 2 and Fig. 5, the structure was found to be safe for a wind speed of 36 m.s⁻¹. Table 1 provides the allowable stress limits for the bamboo members. Based on the available bamboo diameters of "Mes variety" and results of the structural analysis, the diameter of 55±3 mm for columns was selected with minimum thickness of 15 mm, and rest of the members were selected with the diameter of 49 ±3 mm and minimum thickness of 12 mm.

Variations in Micro-climatic Conditions inside Polyhouse

Out of the two bamboo polyhouses, one was constructed with a top vent closed by an insect-proof net (Polyhouse 1), and the other was constructed with a top vent completely open (Polyhouse 2). The purpose of keeping the top vent open and closed with insect proof net was to check the temperature reduction difference. Observations for temperature data were taken during 10 AM to 4 PM on 10th March 2021 for one site and on 11th March 2021 for the second site. Maximum temperature difference of 2.8 °C was observed in Polyhouse 1 at
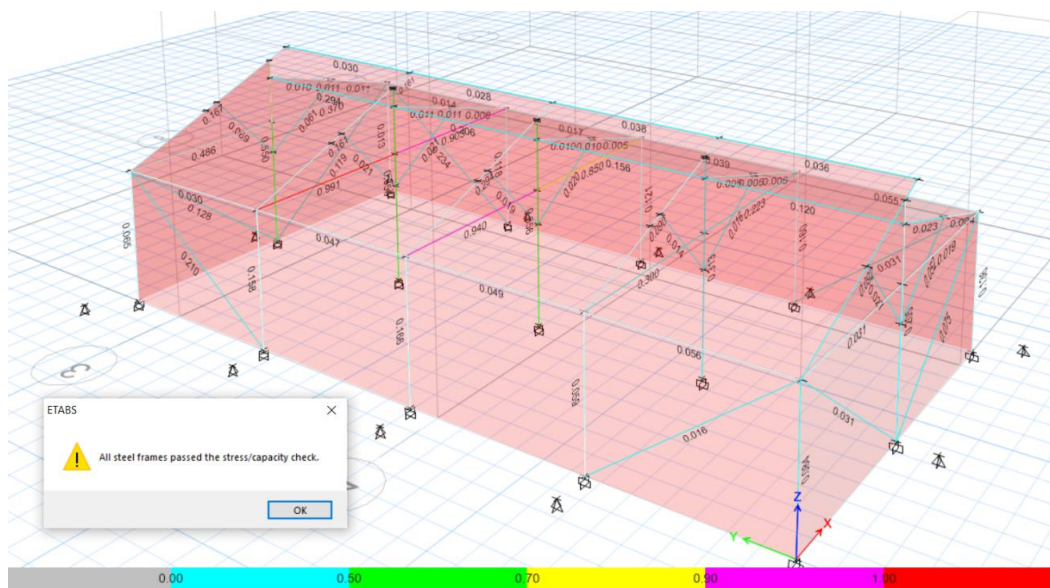

Fig. 5: ETAB simulation results for wind speed of 36 m.s⁻¹

11:51 AM and 1.6 °C for polyhouse 2 at 1:54 PM. The maximum temperature inside the Polyhouse 1 was 40.1 °C (when the ambient temperature was 38.6 °C), while it was 39.8 °C in Polyhouse 2 (when the ambient temperature was 38.6 °C). Both locations of the polyhouses fall under the same climatic region of west coast plains and hills. Since the CO_2 retaining section height was 1 m, the anemometer was placed at 1.5 m height and 2 feet (0.61 m) away from the wall. Maximum incoming wind speed just outside the polyhouse was 1.5 m.s^{-1}, and the incoming wind speed just inside the polyhouse ranged between 0.7 m.s^{-1} and 0.9 m.s^{-1}. The wind-flow from inside to outside the polyhouse through the insect-proof net was at 0.5 m.s^{-1}. The effect of an opened and closed top vent was visible on the walls of the respective polyhouses. For example, the insect-proof net got bulged when the top-vent was closed (Polyhouse 1), which indicated the higher internal pressure on the walls of other side on inlet. Polyhouse 2 also showed the maximum wind speed just inside the polyhouse as 0.8 m.s^{-1}, but the corresponding maximum inlet wind speed just outside the polyhouse was 1.2 m.s^{-1} when the top vent was open. However, the closing/opening of the top-vent is often determined based on the 'insect-proofness' of the polyhouse.

Economics of Bamboo-polyhouse

Table 3 describes the fixed and variable costs involved in constructing the bamboo polyhouse, including the cost of the drip irrigation system. The total cost for construction of the bamboo polyhouse (size: 128 m^2), including installation of the drip, was ₹ 90,165. The variable cost includes the seed and sapling cost, manure and soil preparation cost, and other miscellaneous costs. Thus, the total initial investment of ₹ 99,015 is needed for the construction of bamboo polyhouse and to begin cultivation. The prevailing cost (in year 2021) of a GI/Steel polyhouse of 96 m^2 area was ₹ 2,77,000 (market survey basis), which was almost three times the cost of bamboo polyhouse. Annualised life cycle cost (ALCC) basis of cost comparison of the 2 types of polyhouses was used. Table 4 compares the total costs, ALCC, per m^2 cost, structural life, and risk factors involved. For calculating the ALCC, a discount rate of 12% and an inflation rate of 7% was assumed. Based on the primary market survey in the study area, the life of polyfilm, geomembrane fabric apron, and drip lines was considered as four years. The life of springs and bamboos was considered as five years, and the life of foundations was considered as ten years.

Comparison of the ALCC of treated bamboo polyhouse (₹18,460 for minimum 5 years life) with GI/Steel

Table 3. Itemized costs in construction of bamboo polyhouse

Type of cost	Details	Cost, ₹
Fixed cost [1]	Treated bamboos with transportation (110 Bamboo Poles) at rate of ₹14.5 / feet	30,348
	Polyhouse materials (including shade net, polyfilm, fixtures)	35,000
	Labour for construction (4 workers)	7,500
	Erection labour charges (4 workers)	5,000
	Transportation of materials to site (Nashik to Palghar – overall 200 km)	5,000
	Drip irrigation system (5000 tank +2182 drip+135 sprinklers)	7,317
TOTAL (1)		₹ 90,165
Variable cost (2)	Seed + saplings	2000
	Manure	3850
	Maintenance	1000
	Miscellaneous	2000
TOTAL (2)		8850 ₹. yr^{-1}
Total initial investment cost for 1st year (1)+(2)		₹ 99,015

Table 4. Comparison of polyhouse with treated bamboos and non-treated bamboo polyhouse, and GI polyhouse

Item	Treated bamboo polyhouse	Untreated bamboo polyhouse	GI/ steel polyhouse
Cost, ₹.m^{-2}	735.93	585.93	2770
Life of structure, year	5-10	5	20
Life of poly film and shade net, year	4-5	4-5	4-5
Annualised LCC, ₹	15,382* 18,460 Rs$^{\#}$	13,837	28,927
Risk level	Less risk of getting affected by termite, stem borer, and fungus	More risk of getting affected by termite, stem borer, and fungus	No risk from insect-like stem borer

indicates the ALCC when the life of bamboo is considered as 10 years, LCC – life cycle cost
 # indicates the ALCC when the life of bamboo is considered as 5 year

polyhouse (₹28,927 for 20 years life) showed that bamboo polyhouse is more economical than the GI/ Steel polyhouse (details in table 4). Due to the risk of termite and borer attack, the minimum ALCC (₹13,837) compared to others for a non-treated bamboo polyhouse is not substantial (Table 4).

Vegetable Cultivation from Bamboo Polyhouse

Based on the records maintained by the farmers and field visits to the polyhouse sites, the performance of the polyhouse was analysed based on vegetable production. The quantity of produce was recorded by the farmers for each vegetable. The quantity of production, area under each vegetable, their productivities in polyhouse, and in open cultivation are mentioned in Table 5. The data for open field productivity for the Palghar region was received from the BAIF agricultural experts in Jawhar block of the district. The productivity of the bamboo polyhouse was compared with 3-year (2018, 2019, 2020) average All India productivities (Anon., 2021) of the vegetables (Table 5).

Productivity of capsicum in polyhouse was found to be 2.3 times higher than the open field productivity, and 5.6 times higher than the 3-year All India average. Similarly, the productivity of other vegetables also showed higher productivity than the national average. For tomato and brinjal, constraint of pollination in

Table 5. Crop attributes considered for economic calculations for polyhouse cultivation

Sl. No.	Crop / vegetable	Area under cultivation in polyhouse 1 & polyhouse 2, m^2	Production from Polyhouse 1 & Polyhouse 2, kg	Productivity for Polyhouse 1 & Polyhouse 2, kg. m^{-2}	Average productivity, kg. m^{-2}	Open field productivity of the vegetables*, kg. m^{-2}	All India average productivity at (2018, 2019, 2020)#, kg. m^{-2}	Market rate, ₹. kg^{-1}
1.	Capsicum	9.45	70 & 87	7.41 & 9.21	8.31	3.5	1.45	60.00
2.	Chili	9.45	30 & 35	3.17 & 3.7	3.44	2.2	1.09	50.00
3.	Radish	6.3	17 & 20	2.7 & 3.2	2.95	1.75	1.54	20.00
4.	Spinach	6.3	13 & 10	2.1 & 1.6	1.85	0.85	NA	30.00
5.	Fenugreek	6.3	9 & 11	1.43 & 1.75	1.59	0.9	NA	25.00
6.	French Beans	9.45	28 & 31	2.96 & 3.3	3.13	2.1	1.00	30.00
7.	Tomato	9.45	32 & 35	3.4 & 3.7	3.55	5	2.52	20.00
8.	Brinjal	9.45	26 & 25	2.75 & 2.65	2.7	3.5	1.72	20.00

Indicates the values of productivity based on the opinions of farmers and agricultural experts in the area.
 # Indicates the average productivity at India level data (Ministry of Agriculture and Farmers Welfare, 2021)

polyhouse was observed, and accordingly the farmers were trained for doing manual pollination. Pollination may be a reason for lower productivity of tomato (3.55 kg.m^{-2}) and brinjal (2.7 kg.m^{-2}) crops.

Farmers were able to gain profit of ₹5,000 (Polyhouse 1) and ₹6,000 (Polyhouse 2) after selling the surplus in the local market after 1st cycle of cultivation inside the polyhouse (within first five months). After the first cycle of crops, the farmer of polyhouse 2 cultivated saplings for Jasmine (*Mogra*) flower. He observed higher quality of sapling production in the polyhouse, which was better in terms of quality of leaves, colour of leaves, quantity produced, and growth rate with expected profit of ₹30,000 through sale of 3,500 saplings. Farmers had experienced a problem to sell the surplus at nearby city due to the lockdown during the 2nd wave of COVID 19 pandemic.

Higher yield of French beans was not profitable due to the unfamiliarity of the local people in its consumption. Most of the production from polyhouse went under self-consumption and sharing with others. To understand the actual value of the produce, the average of market rates from Jawhar (near polyhouse 1) and Vikramgad (near polyhouse 2) block market places was considered.

After calculating the profit of each vegetable, total profit of ₹6,065 and ₹6,495 would have been generated through the same cropping plan and same productivity in Polyhouse 1 and Polyhouse 2, respectively. Based on the average productivities of Polyhouse 1 and Polyhouse 2 and market rates, capsicum (8.31 kg.m^{-2} and 60 ₹.kg^{-1}), chili (3.44 kg.m^{-2} and 50 ₹.kg^{-1}), and French beans (3.13 kg.m^{-2} and 30 ₹.kg^{-1}) were found to be best three crop choices. This polyhouse crop plan

can be expected to ensure production diversity and security throughout the year, although they may not be the optimal crop plan to gain profit from the polyhouse.

Considering a scenario of crop planning where farmer intends to achieve a maximum profit, a cropping of capsicum for 8 months (one cycle), and then one cycle of French beans (for next three to four months) may be recommended. Calculated annual income for this plan is ₹41,050 / year. Considering initial investment of ₹99,050 and subsequent annual cost of manure, maintenance, and saplings as ₹5,850; a simple payback period (SPP) of 2.41 years was estimated. The respective Benefit-Cost ratio (B/C ratio) and Internal Rate of Return (IRR) were computed as 1.27 and 30.5%, respectively. If a farmer gets a subsidy of 50% on the cost of polyhouse, the B/C ratio increases to 2.06, payback period reduces to 1.3 years with increased IRR to 73.5 per cent. All three parameters (SPP, IRR, B/C ratio) positively indicated for subsistence farming through polyhouse cultivation.

Possible Design Suggestions

Construction of the designed bamboo polyhouse revealed that more joints on a single bamboo member need extra machining on bamboo, which may not be technically sound as it may provide sites for crack propagation in bamboo members and making it structurally weak. Therefore, a double bamboo column can be integrated as shown in Fig. 6 (b).

Simulating the existing and the improved structure in ETABS software against dead load and wind load, it was found that the structure with the suggested design performed better than the currently constructed bamboo polyhouse structure. The measure of design
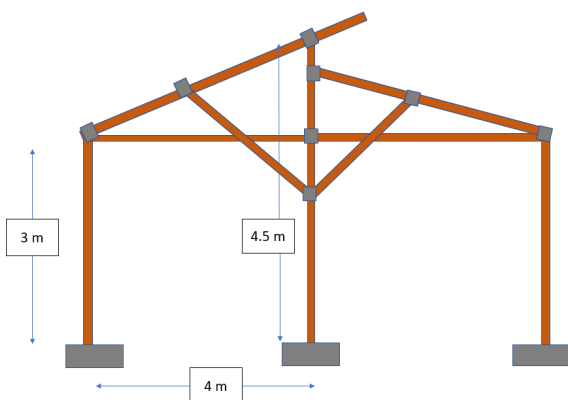

Fig. 6(a): Sectional view of existing bamboo polyhouse structure
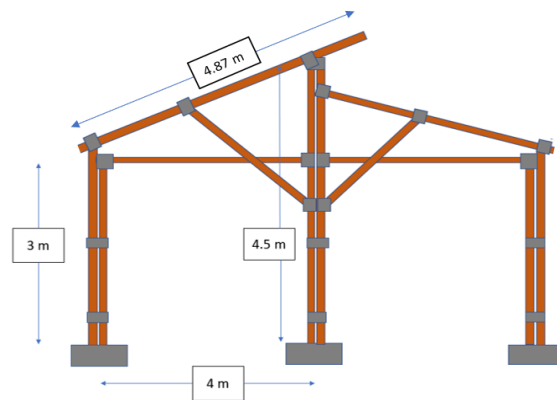

Fig. 6(b): Sectional view of modified bamboo polyhouse structure

improvement is the stress developed in the members, which is again classified based on the stress developed in terms of percentage of allowable stress. In the suggested design improvement, none of the structure member exceeded the stress above 50% of the allowable stress limit. The constructed structure had three members reaching stress more than the 90% of the permissible stress limit.

CONCLUSIONS

Two bamboo polyhouses of 128 m^2 area were designed and installed at Jawhar (Polyhouse 1) and Vikramgad (Polyhouse 2) blocks, Palghar district, Maharashtra. The structure of the bamboo polyhouse was found to be safe against the wind velocity of 36 m.s^{-1}. With the top vent space of the polyhouse completely open, the maximum temperature difference between inside and outside the polyhouse was 1.6 $^{\circ}$C, while when the top vent was closed with insect-proof net, temperature difference was 2.8 ^{0}C. Techno-economic analysis of the bamboo polyhouse indicated the lower investment cost (₹90,165) as compared with conventional polyhouse, and acceptable B/C ratio (1.27). The ALCC (₹18,460) of the treated bamboo polyhouse shows its appropriateness for small-scale farmers to grow diverse vegetables as capsicum, chili, leafy vegetables, tomato, brinjal, etc. A simple payback period of 2.41 years along with an IRR of 30.5% suggest a fast recovery on investment. Government subsidy of 50% can reduce the payback period to 1.3 years with higher B/C ratio (2.06).

Bamboo polyhouse may be a low-cost alternative for GI polyhouse, and can offer sustainable livelihood and nutrition source for rural households.

ACKNOWLEDGEMENT

REFERENCES

Anon. 2019. Infant and Young child feeding and diets. Comprehensive National Nutrition Survey (CNNS) National Report. Ministry of Health and Family Welfare, Government of India, UNICEF and Population Council, New Delhi, 59-70.

Anon. 2021. Area, Production, and yield of Horticulture and Production Crops. Agricultural Statistics ant Glance 2020. Directorate of Economics and Statistics, Dept. of Agriculture Cooperation and Farmers Welfare, Ministry of Agriculture and Farmers Welfare, Government of India, 116-120.

Baghel A; Thakkar A. 2017. Bamboo: A resilient material for mass housing in earthquake prone zones of Gujarat. In: Proc. Sustainable Built Environment, IIT Roorkee, 1-19.

Bhalla S; Gupta S; Sudhakar P; Suresh R. 2008. Bamboo as a green alternative for concrete and steel for modern structures. J. Environ. Res. Develop., 3 (2), 362-370.

BIS. 1997. Recommendations for layout, design, and construction of Greenhouse structures. IS: 14462 – 1997, Bureau of Indian Standards, New Delhi.

BIS. 2015. Design Loads (Other than Earthquake) for Buildings and Structures – Code of Practice. IS:875 (Part 3) – 2015, Bureau of Indian Standards, New Delhi.

BIS. 2018. Structural Design Using Bamboo — Code of Practice. IS:15912– 2018, Bureau of Indian Standards, New Delhi.

Cariappa A G; Acharya K K; Adhav C A; Sendhil R; Ramasundaram P. 2021. Impact of COVID-19 on the Indian agricultural system: A 10-point strategy for post-pandemic recovery. Outlook Agric., 50(1), 26-33.

Dimple; Bhakar S R; Lakhawat S S; Mahesh K. 2017. Determination of crop water requirement of drip irrigated capsicum crop inside naturally ventilated polyhouse. Eng. Technol. India, 6(1), 19-27.

Gillespie S; Harris J; Kadiyala S. 2012. The Agriculture-Nutrition Disconnect in India. Int. Food Policy Res. Inst., Discussion Paper: 01187, 6-15.

Jadhav H T; Rosentrater K A. 2017. Economic and environmental impact analysis of vegetable production in bamboo polyhouse vs galvanized iron pipe polyhouse. ASABE Annual Int. Meeting Washington USA, Paper No. 1701181, 1-7.

Kavitha K; Soumitra P; Padmaja R. 2016. Understanding the linkages between crop diversity and

household dietary diversity in the semi-arid regions of India. Agric. Econ. Res. Rev., 29, 129-137.

Korde C; West R; Gupta A; Puttagunta S. 2014. Laterally restrained bamboo concrete composite arch under uniformly distributed loading. J. Struct. Eng., 4(5), 1- 11.

Kumar P; Kar A; Singh D R; Perumal A; Shivamurthy S G C; Reddy K V; Badal P S; Kamble A L; Kamalvanshi V; Jha G K; Nain M S; Pachiyappan P; Alataway A; Dewidar A; Elansari H O. 2021. Protected cultivation of horticultural crops in Uttarakhand: An economic analysis. Agron., 11 (692), 1-24.

Kurhekar S P; Jain S K; Chavan P P. 2015. Development and testing of bamboo mat boards. Int. J. Agric. Eng., 8(2), 261-264.

National Horticulture Board. 2011. Technical Standards for Naturally Ventilated, Fan and Pad Green House and Shade Net House. Dept. of Agriculture and Cooperation, Ministry of Agriculture, Haryana, No. NHB-PH-Type 02-2011, 1-31.

Sharma P; Kothari M; lakhawat S S. 2015. Water requirement on drip-irrigated tomatoes grown under shade net house. Eng. Technol. India, 6(1), 12-18.

Suri S. 2020. Nutrition gardens: A sustainable model for food security and diversity. ORF Issue Brief, 369, 1-20.

Yadav K; Kalia P; Choudhary H; Zakir H; Brihama D. 2014. Low-cost polyhouse technologies for higher income and nutritional security. Int. J. Agric. Food Sci. Technol., 5(3), 191-196.
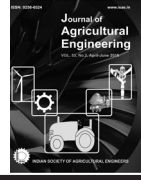
Effect of Drying Parameters on Drying Characteristics and Forskolin Content of Rotary Dried Coleus

V. Chandrasekar[1]*, V. Eyarkai Nambi[2] and S. Shahir[3]

[1]Associate Professor, Department of Food Product Development, National Institute of Food Technology, Entrepreneurship and Management – Thanjavur; [2]Associate Professor, Department of Academics and Human Resource Development, National Institute of Food Technology, Entrepreneurship and Management – Thanjavur; [3]Associate Professor, Department of Agricultural Engineering, Kalasalingam Academy of Research and Education, Virudhunagar, India. *Corresponding author email address: vchandrasekar@iifpt.edu.in,

Article Info	ABSTRACT
  	Coleus *(Coleus forskohli),* a medicinal crop, contains a bioactive component forskolin, which is extracted and used in several ayurvedic medicines in India. Drying is the primary operation to extract forskolin. In this the study, Coleus was dried in a rotary drier by varying slice thickness (2.5, 5.0, 7.5 mm), drying air temperature (45, 55, 65 °C), and feed volume (50, 60, 70 percent); and the forskolin contents were assessed. The moisture content reduced to 16.55% (d.b.) from 464.97% (d.b.) after rotary drying. The drying time ranged from 300 min to 450 min. The effective moisture diffusivity and activation energy ranged from 1.02×10^{-7} mm^2.s^{-1} to 1.33×10^{-6} mm^2.s^{-1} and 5.39 kJ.mol^{-1} to 15.57 kJ.mol^{-1}, respectively. Forskolin content in dried root varied from 0.14% to 1.87 per cent. High forskolin content was found in 2.5 mm thick slice dried at 55 °C and 70% feed volume. Analysis of variance showed that forskolin content in dried Coleus root was significantly ($p<0.0001$) affected by slice thickness and drying air temperature than feed volume ($p<0.01$).

Coleus *(Coleus forskohli)* is a short duration medicinal plant belonging to the Labiatae family. It contains an active principal component called forskolin. Forskolin is a di-terpenoid compound used in several ayurvedic and traditional medicines in India. It activates adenylate cyclase and executes the critical hormonal processes (Seamon *et al.*, 1981). Forskolin stimulates and increase cyclic Adenosine-Mono-Phosphate (AMP) levels to produce protein kinase and activate hormone-sensitive lipase, which can break down the triglycerides of fatty tissue (Allen *et al.*, 1986). Forskolin is used for maintaining lean body mass and aiding weight loss (Badmaev *et al.*, 2002). The presence of forskolin in the coleus roots give commercial importance to the crop is a seasonal, crop and its roots contain more than 80% (w.b.) water; hence spoilage starts immediately after harvest. After harvesting, storing without drying makes the roots unsuitable for forskolin extraction. Therefore, the roots must be dried immediately after harvesting, stored, and used for further extraction of forskolin.

In current practice, harvested coleus roots are cleaned and open sun-dried on the floor. Harvested coleus roots were cleaned and open sun-dried on floor. After sun drying, the roots are pulverized, and the pulverized roots are used for extraction. The drawback of sun drying is, the roots become hard mass (like dried wood); thus, it generates heat at the time of powdering, and leads to a loss in forskolin content. Like other biochemical constituents, the forskolin is affected by temperature and other parameters during the drying of coleus roots. Moreover, sun drying requires more space and time, and incurs more operational costs with less profit. Rotary drier is a drier that rotates continuously and mixes the feed materials by flights and baffles attached inside the rotary drier. Thus, it increases the heat transfer rate and reduces the degradation of heat sensitive materials. Drying time in the rotary drier is lesser and thermal

efficiency is higher than the sun drying or tray drier (Mujumdar, 2004). Hence, a study was conducted to examine the effects of drying parameters on drying characteristics and forskolin content of dry coleus roots dried in a rotary dryer.

MATERIALS AND METHODS

Material

Freshly harvested roots of coleus (Fig. 1a) were obtained from the farmer's holdings at Manjini, Attur *Salem*, Tamil Nadu, India. *C. forskohlii* grows in red sandy loam soils. The crop is harvested five months after planting. The mean diameter of coleus roots calculated by arithmetic and geometric means ranged from 13.43 mm to 11.06 mm, and 13.16 mm to 10.70 mm for the change in the moisture content from 466.62% to 21.52% (d.b.), respectively.

Coleus roots were sliced in to 2.5, 5.0-, and 7.5-mm thicknesses (Fig.1b) for the experiment.

All chemicals used in this study for analysis were purchased from Hi Media, Mumbai.

Moisture determination

The moisture content of fresh and dried *Coleus forskohli* roots were determined by hot air oven method at 105°C for one hour, as prescribed by the AOAC (Horwitz and Latimer, 2005), and recorded on dry basis (d.b.).

Rotary Dryer

A rotary dryer developed at Tamil Nadu Agricultural University, Coimbatore, India, for drying of red chili (Kaleemullah and Kailappan, 2005) was modified and used for drying coleus (Fig. 2). The size of the drum and the flights were modified. The diameter and length of the drying chamber were 150 mm and 300 mm, respectively, to hold 7.5 kg (70% of drier volume) freshly sliced coleus roots with 464.97% (d.b.) moisture content. The dryer consisted of a cylindrical drying chamber, a motor-blower assembly, a heating chamber, a temperature controller-cum-indicator, a

Fig. 1: Coleus root: (a) Whole, (b) Sliced, (c) Dried in rotary drier
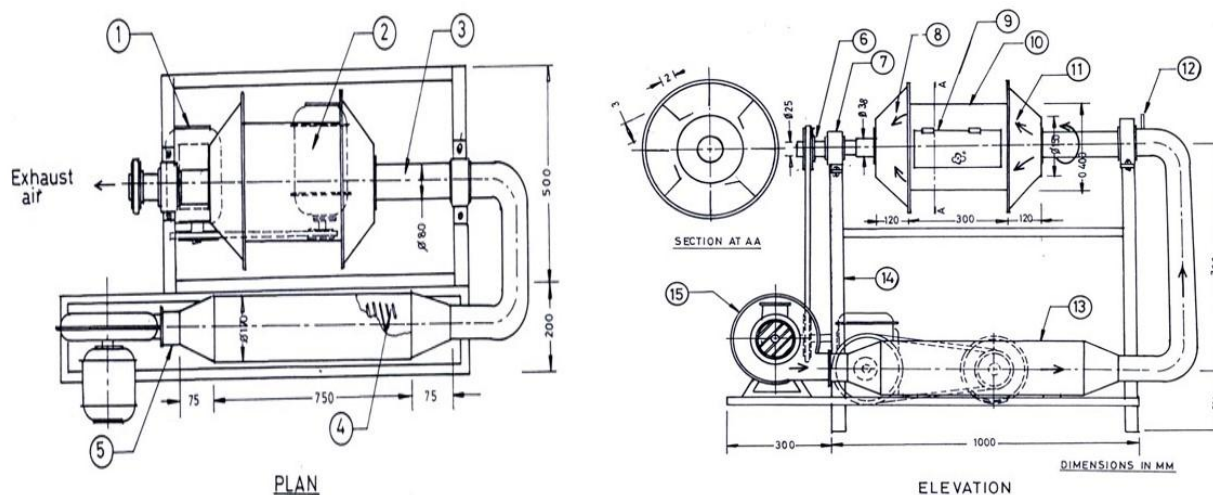
Reduction gear box; 2. Motor; 3. Hollow shaft; 4. Heating coil; 5. Insulation; 6. Exhaust pipe; 7. Bearing; 8. Exhaust chamber; 9. Drying chamber; 10. Rotary drum; 11. Plenum chamber; 12. Thermocouple; 13. Heating chamber; 14. Main frame; 15. Blower; 16. Flights; 17. Baffles

Fig. 2: Schematic diagram of rotary drier

plenum chamber, flights, and a reduction gearbox unit. A blower (capacity: 1.75 m³.min⁻¹) powered by a 0.19 kW electric motor was provided to supply the airflow (1.625 m³.min⁻¹) to dry 7.5 kg of coleus root and overcome the pressure drop generated during drying. The heating chamber consisted of two heating coils (1 kW each) located between the blower and the plenum chamber. A copper–constantan thermocouple connected with a thermostat was provided in the plenum chamber to measure and maintain the drying air temperature with an accuracy of ±1 °C. Four flights (100 x 30 x 18 mm) and four baffles (95 x 30 mm size) were fitted inside the drying chamber at equal distance to lift, move, and uniformly mix the sliced coleus roots. All flights were fixed horizontally, and all baffles were fixed at 45⁰ to the horizontal plane. A three-phase, 0.745 kW electric motor was connected with a gearbox, rotating the drying chamber at 25 rpm. The drying chamber was mounted on a stand using a shaft attached with a ball bearing to rotate the drying chamber freely. The stand was fabricated using an equal angle iron (35 x 35 x 6 mm). The length, width, and height of the stand were 1000, 500 and 900 mm, respectively.

Drying

The sliced roots were filled in to 50, 60, and 70% of drier volume, and dried using hot air at 45, 55, and 65 ⁰C. Based on preliminary studies, the airflow rate and drum rotating rpm were maintained as 1.625 m³.min⁻¹ and 25 rpm.

The product was dried until it reached a constant weight. Weight reduction in coleus roots during drying was recorded at 15 min intervals for first 02 h and 30 min intervals for further drying time.

Determination of Effective Moisture Diffusivity

Moisture diffusion controls the drying process of agricultural produces, and is explained by Fick's second law of diffusion (Eq. 1). Determination of moisture diffusion using experimental method is difficult, therefore by linearizing the differential equation of Fick's second law of diffusion (Eq. 2) and simplified by assuming that the coleus roots were slabs and considering n=1 as the drying process took a long time (Eq. 3) (Arun Kumar *et al.,*2019). Several researchers have shown that Eq.3 was further simplified to a straight-line [ln (MR) = mt+c] equation shown in Eq. 5 (Dincer and Dost, 1995; Dadalı *et al.*, 2007; Wang *et al.*, 2007). A linear equation was fitted by plotting a graph between ln (MR) and time, and the slope was

estimated. Effective moisture diffusivity was estimated by substituting π and r in the slope (m) in the Eq. 5.

$$\frac{dM}{dt} = D_{eff} \times \frac{d^2M}{dr^2} \qquad \ldots (1)$$

$$M = \frac{8}{\pi^2}\sum_{n=1}^{\infty}\frac{1}{(2n-1)^2} \times \exp\left(-(2n-1)^2 \times \frac{\pi^2}{4r} \times \frac{D_{eff}}{r}.t\right) \ldots (2)$$

$$M = \frac{8}{\pi^2} \times \exp\left(-\frac{\pi^2}{4r^2} \times D_{eff}.t\right) \qquad \ldots (3)$$

$$\ln(MR) = \ln\left(\frac{8}{\pi^2}\right) - \left(\frac{\pi^2 \cdot D_{eff}}{4r^2} \cdot t\right) \qquad \ldots (4)$$

$$D_{eff} = \frac{m \times 4r^2}{\pi^2} \qquad \ldots (5)$$

Where,
M = Moisture ratio,
r = Slice thickness of Coleus (diffusion path), mm,
t = Drying time, s,
D_{eff} = Effective moisture diffusivity, mm².s⁻¹, and
m = Estimated slope from equation.

Determination of Activation Energy

The effective moisture diffusivity can be related to the temperature by a simple Arrhenius equation (Eq.7) (Lopez *et al.*, 2000; Akpinar *et al.*, 2003. The Arrhenius equation (Eq. 8) was linearized by taking natural logarithm. Further, the activation energy was determined by substituting the value of R in the slope obtained from the linearized Arrhenius equation (Eq.8).

$$Deff = D_0 \text{ x e } \{-E_a/(RT)\} \qquad \ldots (6)$$

$$\text{In } D_0 - \{Ea/(R*T)\} \qquad \ldots (7)$$

$$E_a = m_a \times R \qquad \ldots (8)$$

Where,
D_{eff} = Moisture diffusivity, mm².s⁻¹,
A = Constant,
t = Thickness of drying material, mm,
E_a = Activation energy, kJ. Mol⁻¹, and
R = Universal gas constant, 8.134 x 10⁻³ kJ.mol⁻¹.K⁻¹, and
m_a = Slope of the equation.

Preparation of Forskolin Extract

The dried roots (Fig.1c) were milled using an attrition mill (SKE-01, 2 kg capacity) and sieved to less than 1.0 mm size powder using 18 mesh sieves. The sieved

powder was stored in airtight zip-lock pouches and used for extraction.

Forskolin was extracted as described by Sasaki *et al.* (1998). One gram of powder was taken in 10 ml of dichloromethane, and heated for 30 min at 40 ℃. After heating, the powder was dried to remove the dichloromethane and dissolved in 10 ml of methanol for 4 h at 40 ℃. The solution was evaporated in a water bath for 30 min to remove the solvent, and filtered through filter paper. The filtrate was used for quantification.

Quantification of forskolin

Forskolin was quantified by High-Performance Thin Layer Chromatography (HPTLC) (Camag Linomat IV model) at JSS College of Pharmacy, Ooty, India. Standard forskolin and other samples were spotted on pre-coated silica gel plates as narrow bands of 4 mm width at a constant rate of 8 $\mu l.s^{-1}$ using a Camag Linomat IV model applicator under nitrogen atmosphere. A mixture of benzene and ethyl acetate (85:15 v/v) was used as the mobile phase. The length of the chromatogram 90 mm and 15 min were required for each run. The plates were sprayed with anisaldehyde sulphuric acid reagent (0.5 ml anisaldehyde + 1 ml H_2SO_4 + 50 ml acetic acid) and heated at 110 °C for 5 min. orange fluorescence observed at 366 nm was detected, and the amount of separated compounds in the chromatogram was quantified at 315 nm using the Camag TLC scanner with CATS 3.17 software. The area of the peaks of standard and sample was quantified. The amount of forskolin was calculated using the formula (Eq.10) and expressed as % w/w of C. forskohli root powder.

$$A_f = \frac{C_{st}}{A_{st}} \times \frac{A_s}{S} \times 100 \qquad \ldots (9)$$

Where,

A_f = Amount of forskolin, %,

A_{st} = Peak area of standard, mm^2,

A_s = Peak area of unknown sample, mm^2,

C_{st} = Concentration of standard, μg; and

S = Quantity of unknown sample, μg.

Modeling of Drying Kinetics

Thin layer drying kinetic model is a mathematical equation used to describe and optimise the drying process through drying constant, k. Following thin-layer drying, kinetic models (Table 1) were assessed to describe the drying process of sliced coleus roots by non-linear least square regression analysis between moisture ratio and drying time. The moisture ratio was calculated by the Eq.10. Equilibrium moisture (M_e) content values used for calculation were obtained from last concurrent values in the drying curves, because thereafter no change in weight indicated that the moisture of roots attained equilibrium with drying atmosphere.

$$MR = \frac{M_\theta - M_e}{M_0 - M_e} \qquad \ldots (10)$$

Where,

M_θ = Moisture content at θ time, % (d.b.),

M_e = Equilibrium moisture content, % (d.b.), and

M_0 = Initial moisture content, % (d.b.).

Design of Experiment and Analysis of Data

A full factorial design of 3^3 with three replications was used to design the experiment using the drying parameters as slice thickness (2.5, 5.0, 7.5 mm), drying air temperature (45, 55, 65 ℃), and feed volume (50, 60,

Table 1. Empirical thin-layer drying kinetic models

Sl. No.	Model name	Model	Reference
1.	Lewis	$MR = e^{(-kt)}$	(Lewis, 1921)
2.	Exponential model	$MR = ae^{(-kt)} + c$	(Henderson and Pabis, 1961)
3.	Page model	$MR = ae^{(-kt^n)}$	(Page, 1949)
4.	Henderson and Pabis	$MR = ae^{(-kt)}$	(Henderson and Pabis, 1961)
5.	Modified Henderson and Pabis Model	$MR = ae^{(-k_1 t)} + be^{(-k_2 t)} + ce^{(-k_3 t)}$	(Şahin and Öztürk, 2018)
6.	Two-term model	$MR = ae^{(-k_1 t)} + be^{(-k_2 t)}$	
7.	Midilli model	$MR = ae^{(-kt^n)} + bt$	

70 %). Upon the design of experiments, maximizing the extraction of forskolin content from the 27 drying treatments using least squares approach to solve the optimization of treatment combinations with the constraints of slice thickness, drying air temperature, and feed volume. A linear mathematical model (Eq.11) was established, and variance analysis was performed to show the effect of each drying parameters, its interactions on drying characteristics, and forskolin content.

$$y = b_0 + b_1S + b_2T + b_3F + b_{12}ST + b_{13}SF + b_{23}TF + b_{123}STF$$
$$\ldots (11)$$

Where,
y   =   Predicted value, %,
S   =   Slice thickness, mm,
T   =   Temperature, ^{o}C,
F   =   Feed volume, % and

b_0; b_1, b_2, b_3; b_{12}, b_{13}, b_{23}; b_{123} = Average effect; main effects; two-way; and three-way interactions effects, respectively.

RESULTS AND DISCUSSION

Effect of Drying Parameters on Moisture Content and Drying Time

The results indicated that the drying time decreased with increasing drying temperature, decreasing slice thickness, and feed volume (Fig. 3). Lowest final moisture content of 17.9% (d.b.) was observed in

5.0 mm slice thickness, while highest final moisture content of 22.31% (d.b.) was observed in 7.5 mm slice thickness. For 2.5 mm slice thickness, 330 min was required for drying 70% feed volume at 45°C, and 270 min was required for 50% feed volume slices dried at 65 ^{o}C. The maximum and minimum drying time for 5.0 mm slice thickness was 270 min at 65 ^{o}C and 50% feed volume and 450 min at 45 ^{o}C and 70% feed volume. Similarly, for 7.5 mm slice thickness, the minimum time taken was 360 min at 65 ^{o}C with 50% feed volume; and the maximum time taken was 480 min at 45 ^{o}C f 70% feed volume. The higher air temperature and small slice thickness had low final (equilibrium) moisture content and less drying time (Fig.3), while the higher feed volume had high final (equilibrium) moisture content and drying time. The drying air temperature and slice thickness had more influence on moisture removal than feed volume. This might be due to increased water evaporation capacity of the air and higher high thermal diffusion in the slices because of large temperature gradient created by the high drying temperature and low thermal resistance caused by less slice thickness. Similar results were reported for carrot, ginger rhizome and okra (Reyes *et al.*, 2002; Hoque *et al.*, 2013; Muliterno *et al.*, 2017). Xiao *et al.* (2010) had reported that drying of carrot slices was significantly influenced by drying air temperature than air velocity. Olawale and Omole (2012) had observed that thinnest sweet potato slices recorded the least final moisture content and fast-drying rate than the thickest slices. Reducing thickness of ginseng significantly decreased the drying time (Xiao *et al.*, 2015).
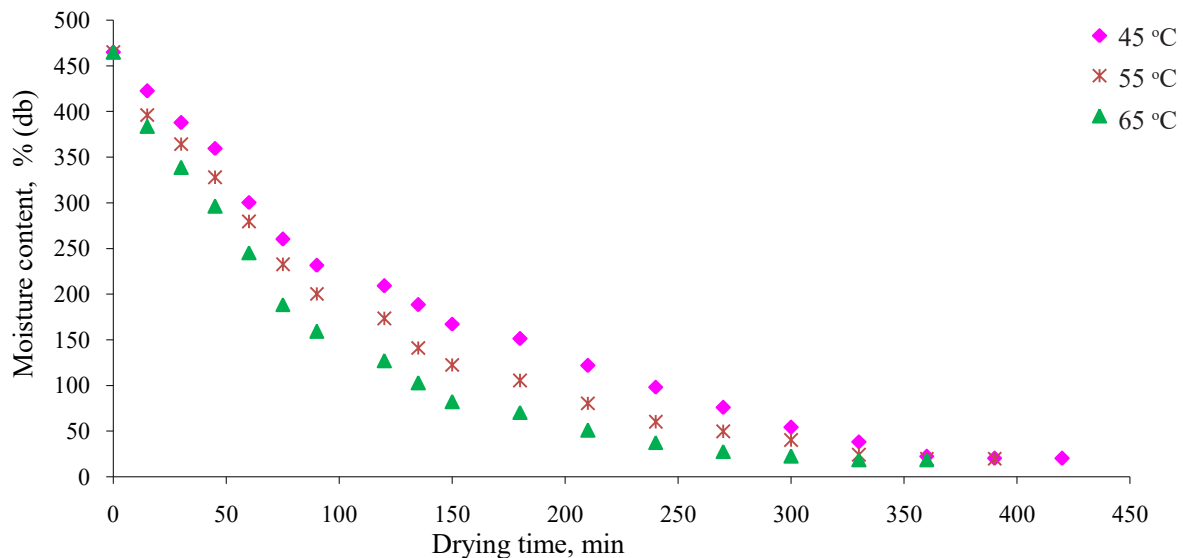

Fig. 3: Effect of drying air temperatures and time on moisture content of 7.5 mm coleus dried at (a) 50 ^{o}C, (b) 60 ^{o}C, and (c) 70 ^{o}C drying temperature

Effect of Drying Parameters on Drying Curve

From Fig. 4, it could be noticed that nearly 60% of moisture content reduced exponentially before 180 min of drying at all drying air temperatures and feed volumes. Absence of constant rate drying period was observed from the curves. This might be because of prevention of moisture diffusion from sliced coleus roots by the shrinkage of surface. The internal mass transfer resistance controls the drying time; higher internal mass transfer resistance facilitates the constant rate falling period. The absence of constant rate drying might be due to quick moisture diffusion mechanism from the centre to the surface and due to the quick moisture removal from the skin (Doymaz, 2004; Kaleemullah and Kailappan, 2005). The falling rate period dominated the drying operation (Asparagus' root) due to lesser internal mass transfer resistance (Kohli *et al.*, 2018). Hoque *et al.* (2013) reported that

the constant drying rate of whole ginger rhizome during drying might be due to prevention of moisture diffusion through the thick skin of the whole ginger rhizomes; whereas the present study observed the falling rate drying in sliced samples. This might be due to higher moisture diffusion because of small diffusion length.

Effect of Drying Parameters on Effective Moisture Diffusivity and Activation Energy

Effective moisture diffusivity of moisture in the sliced coleus roots during drying under various drying conditions was estimated by regression analysis between ln (MR) and drying time (Fig. 5). Effective moisture diffusivities of coleus roots during drying were found in the range of 1.0×10^{-6} mm^2.s^{-1} to 9.93×10^{-7} mm^2.s^{-1}. Effective moisture diffusivity decreased with increasing slice thickness from 2.5 mm to 7.5 mm and
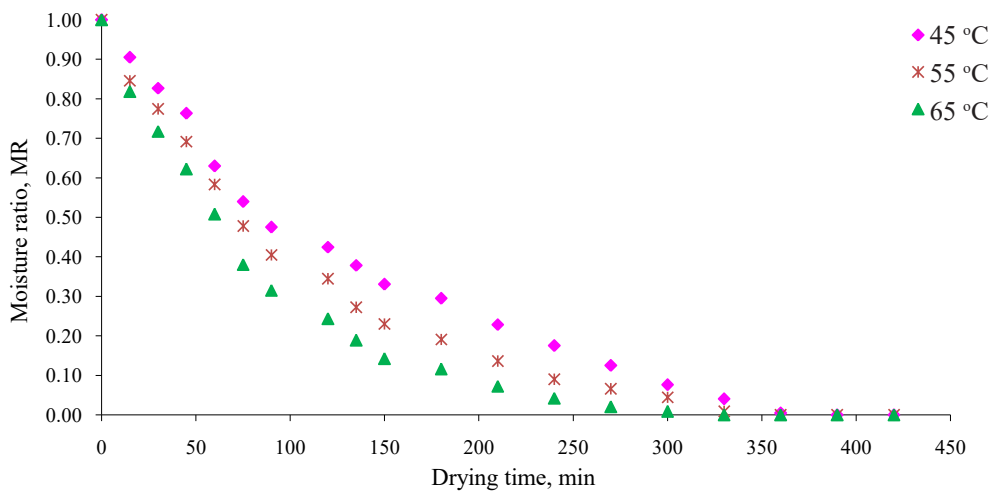

Fig. 4: Effect of drying air temperatures and time on moisture ratio of 7.5 mm coleus dried at (a) 50 ⁰C, (b) 60 ⁰C, and (c) 70 ⁰C drying temperature
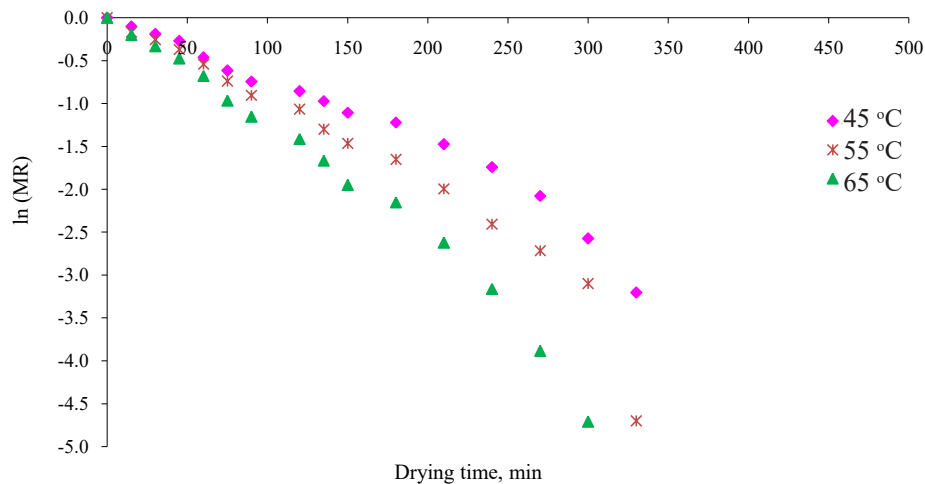

Fig. 5: Effect of drying air temperatures and time on the moisture content of 7.5 mm coleus dried at ((a) 50 ⁰C, (b) 60 ⁰C, and (c) 70 ⁰C drying temperature

increased feed volume from 50% to 70 per cent. D_{eff} increased with increasing hot air temperature. Similar results were reported by Abano and Amoah (2015). The effective moisture diffusivities of Asparagus root dried at 40 - 70 °C in a fluidized bed dryer was found in the range of $1.85 \times 10^{-8} \, m^2.s^{-1}$ to $3.70 \times 10^{-8} \, m^2.s^{-1}$ (Kohli *et al.*, 2018). Moisture diffusivity of ginger treated under high pressure and dried in a cabinet dryer increased from $2.03 \times 10-9 \, m^2.s^{-1}$ to $4.87 \times 10-9 \, m^2.s^{-1}$ with increase in drying temperature from 55 °C to 85°C (George *et al.*, 2018). Further, two cut surfaces with small diffusion length of sliced roots enabled more moisture diffusion and moisture removal (Hoque *et al.*, 2013). High feed volume affects the movement of air, and thus caused low diffusivity.

Activation energy (E_a) was estimated using the plots establishing a linear relationship between ln (D_{eff}) and the inverse of absolute drying temperature (Fig. 6). The activation energy calculated for 50, 60, and 70%

feed volume were 5.39, 15.57, and 10.16 kJ.mol^{-1} for 2.5 mm slice thickness; 9.98, 8.99, and 6.20 kJ.mol^{-1} for 5.0 mm slice thickness; and 12.99, 5.87, and 7.06 kJ.mol^{-1} for 7.5 mm slice thickness. Smaller value of E_a indicates that the movement of moisture within the drying material is more comfortable, and hence drying can be conducted with minimum energy (or) minimum cost. The activation energy of Asparagus root dried in a fluidized bed dryer and ginseng slices dried in a laboratory-scale impingement dryer was 21.687 kJ.mol^{-1} (Kohli *et al.*, 2018) and 46.64 kJ.mol^{-1} (Xiao *et al.*, 2015), respectively.

It could be seen from Table 2, maximum forskolin content was observed in small slice thickness treated under low temperature. As slice thickness, drying air temperature, and feed volume increased, the forskolin content decreased. Maximum of 1.87% forskolin was quantified in 2.5 mm slice thickness coleus roots dried at 45 °C drying air temperatures with 50% feed volume;
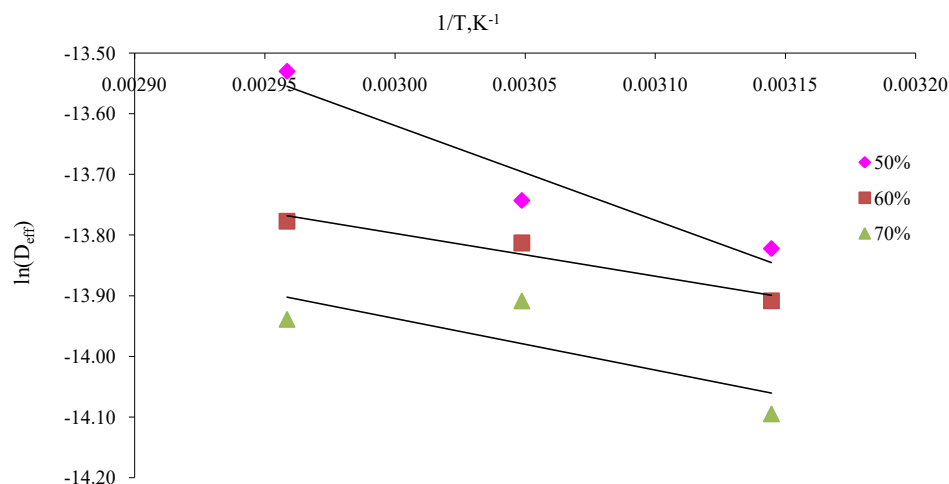

Fig. 6: Relationship between ln (Deff) and reciprocal of drying air temperatures for (a) 2.5 mm, (b) 5.0 mm, and (c) 7.5 mm sliced coleus roots

Table 2. Effect of drying parameters on forskolin content of dried coleus

Slice thickness, mm	Temperature, °C	Feed volume, %		
		50	60	70
	45	1.87	1.84	1.82
2.5	55	1.74	1.75	1.77
	65	1.27	1.15	1.02
5.0	45	1.75	1.43	1.02
	55	0.95	0.92	0.90
	65	0.79	0.60	0.49
7.5	45	0.44	0.36	0.26
	55	0.33	0.28	0.17
	65	0.36	0.21	0.14

whereas a minimum of 0.33% forskolin was quantified in 7.5 mm slice thickness dried at 55°C drying air temperatures with 50% feed volume. It was statistically ascertained by the negative estimates of slice thickness [(-) 0.259], drying air temperature [(-) 0.026], and feed volume [(-) 0.011]. This might be due to the heat sensitiveness of forskolin content. Large slice thickness exposed for long drying time deteriorated the forskolin content in sliced roots. Similar results were reported for Kothimbda (Vyas, 2014) and for ginseng slices (Xiao *et al.*, 2015). Harde and Singhal (2012) had reported that about $0.64 \pm 0.12\%$ w/w of forskolin was obtained from the solvent extract of C. *forskohlii* roots using HPLC; whereas the values obtained in the present study was 1.18% w/w. The yield of higher forskolin might be due variation in drying methods.

Analysis of variance (Table 3) of forskolin content of dried coleus roots showed that slice thickness and the temperature had significantly (p<.0001) affected forskolin content retention during drying, whereas feed volume affected significantly at 1% (P<0.05). Among the interactions between different parameters, the

effect of slice thickness and temperature on forskolin content was significant at 5% level (P<0.01). Other interactions, namely temperature and feed volume, slice thickness and feed volume, and slice thickness and temperature and feed volume on forskolin content, were not significant at 5% level (P<0.05).

The linear mathematical model established to show each drying parameters and interactions between the parameters on forskolin content is given in Eq.12. The coefficient of determination (R^2) and the adjusted coefficient of determination ($Adj.R^2$) of the model were 0.950 and 0.931, respectively. The scatter plot of forskolin content predicted versus actual looks good with even spread of data points around the diagonal line (Fig.7).

$$y = 4.338 - 0.259\,S - 0.026T - 0.011F + 0.006ST$$
$$\dots (12)$$

Drying Kinetics of Optimised Treatment Condition

A total of 27 treatments were conducted for drying of coleus roots to get the maximum amount of forskolin

Table 3. Analysis of variance and parameters estimates

| Source	Estimates	Sum of squares	DF	Mean Square	F-ratio	P value
Intercept	4.338	9.306	26	0.377	51.610	<.0001
S: Slice thickness, mm	(-) 0.259	7.579	2	3.793	294.230	<.0001
T: Drying air temperature, °C	(-) 0.026	1.259	2	0.632	48.867	<.0001
F: Feed volume, %	(-) 0.011	0.203	2	0.101	7.868	0.0113
S ×T	0.006	0.252	4	0.135	9.795	0.0055
S×F	(-) 0.001	0.007	4	0.014	0.272	0.608
T×F	0.001	0.003	4	0.014	0.117	0.7363
S ×T×F	0.000	0.003	8	0.011	0.124	0.7284
R^2	0.950					
Adj. R^2	0.931					
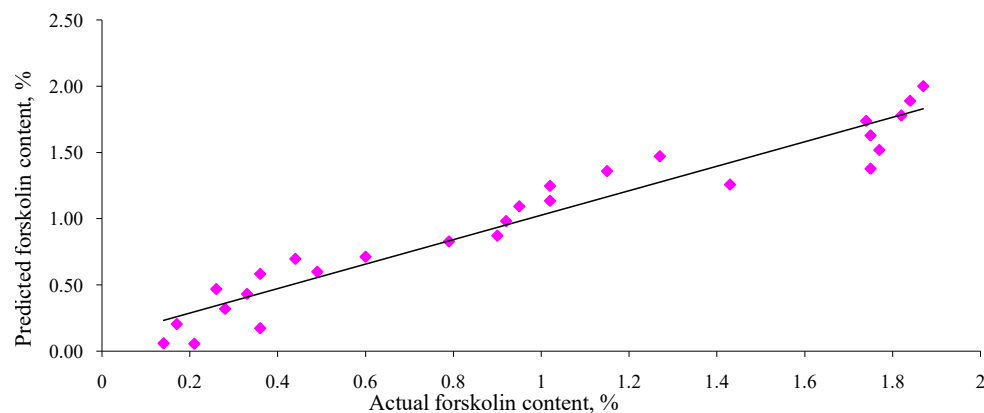
Fig. 7: Actual versus predicted forskolin content of dried coleus roots

Table 4. Kinetic model parameters, constants, coefficient of determination and RMSE

Sl. No.	Model name	Model constant parameter	R^2	RMSE
1.	Lewis	k =0.007	0.983	0.043
2.	Exponential model	a =1.17; c = -0.177; k =0.005	0.996	0.022
3.	Page model	a =1.033; k = 0.023; n = 0.318	0.984	0.043
4.	Henderson and Pabis	a =1.033; k =0.007	0.985	0.042
5.	Modified Henderson and Pabis Model	a =57.92; b =0.272; c =-57.11; k_1=0.002; k_2=0.022; k_3=0.002	0.991	0.035
6.	Two term model	a =-36.07; b =37.01; k_1 =0.011; k_2 = 0.011	0.987	0.041
7.	Midilli model	a= 0.995; b = 0.0003; k = 0.076; n = 0.076	0.996	0.022

content. The treatments were optimised based on the mean square analysis between actual and predicted forskolin content through statistical model. The drying kinetics were employed for optimised treatments only, and results are described here. The absence of a constant rate drying period was observed from the drying curves, and thus the models had exponential components that were fitted to describe the falling rate period of coleus drying. The models were fitted for only optimised drying treatment which has maximum forskolin content.

From Table 4, it could be seen that all empirical models explained the drying process of sliced coleus roots within the design space. However, R^2 values and RMSE value of both exponential and Midilli model were best with R^2 of the models as 0.996 and 0.996, respectively. Similarly, the RMSE values were 0.021 and 0.222, respectively. Previous studies stated that the Page model described the drying kinetics of sweet potato slices dried between 50 °C and 80 °C in a tray dryer (Olawale and Omole, 2012); ginger dried in a box-cabinet natural circulation solar dryer (Deshmukh *et al.*, 2014); diced cassava roots dried in a cabinet dryer (Kajuna *et al.*, 2001); carrot dried by various methods as tunnel dryer, vacuum-freeze dryer assisted by infrared radiation, pulsed fluidized-bed dryer assisted by microwave radiation, and combinations of these methods (Reyes *et al.*, 2008) either with or without infrared radiation; a pulsed fluidized-bed dryer assisted by microwave radiation; and combinations of these methods. It was observed that drying the sliced coleus roots had been thin layer for moisture removal as the slices inside the drum were mixed by a rotary motion.

CONCLUSIONS

The study concluded that decreasing slice thickness,

feed volume, and increasing drying air temperature reduced the drying time. Higher final moisture content occurred with increasing slice thickness and feed volume with decreasing drying air temperature. The effective moisture diffusivities and the activation energy of the Coleus roots were in the range of 1.00×10^{-6} - 9.93×10^{-7} $mm^2.s^{-1}$, and from 5.39 - 15.57 $kJ.mol^{-1}$, respectively. A maximum of 1.87% forskolin was quantified in 2.5 mm thick slice dried at 45 °C and 50% feed volume; while the minimum of 0.33% forskolin was quantified in 7.5 mm thick slice dried at 55 °C and 50% feed volume. Slice thickness and temperature had significantly ($p<.0001$) affected forskolin content retention during drying, whereas feed volume significantly affected at 1% ($P<0.05$). The exponential and Midilli models are suitable for explaining the drying characteristics of sliced coleus root.

REFERENCES

Abano E E; Amoah R S. 2015. Microwave and blanch-assisted drying of white yam (Dioscorea rotundata). Food Sci. Nutr., 3, 586-596.

Akpinar E; Midilli A; Bicer Y. 2003. Single layer drying behaviour of potato slices in a convective cyclone dryer and mathematical modeling. Energy Convers. Manage., 44, 1689-1705.

Allen D O; Ahmed B; Naseer K. 1986. Relationships between cyclic AMP levels and lipolysis in fat cells after isoproterenol and forskolin stimulation. J. Pharmacol. Exp. Ther., 238, 659-664.

Arun K A; Alam M S; Angam Raleng; Yadav Y K. 2019. Drying kinetics of onion (Allium cepa L.) slices using low-humidity air assisted hybrid solar dryer. J. Agric. Eng., 58(3), 262-273.

Badmaev V; Majeed M; Conte A A; Parker J E.

V. Chandrasekar, V. Eyarkai Nambi and S. Shahir   JAE : 59 (1)
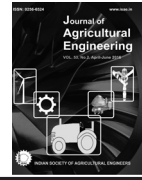
2002. Diterpene forskohli (Coleus forskohlii Benth.): A possible new compound for reduction of body weight by increasing lean body mass. NutraCos, 1, 6-7.

Dadalı G; Apar D K; Özbek B. 2007. Estimation of effective moisture diffusivity of okra for microwave drying. Drying Technol., 25, 1445-1450.

Deshmukh A W; Varma M N; Yoo C K; Wasewar K L. 2014. Investigation of solar drying of ginger (Zingiber officinale): Emprical modelling, drying characteristics, and quality study. Chin. J. Eng., Article ID 305823. 1-7.

Dincer I; Dost S. 1995. An analytical model for moisture diffusion in solid objects during drying. Drying Technol., 13, 425-435.

Doymaz I. 2004. Convective air drying characteristics of thin layer carrots. J. Food Eng., 61(3), 359-364.

George J M; Sowbhagya H B; Rastogi N K. 2018. Effect of high pressure pretreatment on drying kinetics and oleoresin extraction from ginger. Drying Technol., 36, 1107-1116.

Harde S M; Singhal R S. 2012. Extraction of forskolin from Coleus forskohlii roots using three phase partitioning. Sep. Purif. Technol., 96, 20-25.

Hoque M; Bala B; Hossain M; Uddin M B. 2013. Drying kinetics of ginger rhizome (Zingiber officinale). Bangladesh J. Agric. Res., 38, 301-319.

Horwitz W; Latimer G. 2005. AOAC-Association of Official Analytical Chemists. Off. Methods Anal. AOAC Int., 18th Ed., Gaithersburg, Maryland, USA, 45, 75-76.

Henderson S M; Pabis S. 1961. Grain drying theory: Temperature effect on drying coefficient. J. Agric. Eng. Res., 6(3), 169-174.

Kajuna S; Silayo V C K; Mkenda A; Makungu P J J. 2001. Thin-layer drying of diced cassava roots. Afr. J. Sci. Technol., 2(2), 94-100.

Kaleemullah S; Kailappan R. 2005. Drying kinetics of red chillies in a rotary dryer. Biosyst. Eng., 92, 15-23.

Kohli D; Shahi N C; Kumar A. 2018. Drying kinetics and activation energy of asparagus root (asparagus racemosus wild.) for different methods of drying. Curr. Res. Nutr. Food Sci. J., 6, 191-202.

Lewis W K. 1921. The rate of drying of solid materials. Indus. Eng. Chem., 13, 427-432.

Lopez A; Iguaz A; Esnoz A; Virseda P. 2000. Thin-layer drying behaviour of vegetable wastes from wholesale market. Drying Technol., 18, 995-1006.

Muliterno M M; Rodrigues D; de Lima F S; Ida E I; Kurozawa L E. 2017. Conversion/degradation of isoflavones and color alterations during the drying of okara. LWT - Food Sci. Technol., 75, 512-519.

Mujumdar A S. 2004. Dryers for Particulate Solids, Slurries and Sheet-Form Materials. In: Mujumdar, A S (Ed.), Guide to Industrial Drying: Principles, Equipment and New Developments, Three S. Colors, Mumbai, 37-77.

Olawale A S; Omole S O. 2012. Thin layer drying models for sweet potato in tray dryer. Agric. Eng. Int. CIGR J., 14, 131-137.

Page G E. 1949. Factors influencing the maximum rates of air-drying shelled corn in thin layers. Unpublished M.Sc. Thesis, Purdue University, West Lafayette, Indiana, ProQuest Dissertations Publishing, 1300089.

Reyes A; Alvarez P I; Marquardt F H. 2002. Drying of carrots in a fluidized bed. I. Effects of drying conditions and modelling. Drying Technol., 20, 1463-1483.

Reyes A; Vega R; Bustos R; Araneda C. 2008. Effect of processing conditions on drying kinetics and particle microstructure of carrot. Drying Technol., 26, 1272-1285.

Şahin U; Öztürk H K. 2018. Comparison between artificial neural network model and mathematical models for drying kinetics of osmotically dehydrated and fresh figs under open sun drying. J. Food Process Eng., 41(5), 1-14.

Sasaki K; Udagawa A; Ishimaru H; Hayashi T; Alfermann A W; Nakanishi F; Shimomura K. 1998. High forskolin production in hairy roots of coleus forskohlii. Plant Cell Rep., 17, 457-459.

Seamon K B; Padgett W; Daly J W. 1981. Forskolin: Unique diterpene activator of adenylate cyclase in membranes and in intact cells. Proc. Natl. Acad. Sci. U. S. A., 78, 3363-3367.

95

Vyas D M G D. 2014. Studies on effect of slice thickness and temperature on drying kinetics of kothimbda (Cucumis Callosus) and its storage. J. Food Process. Technol., 06.

Wang Z; Sun J; Chen F; Liao X; Hu X. 2007. Mathematical modelling on thin layer microwave drying of apple pomace with and without hot air pre-drying. J. Food Eng., 80, 536-544.

Xiao H W; Gao Z J; Lin H; Yang W X. 2010. Air impingement drying characteristics and quality of carrot cubes. J. Food Process. Eng., 33, 899-918.

Xiao H W; Bai J W; Xie L; Sun D W; Gao Z J. 2015. Thin-layer air impingement drying enhances drying rate of American ginseng (Panax quinquefolium L.) slices with quality attributes considered. Food Bioprod. Process., 94, 581-591.

Prioritization of Sub-watersheds of Kosi River Basin Using Morphometric Analysis and Geospatial Tools

Sourab Singh[1], Vaibhav E. Gosavi[2*], Sandipan Mukherjee[3] and Kireet Kumar[4]

[1]Former Senior Research Fellow, [2*]Scientist - C, [3]Scientist – D, [4]Scientist – G, G. B. Pant National Institute of Himalayan Environment, Kosi-Katarmal, Almora, Uttarakhand, 263643, India. *Corresponding author email address: vaibhavgosavi8@gmail.com

Article Info	ABSTRACT
                	This study aimed to use remote sensing (RS) and geographic information system (GIS) geospatial tools for morphometric investigation of a mid-Himalayan Kosi river basin in Uttarakhand, India. The sub- watersheds (SWs) were identified and prioritized into high, medium, and low level of priority based on the compound factor analysis for conservation of natural resources in the watershed, leading to sustainable watershed management. Total of 10 morphological parameters related to drainage network, basin geometry, and drainage texture were used for compound factor analysis. The drainage network of the river basin was dendritic in nature and exhibited homogeneity in texture and lack of structural control that helped in analysing terrain parameters as drainage density, infiltration capacity, runoff, bedrock nature, which control underground water movement. The stream-order estimated using the digital elevation model (DEM) having 12.5 m × 12.5 m spatial resolution ranged from first to seventh order streams. During prioritization of sub-watersheds using compound factor values, higher priority was assigned to sub-watersheds which yielded lowest compound factor and vice-versa. Sub-watersheds SW5 to SW7 covering an area of 396.18 km^2 were noted to have highest priorities for soil erosion conservation measures; SW2, SW3 and SW8 had medium priorities; and SW1, SW9, and SW4 were assessed with lowest priorities. It is anticipated that the prioritization of sub-watersheds would be useful to planners, decision makers, and relevant stakeholders for implementation of soil and water conservation interventions for sustainable natural resources management within watershed.

Morphometric investigation or analysis is the quantitative assessment used to collect the information of different terrain properties as slope, relief, altitude, drainage network of a geographical area (Chandniha and Kansal, 2017; Singh *et al*., 2021) and is helpful to understand the influence of fluvial morphometry on the natural resources of the watershed (Pendke *et al*., 2018). Subsequently, morphometric techniques could be used to extract information on various secondary terrain parameters as drainage network orientation, stage of erosion, geographic layers, hydrological characteristics of a watershed or basin (Sreedevi *et al*., 2013). Morphometric analysis supplemented by detail drainage network analysis conjointly used for analysing the dynamicity of a geographical area (Withanage *et al*., 2015; Prakash *et al*., 2016a, 2016b; Singh *et al*., 2019) and provides a comprehensive view of the hydrologic behaviour of the watershed (Singh *et al*., 2021). Consequently, morphometric assessment is significant in understanding the geologic structure of watershed or river basin and useful for identifying the surface and sub-surface processes that are effective within the watershed area (Magesh *et al*., 2011; Gosavi *et al*., 2018). Morphometric drainage network assessment of a watershed is further beneficial for demarcating the suitable areas for water harvesting structures and soil-water conservation interventions leading to better management of watershed (Pankaj

and Kumar, 2009; Chandrashekar *et al*., 2015; Gosavi *et al*., 2018). However, due to significant variation in the hydro-meteorological and hydrogeological conditions across the planet, morphometric parameters vary significantly from one basin to other (Samal *et al*., 2015). Therefore, basin or watershed- scale assessment of morphometric characteristics is required to understand the connection between hydrological and geo-morphological parameters (Nag and Chakraborty, 2003).

Basin morphometry has four broad distinctive aspects as drainage network, basin geometry, drainage texture, and relief. Each broad aspect has many different derived morphometric parameters (Nag and Chakraborty, 2003; Magesh *et al*., 2012). These parameters are calculated using the digital elevation model (DEM) data acquired from remote sensing (RS), and processed using the geographic information system (GIS) (Pankaj and Kumar, 2009; Thomas *et al*., 2010; Pate and Dholakia, 2010). Basin morphometric characteristics obtained using these procedures are fairly accurate and are becoming standard for planning natural resources conservation measures, mainly soil-water conservation activities for watershed management. Moreover, this is an effective approach in integrating the spatial data to develop beneficial outputs such as different thematic layers for variables related to pollution risk, land cover monitoring and for possible numerical modelling of water resources (Gupta and Srivastava, 2010; Srivastava *et al*., 2012a; Srivastava *et al*., 2012b). As use of geospatial tools such as RS and GIS for morphometric analyses is amenable to quick evaluation of drainage and hydrological characteristics, products or inferences from GIS aided morphometric analyses are rapidly becoming handy tool in decision making for framing acceptable measures in water scarce basins or watersheds (Srivastava *et al*., 2011; Magesh *et al*., 2011; Srivastava *et al*., 2012a).

Although the Himalayas have more than 33,000 km^2 of glaciated basins that store approximately 12,000 km^3 of fresh water (Hua *et al*., 2009) through more than 9000 glaciers (Raina and Srivastava, 2008), densely populated mid-Himalayan basins are extremely dependent on numerous springs, streams and seepages for fresh water (Kumar *et al*., 2019). Moreover, such springs and streams are known to be lifelines of some of the major rivers that support the unique bio-diversities, agricultural practises, and day- to-day water demand of millions of people. However, such stream and spring-fed rivers across the north- western

Indian Himalayan regions are increasingly reported to be experiencing decline in annual discharges due to many socio-economic and climate induced impacts. Moreover, extreme rainfall induced events of flash flood are increasing in western and central part of the Himalaya (Kumar *et al*., 2018) which trigger soil erosion in the watershed. Subsequently, there is a need to frame basin-specific adaptations plan and mitigation policies through targeted watershed conservation and management activities. Morphometric investigation of watershed using geospatial tool could prioritize sub-watersheds within a watershed wherein suitable soil and water conservation measures or groundwater development activities such as water harvesting or recharge structure could be proposed (Nooka *et al*., 2005) or soil and water conservation activities could be carried out depending upon situation and need. Such prioritization of sub- watersheds or micro-catchments are primarily linked with erodibility criteria and could lead to focused efforts on groundwater recharge and drainage development activities such as positioning water harvesting structures that leads to soil and water conservation as well (Patel *et al*., 2011; Patel *et al*., 2012; Sushanth and Bhardwaj 2019; Singh *et al*., 2021; Mali *et al*., 2021).

Therefore, the present study aimed to prioritize sub-watersheds for conservation of natural resources, and their efficient management through morphometric investigation using RS and GIS for a mid-Himalayan densely populated basin (Kosi river basin of Kumaun region) that covers broadly Almora and Nainital districts of Uttarakhand, India, and reported to be experiencing high water scarcity (Kumar *et al*., 2019).

MATERIALS AND METHODS

Study Area

The study was conducted in Centre for Land and Water Resources Management (CLWRM) of G. B. Pant National Institute of Himalayan Environment (GBP-NIHE) located at Kosi-Katarmal, Almora, in Uttarakhand state. The study was carried out for the Kosi River basin of Uttarakhand, India, situated between 29°23'0" N and 29°52'0" N latitudes and 79°05'00" E and 79°51'00" E longitude (Fig. 1). The Kosi basin covers an area of 1863 km^2. In the upstream section, i.e. upper Kosi watershed, river originate in Rudradhari hills and flows from North to South direction. As it flows further downwards, it flows from East to West direction in the middle section of the watershed, incising the bedrocks and forming broad

valleys, straight as well as unpaired terraces (Fig. 1).

Kosi River is a 7th order channel and has produced an actively eroded landscape with bedrock incision evident at several locations. Originating from Dharpanidhar, Rudradhari hills in Bageshwar district of Uttarakhand, India, Kosi River confluences with Ramganga River in Uttar Pradesh state, India. The annual discharge of the Kosi River varies between $0.8 – 790.0 \ m^3s^{-1}$, whereas the average annual rainfall over the basin is around 1200 mm, and monsoon contributes around 740 mm rainfall (Mukherjee *et al.*, 2015a, 2015b, 2018). The average numbers of heavy rainy days (daily rainfall > 35.5 mm) over the watershed is around 2.48 per monsoon season as in the case of Uttarakhand state (Mukherjee, 2021). The region is also expected to receive higher summer monsoon rainfall and lower winter-season wet days by the end of this century under the Representative Concentration Pathway

(RCP) based projected climate change scenarios of RCP4.5 and RCP8.5 (Mukherjee *et al.*, 2019; Ballav *et al.*, 2021).

The basin is unique as it represents a protected national park, a central Himalayan River that is not glacier-fed, and mid-Himalayan peaks with two major towns having high population density. The watershed consists of two major districts of Uttarakhand, Almora and Nainital, two major urban areas Almora district Headquarter and Ramnagar, and a part of the Corbett National Park. The general forest cover of the Kosi watershed is more than 50 per cent. Water from the Kosi River is mainly used for domestic consumption, fishing, and agriculture. The Kosi watershed is vulnerable in terms of fresh water availability, and Takula and Ramgarh administrative blocks of Almora and Nainital district are facing high scarcity of potable water (Kumar *et al.*, 2019).
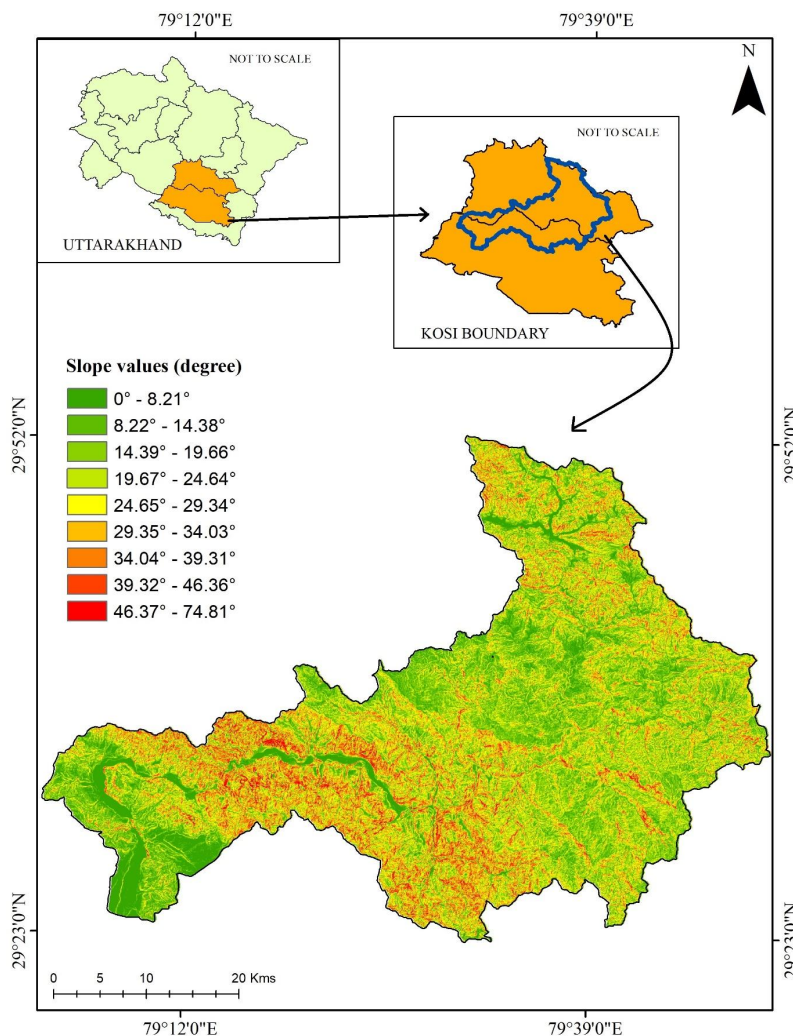

Fig. 1: Study area map of Kosi basin

Data Used and Methodology

The Kosi basin boundary shape file was prepared using the Survey of India topographical maps of scale 1:50,000. The shape file was used to generate the drainage network developed using ALOS PALSAR (ALOS - Advanced Land Observing Satellite, PALSAR - Phased Array type L-band Synthetic Aperture Radar) (https://search.asf.alaska.edu/#/) digital elevation model (DEM) having a spatial resolution of 12.5 m × 12.5 m. Subsequently, two procedures were adopted, (i) complete analyses of 10 morphometric parameters, and (ii) prioritization of sub-watersheds using selected morphometric parameters. The general flow chart of methodological processes is provided in Fig. 2. The morphometric investigation involved development of watershed boundary, computation of slope and aspect, analysis of drainage network, estimation of watershed geometry, and drainage texture using Arc-GIS (v 10.4), and following the approach of Strahler (1957). A total of 10 morphometric parameters covering the aspects of drainage network, drainage texture, basin geometry,

Fig. 2: Methodology for prioritization of sub-watersheds using morphometric parameters

and relief, were estimated using formulations as provided in Table 1. Although total of 34 morphometric parameters for the Kosi basin was estimated, 10 morphometric parameters used for estimation of compound factor and prioritization of sub-watersheds into high, medium and low level of priority for natural resources management are presented and discussed considering the limitation of manuscript length.

The analysis of morphometric parameters was carried out for nine sub-watersheds (SW1 to SW9) within the basin (Fig. 3 and Fig. 4). The sub-watershed demarcation was based on 6th order stream pour point of each outlet to the main stream and superimposing this network on the ALOS PALSAR digital elevation model (Balasubramanian *et al*., 2017). The 6th order stream was chosen to select workable numbers of sub-watersheds for further analysis as identification of 5th and 7th order stream pour point of each outlet to the main stream and superimposing this network to DEM resulted either very large or very small numbers of sub-watersheds. Subsequent to the estimation of morphometric parameters, the sub-watersheds were prioritized through a compound score and successive ranking criteria. The linear and shape parameters used to compute compound score were bifurcation ratio (Rb), drainage density (Dd), stream frequency (Sf), length of overland flow (Lg), drainage texture (Dt), circulatory ratio (Rc), form factor (Ff), shape factor ratio (Rs), elongation ratio (Re), and compactness coefficient (Cc); wherein, Dd, Sf, Dt, and Lg are linear in nature and directly associated with the erodibility factor, and shape factors such as Ff, Rs, Re, Cc, and Rc are inversely related to the erodibility factor (Balasubramanian *et al*., 2017). These ten morphometric parameters representing three aspects, namely drainage network, drainage texture, and basin geometry represent erosion risk, and are traditionally used for sub-watershed prioritisation (Biswas *et al*., 1999). As the linear and shape parameters are directly and inversely proportional to the erodibility factor, respectively, the final compound factor was estimated using individual scores of linear and shape parameters. Prioritization of sub-watersheds were carried by assigning ranks or ranking to individual parameters. For linear parameters, highest value of linear parameter was assigned highest rank, i.e. rank 1; while in case of shape parameter, lowest value of shape parameter was assigned highest rank, i.e., rank 1. Finally, the compound factor was calculated by summing the ranks of both linear and shape parameters and dividing by total number of
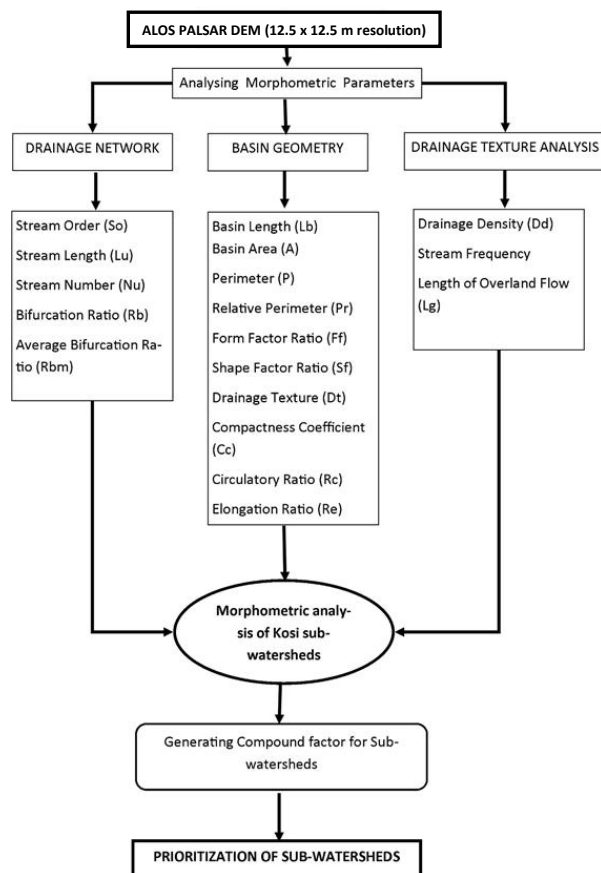
Table 1. Formula used for computing various morphometric parameters

Morphometric aspect	Parameter	Formula	Reference
Drainage network	Stream order (*So*)	Hierarchical rank	Strahler (1964)
	Stream length (*Lu*), km	$Lu = L_1 + L_2 + ... + L_n$	Strahler (1964)
	Stream number (*Nu*)	$Nu = N_1 + N_2 + ... + N_n$	Strahler (1964)
	Bifurcation ratio (*Rb*)	$Rb = Nu/Nu+1$	Schumm(1956)
		Where, *Rb* = Bifurcation ratio	
		Nu = Total number of stream segment of order 'u'	
		Nu+1 = Number of stream segment of next higher order	
Basin geometry	Basin length *(Lb)*, km	GIS analysis	Schumm(1956)
	Basin area *(A)*, km²	GIS analysis	Schumm(1956)
	Basin perimeter *(P)*, km	GIS analysis	Schumm(1956)
	Form factor ratio *(Ff)*	$Ff = A/Lb^2$	Horton (1945)
		Where, *A* = Basin area	
		Lb^2 = Square of basin length	
	Shape factor ratio *(Rs)*	$Rs = Lb^2/A$	Horton (1945)
		Where, Lb^2 = Square of basin length	
		A = Basin area	
	Drainage texture *(Dt)*	$Dt = Nu/P$	Horton (1945)
		Nu = Number of streams, *P* = basin perimeter	
	Compactness coefficient *(Cc)*	$Cc = 0.2821*P/A^{0.5}$	Horton (1945)
		Where, *A* = Area of basin (km²)	
		P = Perimeter of the basin (km)	
	Circulatory ratio *(Rc)*	$Rc = 4*\pi*A/P^2$	Miller (1953)
		Where, *Rc*= Circulatory ratio, π = "Pi" value that is 3.14,*A* = Area of the basin (km²),*P* = Perimeter (km)	
	Elongation ratio *(Re)*	$Re = (2/Lb)*(A/\pi)^{0.5}$	Schumn (1956)
		Where, *Lb* = Length of basin (km)	
		A = Area of the basin (km²)	
Drainage texture	Drainage density (*Dd*), km.km⁻²	$Dd = Lu/A$	Horton (1945)
		Where, *Lu* = Total stream length of all order	
		A = Area of the basin	
	Stream frequency (*Sf*) (Number. km⁻²)	$Sf = Nu/A$	Horton (1945)
		Nu = Total number of streams of all orders	
		A = Area of the basin (km²)	
	Length of overland flow (*Lg*), km	$Lg = 0.5/Dd$	Horton (1945)
		Where, *Dd* = Drainage density	

parameters (Biswas *et al*., 1999; Patel *et al*., 2012; Balasubramanian *et al*., 2017).

To prioritize sub-watersheds, linear and shape parameters were normalized using the expression as follows:

$$X_i = \frac{X - X_{min}}{X_{max} - X_{min}} \qquad ...(1)$$

Where,
X_i = Normalized data,
X = Actual value of a parameter to be normalized,
X_{min} = Minimum value of the parameter, and
X_{max} = Maximum value of the parameter.

The compound factor (*CF*) was then determined by using the expression as follows:

$$CF = \frac{(L)+(1/S)}{Number\ of\ parameters} \qquad ...(2)$$

Where,
L = Normalized linear parameters, and
S = Normalized shape parameters.

Values of *CF* were used to prioritize ranks of sub-watersheds. Lower CF value of a sub-watershed indicates higher degrees of erosion, and hence requires higher priority for its management. The lowest CF value was assigned as the highest priority (priority rank 1); next higher value was assigned the second priority and so on.
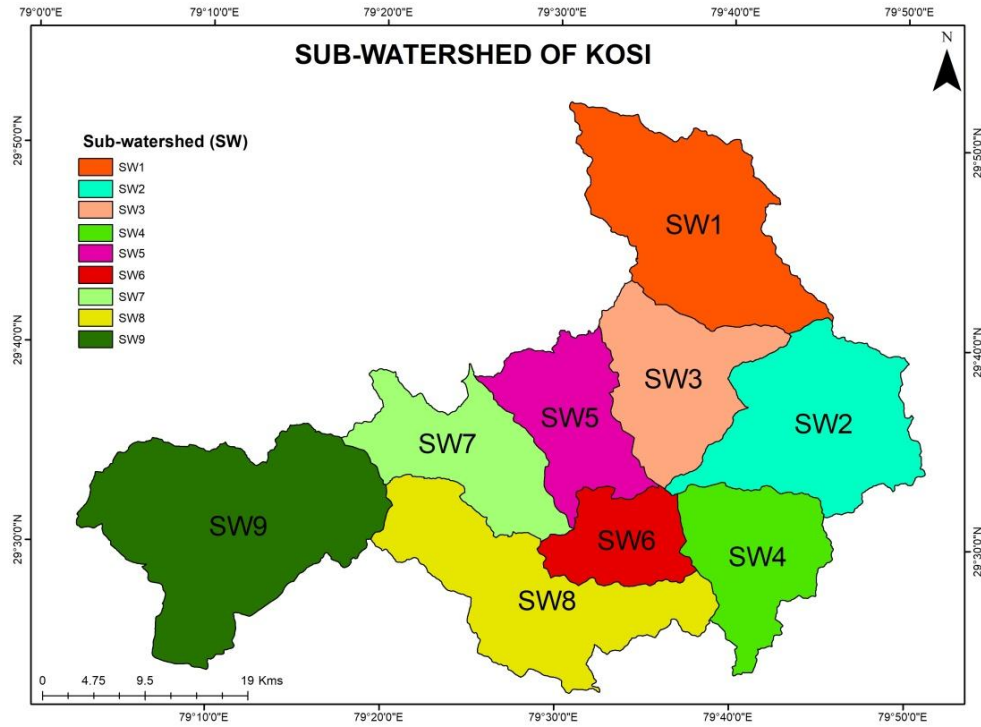
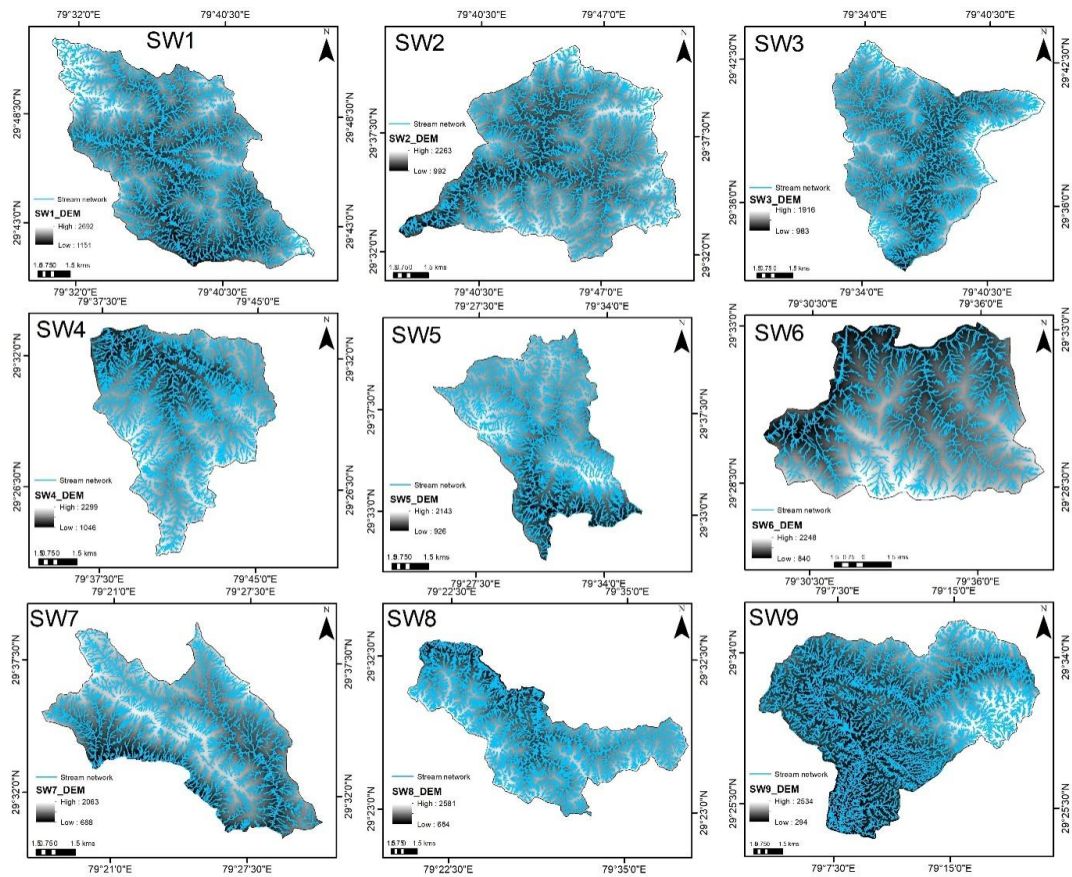**Fig. 3: Division of Kosi basin in sub-watersheds (SW 1 to SW 9)**

Fig. 4: ALOS PALSAR DEM and drainage maps of sub-watersheds of Kosi basin

RESULTS AND DISCUSSION

Results are presented in two sections, (i) details of morphometric analysis in all sub-watersheds, and (ii) prioritization of nine sub-watersheds is elucidated with results for compound factor analysis.

Detail Morphometric Characteristics of Kosi Basin

Detail morphometric characteristics of the basin are elaborated with respect to three broad distinctive aspects of drainage network, basin geometry, and drainage texture.

Drainage network

Drainage network represents the relationship of basin channel characteristics and the stream flow. Hence, parameters within the drainage network aspect of a watershed are significant in quantifying different hydrological processes that reflect the natural evolution of the basin. Linear parameters of the Kosi watershed were strongly associated with the clearly defined path called channels of the stream network. The topographical characteristics of the stream patterns of the river stream network or drainage network were investigated. The drainage network characteristics of the Kosi basin are given below.

Stream order (*So*)

Identifying the stream order is one of the primary processes in drainage morphometric analysis of any basin. The Kosi basin area represented a maximum of 7th order stream with dendritic to sub-dendritic pattern (Fig. 5). Out of 9 sub-watersheds, 7 sub-watersheds represented 7th order streams (SW1-5, SW8-9), and 2 sub-watershed represented 6th order streams (SW6-7). A total of 67,497 streams were identified in the study area. Out of 67,497 streams, 52,353 were 1st order, 11,879 were 2nd order, 2,570 were 3rd order, 548 were 4th order, 112 were 5th order, 28 were 6th order, and 7 were 7th order streams (Fig. 5). Generally, the lowest stream order had maximum number of streams, and the higher stream order had less number of streams; whereas highest stream order had only one stream. It could be noted from Fig. 5 that the highest stream segments were in SW9 (12,868) and the lowest stream segments were in SW6 (3,434).
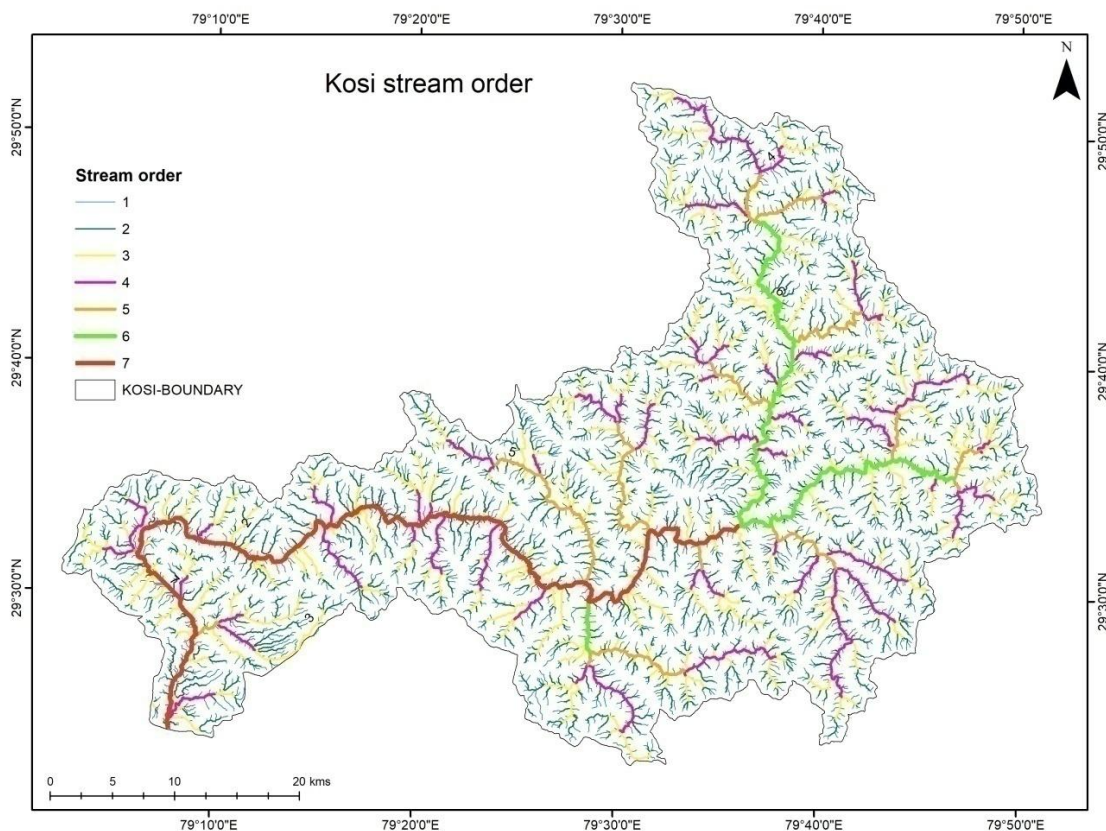

Fig. 5: Stream order map of Kosi basin

Stream length (*Lu*)

The total length of stream of an order was calculated by adding each stream length for the given order. There was a total of 12,015.87 km length of stream network, as extracted from ALOS PALSAR DEM data, for Kosi basin, out of which 6,781.52 km (56.44%) was first order streams, 2,588.55 km (21.54%), 1,312.99 km (10.93%), 702.12 km (5.84%), 345.99 km (2.88%), 162.98 km (1.36%), and 121.72 km (1.01%) were 2nd to 7th order streams, respectively. The length of 1st and 2nd order streams covered nearly 78% of the total *Lu*. Sub-watershed wise analysis of *Lu* showed that SW9 had maximum stream length of 2,403 km, followed by SW8, SW1, SW2, SW4, SW7, SW3, SW5, and SW6. Moreover, watersheds numbers 1-4, 7-8, and 9 had stream lengths more than 1,000 km. This significant variation of *Lu* across sub-watersheds indicated a distinctive property of the drainage network and a change in topographic elevation and slope of the Kosi-basin. Stream length and stream number were further used to calculate values of bifurcation ratio, drainage texture, drainage density, and stream frequency.

Bifurcation ratio (*Rb*) and average bifurcation ratio (*Rbm*)

Computed *Rb* values of the Kosi river basin with sub-watersheds are presented in Table 2. The mean bifurcation ratios (*Rbm*) of the sub-watersheds were 4.63, 4.40, 4.12, 4.28, 4.10, 4.85, 4.67, 4.47, and 4.66 for SW 1-9, respectively. All sub-watersheds had *Rbm* more than 4 indicating the elongated shape of the basin (Khare *et al*., 2014), the control of geological structure over the area, and less permeable rocks with high slope (Pareta and Pareta, 2011). Higher values of *Rb* and *Rbm* were also indicators of early hydrograph peaks with a potential for flash flood during storm events.

Maximum *Rbm* of 4.85 was noted for SW6 amongst all the sub-watersheds, indicating early hydrograph peak (i.e. smaller basin lag time) associated with strong structural control on the drainage development. The minimum *Rbm* (4.10) was observed for SW5 (Table 2), indicating a delayed hydrograph peak with relatively less flash flood risk.

Basin Geometry of Kosi River

The hydrology of any watershed is connected with the watershed geometric parameter, particularly through area-length relationship which reflects peak discharge behaviour or distribution along the flow path of the river channels. Understanding the relationship and quantification of different geometric parameters as investigated in present study varied between sub-watersheds, and helps in analysing the effect of these geometric parameters on peak discharge of the watershed and subsequent hydrological behaviour of the watershed.

Length of basin (*Lb*)

One of the important linear features of a watershed is the length of basin (*Lb*), which according to Schumm (1956) is the longest measurement of the basin or watershed parallel to the principal drainage line.

The basin length of SW1-9 was computed to be 39.02 km, 34.94 km, 29.36 km, 26.72 km, 25.71 km, 16.43 km, 28.43 km, 29.97 km, and 56.23 km, respectively. Therefore, SW9 had the longest basin length; whereas SW6 had the smallest basin length among all the nine sub-watersheds.

Basin area (*A*) and perimeter (*P*)

Basin area (*A*) and perimeter (*P*) signify the contributing area that determines the volume of water generated by rainfall events.

Table 2. Morphometric parameters of Kosi sub-watersheds

Sub-watershed (SW)	Average Bifurcation ratio (*Rbm*)	Drainage density (*Dd*), km.km⁻²	Drainage texture (*Dt*)	Length of Overland Flow (*Lg*), km	Stream frequency (*Sf*), Number.km⁻²	Form factor ratio (*Ff*)	Shape factor ratio (*Rs*)	Compactness coefficient (*Cc*)	Circulatory ratio (*Rc*)	Elongation ratio (*Re*)
SW1	4.63	5.78	109.28	0.086	34.42	0.180	5.52	1.47	0.459	0.480
SW2	4.40	5.84	101.59	0.085	34.08	0.199	5.01	1.47	0.459	0.503
SW3	4.12	6.08	86.54	0.082	33.19	0.200	4.99	1.42	0.494	0.504
SW4	4.28	8.12	128.23	0.061	51.36	0.213	4.67	1.39	0.512	0.521
SW5	4.10	6.23	69.91	0.080	34.12	0.213	4.68	1.63	0.374	0.521
SW6	4.85	6.61	71.43	0.075	35.68	0.356	2.80	1.38	0.523	0.673
SW7	4.67	6.68	74.78	0.074	35.89	0.196	5.08	1.70	0.342	0.500
SW8	4.47	6.79	89.44	0.073	36.76	0.282	3.53	1.84	0.292	0.600
SW9	4.66	6.51	131.53	0.076	34.86	0.116	8.56	1.43	0.484	0.385

The basin area for sub-watersheds varied from 96.22 km^2 (SW6) to 369.07 km^2 (SW9); whereas, the perimeter (*P*) varied from 48.07 km (SW6) to 104.40 km (SW8). The values of *Lb, A* and *P* were further used to calculate the relief ratio, form factor, shape factor, and elongation ratio of the watershed, respectively, using the formulae of Horton (1932, 1945) and Schumm (1956)**.**

Form factor (*Ff*)

Ff represents the shape of the watershed, where *Ff>* 0.79 indicates a perfectly circular basin (Gajbhiye *et al*., 2014). Lesser the value of *Ff*, more the basin would be elongated, and vice versa. A basin with high *Ff* is categorized having peak flow of shorter duration, whereas an elongated basin with low *Ff* could be categorized with lower peak flow with longer duration.

In the present study, minimum and maximum *Ff* were obtained for SW9 (=0.116) and SW6 (=0.356), respectively. *Ff* values of Kosi watershed inferred that all sub-watersheds within the Kosi basin were elongated in shape having flatter peak-flows with longer durations. Subsequently, flatter peak-flows with longer duration experiences with no rapid peak discharge at the outlet of the watershed creating enough potential for flood management activities in terms of handling amount of discharge (i.e. lower peak flows) and duration of discharge (i.e. longer duration) in elongated Kosi River basin than those of the circular basins of Himalaya.

Shape factor ratio (*Rs*)

Rs gives an impression about the circular character of the watershed; where greater circular character results in the rapid response of the basin after a storm event.

In the present study area, *Rs* was minimum for SW6 (= 2.80) and maximum for SW9 (= 8.56). Therefore, it could be inferred that the SW6 had the longest basin lag time, and SW9 had the shortest lag time.

Drainage texture (*Dt*)

Drainage texture (*Dt*) reflects the basic lithology, infiltration capacity, and relief of the topography. It is defined as the total number of stream segments of all orders per unit basin perimeter (Horton, 1945). The classification of *Dt* was given by Smith (1950) where *Dt* values within 4 to 10 represent medium, 10 to 15 represent fine, and greater than 15 represents ultra-fine texture.

Since all nine sub-watersheds of this study area had *Dt* greater than 69.91 (Table 2), it was concluded that the entire Kosi basin had ultra-fine drainage texture. This implied the dominance of impermeable soft rock with low resistance against erosion, and thus it has more risk of soil erosion.

Compactness Coefficient (*Cc*)

Cc is calculated as a ratio of basin perimeter divided by the circumference of the circle of the area of a particular sub-watershed (Balasubramanian *et al*., 2017). Generally, a circular basin has the shortest time of concentration before peak flow.

The values of *Cc* for all the sub-watersheds of this study were 1.47, 1.47, 1.42, 1.39, 1.63, 1.38, 1.70, 1.84, and 1.43, respectively for SW1 to SW9. Consequently, SW8 had the greatest deviation from the circular pattern, and on the basis of *Cc* values alone, SW8 have the longest *Tc*, i.e. time of concentration before peak flow. Similarly, SW6 had the lowest deviation from the circular nature amongst all the sub- watersheds, and should have the shortest time of concentration before peak flow. *Cc* values of this study indicated that all the sub-watersheds belonged to low to high elongated watersheds yielding comparatively greater time of concentration before the onset of peak flow.

Circularity ratio (*Rc*)

Circularity ratio (*Rc*) is the ratio of basin or watershed area to the area of a circle having the equal perimeter as that of the basin (Miller, 1953; Strahler, 1964). It is mainly controlled by geological structure, lithological character, relief, slope, climate variability, stream frequency, stream length, and landuse and land cover change (LULC) within the basin area (Patel and Srivastava, 2013; Pendke et al., 2018; Singh et al., 2020). *Rc* varies between 0 and 1, where zero represent line and one or unity represents circle (Bali *et al*., 2012). The sub-watersheds with *Rc* less than 0.5 will have an elongated basin, while *Rc* greater than 0.5 will be more of a circular shape indicative of a structurally controlled basin (Balasubramanian *et al*., 2017).

For Kosi sub-watersheds, the *Rc* values were 0.459, 0.459, 0.494, 0.512, 0.374, 0.523, 0.342, 0.292, and 0.484 for SW1 to SW9, respectively. Therefore, *Rc* values indicated that SW1-3, SW5, SW7-9 were mostly elongated in shape; and SW4 and SW6 were mostly circular in shape. Moreover, lower *Rc* values

could be linked to slower discharges from respective sub-watersheds.

Elongation ratio (*Re*)

Elongation ratio (*Re*) is computed as the ratio of diameter of a circle having same area as that of the basin to the maximum basin length (Schumm, 1956). The basin can be categorized according to *Re*, i.e., circular (*Re* = 0.9–0.10), oval (*Re* = 0.8–0.9), less elongated (*Re* = 0.7–0.8), elongated (*Re* = 0.5–0.7), and more elongated (*Re* < 0.5).

The *Re* values of Kosi sub-watersheds were found to be 0.480, 0.503, 0.504, 0.521, 0.521, 0.673, 0.500, 0.600, and 0.385 for SW1 to SW9, respectively. Therefore, it was concluded that SW2 to SW8 were elongated, and SW1 and SW9 were more elongated. The *Re* values of Kosi sub-watersheds were noted to corroborate well with the estimation of previous parameters (i.e., *Ff* and *Re*) where the elongated shapes of sub-watersheds were reflected.

Drainage Texture of Kosi Basin

Drainage texture reflects the lithology of the basin through which drainage pattern of river basin, including infiltration capacity and relief of the topography, can be studied. Drainage texture analysis helps in erosion risk-assessment of a river basin.

Drainage density (*Dd*)

Drainage density is a measurement of the sum of the channel lengths per unit area, and reveals the number of channels in a watershed. Highly permeable earth surface and dense vegetation area of low relief exhibits low *Dd*; whereas, impermeable subsurface having sparse vegetation area and high relief exhibits higher *Dd* (Suresh, 2007; Balasubramanian *et al*., 2017). Smith (1950) had classified *Dd* as: extremely low (0–1), low (1–2), moderate (2–4), moderately high (4–6), and high (> 6).

The *Dd* values of SW1-9 within Kosi basin were computed as 5.78, 5.84, 6.08, 8.12, 6.22, 6.61, 6.68, 6.79, and 6.51 km.km^{-2}, respectively (Table 2, Fig. 6). Among the 9 sub-watersheds, SW1 and SW2 had moderately high *Dd*, and rest of the sub-watersheds had high drainage density indicating the weak or impermeable sub-surface material, sparse vegetation in watershed area, and mountainous relief (Bali *et al*., 2012).
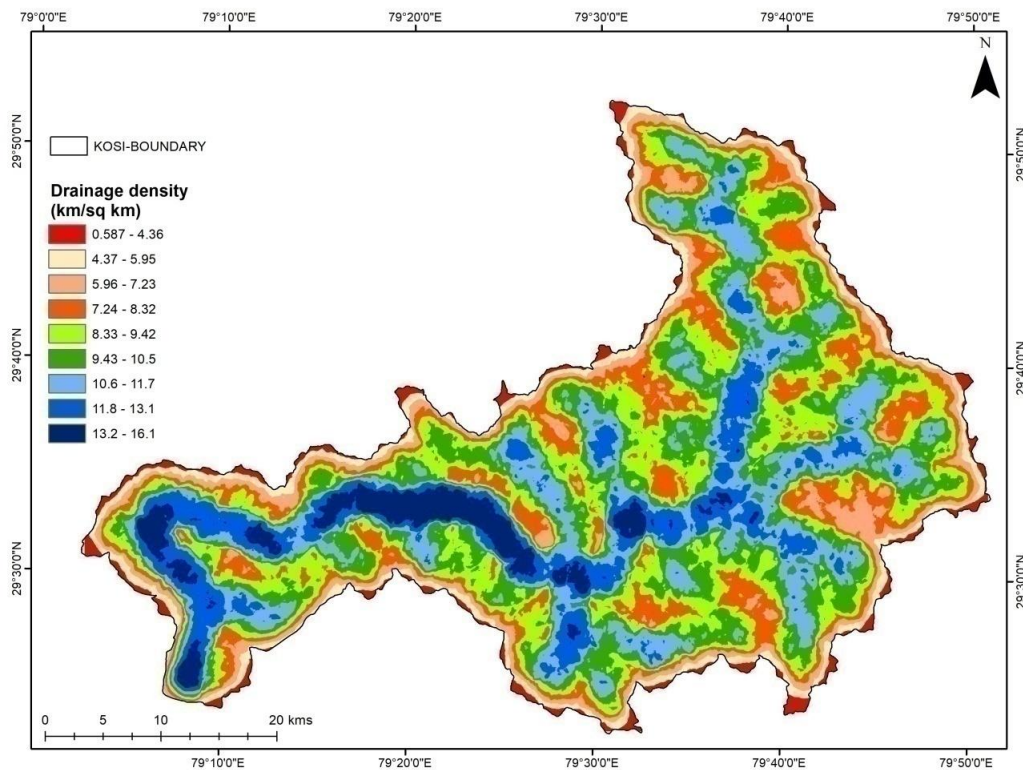

Fig. 6: Drainage density map of Kosi basin

Stream frequency (*Sf*)

Stream frequency (*Sf*) denotes the total number of streams of all orders per unit watershed area (Horton 1932). *Sf* primarily depends on lithology of the basin and reveals the texture of the drainage network (Balasubramanian *et al*., 2017).

Sf values for sub-watersheds within Kosi basin were found to vary between 33.19 km^{-2} (SW3) and 51.36 km^{-2} (SW4) (Table 2). The observed *Sf* values of Kosi basin indicated positive correlation with the *Dd* of all the sub-watersheds, suggesting increase in stream numbers with respect to increase in value of drainage density.

Length of overland flow (*Lg*)

The *Lg* is inversely related to the average channel slope, and can be considered as an indicator for channel erosion (Patel *et al*., 2012).

The *Lg* values were found to vary between 0.086 km and 0.061 km for SW1-9 (Table 2). The *Lg* values reflected that all sub-watersheds of Kosi basin exhibit channel erosion.

Prioritization of Sub-watersheds

Compound factor (*CF*)

The drainage pattern presented for Kosi basin highlighted the geospatial relationships among the river, streams, and rock resistance, slope, structural control as well as the geological status of the basin. Using the morphometric investigation, the prioritization of Kosi sub-watersheds was carried out. Table 2 represents the values of 10 parameters (5 linear, 5 shape parameters) that were selected for prioritization analysis. Linear parameters included average bifurcation ratio (*Rbm*),

drainage density (*Dd*), drainage texture (*Dt*), length of overland flow (*Lg*), stream frequency (*Sf*). The shape parameters were circularity ratio (*Rc*), form factor (*Ff*), elongation ratio (*Re*), shape factor ratio (*Rs*), and compactness coefficient (*Cc*). Compound factor was calculated for all sub-watersheds of the Kosi River basin. Generally, lower the *CF* value of a sub-watershed, higher is the degrees of erosion.

Table 3 and Fig. 7 represents the final score and ranking of the nine sub-watersheds of the Kosi basin. In Kosi River basin, *CF* value for SW5 was lowest (12.63) and assigned prioritized rank 1; whereas, *CF* value for SW9 was highest (20.38) and was assigned lowest priority rank 9. It could be noted from Table 3 that SW5 to SW7 had lower CF value (12.63 to 13.48), indicating higher erosion risk, and had the higher priority with ranks of 1-3. These three sub-watersheds (SW5 to SW7) encompasses 21.26% of total Kosi basin area. Similarly, SW3, SW8, and SW2 with CF values 14.24, 14.73, 15.84, respectively, had medium priorities with ranks 4 to 6 and encompassing 35.94% of total Kosi basin area. The sub-watershed SW1, SW9, and SW4 with higher CF values (16.76- 20.38) had lower priorities with ranks 7 to 9 encompassing 42.8% of total Kosi basin area. Lower values of *CF* denote the possible soil erosion in particular watersheds and vice versa. SW5, SW6, and SW7 were considered as a high priority sub-watersheds based on lower *CF* values, which signify the highly erosion intensive nature of the sub-watersheds, where it is necessary to implement soil conservation measures on priority to prevent soil erosion.

CONCLUSIONS

The present study used GIS techniques for morphometric analysis, and the prioritization of 9 sub- watersheds

Table 3. Calculation of compound factor and prioritization ranks

| Sub-watershed	Linear factor					Shape factor					Compound factor (CF)	Prioritized ranks	Interpretation
	Dd	*Dt*	*Rb*	*Lg*	*Sf*	*Ff*	*Rs*	*Re*	*Cc*	*Rc*			
SW1	0.0521	1	0.0416	0	0.3144	0	1	0.0562	0.2416	0.0522	16.76	7	Low
SW2	0.0567	1	0.0425	0	0.3349	0	1	0.0632	0.2642	0.0540	15.84	6	Medium
SW3	0.0694	1	0.0467	0	0.3829	0	1	0.0635	0.2547	0.0614	14.24	4	Medium
SW4	0.0629	1	0.0329	0	0.4002	0	1	0.0691	0.2641	0.0671	20.38	9	Low
SW5	0.0881	1	0.0576	0	0.4875	0	1	0.0690	0.3172	0.0360	12.63	1	High
SW6	0.0916	1	0.0669	0	0.4990	0	1	0.1297	0.4190	0.0683	12.68	2	High
SW7	0.0884	1	0.0615	0	0.4794	0	1	0.0622	0.3079	0.0299	13.48	3	High
SW8	0.0752	1	0.0492	0	0.4105	0	1	0.0979	0.4797	0.0031	14.73	5	Medium
SW9	0.0489	1	0.0349	0	0.2646	0	1	0.0319	0.1556	0.0436	19.71	8	Low
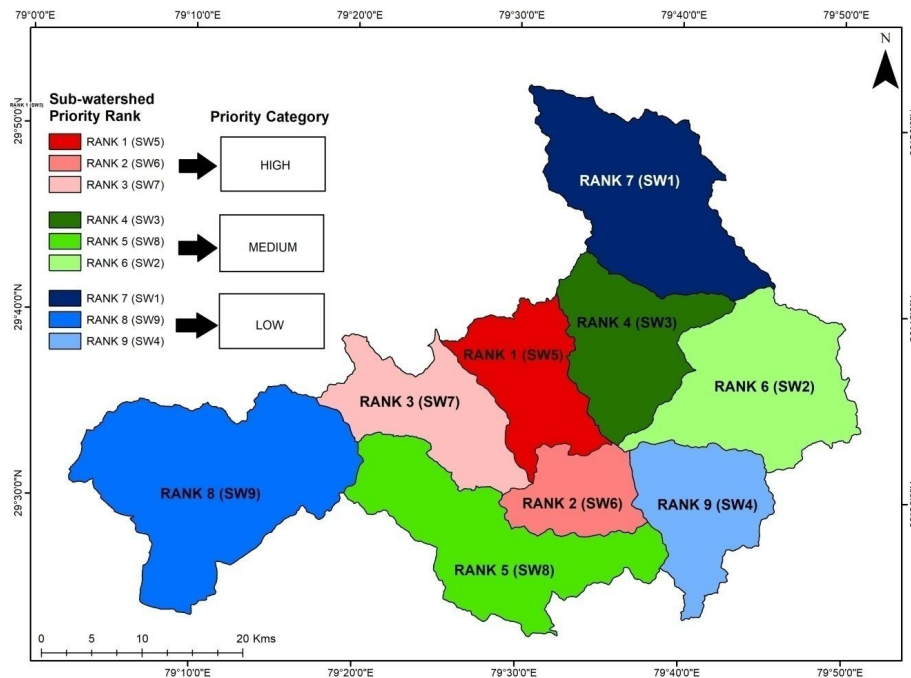
Fig. 7: Prioritization of sub-watersheds of the Kosi basin

in Kosi River basin was further carried out using compound factor concept. Sub-watersheds SW5, SW6, and SW7 were under high priority category that encompasses a total area of 396.18 km^2; SW3, SW8, and SW2 were under medium priority category with total area of 669.75 km^2; and SW1, SW9, and SW4 with total area of 796.67 km^2 were in low priority category for appropriate conservation measures. The results indicated that the sub-watersheds SW5-7 are prone to soil erosion and need appropriate soil and water conservation measures. Targeting areas having stream of stream orders 1 to 3 for construction of check dams, improving vegetative cover within sub-watersheds SW 5-7 could be one way to address the problem soil erosion and simultaneously recharge the groundwater. Prioritization of sub-watershed could be used for planning location-specific bio-engineering measures that can help in conservation and management natural resources at sub-watershed levels in Kosi River basin.

ACKNOWLEDGEMENT

REFERENCES

Balasubramanian A; Duraisamy K; Thirumalaisamy S; Krishnaraj S; Yatheendradasan R K. 2017. Prioritization of sub-watersheds based on quantitative morphometric analysis in lower Bhavani basin, Tamil Nadu, India using DEM and GIS techniques. Arab J. Geosci., 10, 552. https://doi.org/10.1007/s12517-017-3312-6

Bali R; Agarwal K K; Ali S N; Rastogi S K; Krishna K. 2012. Drainage morphometry of Himalayan Glacio-fluvial basin, India: Hydrologic and neotectonic implications. Environ. Earth Sci., 66, 1163–1174.

Ballav S; Mukherjee S; Gosavi V E; Dimri A P. 2021. Projected changes in winter-season wet days over the Himalayan region during 2020-2099. Theor. Appl. Climatol., 146, 883-895. https://doi.org/10.1007/s00704-021-03765-z

Biswas S; Sudhakar S; Desai V R. 1999. Prioritisation of sub-watersheds based on morphometric analysis of drainage basin: A remote sensing and GIS approach. J. Indian Soc. Remote Sens., 27, 155-166. https://doi.org/10.1007/BF02991569

Chandniha S K; Kansal M L. 2017. Prioritization of sub-watersheds based on morphometric analysis using geospatial technique in Piperiya watershed, India.

Appl. Water Sci., 7, 329–338. https://doi.org/10.1007/s13201-014-0248-9

Chandrashekar H; Lokesh K V; Sameena M; Roopa J; Ranganna G. 2015. GIS-based morphometric analysis of two reservoir catchments of Arkavati River, Ramanagaram district, Karnataka. Aqua Proc., 4, 1345-1353. https://doi.org/10.1016/j.aqpro.2015.02.175

Gajbhiye S; Mishra S K; Pandey A. 2014. Prioritizing erosion-prone area through morphometric analysis: an RS and GIS perspective. Appl. Water Sci., 4(1), 51-61.

Gosavi V E; Thakur P; Kumar K. 2018. Study of drainage system and its hydrological implications using geo-spatial techniques: A morphometric analysis in Mohalkhad watershed of Kullu district, Himachal Pradesh, India. Environ. Int. J. Adv. Res., 6(12), 456-463.

Gupta M; Srivastava P K. 2010. Integrating GIS and remote sensing for identification of groundwater potential zones in the hilly terrain of Pavagarh, Gujarat, India. Water Int., 35(2), 233-245.

Horton R E. 1932. Drainage-basin characteristics. Eos. Trans. Am. Geophys. Uni., 13, 350-361. https://doi.org/10.1029/TR013i001p00350

Horton R E. 1945. Erosional development of streams and their drainage basins; hydrophysical approach to quantitative morphology. Geol. Soc. Am. Bull., 56, 275-370.

Hua O; Eriksson M; Vaidya R A. 2009. Water Storage: A Strategy for Climate Change Adaptation in the Himalayas. Sustainable Mountain Development, International Centre for Integrated Mountain Development (ICIMOD), Kathmandu, Nepal, No. 56, pp: 60.

Khare D; Mondal A; Mishra P K; Kundu S; Meena P K. 2014. Morphometric analysis for prioritization using remote sensing and GIS techniques in a hilly catchment in the state of Uttarakhand, India. Indian J. Sci. Technol., 7 (10), 1650-1662.

Kumar A; Gupta A K; Bhambri R; Verma A; Tiwari S K; Asthana A K L. 2018. Assessment and review of hydrometeorological aspects for cloudburst and flash flood events in the third pole region (Indian Himalaya). Polar Sci., 18, 5-20. https://doi.org/10.1016/j.polar.2018.08.004

Kumar K; Tiwari A; Mukherjee S; Agnihotri V; Verma R K. 2019. Water At a Glance. Technical Report, Uttarakhand, G. B. Pant National Institute of Himalayan Environment and Sustainable Development, Almora, Uttarakhand, India, pp:37.

Magesh N S; Chandrasekar N; Soundranayagam J P. 2011. Morphometric evaluation of Papanasam and Manimuthar watersheds, parts of Western Ghats, Tirunelveli district, Tamil Nadu, India: A GIS approach. Environ. Earth Sci., 64, 373-381. https://doi.org/10.1007/s12665-010-0860-4

Magesh N S; Jitheshlal K V; Chandrasekar N; Jini K V. 2012. GIS based morphometric evaluation of Chimmini and Mupily watersheds, parts of Western Ghats, Thrissur District, Kerala, India. Earth Sci. Inform., 5, 111-121. https://doi.org/10.1007/s12145-012-0101-3

Mali S S; Naik S K; Raghav D K; Kumar O; Singh A K. 2021. Runoff, Sediment and Nutrients Loss from Two Small Watersheds in Eastern Plateau and Hill Region of India. J. Agric. Eng., 58(2), 149-166.

Miller V C. 1953. A quantitative geomorphic study of drainage basin characteristics in the Clinch Mountain area, Virginia and Tennessee. Project NR 389042, Columbia University, Department of Geology, ONR, Geography Branch, N Y., Tech. Rept. 3.

Mukherjee S; Ballav S; Soni S; Kumar K; De U K. 2015a. Investigation of dominant modes of monsoon ISO in the northwest and eastern Himalayan region. Theo. Appl. Climatol., 125(3-4), 489-498. https://doi.org/10.1007/s00704-015-1512-0

Mukherjee S; Joshi R; Prasad R; Vishvakarma S; Kumar K. 2015b. Summer monsoon rainfall trends in the Indian Himalayan region. Theo. Appl. Climatol., 121(3-4), 789-802. https://doi.org/10.1007/s00704-014-1273-1

Mukherjee S; Joshi R; Kumar K. 2018. Compendium of Meteorological Data 2012-2016. Field Station Kosi-Katarmal, Almora, Uttarakhand, Indian Himalayan region, G.B. Pant National Institute of Himalayan Environment, pp: 63.

Mukherjee S; Hazra A; Kumar K; Nandi S K; Dhyani P P. 2019. Simulated projection of ISMR over Indian Himalayan region: Assessment from CSIRO-CORDEX South Asia experiments. Meteorol. Atmos. Phys., 131, 63-79. doi: 10.1007/s00703-017-0547-4

Mukherjee S. 2021. Nonlinear recurrence quantification of the monsoon-season heavy rainy-days over northwest

Prioritization of Sub-watersheds of Kosi River Basin Using Morphometric Analysis and Geospatial Tools

Himalaya for the baseline and future periods. Sci. Total Environ., 789, 147754. https://doi.org/10.1016/j.scitotenv.2021.147754

Nag S K; Chakraborty S. 2003. Influence of rock types and structures in the development of drainage network in hard rock area. J. Indian Soc. Rem. Sens., 31, 25-35. https://doi.org/10.1007/bf03030749

Nooka Ratnam K; Srivastava Y K; Venkateswara Rao V. 2005. Check dam positioning by prioritization of micro-watersheds using SYI model and morphometric analysis - Remote sensing and GIS perspective. J. Indian Soc. Rem. Sens., 33, 25-38. https://doi.org/10.1007/BF02989988

Pankaj A; Kumar P. 2009. GIS-based morphometric analysis of five major sub-watersheds of Song River, Dehradun district, Uttarakhand with special reference to landslide incidences. J. Indian Soc. Rem. Sens., 37, 157-166. https://doi.org/10.1007/s12524-009-0007-9

Pareta K; Pareta U. 2011. Quantitative morphometric analysis of a watershed of Yamuna Basin, India using ASTER (DEM) data and GIS. Int. J. Geomatics Geosci., 2(1), 248-269.

Patel D; Srivastava P K. 2013. Flood hazards mitigation analysis using remote sensing and GIS: correspondence with town planning scheme. Water Resour. Manage., 27, 2353-2368.

Patel D P; Dholakia M B; Nareh N; Srivastava P K. 2011. Water harvesting structure positioning by using geo-visualization concept and prioritization of mini-watersheds through morphometric analysis in the Lower Tapi Basin. J. Indian Soc. Rem. Sens., 40(2), 299-312.

Patel D P; Gajjar C A; Srivastava P K. 2012. Prioritization of Malesari mini-watersheds through morphometric analysis: A remote sensing and GIS perspective. Environ. Earth Sci., 69, 2643-2656. https://doi.org/10.1007/s12665-012-2086-0

Pendke M S; Sreenivasan G; Bhuibhar B W; Kadale A S; Khodke U M. 2018. Impact of Morphometric Parameters and Change in Land Use on Peak Runoff Rates of Pingalgarh Watershed Using Geospatial Techniques. J. Agric. Eng., 55(1), 72-81.

Prakash K; Singh S; Shukla U K. 2016a. Morphometric changes of the Varuna river basin, Varanasi district, Uttar Pradesh. J. Geomat., 10, 48-54.

Prakash K; Mohanty T; Singh S; Chaubey K; Prakash P. 2016b. Drainage morphometry of the Dhasan river basin, Bundelkhand craton, central India using remote sensing and GIS techniques. J. Geomat., 10(2), 121-132.

Raina V K; Srivastava D. 2008. Glacier atlas of India. Geological Society of India, Bangaluru, pp: 315. ISBN: 978-81-85867-80-9.

Samal D R; Gedam S S; Nagarajan R. 2015. GIS based drainage morphometry and its influence on hydrology in parts of Western Ghats region, Maharashtra, India. Geocart. Int., 30, 755-778. https://doi.org/10.1080/10106049.2014.978903

Schumm S A. 1956. Evolution of drainage systems and slopes in Badlands at Perth Amboy, New Jersey. Geol. Soc. Am. Bull., 67, 597-646. https://doi.org/10.1130/0016-7606

Singh M C; Singh R; Yousuf A; Prasad V. 2021. Geo-informatics based morphometric analysis of a reservoir catchment in *Shivalik* foothills of North-West India. J. Agric. Eng., 58(3), 286-299.

Singh N; Jha M; Tignath S; Singh B N. 2020. Morphometric analysis of a badland affected portion of the Mandakini River sub-watershed, central India. Arab J. Geosci., 13, 423. https://doi.org/10.1007/s12517-020-05405-8

Singh S; Kanhaiya S; Singh A; Chaubey K. 2019. Drainage network characteristics of the Ghaghghar River Basin (GRB), Son Valley, India. Geol. Ecol. Landscape, 3, 159-167. https://doi.org/10.1080/24749508.2018.1525670

Smith K G. 1950. Standards for grading texture of erosional topography. Am. J. Sci., 248, 655-668. https://doi.org/10.2475/ajs.248.9.655

Sreedevi P D; Sreekanth P D; Khan H H; Ahmed S. 2013. Drainage morphometry and its influence on hydrology in a semi-arid region: Using SRTM data and GIS. Environ. Earth Sci., 70, 839-848. https://doi.org/10.1007/s12665-012-2172-3

Srivastava P K; Mukherjee S; Gupta M; Singh S. 2011. Characterizing monsoonal variation on water quality index of River Mahi in India using geographical information system. Water Qual. Expo. Health, 2(3), 193-203. doi:10.1007/s12403-011-0038-7

Srivastava P K; Gupta M; Mukherjee S. 2012a. Mapping spatial distribution of pollutants in groundwater of a tropical area of India using remote sensing and GIS. Appl. Geomat., 4(1), 21-32. https://doi.org/10.1007/s12518- 011-0072-y

Srivastava P K; Han D; Gupta M; Mukherjee S. 2012b. Integrated framework for monitoring groundwater pollution using a geographical information system and multivariate analysis. Hydrol. Sci. J., 57(7), 1453-1472. doi:10.1080/02626667.2012.716156

Strahler A N. 1957. Quantitative analysis of watershed geomorphology. Eos. Trans. Am. Geophys. Union, 38, 913-920. https://doi.org/10.1029/TR038i006p00913

Strahler A N. 1964. Quantitative Geomorphology of Drainage Basins and Channel Networks. In: Chow V T (Ed.) Handbook of Applied Hydrology, McGraw-Hill, New York, 4-39-4-76.

Suresh R. 2007. Soil and Water Conservation Engineering. Standard Publishers and Distributors, Delhi, 799-812.

Sushanth K; Bhardwaj A. 2019. Assessing Geomorphologic Characteristics and Demarcating Runoff Potential Zones using RS and GIS in *Patiala-Ki-Rao* Watershed of *Shivalik* Foot-Hills, Punjab. J. Agric. Eng., 56(1), 45-54.

Thomas J; Sabu J; Thrivikramaji K P. 2010. Morphometric aspects of a small tropical mountain river system, the Southern Western Ghats, India. Int. J. Digit. Earth, 3, 135-156.

Withanage N S; Dayawansa N D K; De Silva R P. 2015. Morphometric analysis of the Gal Oya river basin using spatial data derived from GIS. Trop. Agric. Res., 26, 175-188. https://doi.org/10.4038/tar.v26i1.8082

INFORMATION FOR AUTHORS

The Journal of Agricultural Engineering contains only original research papers, and submission of a manuscript will be considered to imply that no similar manuscript has been or is being submitted elsewhere. Soft copy of the manuscript in MS Word, along with a request letter, should be submitted to the Chief Editor through website of ISAE, IndianJournals.com, or through e-mail (jae.chiefeditor@gmail.com). The manuscript is to be written in English language, typed in double space on A-4 size. The e-mail address and mobile number of the corresponding author must be indicated for further correspondence.

The subject matter reflects the full range and interdisciplinary nature of research in engineering and allied disciplines for agriculture. Manuscripts describing engineering innovations for field crops, horticulture, livestock, fisheries, and those reporting research seeking to understand and model the physical processes underlying agricultural systems are welcome.

The following three types of manuscripts are invited for publication. Research manuscripts are the normal type of papers published and make up the main content of the Journal. They should not normally exceed 15 Journal pages. Research notes enable important findings to be speedily communicated, and facilitate the reporting of work not meriting a full-length paper. They should not exceed five Journal pages. Review papers are intended to be in-depth studies of the state-of-the-art in the chosen subjects. They should not normally exceed fifteen Journal pages.

The manuscript should be arranged as follows:

Softcopy in MS Word (Times New Roman), Font size for various sections are: Font: Times New Roman, Title heading: 14 pt bold upper lower, Author name: 11.5 pt italic bold u/L, Abstract heading: 11pt bold cap, Abstract text: 9 pt normal, Text: 10.5 pt normal, Sub-heading : 9 pt Cap bold centre, Fig/ table caption: 10 pt bold u/l centre, Conclusion and references: same as text, Footnote: 8 pt italics.

- *Title, authors'name(s), affiliations, addresses.* Please necessarily include e-mail address of the corresponding author.

- *Abstract and key words.* The Abstract of not more than 200 words should state the problem investigated, outline the methods used and summarize the main conclusions. A list of maximum seven keywords or phrases must follow the abstract.

- *Main body text.* The main body of the text should be divided under suitable headings, in proper hierarchical order. Some or all of the following headings may be appropriate.

    - *Introduction:* This should explain the problem investigated, review of recent (*not older than 10 years, unless of classical nature*) related studies, and statement on the intention of the present manuscript. The objective(s) of the reported investigation must be stated.

    - *Materials and Methods*: Include theoretical considerations appropriate to explain or develop a theory to shed light on a problem or to correlate experimental results, design of experiment, experimental procedures and details, technical details of instruments/ equipment used, statistical procedures used, as applicable

    - *Results and Discussion*: The results should be presented with reference to appropriate figures and tables. The most appropriate presentations should be chosen and tabulated data should not duplicate that shown graphically. The discussion must include the comparison of findings with the previous research studies done

    - *Conclusions:* Research and Review papers must have this final section, but it is optional in Research Notes. Conclusions emerging from the work should be succinctly summarized. These conclusions must have been discussed in the manuscript and new material must not be introduced at this stage. The contents of the Abstract and Conclusions should not be repetitive.

- *List of symbols*

- *Acknowledgments:* Optional.

- *References:* Citations of references in the text should be in the format of surnames of authors, followed by the year of publication of the appropriate reference, separated by a semi colon. The artifice "Leading author *et al*." should be used in the text for multiple (more than two) authorship papers. Each reference should give the names of all authors (or, if anonymous, the name of the organisation), the year of publication, the title in that order. Some examples of references are given below.

    In the text: "Previous work has shown (Hammer and Langhans, 1972; Federer, 1955) ..."

    In the references 1ist (to journals):
    Sharma P; Sharma S R; Mittal T C. 2020. Effects and application of ionizing radiation on fruits and vegetables: A review. J. Agric. Eng., 57 (2), 97-126.
    Reference list (to books): **Saldivar S O S.** 2015. Snack Foods: Types and Composition. Reference Module in Food Science Encyclopaedia of Food and Health, Elsevier, 13-18.

- *Appendices:* It may be appropriate to place detailed mathematical derivations in appendices, rather in the main body of the text.

- *Figure captions:* These should be listed, together with any 'key' information necessary to aid interpretation.

- *Tables:* Each table must be placed on a separate page after References, and chronologically numbered throughout the text (with Arabic numerals), and referred to as Table 1, Table 2, etc. There must be a caption (Table 1. Estimated saturated hydraulic conductivity using different particle sizes) at the top of each Table.

- *Figures*: Figure 1, Figure 2, etc. Figure captions should be placed beneath each figure (Fig. 1: Effect of germination and roasting on colour of chickpea), and should also be placed in separate page after References. The publisher will suitably organise them after acceptance of the manuscript.

All illustrations, whether line drawings, graphs or photographs, are presented as figures and are given numbers (e.g. Fig. 1) in ascending numerical order as reference is first made to each in the text. All graphs must be submitted in EXCEL software embedded in the Word file, and the respective data made available in a separate spreadsheet included with the softcopy of the manuscript. All figures must be in pleasing colours in good contrast. The style of graphs may be seen in any recent issue of the Journal. Softcopies of the line drawings is acceptable, without title, provided they are in printable quality.

Indian Society of Agricultural Engineers
Executive Council, 2021-2024

President	Shyam Narayan Jha	snjha_ciphet@yahoo.co.in
Immediate Past President	Indra Mani	maniindra99@gmail.com
Vice President (Activity Council)	D.M. Kadam	dmkadam11k@gmail.com
Vice President (Technical Council)	Ambrish Kumar	aktswc@gmail.com
Secretary General	P.K. Sahoo	sahoopk1965@gmail.com
Secretary-I	Tapan Kumar Khura	tapankhura2020@gmail.com
Secretary-II	Chandra Shekhar	agm.engg@indiaseeds.com
Treasurer	Abhay Kumar Thakur	drakthakur65@gmail.com
Editor-in-Chief (Journal of Agricultural Engineering)	Dipankar De	dipankar52@gmail.com
Editor-in-Chief (Agricultural Engineering Today)	D.K. Singh	isae.aet2019@gmail.com
Chief Editor (E-Newsletter)	Chandra Shekhar	agm.engg@indiaseeds.com
Director (Education, Research, Extension & Placement)	U.M. Khodke	umkhodke@rediffmail.com
Director (Membership & Public Relations)	M.S. Seveda	sevda_mahenda@rediffmail.com
Director (Business & Industry)	D S Balachandra Babu	balachandra.babu@gmail.com
Director (International Co-operation)	Ashutosh Singh	asingh47@uoguelph.ca
Director (Awards)	K.P. Singh	kp.kp.24@gmail.com
Director (Farm Machinery & Power)	T. Senthilkumar	thasekumar@gmail.com
Director (Processing, Dairy & Food Engineering)	Prabha Kant Pathak	pkpathak65@gmail.com
Director (Soil & Water Engineering)	B.C. Kusre	kusrebharat@gmail.com
Director (Energy & other Areas)	Atul Mohod	atulmohod72@gmail.com
Director (State Services)	Rajeev Choudhary	rajeevchoudhary62@gmail.com
Director (E-Services)	S.B. Lal	sblall16@gmail.com
Director (Gender Issues)	Kalpana Rayaguru	rayagurukalpana@yahoo.com
Head (Publication Cell)	M. Hasan	hasaniari40@gmail.com
Co-opted Member	Suchita V. Gupta	suchitavgupta@yahoo.co.in
Co-opted Member	V.R. Sinija	sinijavr@rediffmail.com
Co-opted Member	Manoj Kumar Sharma	ms@spltech.in

Journal of Agricultural Engineering

Contents

INDIAN SOCIETY OF AGRICULTURAL ENGINEERS